

43 (1)  
Copies

**NASA TECHNICAL  
MEMORANDUM**

NASA TM X-53558

December 1966

NASA TM X-53558

**N 67-24268**  
(ACCESSION NUMBER)  
1 284  
(PAGES)  
**TMX-53558**  
(NASA CR OR TMX OR AD NUMBER)

**N 67-24280**  
(THRU)  
1  
(CODE)  
**30**  
(CATEGORY)

**PROCEEDINGS OF THE INTERDISCIPLINARY SYMPOSIUM  
ON APOLLO APPLICATION PROGRAMS (12-13 JANUARY 1966)**

Society of Engineering Science  
Huntsville, Alabama

**NASA**

*George C. Marshall  
Space Flight Center,  
Huntsville, Alabama*

NASA - GEORGE C. MARSHALL SPACE FLIGHT CENTER

---

TECHNICAL MEMORANDUM X-53558

---

PROCEEDINGS  
OF THE  
INTERDISCIPLINARY SYMPOSIUM  
ON  
APOLLO APPLICATION PROGRAMS,  
12-13 JANUARY 1966

SOCIETY OF ENGINEERING SCIENCE  
HUNTSVILLE, ALABAMA

## COOPERATING ORGANIZATIONS

University of Alabama

University of Florida

Illinois Institute of Research

National Aeronautics and Space Administration

U. S. Army Missile Command

The Boeing Company

Brown Engineering Company

Chrysler Corporation

General Electric, Apollo Support Department

Hayes International Corporation

Rohm and Haas

Spaco, Inc.

Thiokol Chemical Corporation

Wyle Laboratories

## SYMPOSIUM COMMITTEE

Rolland G. Sturm, Chairman  
David M. Adams  
Carold Bjork  
Frediano Bracco  
Rudolph Hermann  
William C. Pittman  
Ervin Y. Rodin  
Charlie Scott

## S. E. S. HUNTSVILLE CHAPTER

Ervin Y. Rodin, President  
David M. Adams, Treasurer  
Carold Bjork, Director  
Charles Parr, Secretary  
Rolland G. Sturm, Director  
George von Pragenau, Director

## FOREWORD

The Society of Engineering Science, Huntsville Chapter, organized the Symposium, the proceedings of which are presented on the following pages. The purpose of the two-day meeting was to provide a forum for the presentation and discussion of various ideas in connection with the continuation and utilization of the United States Apollo space program. In fact, the Symposium had been conceived and planned prior to any official definition of aims or goals by the National Aeronautics and Space Administration. This is the reason for the great variety of problems discussed herein; the connecting thread between the various papers is the possibility of future application to what at first was known as Apollo extensions, but now has the name of Apollo Applications.

In the course of preparing for the Symposium, the indefatigable chairman of this event, Dr. Rolland G. Sturm, has suffered a great personal loss. This is why the following resolution was adopted by the Executive Committee of the Society of Engineering Science, Huntsville Chapter: "Be it resolved, that the Proceedings of this Symposium shall be dedicated to the memory of Mrs. Rolland G. Sturm".



PRECEDING PAGE BLANK NOT FILMED.

TABLE OF CONTENTS

	Page	
WELCOME by Ervin Y. Rodin . . . . .	1	
SOME PROBLEMS IN DESIGNING A LUNAR PHOTOGRAPHIC SURVEY MISSION by W. L. Austin and J. L. Harden . . . . .	5	✓
LUNAR TERRAIN ANALYSIS by R. L. Sanders and W. M. Greene. . . . .	21	✓
A DISCUSSION OF PROPOSED LANDING SITES FOR AAP LUNAR MISSIONS by J. R. Rogers . . . . .	39	✓
DEVELOPMENT OF A LUNAR PHOTOMETRIC FUNCTION FROM EXPERIMENTAL DATA by E. F. Snyder . . . . .	61	✓
ANALYSIS AND CORRELATION OF THERMODYNAMIC CYCLES FOR SPACE APPLICATIONS by D. M. Adams . . . . .	117	✓
MATHEMATICAL ADVANCES IN THE THEORY OF ONE DIMENSIONAL FLOW by Ervin Y. Rodin . . . . .	143	✓
LOW FREQUENCY RADIO ASTRONOMY IN SPACE by N. F. Six, G. R. Lebo and A. G. Smith . . . . .	161	✓
REMOTE SENSING WITH OPTICAL CROSS-CORRELATION METHODS by F. R. Krause and M. J. Fisher . . . . .	191	✓
SOME CONCEPTS FOR AN EMPLACED SCIENTIFIC STATION ON THE LUNAR SURFACE by R. Shelton. . . . .	215	✓
SIMULATED WEIGHTLESSNESS UNDER NEUTRAL BUOYANCY by R. D. Dean and R. P. Langan. . . . .	229	✓
DEVELOPMENT OF A DEVICE FOR PHYSICAL CONDITIONING DURING WEIGHTLESSNESS by G. Chase, C. Grave J. Goode and G. Graham . . . . .	241	✓
HYPersonic NONEQUILIBRIUM FLOW AT RE-ENTRY OF SPACE VEHICLES AND ITS THERMODYNAMIC RELATIONS by Rudolf Hermann . . . . .	249	✓

## WELCOME

by

Ervin Y. Rodin

I welcome you to our Symposium on Apollo Applications; a meeting which marks at least two "firsts". The first step is the fact that what is now called Apollo Applications, but which probably will change its name many times in the future, is now going to be discussed in the form of a symposium for the first time. The second first is for the Huntsville Chapter of the Society of Engineering Science: this is our first symposium. I would like to say a few words about both of these things. I shall start with the one on which less money was, is being, and shall be spent than on Apollo Applications: Our Society.

In the last few decades advances made both in engineering and research have reached such staggering proportions that it became entirely impossible for any one person to have an all encompassing knowledge of the kind that 19th century scientists used to have. Some of this is of course unavoidable; however, we can blame only ourselves for a significant portion of this inability for the assimilation of more knowledge. In particular, I am sure that all of us here have encountered many times the basic communication and research gap between engineers and scientists. There are frustrating situations when the engineer cannot interpret the results of the research worker or when the research worker comes up with conditions and requirements unattainable by the engineer, or when a problem defies idealization and thus transcends and cuts across the boundaries of many disciplines.

In order to meet such problems and to try to find answers for them, a group of eminent scientists and engineers from many different fields of endeavor got together and founded the Society of Engineering Science. This happened at Purdue University about four years ago.

However, a few of us here in Huntsville felt that what the National Society had to offer was not sufficient; we wanted a more concentrated program, right on the local scene and level. So, just about a year ago we formed the first Professional Chapter of the Society.

I believe that this first year of ours was a successful one. We had three technical meetings, addressed respectively by Dr. Edward Teller of the University of California, Dr. Rudolf Hermann of the Alabama Research Institute and Mr. Jim Farrior of Lockheed, and, finally, by Dr. Henry Eyring of the University of Utah. These men, eminent representatives of physics, aerodynamics, management and chemistry helped us in a large measure towards the attainment of better interdisciplinary cooperation.

This symposium is essentially the culmination of our first year's efforts. We are certainly gratified by the response to it, as exhibited in our program; government, universities, and industry are all represented here. We take this as yet another indication that scientists and engineers welcome the opportunity to meet each other and exchange their ideas in a way so that the physicist will interest the space physician and the mining engineer will want to integrate his efforts with those of the mathematician.

A final few words about Apollo Applications. What is the philosophy behind our symposium? It was, I think, summarized in advanced by what Dr. Teller had said during his visit here:

**The growth of technology is exponential. This in part is a correct statement based on experience. With some optimism one could even call it a mathematical statement.**

More knowledge produces more problems and more problems, more demands. It is reasonable to expect and it seems to be true that progress at any time is proportional to general development up to that time. But such simple description of the growth of the topics in which we are all interested is really and obviously an improper simplification. The growth is very much a structured growth. The field is becoming more complex and more specialized. It is also becoming more interrelated.

Thus, an exchange of ideas, both structured and specific, becomes imperative.

This Symposium, we hope, will be a forum for just such an exchange. We hope that all who come to present ideas, will have ample opportunity to discuss them. And we hope that those who are here to assess the state of these arts will also be able to do so.

Thus, I now declare this Symposium to be in session.

# SOME PROBLEMS IN DESIGNING A LUNAR PHOTOGRAPHIC SURVEY MISSION

By

W. L. Austin and J. L. Harden  
General Electric Company

## INTRODUCTION

### Objective and Scope

N 67-24269

The objective of this paper is to discuss some of the problems associated with the design of a lunar photographic survey mission. The specific problems to be discussed are the lighting conditions on the lunar surface and the translunar trajectory.

### Definitions and Limitations

Of prime importance to this photographic mission is the illumination of the lunar surface. The photographs that can be produced by any given camera will vary in detail depending on the lunar surface shadows. Of least detail will be those lunar surface points that are near the lunar terminator because the angle of incidence is too small and those that are near the subsolar point because the angle of incidence is too large. The terminator is defined as a great circle along the lunar surface and normal to a line drawn from the center of the sun through the center of the moon. The subsolar point is the juncture of this line with the lunar surface and is within  $1^{\circ} 34'$  of the lunar equator. Between these two extreme points of poor photographic detail is an area of optimum photographic detail. For this discussion, the area that yields optimum photographic detail will be referred to as the preferred lighting ring. (See Figure 1.)

The purpose in analyzing the preferred lighting ring is twofold: (1) The lighting conditions on the lunar surface that are required to obtain photographs of acceptable quality partly establish the lunar boundary conditions for orbital insertion, and (2) to show the relationship of the orbiting vehicle to the preferred lighting ring during a 28-day mission in a polar orbit.

The translunar trajectories to be discussed should not be accepted as general results since they are for a particular day in a particular synodic month. However, we may accept as a general result that once the lunar lighting conditions and lunar arrival longitude are specified, there is at best one launch window in any given lunar synodic month. (A synodic month is 29.53 days long and is measured from full moon to full moon.)

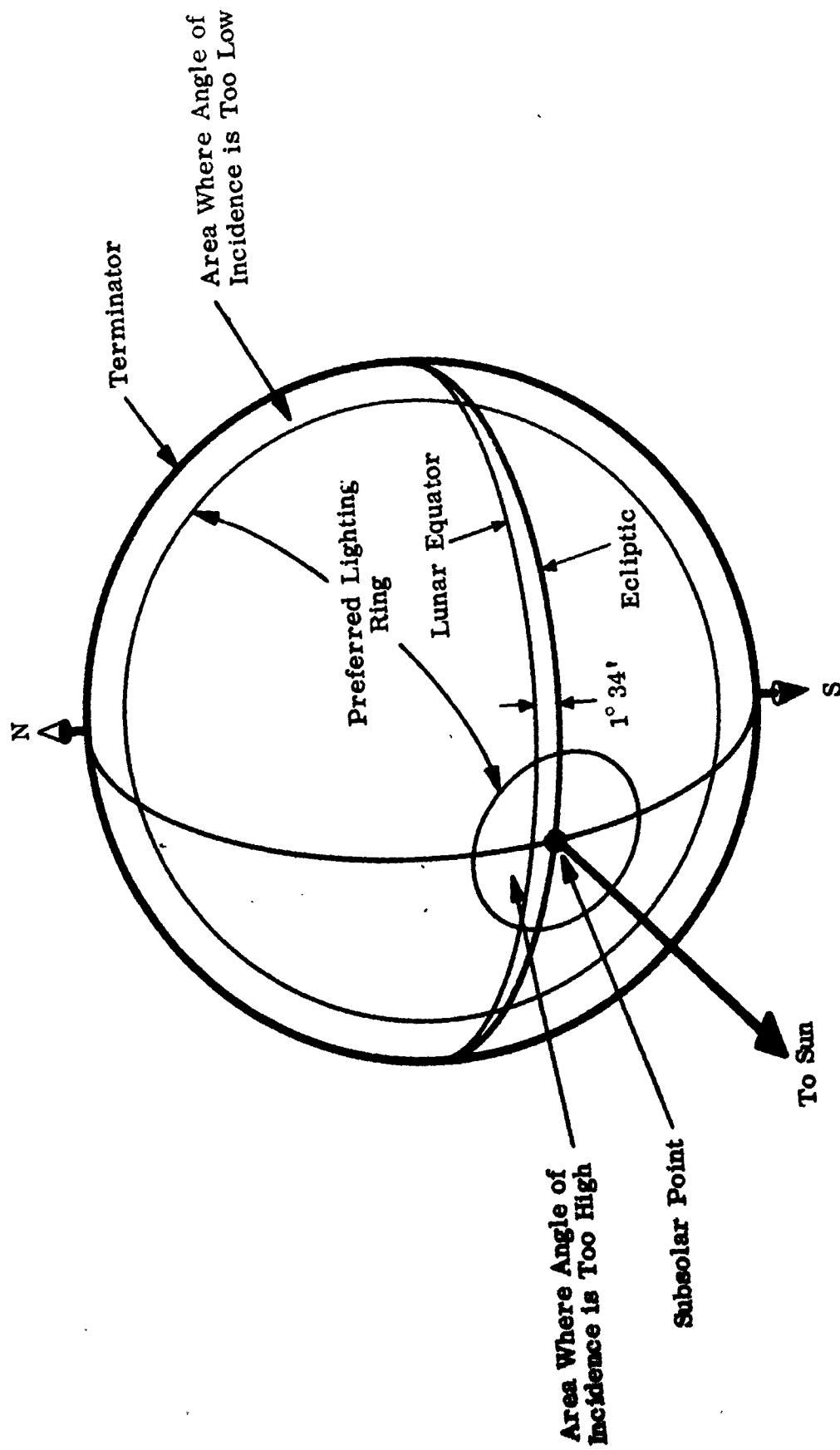


Figure 1. General Lunar Lighting Conditions

## MISSION DESCRIPTION

### Mission Objectives

The photographic mission envisioned will have two functions, mapping and surveying. The purpose of the mapping camera is to photograph as much of the lunar surface as possible, irrespective of sun angles, as long as there is illumination. A number of preselected sites, survey sites, will be photographed at preferred sun angles by a high-resolution camera.

### Lunar Orbit Parameters

An 80-nautical mile lunar circular orbit was chosen for analysis purposes. A polar orbit was chosen in order to maximize latitude coverage. There exists a definite trade-off between photographic quality, lunar orbit stay-time, and propulsion requirements. This is the reason why transearth trajectories were not considered since the time of transearth injection from lunar orbit insertion greatly affects the characteristics of the transearth trajectory. However, the lighting analysis is based on a 28-day lunar orbit duration in order to illustrate the maximum possible surface coverage.

### Arrival Longitude

In order to maximize the information gained by photographing the far side in the early part of the mission, an approximate arrival longitude of 81 degrees west was chosen. This arrival permits several hours for checkout and orbit refinement before initiating photography at 90 degrees west. The Russians have photographed the far side; however, qualitatively and quantitatively a great deal of information would be gained by re-photographing the area. Looking down from the lunar North Pole, Figure 2 depicts the equatorial longitudes that were photographed by the Russians. Moreover, the 81-degree west arrival longitude is near the minimum change of velocity ( $\Delta V$ ) required for translunar injection and deboost into lunar orbit (NASA Lunar Flight Handbook, Volume 2, Part 2). This arrival longitude is a goal. How well it is met will be illustrated subsequently. Now that the mission objectives are generally defined, the next step is to derive the general equations for the preferred lighting ring and to solve them for an example mission.

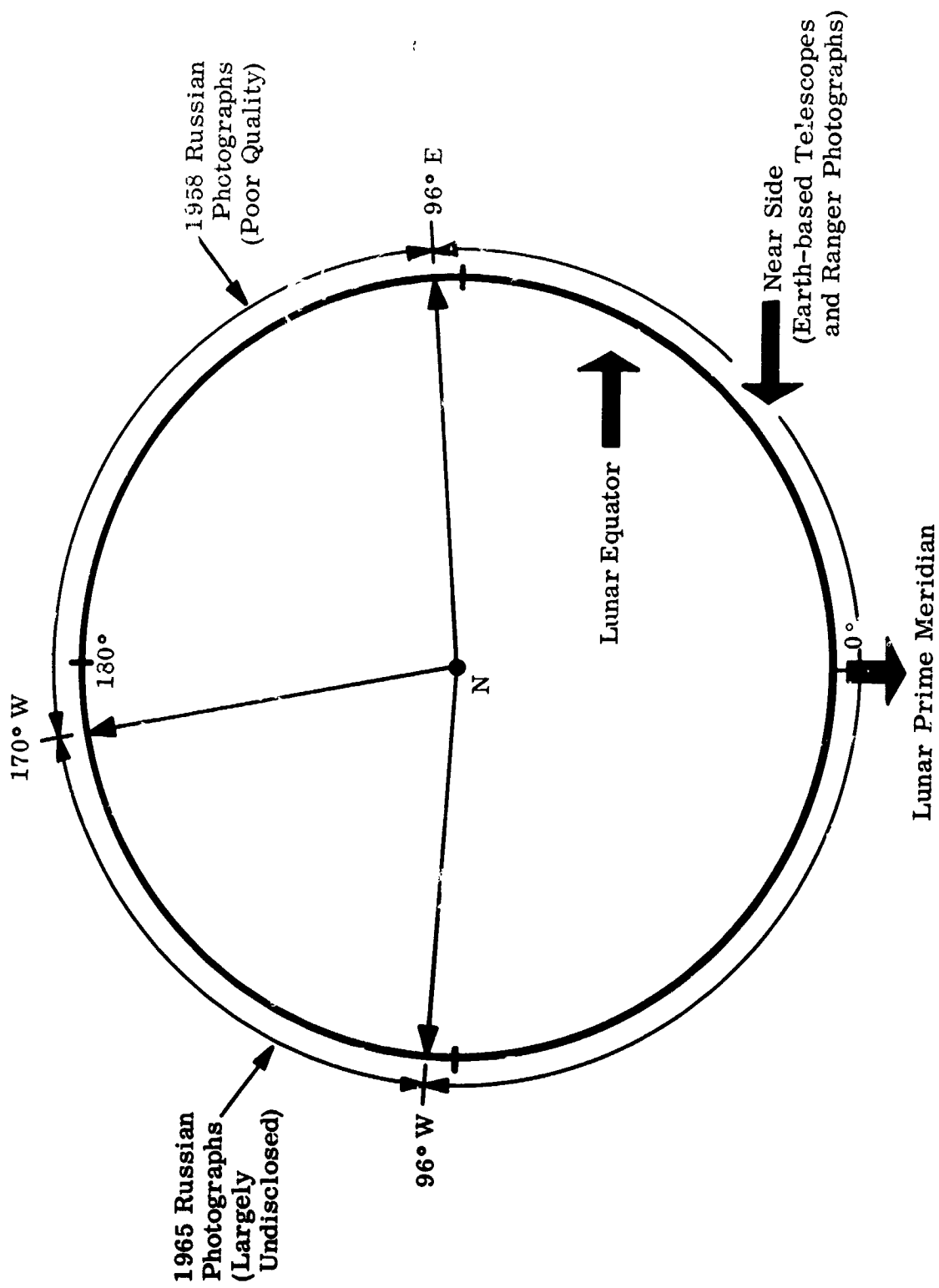


Figure 2. Photographed Areas of the Lunar Surface



## LUNAR LIGHTING CONDITIONS

### Preferred Lighting Ring

The preferred lighting ring was previously defined as the preferred lunar lighting conditions that are required by a survey camera to produce meaningful photographs. Another way of defining it is the surface area of the moon within which the sun angle at every point in the area is within acceptable lighting limits. Thus, when a point in the preferred lighting ring is photographed, the resulting picture is of acceptable quality. The sun angle,  $S_A$ , is defined as the elevation of the sun at a point on the lunar surface with respect to the local horizontal. For analysis purposes (see Figure 3) consider the ring to be bounded by two variables,  $\alpha_1$  and  $\alpha_2$ , which are lengths of arc across the lunar surface.  $\alpha_1$  is the minimum and  $\alpha_2$  the maximum angular distances from the subsolar point allowed for photographic purposes. The point where  $S_A = 90^\circ$  is another definition of the subsolar point. This implies that the sun angles of  $\alpha_1$  and  $\alpha_2$  are  $90^\circ - \alpha_1$  and  $90^\circ - \alpha_2$ , respectively. Thus, a site is within photographic limits when the site sun angle,  $S_A$ , is:  $(90^\circ - \alpha_2) \leq S_A \leq (90^\circ - \alpha_1)$ .

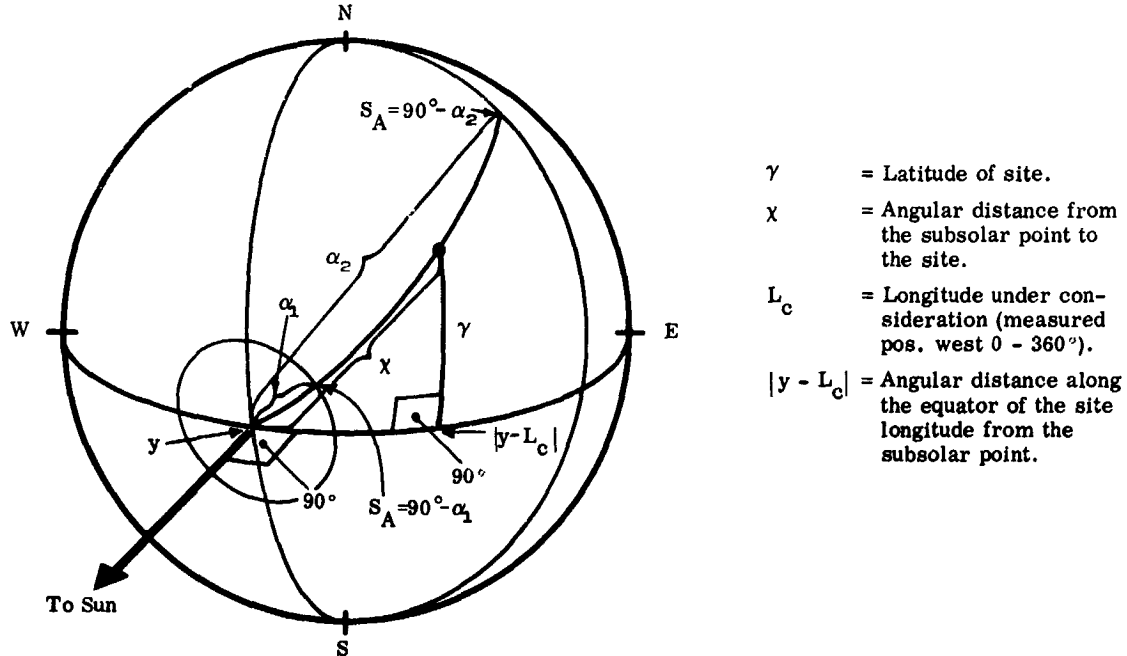


**Figure 3. Geometry Required to Derive the General Equations for the Preferred Lighting Ring**

Given any point on the lunar surface, the time of the synodic month and declination of the point with respect to the ecliptic determine the angle the sun makes with the local horizontal at the point on the surface. If this point is one of any of the predetermined survey sites, then the sun angle is critical. The general equations to determine the position of the preferred lighting ring with respect to the lunar surface can easily be found. Thus, for specific values of  $\alpha_1$  and  $\alpha_2$  latitude coverage may be determined simply by substituting the  $\alpha$  values for  $\chi$  in Equation 1 and solving for  $\gamma$ .

In deriving the general equations, a spherical moon is assumed with the moon's equator in the plane of the ecliptic. Thus, the declination of the site with respect to the ecliptic is equal to the site latitude. Also, the distance from the center of the sun to any point on the illuminated side is treated as a constant. The initial time reference point is the beginning of the synodic month or full moon.

The easterly sidereal rotation of the moon is 0.549 degrees/hour. The terminator rotates easterly at the rate of 0.041 degrees/hour. If the effects of lunar librations are omitted, then the subsolar point,  $y$ , is located approximately  $(0.549 - 0.041)X$  or  $0.508X$  degrees west of the lunar prime meridian, where  $X$  is the time in hours from the last full moon. This approximation may be refined by using ephemeris data.

In order to calculate the sun angle,  $S_A$ , for any given latitude and longitude, Napier's rules apply (see Figure 3).

By Napier's rules for right spherical triangles:

$$\cos \chi = \cos \gamma \cos |y - L_c| \quad (1)$$

$$\chi = \text{Arc Cos} [\cos \gamma \cos |0.508X - L_c|] \quad (2)$$

where,  $L_c$  is the longitude under consideration.

Thus, for any given latitude, longitude, and time of synodic month, the  $S_A$  of that latitude and longitude is given by:

$$S_A = 90^\circ - \chi = 90^\circ - \text{Arc Cos} [\cos \gamma \cos |0.508X - L_c|] \quad (3)$$

In determining the boundaries of the preferred lighting ring with respect to the subsolar point, it is necessary to consider the two boundary points on  $\chi$ ,  $\alpha_1$ , and  $\alpha_2$ , where

$0^\circ < \alpha_1 < \alpha_2 < 90^\circ$ . For the  $\alpha_2$  value,  $0^\circ \leq |0.508X - L_c| \leq \alpha_2$  and for the  $\alpha_1$  value,  $0^\circ \leq |0.508X - L_c| \leq \alpha_1$ . The first inequality defines the outer boundary, and the second, the inner boundary of the preferred lighting ring.

In the example mission which I will present, the preferred lighting ring is bounded by  $\alpha_1 = 30^\circ$  and  $\alpha_2 = 80^\circ$ . Thus, the photographs of a site with a sun angle less than or equal to  $90^\circ - \alpha_1 = 60^\circ$  and greater than or equal to  $90^\circ - \alpha_2 = 10^\circ$  would be of acceptable quality. The rest of this section will be concerned with the development of the parameters of the preferred lighting ring used for the example mission. Figure 4 is a general description of one quadrant of this preferred lighting ring which relates latitude coverage with the number of degrees,  $|y - L_c|$ , from the subsolar point. Note that the relation is symmetric about both axes, thus only one quadrant need be drawn. Also, the maximum latitude coverage is  $\pm 78.5$  degrees when photography is initiated 30 degrees west of the subsolar point. This point occurs at  $|y - L_c| = 30^\circ$  which is readily seen in Figure 4. The latitudes in the figure were calculated in the following manner. In Equation 1 let  $\chi = 80^\circ$ , hence:

$$\cos 80^\circ = \cos \gamma \cos |y - L_c| \Rightarrow \quad (4)$$

$$\gamma = \arccos \left[ \frac{0.17364818}{\cos |y - L_c|} \right], \text{ where } 0^\circ \leq |y - L_c| \leq 80^\circ \quad (5)$$

This results in a projection on the lunar surface of the 10-degree  $S_A$  line which shows the outer limit of the preferred lighting ring.

In Equation 1, let  $\chi = 30^\circ$ ; therefore

$$\cos 30^\circ = \cos \gamma \cos |y - L_c| \Rightarrow \quad (6)$$

$$\gamma = \arccos \left[ \frac{0.86602540}{\cos |y - L_c|} \right], \text{ where } 0^\circ \leq |y - L_c| \leq 30^\circ \quad (7)$$

This is a projection on the lunar surface of the 60-degree  $S_A$  line which is the inner limit of the preferred lighting ring. Also, the 20-, 30-, 40-, and 50-degree  $S_A$  lines were calculated and plotted in Figure 4.

#### Polar Orbit and Latitude Coverage

The vertical dotted lines in Figure 4 represent the relationship of the vehicle's orbit to the sun angle lines, and show the latitude coverage with respect to the sun angle lines

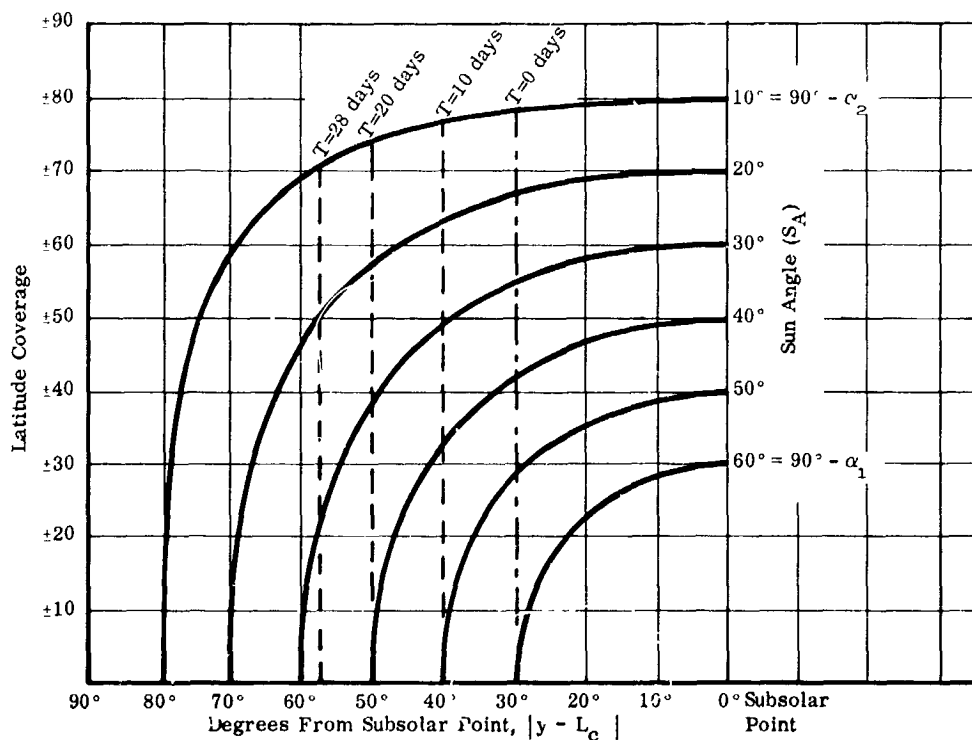


Figure 4. Relationship Between Orbiting Vehicle and an Orbital Insertion of 30° West of the Subsolar Point

at the 0-, 10-, 20-, and 28-day time points in the orbit. The reason for the change is due to the rotation of the terminator. Table 1 is a summary of the latitude coverage at  $T = 0, 10, 20,$  and 28 days. Figure 5 shows the relationship between the Earth, Sun, and the Moon's terminator for one synodic month.

Table 1  
Latitude Coverage

$S_A$ Line	$T = 0$	$T = 10$	$T = 20$	$T = 28$
10°	±78.5°	±77.0°	±73.5°	±71.0°
20°	±67.0°	±63.5°	±57.5°	±51.0°
30°	±54.5°	±49.0°	±39.0°	±21.5°
40°	±42.0°	±33.0°	± 2.5°	0.0°
50°	±28.0°	± 5.0°	0.0°	0.0°
60°	0.0°	0.0°	0.0°	0.0°

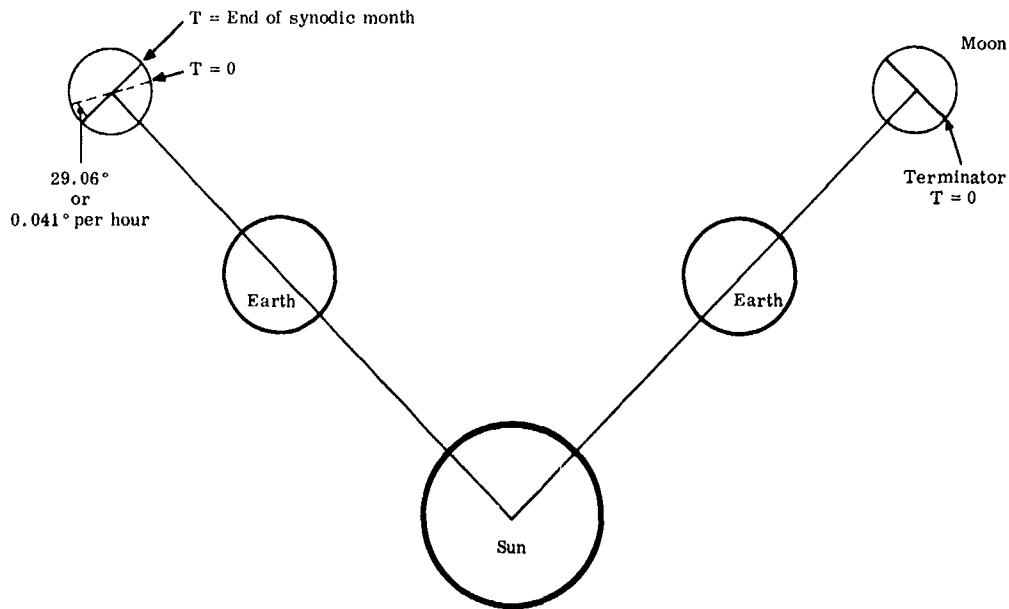
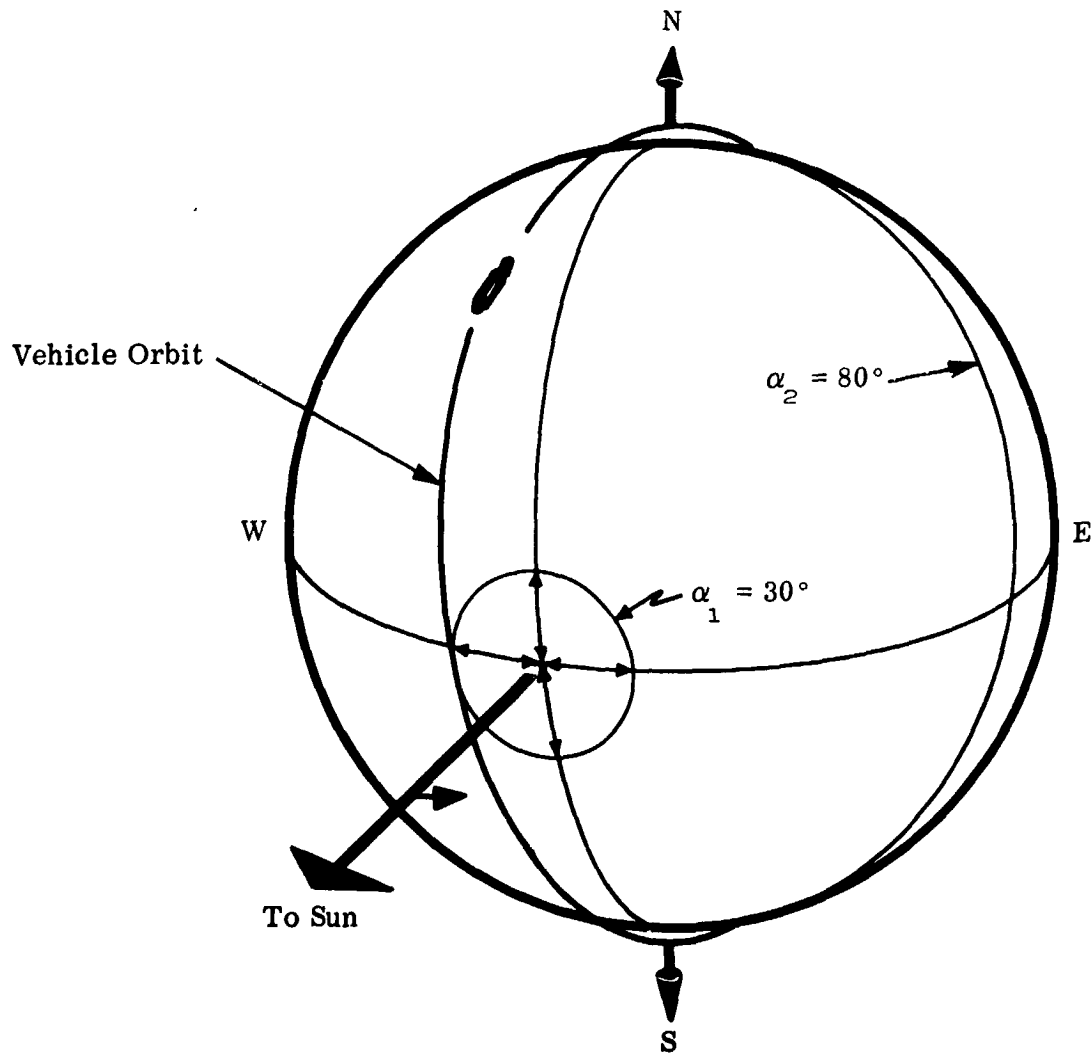


Figure 5. Relationship Between the Earth, Moon, and Sun for Any Synodic Month

#### Direction of Latitude Decay

Referring to Figure 4, there is no apparent reason why the times stated for the dotted lines could not be reversed; i.e., the vehicle could arrive east or west of the subsolar point. If the vehicle arrived east of the subsolar point, then the equatorial  $S_A$  on the illuminated side would be 32.5 degrees at arrival and 60 degrees at the end of the mission. This increase in sun angle with respect to time is due to the easterly rotation of the terminator. The maximum latitude coverage at the beginning of the mission would be  $\pm 71$  degrees and  $\pm 78.5$  degrees at the end of the mission with a minimum sun angle of 10 degrees. If the vehicle arrived 30 degrees west of the subsolar point, then the equatorial  $S_A$  would be 60 degrees at arrival on the illuminated side with  $\pm 78.5$ -degree latitude coverage. At the end of the mission, the equatorial  $S_A$  would decay to 32.5 degrees with  $\pm 71$  degrees in latitude coverage at a minimum sun angle of 10 degrees. Thus, an arrival at 30 degrees west of the subsolar point results in a 15-degree greater latitude coverage north and south, as opposed to arrival at 57.5 degrees east of the subsolar point. Since it was assumed that the far side would be photographed first, the vehicle will be assumed to arrive 30 degrees west of the subsolar point in order to maximize latitude coverage in the early part of the mission. This would be particularly desirable for a 14-day mission. Figure 6 shows the relationship of the vehicle to the

moon at arrival. Now that all of the lunar orbit parameters, including lighting, are established, the next step is to discuss the survey site coverage and to present an example mission.



**Figure 6. Relationship of Orbiting Vehicle to the Lunar Lighting Conditions**

## EXAMPLE MISSION

### Survey Site Coverage

Figure 7 is an equigridded lunar map with the sun angle lines projected on it. These lines show the decrease in latitude coverage for the various sun angles over a 28-day mission. The outer limits of the lunar area which fall within the photographic limits are defined by the 10-degree sun angle lines. This is due to the lighting constraints required to obtain photographs of acceptable quality and due to the slope of the minimum permissible sun angle line, which in this case is 10 degrees. However, all of the lunar surface above and below this region is out of the acceptable photographic limits chosen for the example mission.

If a minimum latitude decay is desired, then a choice must be made between photograph quality and longitudinal change capability. For if the latitude coverage decay over a 28-day mission should be below some preselected value, longitudinal changes would be necessary at some point or points in the mission to prevent it. The nature of the change would be easterly in the direction of the subsolar point. Such a change would place the orbit closer to the subsolar point and then increase latitude coverage.

If the changes are large and the propellant is not available for these changes for a 28-day mission, then perhaps a shorter mission duration should be considered. Consequently, a trade-off exists between mission length, photographic quality, and permissible latitude coverage decay. Ideally, the best mode is to avoid making any longitudinal changes at all. However, it is interesting to note how much incremental change in velocity ( $\Delta V$ ) would be required per degree of longitudinal change for an 80-n. mi. circular orbit. This is illustrated in Figure 8. These values may not appear to be very large, but when they are added to all of the other  $\Delta V$  requirements, their significance is better enhanced.

### Trajectory Discussion for June 23, 1970

The month of June, 1970, was arbitrarily selected to illustrate the problems involved in determining an acceptable translunar trajectory which meets prescribed boundary conditions at the moon. For this example mission, the boundary conditions at the

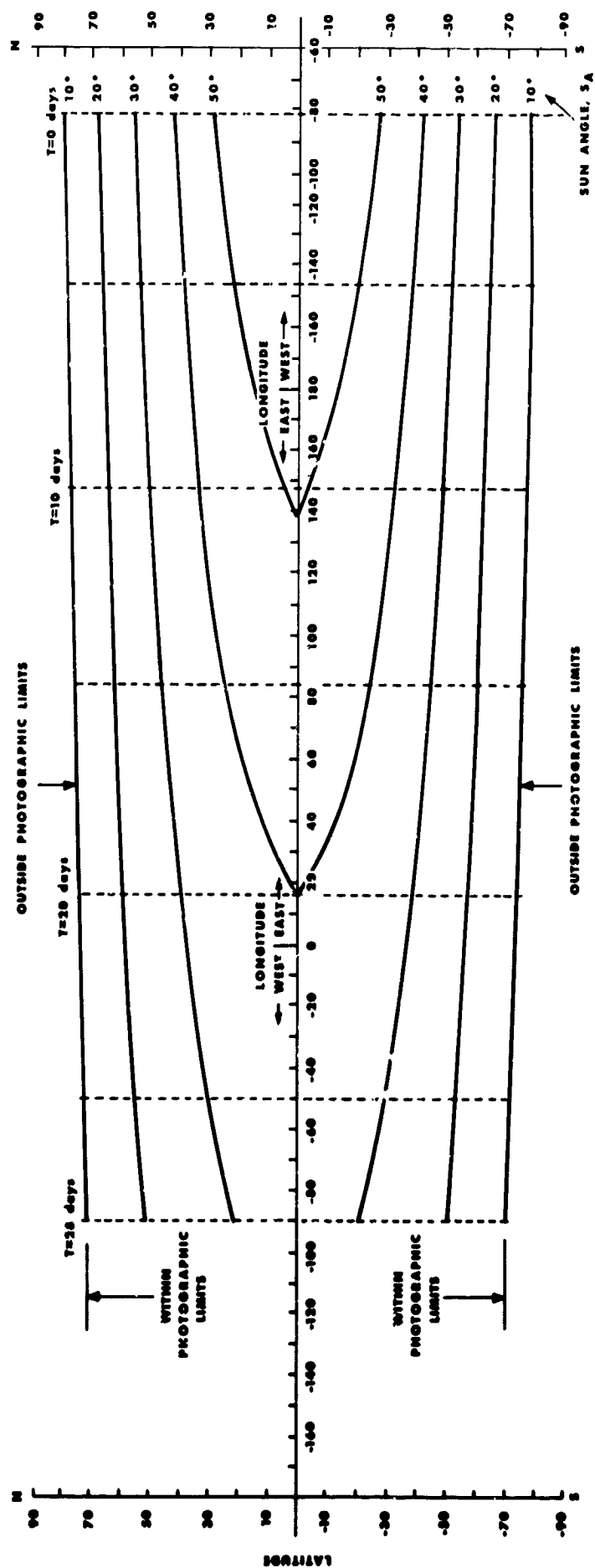


Figure 7. Lunar Surface Lighting for 28-Day Mission, 81° West Orbital Insertion



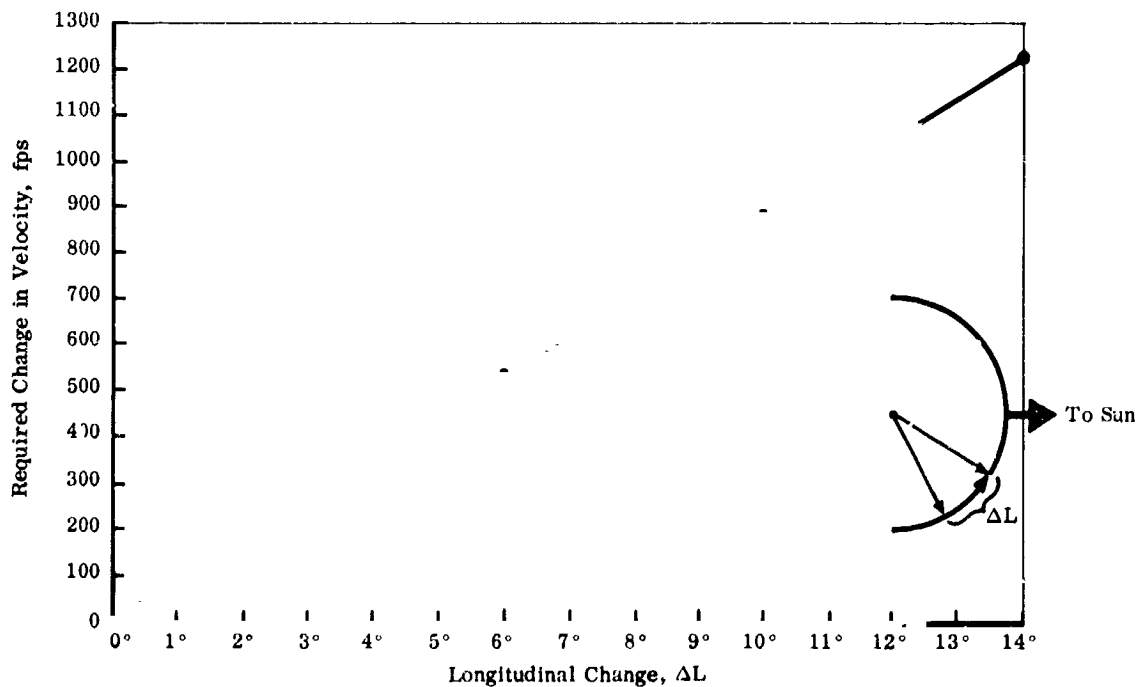


Figure 8. Velocity Requirements for Longitudinal Changes,  $\Delta L$

moon are a polar lunar orbit with an 80-n. mi. pericyynthion, an 81-degree west selenographic insertion longitude, and a 60-degree equatorial sun elevation angle on the illuminated side of the lunar surface at insertion.

For a 60-degree equatorial sun elevation angle at 81 degrees west longitude, the selenographic longitude of the sun must be 51 degrees west at lunar orbit insertion. From solar and lunar ephemeris data, it was found that the subsolar point is 51 degrees west at 8.82 hours Universal Time on June 23, 1970.

A set of patched conic non-free-return trajectories with various flight times were computed for arrival at the moon on June 23, 1970. Translunar injection is from a 100-n. mi. earth parking orbit at the earliest opportunity, i. e., first parking orbit and launch azimuths are restricted to AMR range safety values, 72 to 108 degrees. The lunar arrival window resulting from these computations is shown in Figure 9. In this figure, the longitude of insertion for a 60-degree sun elevation angle is plotted as a function of time of arrival and is called the "motion of  $\alpha_1$ ". Superimposed is a grid of launch azimuths and translunar flight times from the patched conic trajectories. Thus, the earliest lunar arrival occurs at 9.2 hours Universal Time on June 23, 1970, with a launch azimuth of 72 degrees, a translunar flight time of 90.2 hours, and a selenographic longitude of insertion of 81.2 degrees west.

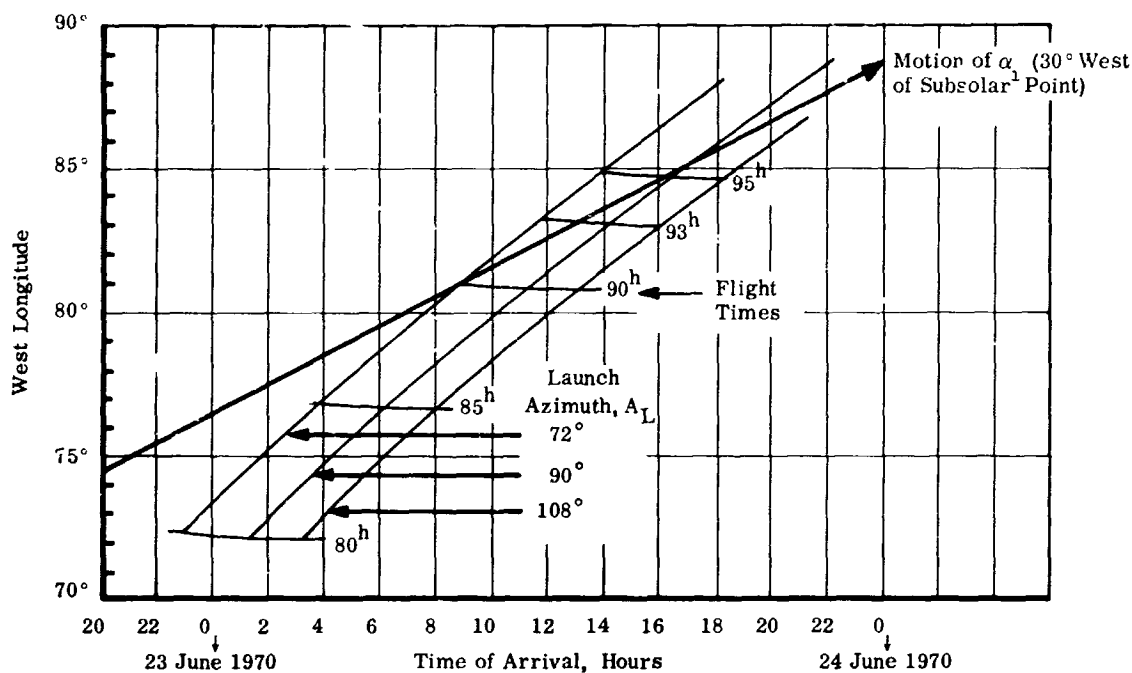


Figure 9. Lunar Arrival Window

The launch window on June 19, 1970, is shown in Figure 10. In this figure, time of launch is plotted as a function of launch azimuth for a 60-degree equatorial sun elevation angle at lunar orbit insertion on June 23, 1970. Thus, the launch window begins at 14.65 hours Universal Time on June 19, 1970, with a launch azimuth of 72 degrees.

From Figures 9 and 10, it is apparent that a translunar trajectory may be obtained with an 81.2-degree west insertion longitude and a sun elevation angle of 60 degrees. This is within 0.2 degree of the originally specified arrival of 81-degree west longitude. Translunar injection occurs on the first parking orbit with a  $\Delta V$  of approximately 10,280 fps, and the lunar orbit deboost  $\Delta V$  is approximately 2,730 fps; however, the lunar arrival time of 9.2 hours Universal Time on June 23, 1970, is at the beginning of the lunar arrival window. If it is necessary to delay translunar injection to the second parking orbit, the grid of launch azimuths and flight times in Figure 9 would be shifted about 1.5 hours later, and a more westerly insertion longitude would be necessary to meet the 60-degree sun elevation angle. It should also be noted that Figures 9 and 10 are only valid for the month of June, 1970. A different synodic month would have a different lunar arrival window and a different launch window. In fact, for another month it may not be possible to arrive near the 81-degree west arrival longitude at the correct sun elevation angle.

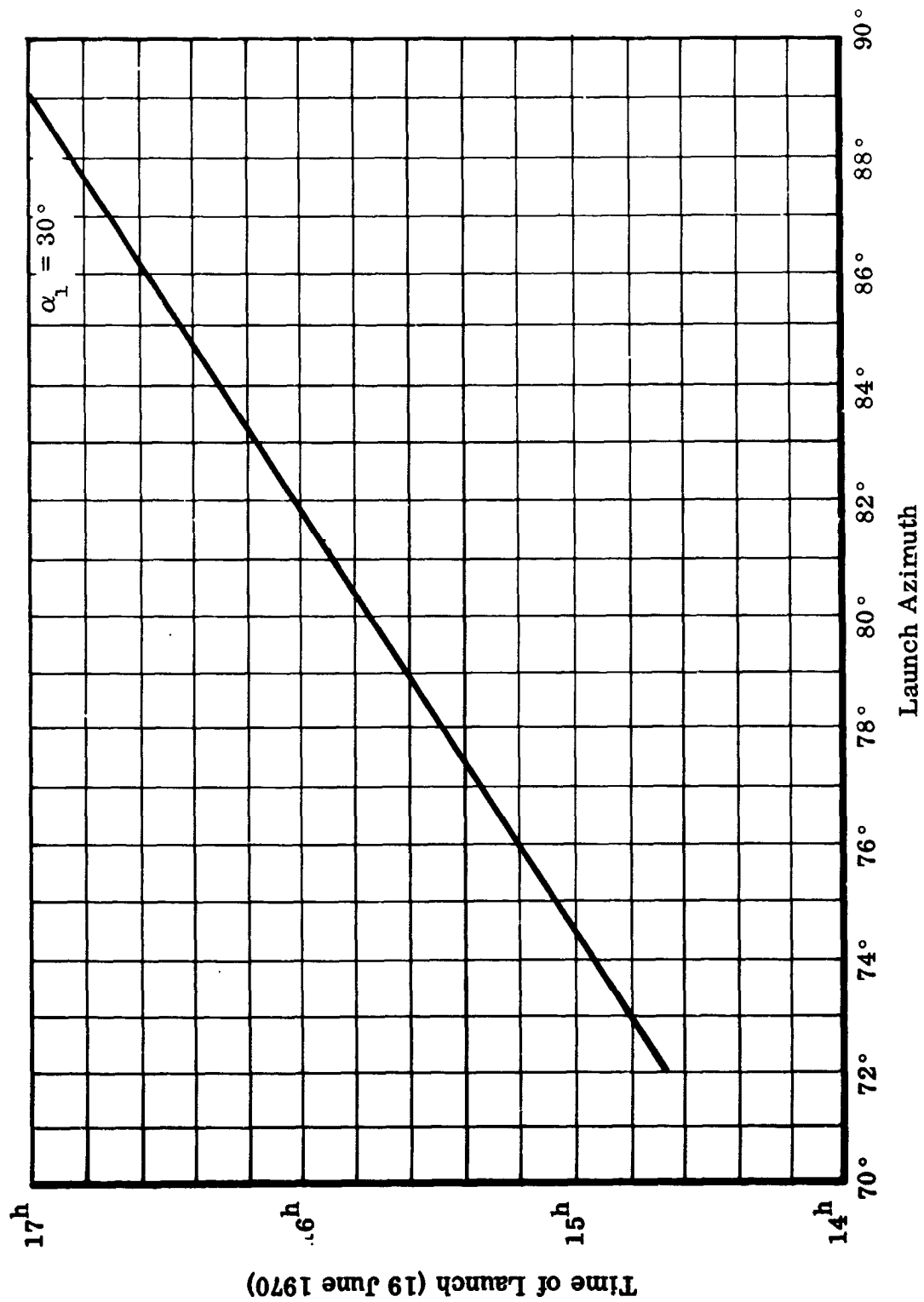


Figure 10. Earth Launch Window

## SUMMARY

The purpose of this paper has been to discuss some of the problems in designing a lunar photographic survey mission, specifically the translunar trajectory and preferred lighting ring. The preferred lighting ring was discussed in general terms in order to show its characteristics over a 28-day lunar orbit. A 28-day orbit duration is desirable; since regardless of the polar-orbit altitude, the entire surface would rotate under the spacecraft in 27.32 days.

The trajectories that were discussed were for a particular day in a particular synodic month and are not to be taken as general results. It is a general result, however, that once an arrival longitude and sun angle are specified, there is at best one launch window in any given synodic month. In order to open up this launch window, it would be necessary to vary the boundary conditions at lunar orbit insertion.

In conclusion, the authors would like to emphasize the fact that this paper deals only with lunar lighting conditions and translunar trajectories. The transearth trajectories, lunar orbit duration, and lunar orbit aborts are complete studies in themselves and should be studied in great detail.

# LUNAR TERRAIN ANALYSIS

By

R. L. Sanders and W. M. Greene  
Hayes International Corporation

## ABSTRACT

N67-24270

The purpose of the Lunar Terrain Analysis was to analyze the distribution of lunar topographic and geologic features of scientific interest in order to assess surface mobility requirements for early lunar exploration missions.

The study provided an analysis of lunar geology and geologic age classification. It classified, reviewed and analyzed Aeronautical Chart and Information Center (ACIC-LAC) charts and United States Geological Survey (USGS) maps. A presentation of singular lunar sites of special interest was made, and a study of the Apollo Landing Belt was effected.

The work is described in detail in Technical Report H-MOL-20, prepared by Hayes International Corporation, in response to Contract NAS 8-5307 for the George C. Marshall Space Flight Center, National Aeronautics and Space Administration, Huntsville, Alabama.

## INTRODUCTION

Work performed by the Department of Lunar and Planetary Sciences of Hayes International Corporation's Missile and Space Support Division at Huntsville, Alabama, has been designed primarily to solve problems dealing with meaningful exploration programs on the lunar surface. The scope of research has not been simply to collect and amass data but to solve specific geological problems. To this end, activity has been conducted in geological and geophysical studies, Ranger and telescopic photographic studies (with general goals of specifying astronaut activities on the lunar surface) and in compilation of data from existing literature.

The geology of the moon is an important key to the history of the earth. The broad-based lunar exploration program now in progress is designed to provide information concerning the origin of the moon, the earth and the solar system.

Part of the program included a review and analysis of Aeronautical Chart and Information Center charts. These maps have been and are continually being prepared by the Aeronautical Chart and Information Center of the United States Air Force at Lowell Observatory in Flagstaff, Arizona. Morphological features of the lunar surface are presented at a scale of 1:1 000 000. The ACIC map coverage to date is shown in black on Figure 1. Areas currently being mapped, in various stages of completion, are shown in gray. Maps completed and scaled at 1:500 000 are shown lined diagonally. A typical ACIC-LAC map shown in Figure 2 is LAC 74 Grimaldi on the western limb of the lunar disc just below the equator.

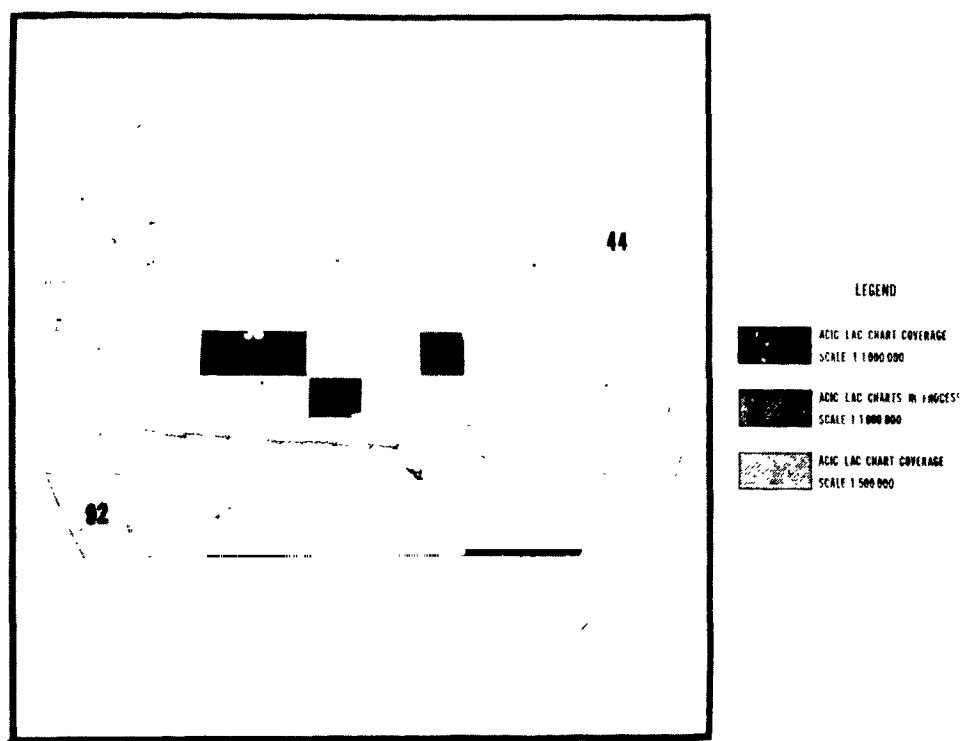


FIGURE 1. LUNAR CHART INDEX (ACIC LAC)

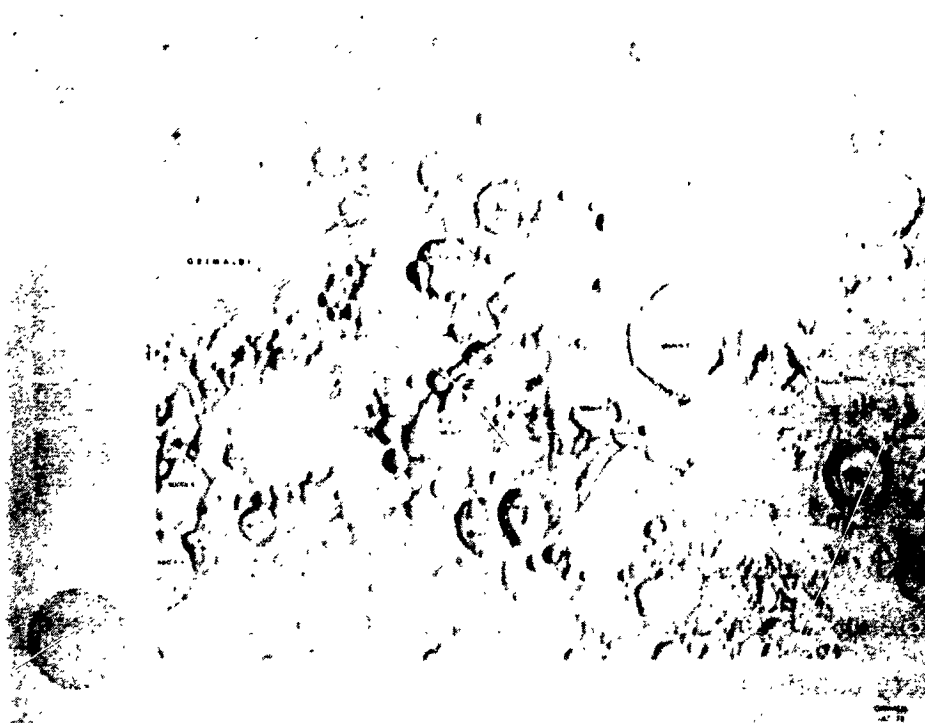


FIGURE 2. LUNAR CHART: GRIMALDI LAC 74

The results of the chart analysis were:

1. Within coverage of the charts, 18 areas of geologic interest were analyzed on the basis of morphology. As geologic coding and interpretation are not shown on these maps, as they are on USGS maps, suggested vehicle traverses were not drawn.

2. Features of varying nature were listed by type and by occurrence (duplication).

3. These features were listed on charts to permit rapid comparison of quality and quantity content of features for each area.

Another part of the study includes a review and analysis of United States Geological Survey maps.

The USGS maps have been and are continually being prepared for NASA by the USGS at Flagstaff, Arizona, and show geological features and geological interpretations on maps scaled at 1:1 000 000. The USGS map coverage to date is shown in gray on Figure 3. Areas currently being mapped, in various stages of completion, are shown in black. The results of the USGS map study were:

1. Selection and listing of major geological features in chart form

2. Suggested scientific traverses for the astronaut manned lunar roving vehicle were based on geologic features of interest in 18 areas of feature concentration. These areas are shown in Figure 4.

3. It was determined by feature density analysis that circles of 80 kilometers (50 miles) radius were optimum. Larger circles provided little or no significant increase in feature variety, and smaller areas usually decreased the variety considerably.



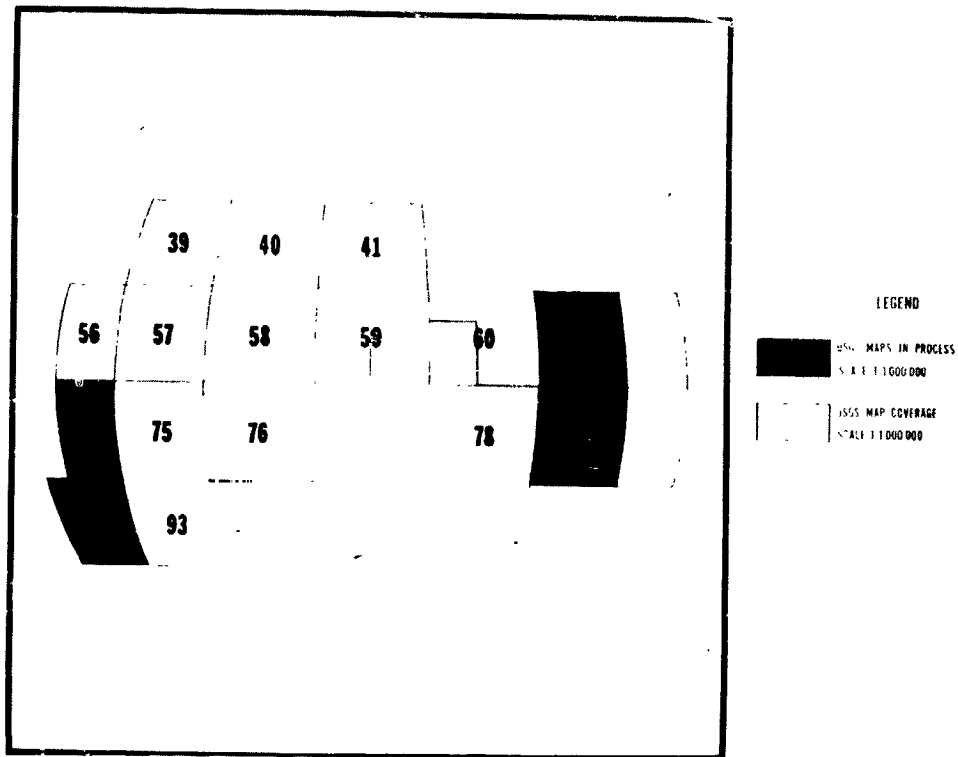


**FIGURE 3. LUNAR CHART INDEX (USGS)**

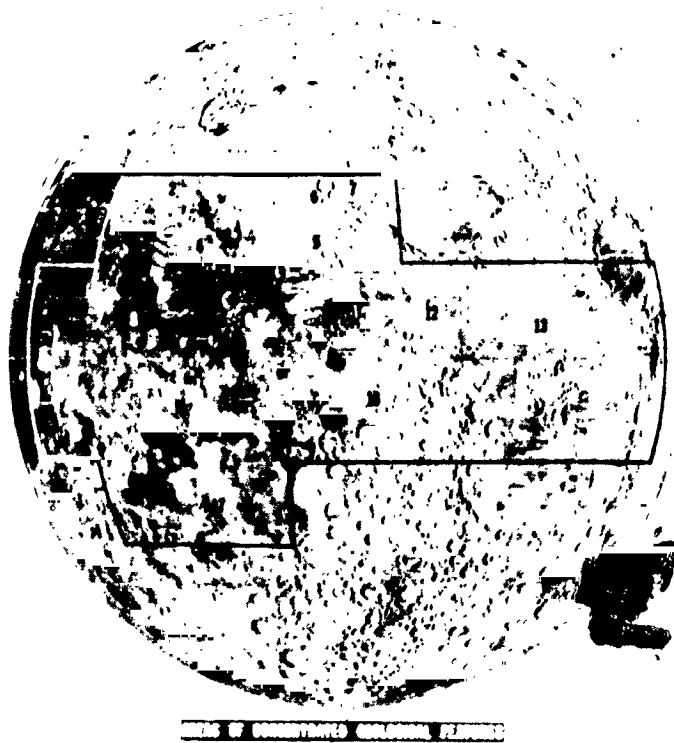


**FIGURE 4. AREAS OF CONCENTRATED GEOLOGICAL FEATURES**

A typical USGS map is seen in Figure 5. The circles have radii of 80 kilometers (50 miles) and after a thorough analysis of the map, have been

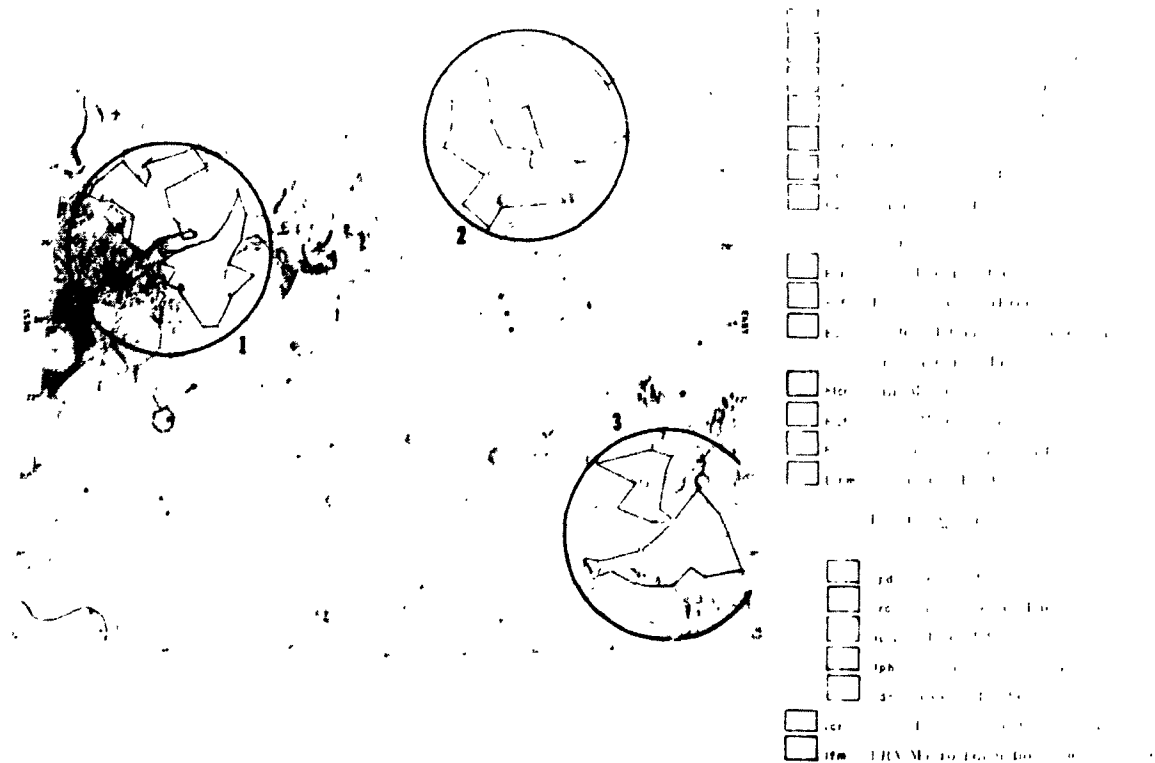


**FIGURE 5. ARISTARCHUS**

drawn to include as many geologic features as possible. Of the total 18 areas of concentration, these first three are quite typical of all. Area number one shows two traverses, each approximately 480 kilometers (300 miles) long, drawn along the route of a maximum quantity of geological features of interest.

Singular or non-reoccurring lunar sites of special interest were also studied. Figure 6 shows 125 of these areas that have significant individual interests. A priority value was not established because many known factors remain to be solved before this analysis can be completely accomplished. The sites include areas which have been reported and described by various astronomers as showing, among other things, activity resembling fog, mist, smoke,

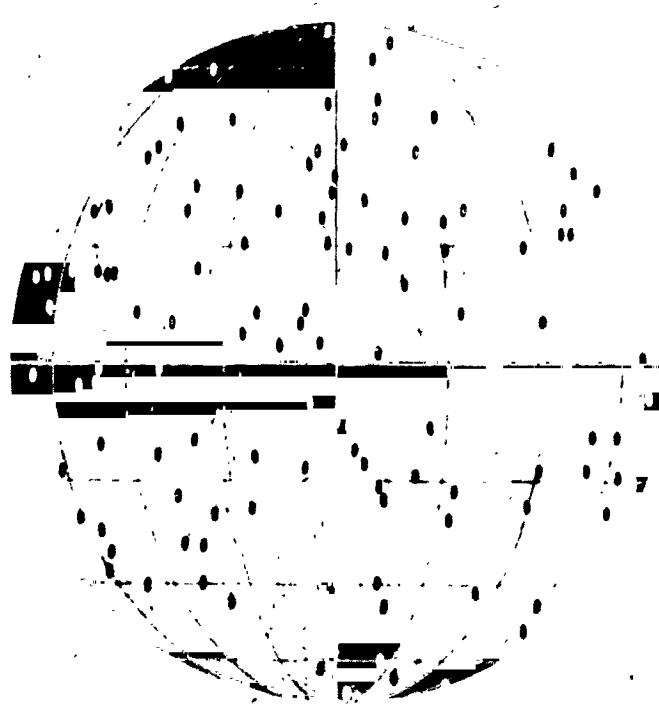


**FIGURE 6. SINGULAR LUNAR SITES**

steam, light and coloration changes. Others were selected for unusual morphology and still others because they were extremes, such as Grimaldi which is the darkest area of the moon, significantly darker than any other crater. The sites were all selected as potential areas of scientific interest which could contribute to the geologic knowledge of the moon.

The next five slides are telescopic photos taken from the Lunar Atlas, which was compiled by the United States Air Force under the supervision of Dr. G. P. Kuiper and were selected to present typical examples of the 125 significant lunar features.

**FRIGORIS, TOP NORTH CENTRAL REGION OF MOON**

Figure 7 shows the northern limb of the moon. Mare Frigoris extends across the center of the picture, and Plato is shown as the prominent crater in the foreground.

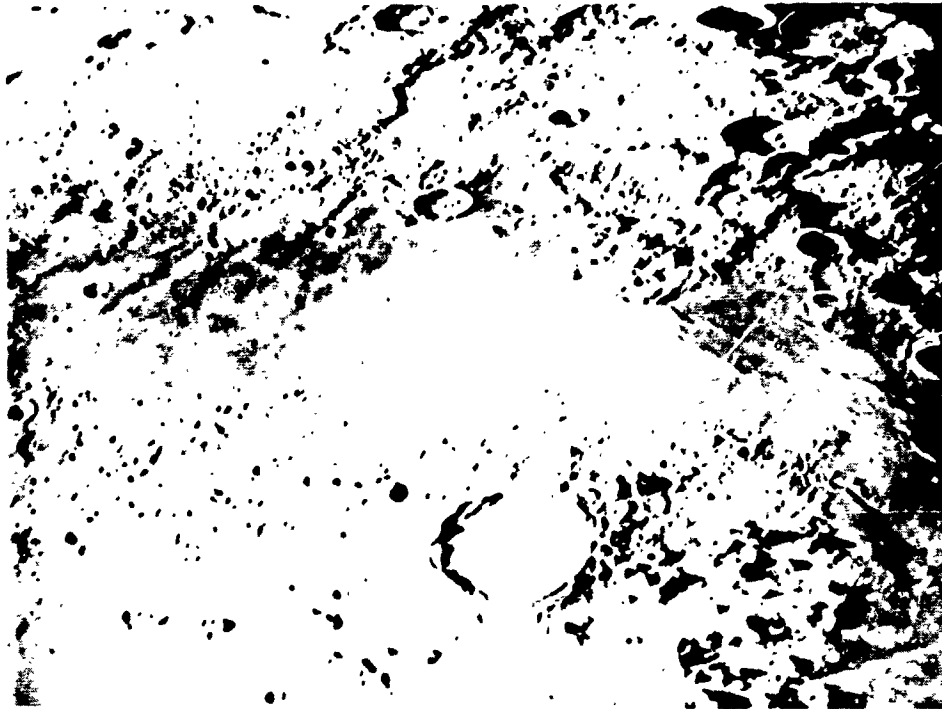


**FIGURE 7. FRIGORIS**

Philolaus (top center with two central peaks), a crater 68 kilometers (46 miles) in diameter with walls 3650 meters (12 000 feet) high, was reported a scene of recent activity when a red glow within the crater was observed. This was reported by R. M. Baum and referenced in two books, "Our Moon" and "Moon Maps".

Plato, a Post-Maria crater with a diameter of 100 kilometers (62 miles) and walls 1000 to 2000 meters high (3000 to 6000 feet), has a smooth floor darker than the surrounding mare material, and contains several craterlets and bright spots. Several observers have at various times reported sighting fog or a similar substance responsible for obscuring portions of Plato.

Several valleys in perpetual shadow and peaks in perpetual sunlight are found near both the North and South Poles of the moon. These areas seem valuable as areas for solar power stations and sites for making heat flow estimates from surface temperature measurements. If the lunar magnetic pole is located on or near the geographic North Pole, as it is on Earth, the region could be considered for magnetic studies.

The Alpine Valley, 130 kilometers (80 miles) long, is shown in the lower right corner of the figure, and is located between Mare Frigoris and Mare Imbrium. It is unusually straight with a flat floor on which are a few thin cracks and small craterlets.

#### PLATO, NORTH CENTRAL PORTION OF MOON

Figure 8 shows an area south of Mare Frigoris. The crater Plato and Alpine Valley are seen at the top of the figure. Mare Imbrium occupies most of this photo and is about 1110 kilometers (700 miles) in diameter. It is thought to be impact in origin and has been accepted as an important geological time marker. The inner ring of mountain peaks seems to represent the original rim of the impact area while the outer ring of mountain chains may have been formed by a subsequent tectonic adjustment. It appears as though the flooding, which occurred after the Imbrium impact, invades the craters Plato and Archimedes (not shown here) and marks them as craters formed after the impact and before the flooding of this region.

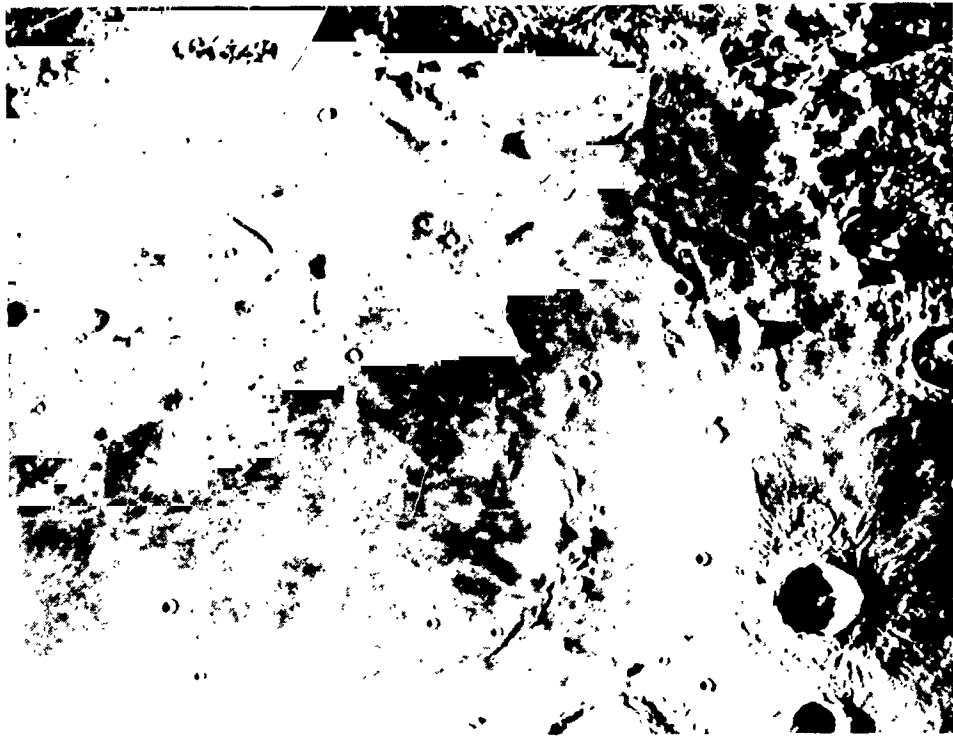


FIGURE 8. PLATO

Mt. Pico and Piton are bright, prominent peaks about 2300 meters high (7550 feet) thought to be formed of ejecta material at the time of the original Imbrium explosion. Pico, with three peaks, is south of Plato, while Piton, with a summit craterlet and two peaks, is west of Cassini. A cloud briefly masking Piton has been reported in "Geophysics as Applied to Lunar Exploration" by J. Green.

#### HYGINUS, CENTRAL PART OF MOON

The area in Figure 9 is located near the center of the lunar sphere near zero latitude and zero longitude. The Ariadaeus rille extends across the center of the picture for 240 kilometers (150 miles) and ends with the small, 14-kilometer (9-mile) diameter crater Ariadaeus. The rille, appearing to be broken by subsequent land slides, is probably a strike slip fault or an en echelon fracture.

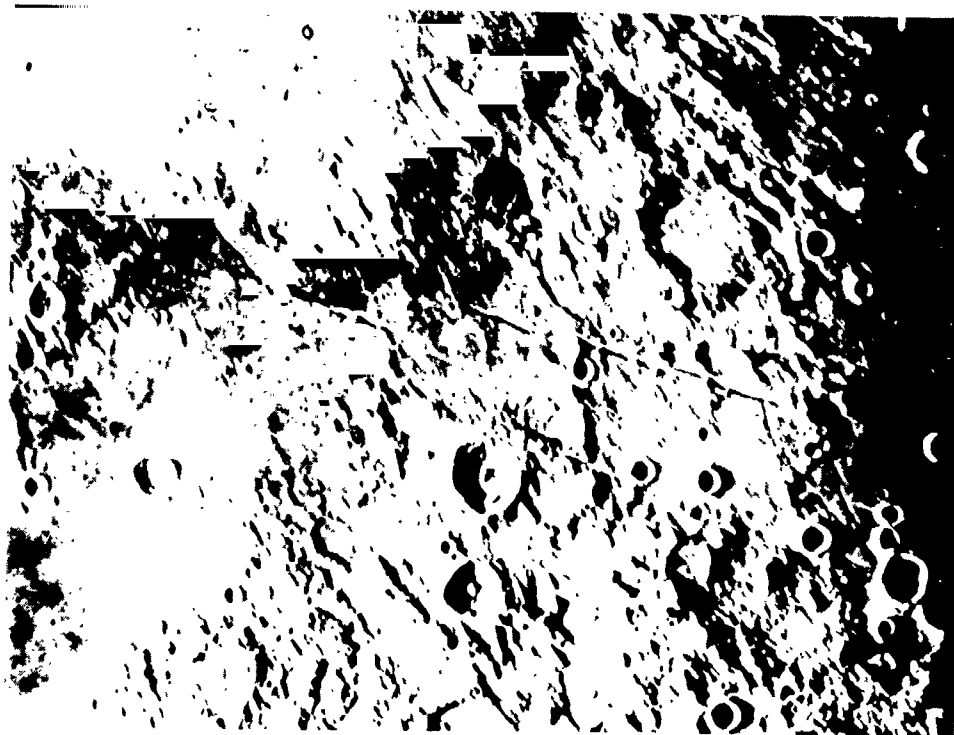


FIGURE 9. HYGINUS

Hyginus, a crater 6 kilometers (4 miles) in diameter, has a small craterlet on the north rim. The Hyginus rille is roughly parallel to the Ariadaeus rille, leading to speculation that the two could probably be related. West of the crater Hyginus are large chain craters associated with the rille.

Just below Hyginus in Sinus Medii is found the 23-kilometer (14-mile) diameter crater Triesnacker and its associated rille system which has an angular outline suggesting seismic origin. These rilles have a maximum width of two miles, and are believed to be the deepest on the moon.

Julius Caesar, north of the Ariadaeus rille, is an unusual Pre-Maria Age crater having an irregular formation with a gap or burial of the southeast wall. The floor of Julius Caesar is rather interesting in that it appears to

slope as well as contain different age materials. The darkest portion of the floor on the north side appears similar to other dark areas around Julius Caesar.

#### **SCHICKARD, EXTREME SOUTHWEST QUADRANT**

Figure 10, a photo of the southwestern limb of the moon area, includes the crater Schickard, a Pre-Maria ring 200 kilometers (124 miles) in diameter with walls about 1276 meters (4200 feet) high. The floor includes rilles, craterlets and areas of discoloration. Cloud-like appearances have occasionally been reported.

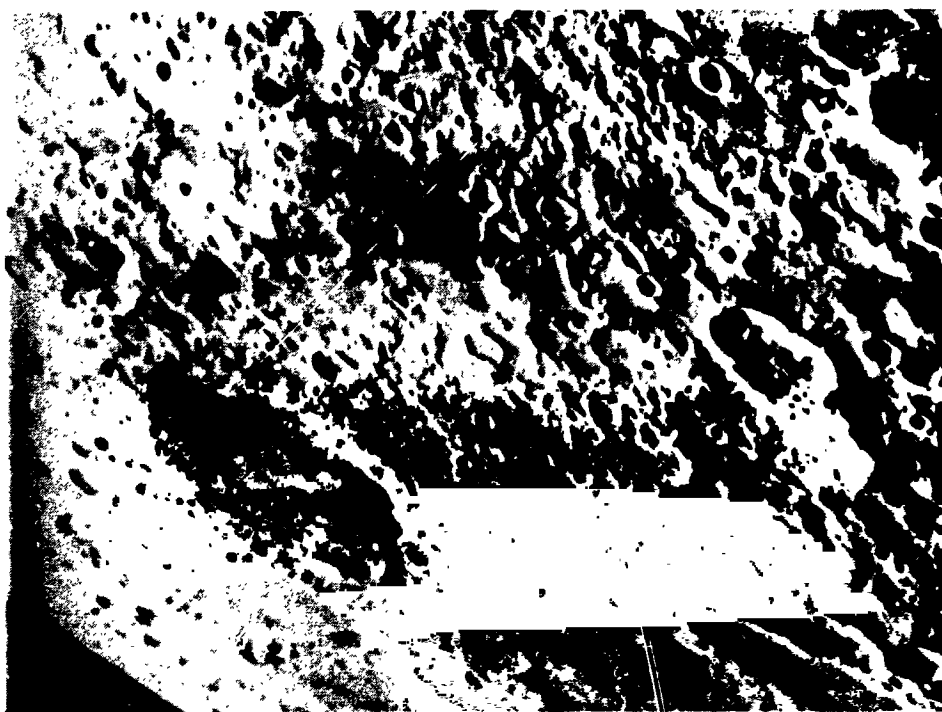


**FIGURE 10. SCHICKARD**



Wargentín, which is undiscernible in this picture but is southwest of Schickard on the extremity of the limb, is an important crater 90 kilometers (56 miles) in diameter and flooded to the lowest point in the rim. The floor, containing a few rilles and craterlets, is almost 300 meters (1000 feet) above the outside level. The evidence of overflow has been the object of various theories regarding its source and the origin of lunar features in general.

Hainzel, almost due east of Schickard, another singular site in this area, is a very irregular formation composed of two joined crater rings. Its maximum diameter is approximately 100 kilometers (62 miles) and the walls, nearly 3000 meters (9840 feet) high, are covered with craterlets.

#### **TYCHO, SOUTH CENTRAL QUADRANT**

Figure 11 shows the lunar disc with full illumination, accentuating the bright ray patterns associated with all the more recent craters.



**FIGURE 11. LUNAR EARTHSIDE HEMISPHERE**

Tycho is the most spectacular feature in the picture because of its large ray pattern. Tycho is 80 kilometers (50 miles) in diameter with walls 3500 meters (11 500 feet) above the floor. Crater ray patterns probably are important geological features; therefore, the extreme size of Tycho's rays qualifies it as a significant singular feature.

#### **ALTI SCARP, CENTRAL SOUTHEAST QUADRANT**

Figure 12 showing the Alti Scarp, a ridge 500 kilometers (315 miles) long, is one of the Herbig series of photographs made at Lick Observatory.

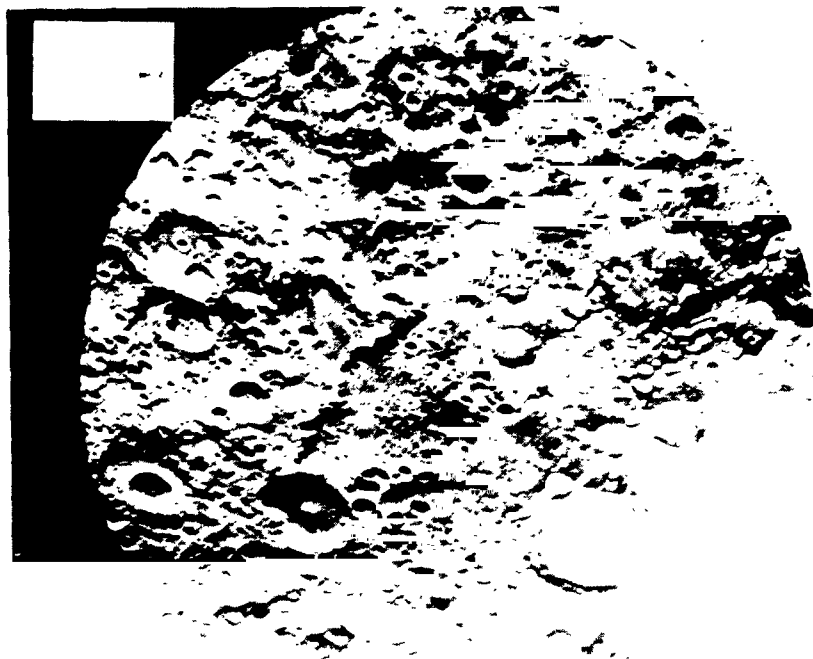


**FIGURE 12. ALTI SCARP**

There is a question as to the origin of this scarp and its relationship to Mare Nectaris which is northeast, beyond this photo. Interesting features of the

escarpment include the shelf below, indicating that the feature is very old; the height of the features, 4000 meters (13 000 feet) at its highest point; and the possibility of exposure of old material layers along its face.

The southern end of the scarp intersects Piccolomini, a crater 86 kilometers (56 miles) in diameter, south of Mare Nectaris, with a wall up to 4560 meters (15 000 feet) high. The crater floor has hills, craterlets and old rings including a divided central hill. On the south rim of Piccolomini, there is a formless deposit of unknown origin and outside the western wall are rilles parallel to the Alti Scarp.

#### LUNAR EQUATORIAL APOLLO LANDING BELT

There has been recent interest in short traverses and terrain conditions at the landing sites located on or near the equator. Dr. John McCauley of USGS in Flagstaff has analyzed this area of the moon by photometric methods and color-coded five different grades of surface roughness. There are 14 singular features and some part of seven concentration areas that fall within this belt. An application of this preliminary study has been made to the geological sites located within this equatorial region.

At present 10 landing sites are being studied within the equatorial belt. The sites have been selected on the basis of scientific data potential and restrictions imposed by blast off and orbital rejoining criteria.

Based on the observations and results of this first study, the Hayes' Department of Lunar and Planetary Sciences is currently continuing its studies of the lunar surface for NASA to accomplish a delineation of major geologic problem areas and features and, on this basis, determine major and auxiliary geophysical methods best applied to a given landing site.

## REFERENCES

1. Wilkins, H. P.: Monthly Notices of Royal Astronomical Society. Vol. 119, No. 4, 1959, p. 421.
2. Barker, R.: Monthly Notices of Royal Astronomical Society. Vol. 109, No. 2, 1948-49, p. 176.
3. Wilkins, H. P.: Our Moon. Fredrick Muller Ltd. , 1958.
4. Unpublished Manuscript.
5. Ley, W.: Conquest of Space. Viking Press, 1956.
6. Wilkins, H. P.: Moon Maps. Taber and Taber Ltd. , 1960.
7. Benzko, J.; Shotts, R. Q.: Lunar Resources (Internal Note). R-RP-Int-63-21.
8. Landing Site Seminar.
9. Goodacre, W.: The Moon. 1931, pp. 245-246.
10. Moore, P.: A Guide to the Moon. 1953.
11. Niedz, F. J.: Survey of the Physical and Environmental Parameters of the Moon. Apollo Support Group, General Electric Company, Daytona Beach, Florida, NASw-410-20-13-10, February 1963.
12. Green, J.: Geophysics as Applied to Lunar Exploration ( Final Report). Aero-Space Laboratories, Missile Division, North American Aviation, AFCRL-TR-60-409, 30 June 1960.
13. de Callatay, N.: Atlas of the Moon. St. Martin's Press, New York, 1964.
14. Kopal, Zdenek: Physics and Astronomy of the Moon. Academic Press, New York, 1962.
15. Hackman, Robert J.; and Mason, Arnold C.: Engineer Special Study of the Surface of the Moon. Prepared for Office, Chief of Engineers, Department of the Army, U. S. Geological Survey, Washington, D. C. , 1961.

## REFERENCES (Cont'd)

16. Wilkins, H. P.: Recent Research on the Moon - 1, The Journal of the British Interplanetary Society. Vol. 14, No. 3, May to June, 1955.
17. McCauley, J. F.: A Preliminary Report on the Geology of the Hevelius Quadrangle, Astrogeologic Studies. Annual Progress Report of the USGS, August 25, 1962 to July 1, 1963.
18. Baldwin, Ralph B.: The Measure of the Moon. University of Chicago Press, 1963.
19. Green, Jack: Lunar Vulcanism. Conference on Lunar Exploration, Part B, Va. Polytech. Inst. Bull., Vol. LVI, No. 7, 1962.
20. Hackman, R. J.: Geologic Map and Sections of the Kepler Region of the Moon. U. S. Geol. Surv., I-355 (LAC 57), 1962.
21. Kuper, Gerard P.: The Exploration of the Moon, Vistas in Astronautics. Vol. II, Pergamon Press, New York, 1959, pp. 273-312.
22. Shoemaker, Eugene M.: Interpretation of Lunar Craters, Physics and Astronomy of the Moon. Academic Press, New York, 1962, pp. 283-359.
23. Shoemaker, Eugene M.: The Geology of the Moon, Scientific American. Vol. 211, No. 6, 1964, pp. 38-47.
24. Interim Report, BSR 1074, The Bendix Corporation, December 1964.
25. McCauley, J. F.: Terrain Analysis of the Lunar Equatorial Belt. USGS, Preliminary Report, July 1, 1964.
26. Rogers, J. R.; and Vaughan, O. H.: Lunar Environment. NASA TM X-53124, September 1964.
27. Bensko, J.: Selenology, Handbook of Astronautical Engineering. McGraw-Hill Book Company, 1961.
28. Shoemaker, E. M.: Ballistics of the Copernican Ray System, Proceedings of the Lunar and Planetary Exploration Colloquium, Space and Information Systems Division, North American Aviation, Inc., Downey, Calif., March 17, 1960.

#### REFERENCES (Concluded)

29. Tudali, R. F.: Lunar Surface Characteristics. Bellcom, Inc., Washington, D. C., June 25, 1963.
30. Glossary of Geology and Related Sciences, American Geological Institute, NAS-NRC Publication 501, Washington, D. C., 1957.
31. Billings, M. P.: Structural Geology. Prentice Hall, Inc., 1954.
32. Moore, H. J.: The Geology of the Aristarchus Quadrangle of the Moon, Astrogeology Studies. 1962-1963, pp. 40.
33. Shoemaker, E. M.; R. J. Hodsman; and R. E. Eggleton: Interplanetary Correlation of Geologic Time, Advances in the Astronautical Sciences. Vol. 8, Plenum Press, Inc., New York, 1962.
34. Gilbert, G. K.: The Moon's Face: A Study of the Origin of Its Features. Philos. Soc. Washington Bulletin, Vol. 12, 1893.
35. Hackman, R. J.: Geologic Map and Sections of the Kepler Region of the Moon. Map I-355, U. S. G. S., Washington, 1962.

A DISCUSSION OF PROPOSED LANDING SITES  
FOR AAP LUNAR MISSIONS

By

John R. Rogers  
Brown Engineering Company

ABSTRACT

N 67-24271

Five sites on the lunar surface have been recommended for AAP missions: Hyginus Crater and Rill, Floor of the Crater Alphonsus, Hadley's Rill Region, Censorinus C, and Moltke B. The discussion in this paper includes comments on the scientific reasons for selecting each site and information on the nature of geological problems which might be investigated. A possible traverse around Site 2 (Floor of Alphonsus) is outlined. Recommendations for the planning of surface missions are made, based on new detailed information available from Ranger photographs.

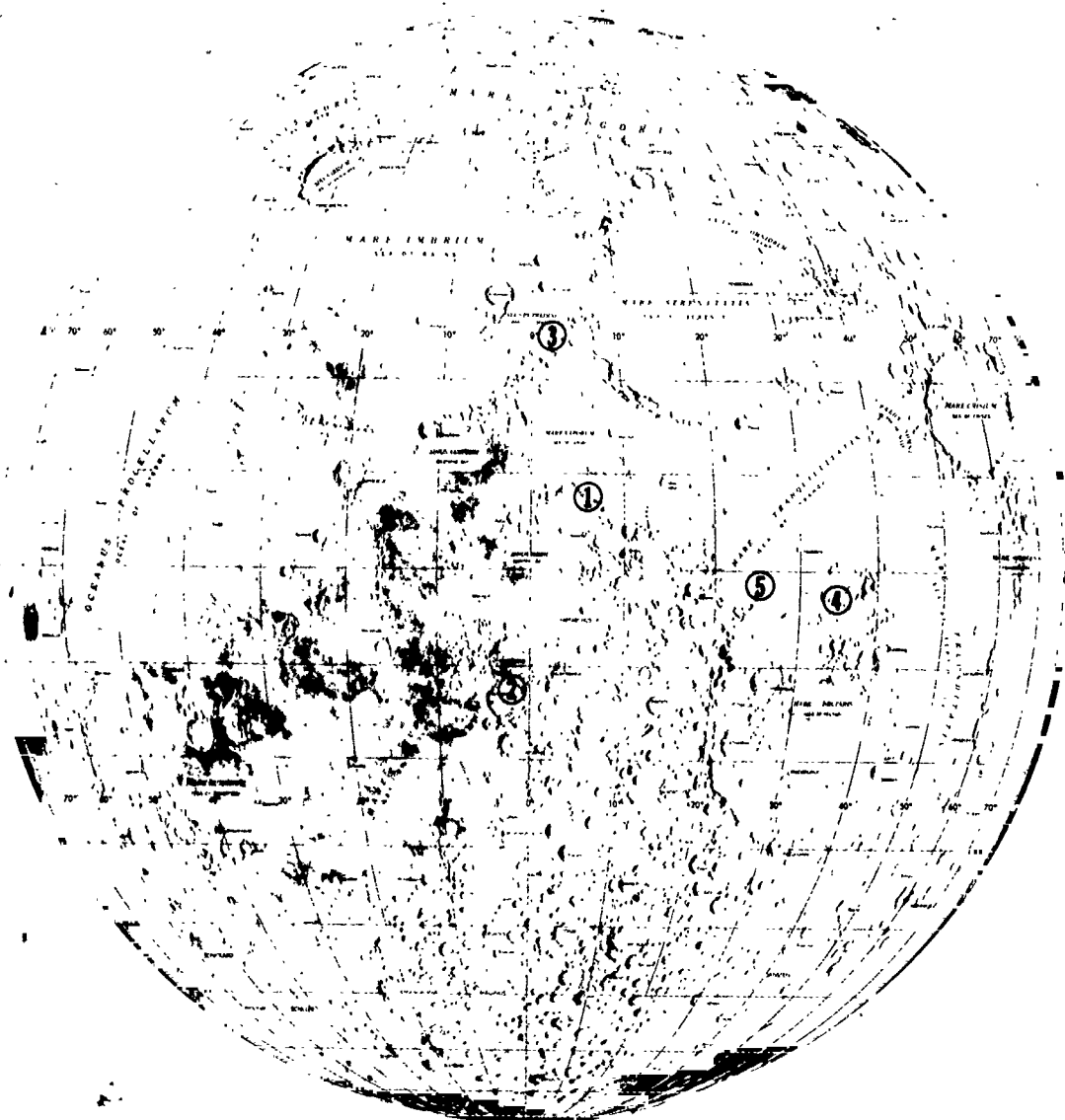
## INTRODUCTION

Scientific missions at various sites on the lunar surface will be directed toward achieving the major geoscience objectives of the post-Apollo lunar exploration programs. These objectives include detailed studies of:

- lunar stratigraphy
- surface and subsurface structure of the maria, highlands, and various types of craters
- lunar internal processes, such as volcanism, isostasy and tectonism
- lunar external processes, such as erosion and deposition
- thermal anomalies and gaseous emissions
- distribution of mass in the subsurface
- chemical differentiation of the moon

Five sites which have been previously selected<sup>1, 2</sup> are analyzed in this report (see Figure 1). The major consideration for selection was that the sites provide a maximum in geological information, with both stratigraphic and structural problems considered. The discussion, in the following sections, includes comments on the scientific reasons for selecting each site and information on the nature of the geological problems that might be investigated.





1. Hyginus Crater and Rill
2. Floor of Alphonsus
3. Hadley's Rill
4. Censorinus C
5. Moltke B

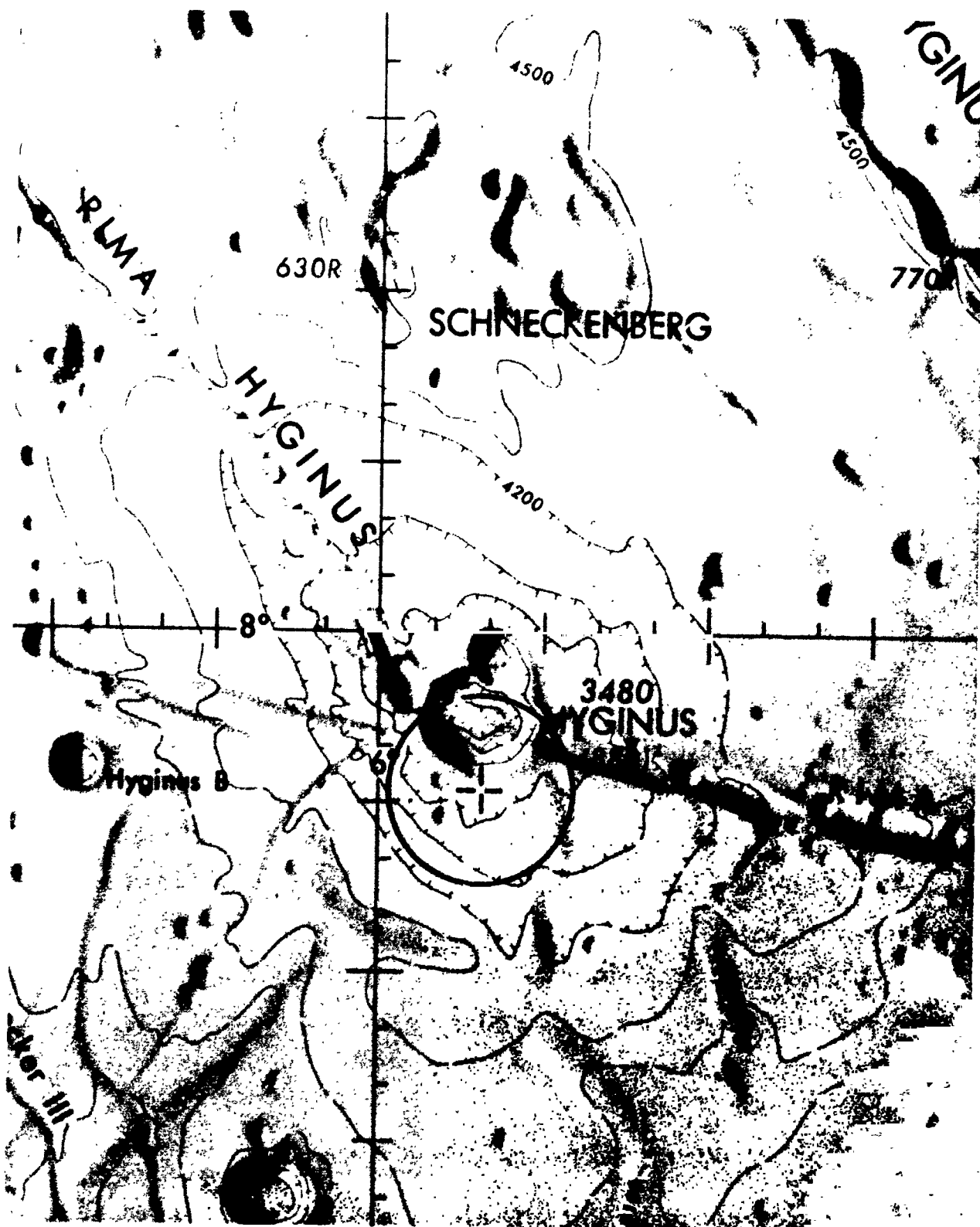
FIGURE 1. LOCATION MAP OF FIVE SITES

## PROPOSED POST-APOLLO SITES

### Site 1 - Hyginus Crater and Rill

The coordinates of this site are  $7^{\circ}36'$  N,  $6^{\circ}18'$  E (see Figure 2). The crater Hyginus is approximately 9 km wide and 880 m deep. It is situated near the midpoint of the Hyginus Rill, a roughly NW-SE trending rill approximately 175 km long. Situated along the Hyginus Rill are numerous chain craters.

A site on the floor of the crater Hyginus was selected in the Sonnett report<sup>3</sup> as a lunar landing site. The reasons for selecting this site were to investigate the material of the crater floor and to determine whether this is a maar-type crater. The belief that Hyginus is a maar crater is also reported in Shoemaker<sup>4</sup> who compares Hyginus with a diatreme. A diatreme is defined<sup>5</sup> as "a general term for a volcanic vent or pipe drilled through enclosing rocks by the explosive energy of gas-charged magmas". A maar crater, as used here, is a crater caused by a volcanic explosion; it is essentially the topographic expression of the same phenomenon which causes a diatreme. The most significant reason for visiting Hyginus is that volcanic explosion craters of this type are known to bring up material from deep within the interior of the planet, possible as much as 30-40 km below the surface. Rocks from this depth would be very significant in determining whether the moon has undergone differentiation into a crust and mantle. If the moon has undergone differentiation, this fact would have far-reaching implications concerning the cooling history of the moon and its density and elemental distributions. Additional reasons stated in the Sonnett report for studying Hyginus Rill are to detect and study any stratified rocks which may crop out along the Hyginus Rill and to study discontinuities in the rill and various bordering small craters.



Topographical Map, LAC 59

Circle Radius 8km

FIGURE 2. HYGINUS CRATER AND RILL (Site Number 1)

This report differs from the Sonnett report in recommending that the landing site be moved from the bottom of the crater Hyginus to its rim. The basis for this recommendation is the belief that, with almost any mobility system employed, operating on the rim would offer greater accessibility to places lying along the rill, e. g. , to the chain craters or discontinuities which lie along the rill. The petrographic information concerning the interior of the moon should be just as abundant in rocks lying on the rim as in those on the floor, since the crater origin has been attributed to a violent explosion, a phenomenon which would have ejected material from the bottom outward.

One commonly used constraint is an 8 km radius of operations for the missions. Therefore it would be possible to visit two small craters located 4 km south of the rim landing site. Also, there are abundant deposits of the Procellarum group located around the landing site. Since this site is near the edge of Mare Vaporum, it is likely that the Procellarum deposits will not be very thick at this site and that a vertical investigation along the crater or rill might reveal bedded ejecta blanket deposits derived from several of the nearby maria. The superposition of these strata could provide significant stratigraphic data for determining the relative ages of the maria. The contact between the Procellarum and Fra Mauro formations should be present along the rill wall. If good exposures of strata occur along rills such as this, a technique should be developed for sampling their walls since it does not seem feasible that any manned vehicle would be able to perform this task.

#### Site 2 - Floor of the Crater Alphonsus

The coordinates of this site are 12°45'S, 1°38'W (see Figures 3, 4 and 5). Alphonsus has a diameter of slightly over 100 km and a maximum relief of 3200 m. Rising from the center of its almost flat floor is a central peak 1080 m high.



Topographical Map, Lac 77

Circle Radius 8km

FIGURE 3. FLOOR OF ALPHONSUS (Site Number 2)



Ranger IX Photograph

Circle Radius 8km

FIGURE 4. A POSSIBLE TRAVERSE AT SITE 2  
(Floor of Alphonsus)

"REPRODUCIBILITY OF THE ORIGINAL PAGE IS POOR."

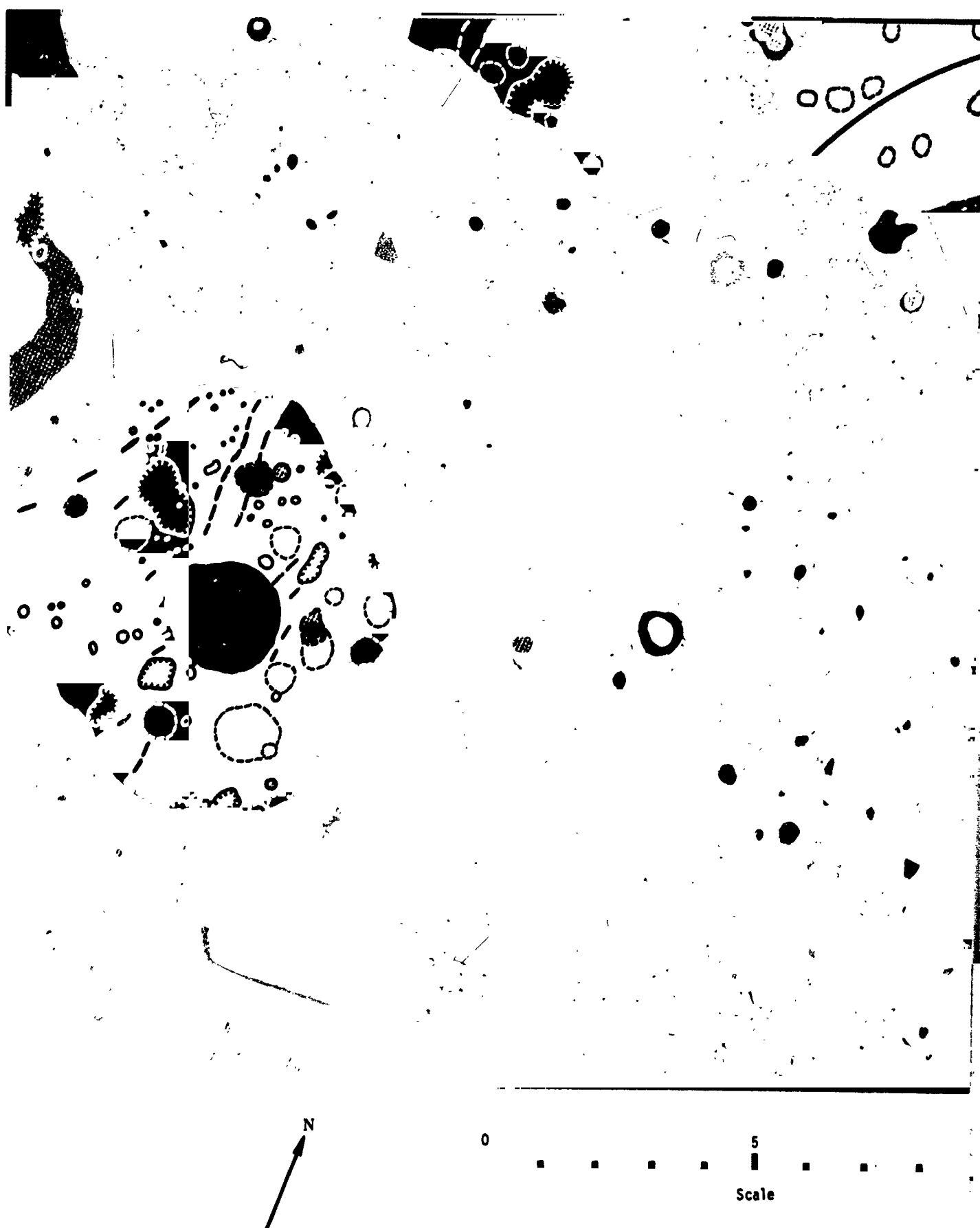











FIGURE 5. PHOTOGEOLOGIC MAP OF THE FLOOR



"REPRODUCIBILITY OF THE ORIGINAL PAGE IS POOR."



Stratigraphic Units

-  Crater slope material
-  Funnel craters
-  Concave rim craters
-  Convex rim craters
-  Dark floor material
-  Smooth floor material
-  Subdued rim craters
-  Cratered floor material
-  Alphonse wall material

Structural Symbols

-  Craters indistinct
-  Irregular depressions

10 km

OF ALPHONSUS (After McCauley)

48



The floor of Alphonsus was also named as a landing site in the Sonnett report<sup>3</sup>. The reasons stated for selecting this region included the following: 1) to study the dark halo craters which are probably maars, and 2) to study the rills on which some of these craters are located. The Sonnett report also pointed out the central peak and the Apenninian material on the floor of Alphonsus as subjects of geological interest.

On a typical traverse (see Figures 4 and 5) within an 8-km radius around the proposed landing site the explorers would be able to achieve all of the objectives of the Sonnett report except the study of the central peak. The particular site selected in this report would provide the opportunity to investigate the crater wall and sample it in several places. In addition, the landing site is about 3 km SW of the intersection of a large NW-SE trending rill and a large NS trending rill. These rills should provide an opportunity to study the structural geology of the rills themselves, and the stratigraphic sequences exposed along them. The study of the stratigraphy coupled with active refraction seismic and gravity experiments should disclose the tectonics and structural development of the large crater Alphonsus. Furthermore, the information derived from the stratigraphic and geophysical analysis would be of particular interest in helping to resolve the isostatic rebound theory of craters which have central peaks as postulated by Masursky<sup>6</sup>.

Numerous small halo craters lie along the rills on the floor of Alphonsus. It will be especially useful to investigate these craters to determine whether they are maar craters or some other kind of fissure eruption. The implications of the maar craters have already been discussed concerning Site 1 of this report. If they are of some other type of volcanic origin, they may still be very important in providing mineral resources and shelter for the lunar explorers.

The floor material of Alphonsus has been reported to be Apenninian<sup>3</sup>. It will be important to confirm this observation. Also,

as in the case of Hyginus Rill, it will be important to determine the thickness of the floor material perhaps by finding stratigraphic contacts in the rills. The stratigraphic sequence will likewise be a subject of great importance in determining the geological history of the Alphonsus region.

As at all the sites, an evaluation should be made of the impact process and its effect on the surficial layer. This study would include an investigation of some of the impact craters and sampling and mapping their related deposits. Since gases have been reported coming from Alphonsus, some emphasis should be placed on the problem of gas detection, particularly in planning the instrument program for exploring the chain craters and rills.

The work of McCauley<sup>7</sup> at the Branch of Astrogeology offers a new dimension to mission planning. McCauley has prepared a geological map of the floor of Alphonsus at a scale of 1:100 000 from the Ranger IX photographs. This represents approximately an order of magnitude increase in scale and resolution over present maps. A map, after that of McCauley, and a possible traverse are included (Figure 5) to illustrate the amount of detail that is now available to the mission planner.

Note that the traverse shown in Figure 4 on the untouched photograph is the same as the one shown on the geologic map of Figure 5. Table 1 shows a detailed description of the stations along this traverse. Clearly, the choice of stations along the traverse are influenced by the surface geologic interpretation. From an untouched photograph alone, only a relatively few features appear to be significant.

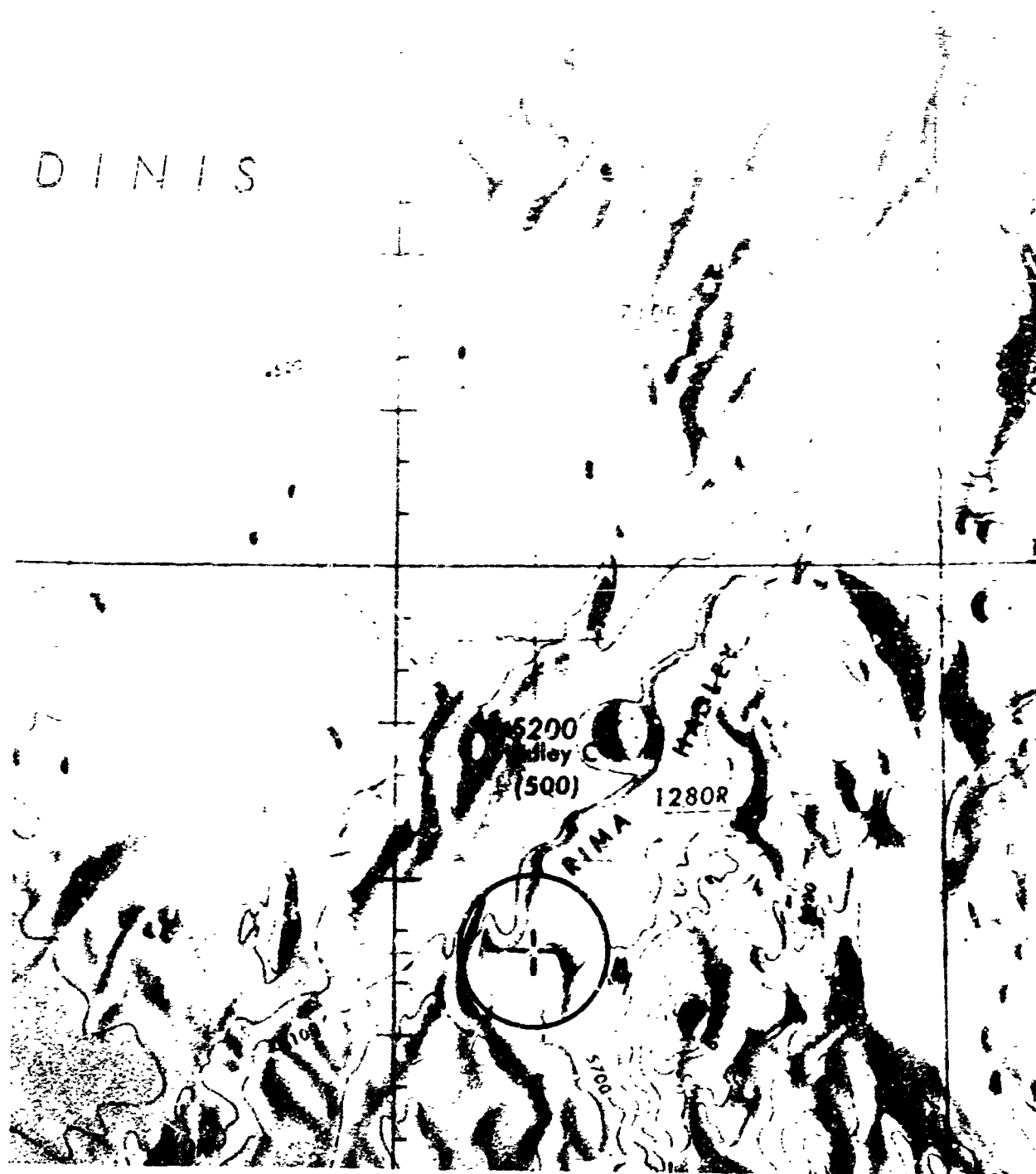
### **Site 3 - Hadley's Rill Region**

The coordinates of this site are 24°45'N, 2°30'E (see Figures 6 and 7). It is on the floor of Mare Imbrium, very near the base of the Apennine Mountains. The escarpment of the Apennine Mountains rises

TABLE 1

## TYPICAL TRAVERSE AT SITE 2 (NEEDOR OF ALPHONSUS)

Station	Distance (km)	Major Geological Features
LS	0	Imbrian cratered floor material
1	1.5	Contact between Imbrian cratered floor material and convex rim deposit
2	1.5	Indistinct crater
3	2.25	Edge of subdued rim crater
4	1.25	Contact between convex rim deposit and Eratosthenian dark floor material
5	1.25	Contact between Eratosthenian dark floor material and concave rim deposit
6	0.50	Edge of concave rim crater
7	1.25	Contact between concave rim deposit and Eratosthenian dark floor material
8	1.00	Contact between Eratosthenian dark floor material and crater wall material of Alphonsus
9	0.50	Edge of crater Alphonsus
10	0.75	Contact between crater wall material of Alphonsus and Eratosthenian dark floor material
11	3.25	Contact between Eratosthenian dark floor material and convex rim deposit
12	0.25	Edge of convex rim crater
13	1.75	Contact between convex rim deposit and Eratosthenian dark floor material
14	0.75	Edge of funnel crater
15	0.50	Edge of rill
16	2.75	Edge of funnel crater
17	0.25	Contact between funnel crater and convex rim deposit
18	0.25	Edge of Satellite crater
19	1.75	Summit of rim of convex crater
20	1.50	Contact between convex rim deposit and Eratosthenian cratered floor material
Total	26.50	



Topographical Map, LAC 41

Circle Radius 8km

FIGURE 6. HADLEY'S RILL REGION (Site Number 3)



Herbig Photograph (Courtesy of Lick Observatory)

Circle Radius 8km

FIGURE 7. HADLEY'S RILL REGION (Site Number 3)

abruptly 1800 m above the floor near this site. The exposure of rocks in the Apennine Mountains escarpment should provide valuable information about the rocks of the Imbrian System and perhaps the pre-Imbrian rocks. By investigating this escarpment, it will be possible to test the hypotheses upon which the stratigraphy of the Imbrian System is based. Furthermore, this site should allow us to determine the nature of the basin and range margin and could provide valuable data on the tectonic development of these two major structural features.

From the deposits lying on the floor of Mare Imbrium the mineralogical and chemical composition, mode of deposition, and geological significance can be determined. The single most striking feature of this site is Hadley's Rill. This is a sinuous rill which is probably not related to faulting or jointing as most rills appear to be. It has been suggested<sup>8</sup> that this sinuous rill may have been caused by nuée ardente (a gas charged, volcanic cloud) which issued from a small volcano-like crater at its southwest extremity. Both the rill and the craterlet are within 8 km of the landing site. Located about 22 km NE of the landing site is another volcano-like feature which is much larger than the one related to the rill. This low conical feature has a crater 4 or 5 km across and is possibly a caldera. It is possible that this feature could be reached by a Lunar Flying Vehicle (LFV).

#### Site 4 - Censorinus C

The coordinates of this site are 2°43'S, 34°44'E (see Figure 8). Site 4 is on a relatively smooth area just east of the crater Censorinus C. Near the landing site are a number of small craters of 2 to 4 km diameters. Also there is a set of NW-SE trending rills or lineaments which pass near the landing site.

This is a highlands location selected for the purpose of investigating the stratigraphy in a highlands region. According to Elston<sup>9</sup>, there

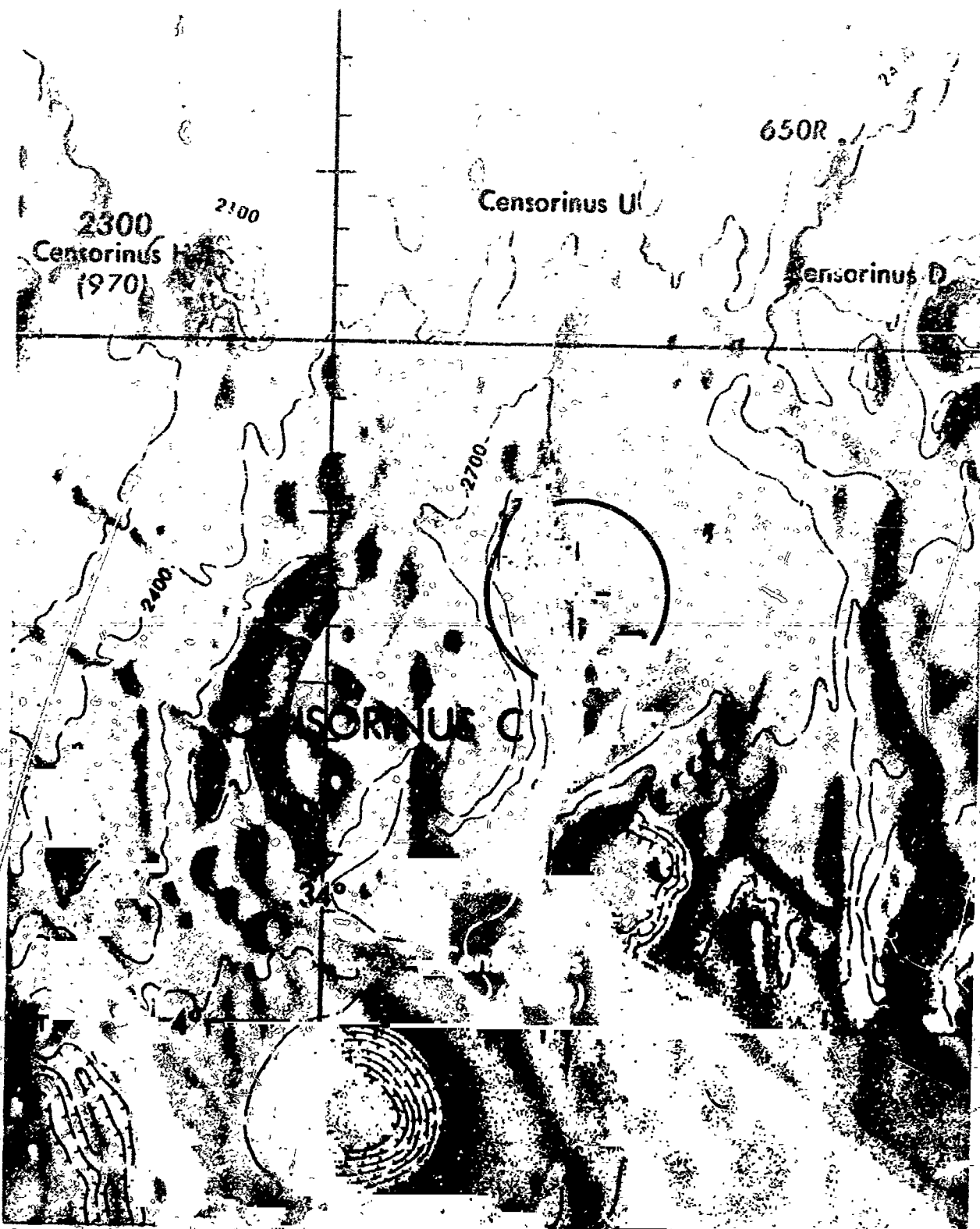


FIGURE 8. CENSORINUS C (Site Number 4)

are three ages of material in the Columbo region. These ages of material correspond to a regional depositional blanket of material from Mare Nectaris (the oldest unit), the deposits of broken wall polygonal craters of the Gutenberg type (the middle unit), and a regional depositional blanket of material from Mare Tranquillitatis (the youngest unit).

Apparently Censorinus C is a Gutenberg (broken wall) type crater which has been masked by the younger ejecta blanket from Mare Tranquillitatis. The walls of young, fresh, impact craters in the area of the landing site might provide a "window" to study the stratigraphy of the three units in this region which have been recognized. In addition to the regional stratigraphy there is photographic evidence of local lava flows in this region of relatively recent origin. Many of the NW-SE trending rills cut across all three of the stratigraphic units and are therefore younger than the units they cut across. Another significant stratigraphic problem at this site will be to correlate these three regional stratigraphic units with the other stratigraphic units on the moon. Presently the units at this site are classified as pre-Imbrian.

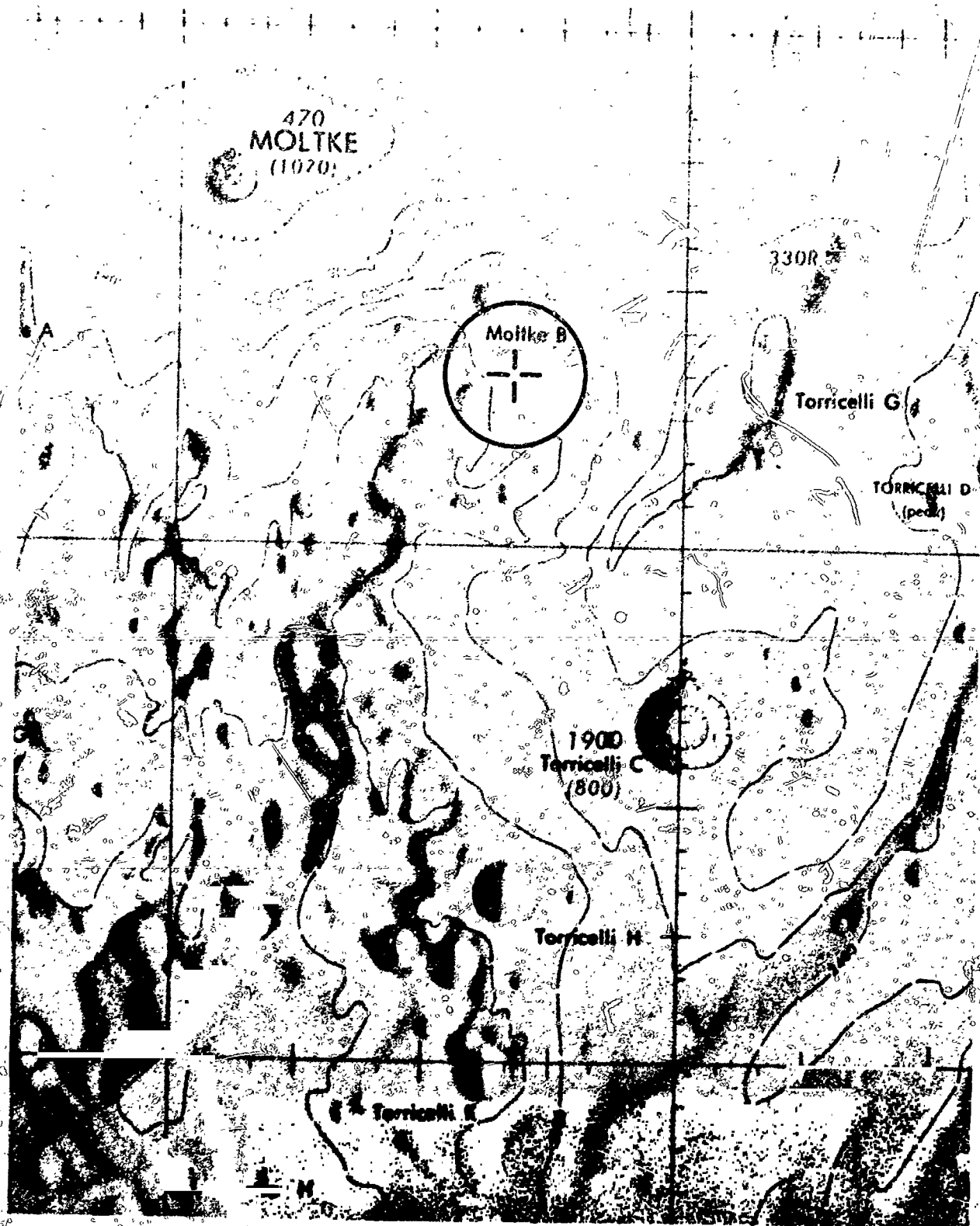
#### Site 5 - Moltke B

The coordinates of this site are  $1^{\circ}20'S$ ,  $25^{\circ}20'E$  (see Figure 9).

Site 5 was recommended by the Bendix Systems Division<sup>2</sup> primarily because of its proximity to the boundary of a mare and highlands region.

At this site both pre-Imbrian material from the highlands and Procellarum material of the mare should be within range. In addition, it should be possible to construct a subsurface map of the shallow basin floor in this region based on seismic and gravity profiles. Probably the Procellarum will only be a few hundred feet thick over most of the region, but it will be significant to determine if there is a regular increase in the thickness of this deposit away from highlands as one might suspect.





Topographical Map, LAC 78

Circle Radius 8km

FIGURE 9. MOLTKE B (Site Number 5)

The LAC map of this region indicates several interesting features situated within an 8-km radius of the landing site. These features include several craters of unknown origin, one dome of about 3 km diameter, and a set of criss-crossing rills that intersect almost in the center of Moltke B.

Some of the geological problems at this site include the nature of the contact between the mare and highlands and the shallow subsurface of the mare, possible stratigraphic contacts situated on the walls of the rills or the walls of Moltke B, and possible volcanic activity or volcanic deposits and related mineralization associated with the dome-shaped hill.

The problems at this site may be somewhat simpler than at some of the other sites and perhaps less challenging. Some of the geological questions posed here may be answered on the first two or three Apollo missions. On the other hand, the problems of lunar geology may turn out to be more complex than we now anticipate and a site such as this will be welcomed.

## CONCLUSIONS

It is believed that the five sites are well suited for solving problems of a regional geological nature. However, it is realized that there are many other sites which are potentially as informative as these and the selected sites should not be considered as having the ultimate in scientific value.

The results of this study indicate that data on the lunar surface at this time is of sufficient detail and quality to define a major portion of the lunar exploration problems and to discuss methods of solving these problems. However, in view of recent advances in interpreting the Ranger VII, VIII, and IX photographs at the Branch of Astrogeology, it should now be possible to construct mission profiles which are much more detailed and significant than those previously prepared. This investigator strongly recommends that a study of mission profiles be made based on the large-scale (1:100,000 to 1:10,000) geological maps now available from the Branch of Astrogeology (Figure 5).

The mission profiles should include a set of subsurface models in addition to considerations of surface traverses and their related sampling, surface probes, and mobility problems. These models would predict the subsurface geometry which is anticipated in the regions in which large-scale maps are available. The "predicted" subsurface configuration at the same scales which will be used on actual lunar missions could then be used to indicate the responses anticipated from geophysical surveys, drilling, and subsurface probes.

## REFERENCES

1. Elston, D. P., (Personal Communication, May 1965)
2. "Scientific Mission Support Study, Apollo Extension System", BSR-1153, Bendix Corp., Bendix Systems Division, July 1965
3. Sonnett, C. P., "Draft Report of the Ad Hoc Working Group on Apollo Experiments and Training on the Scientific Aspects of the Apollo Program", 1962
4. Shoemaker, E. M., "Interpretation of Lunar Craters", Physics and Astronomy of the Moon, F. Kopal, ed., Academic Press, New York and London, 1962
5. Glossary of Geology and Related Sciences, American Geological Institute, NAS-NRC Publication 501, Washington, D. C., 1957
6. Masursky, Harold, "A Preliminary Report on the Role of Isostatic Rebound in the Geological Development of the Lunar Crater, Ptolemaeus", Astrogeological Studies, Annual Progress Report, July 1, 1963 to July 1, 1964
7. McCauley, John F., "Intermediate Scale Geologic Map of a Part of the Floor of Alphonsus", unpublished report, Branch of Astrogeology, United States Geological Survey, Flagstaff, Arizona, 1965
8. Cameron, W. S., "An Interpretation of Schroter's Valley and Other Lunar Sinuous Rills", Journal of Geophysical Research, Vol. 69, No. 12, pp. 2423-2430, June 15, 1964
9. Elston, Donald P., "Stratigraphic Relationships in the Eastern Part of the Moon" (abs), Abstracts for 1964, Geological Society of America Special Paper Number 82, 1965

# DEVELOPMENT OF A LUNAR PHOTOMETRIC FUNCTION FROM EXPERIMENTAL DATA

By

E. F. Snyder  
Chrysler Corporation

## ABSTRACT

N67-24272

The lunar surface possesses some very unusual light reflection characteristics. Perhaps the most striking feature is the preference for moonlight to be reflected toward the sun, or always predominately in the direction from which it came. This effect is seen in the pronounced brightening of the moon at full moon. The need exists for an accurate photometric model of the lunar surface's directional reflection characteristic under all angles of solar illumination. Using an empirical approach and some mathematical theory, a functional expression is developed to describe the existing lunar directional reflectance characteristics. A two-dimensional equatorial photometric function is developed initially, and is expanded into a three-dimensional photometric function. For ten widely distributed lunar craters, and for the entire range of phase angles, very good agreement is demonstrated between the experimental results and the predicted results using the developed lunar photometric function. The developed three-dimensional lunar photometric function has been integrated over the face of the moon for many phase angles. The integrated brightness at phase angle using the developed photometric function is in excellent agreement with experimental results of Rougier and other investigators.

## LUNAR PHOTOMETRY - GENERAL

Lunar photometry is concerned with the investigation of the variation in lunar surface brightness seen with changing solar phase angles and locations on the lunar surface. Photometry, in general, is concerned with making luminous intensity measurements, luminous flux measurements, and brightness measurements of an object. The directional reflectance characteristics of the lunar surface specify the degree of surface brightness that will be seen from various directions, when the lunar surface is illuminated by the sun from any direction.

### THE MOON'S PECULIAR PHOTOMETRIC CHARACTER

The moon has long been known to possess some rather unusual photometric or reflectance characteristics. The most striking is its strong scatterback characteristic, which the entire lunar surface possesses to a degree far in excess of any natural terrestrial surface. Most very rough surfaces, other than the moon's, possess the characteristics that the incident radiation is scattered or reflected with nearly equal probability in all directions, in a manner similar to that of the idealized Lambert or perfectly diffuse surface. It is a characteristic of a perfectly diffuse sphere illuminated by what is essentially a point source, such as the sun, that its illuminated portions will appear equally bright regardless of the viewing angle or illumination angle. If the moon were a perfectly diffuse reflector, its relative intensity curve would be identical to the portion of the lunar disc area illuminated at various lunar phase angles. This, however, is very far from being the case. Figure 1 shows the visible lunar brightness integrated over the entire lunar surface relative to full moon brightness as measured by Bougier<sup>1</sup>, compared with the illuminated portion of the lunar disc. Note that the illuminated portion of the moon is only about 1/2 as bright at a  $30^\circ$  phase angle, ( $\alpha = 30^\circ$ ), as this corresponding portion at full moon, ( $\alpha = 0$ ). At first and last quarter, ( $\alpha = 90^\circ$ ), the illuminated portion of the moon is only about 15% as bright as the corresponding portion at full moon. At  $20^\circ$  from new moon, ( $\alpha = 160^\circ$ ), the average lunar brightness of the illuminated area is lower than the full moon brightness of the corresponding area by a factor of twenty.

Even though the moon exhibits extreme variation in brightness with lunar phase angle, the full moon surface is uniformly bright across its face, except for relatively minor local albedo (reflectance) variation. Limb darkening is completely absent at full moon. However, both before and after full moon, limb brightening is observed on the terminator closest the sun and limb darkening is observed on the terminator farthest from the sun. Another observed effect is that there is relatively little variation in brightness along the lines of illumination longitude.

Even at its brightest, at full moon, the lunar reflectance is very low, possessing a full moon albedo of about .10 to sunlight, with relatively small brightness variation for various surface features. Local albedos differ by

less than a factor of two from the average reflectance; so features of the moon exhibit very little brightness contrast, except as provided by shadows. At near shadow conditions, variation in surface orientation produces very marked contrast. Another characteristic is the yellow-grayness and/or lack of color contrast which characterizes the moon. The moon possesses a higher reflectance (.17) at the red end of the spectrum than at the blue end (.07). This produces a natural yellow tinge which is augmented as seen from the earth, due to the deficiency in blue light transmission, since blue light cannot pass through the earth's atmosphere without suffering scattering. A goal of lunar photometry has been to find a surface that simultaneously matches the spectral, directional, and polarimetric reflectance characteristics of the moon.

### SURFACE CLASSIFICATION

Surfaces may be classified by their directional reflectance characteristics to visible radiation. Experience with terrestrial surface reflections reveals two common basic types of surfaces, with majority of terrestrial surfaces lying somewhere in between. These types are (1) a smooth mirror surface, typified by a quiet lake, plate glass, waxed table top, automobile finish, or a sheet of smooth aluminum foil; (2) a diffuse surface typified by a piece of writing paper, a piece of cotton cloth, a wood surface, and desert sands.

For a smooth surface, Fresnel's reflection laws may be used to predict accurately the spectral directional reflectance and polarization. Microscopically, a rough surface presents a wide assortment of surface normal directions. The vast majority of surfaces encountered in nature are semi-diffuse, semi-mirror surfaces. That is, they tend to reflect light in a variety of directions, with the greatest reflective intensity occurring in the specular direction.

The moon, however, does not possess the semi-diffuse, semi-specular reflectance characteristic that is typical of the great majority of terrestrial surfaces. Instead it possesses a characteristic that is quite rare among terrestrial surfaces. The moon has a very pronounced tendency to reflect light back in the direction from which it came irrespective of the direction of incidence. This property is characteristic of a very porous surface, composed of cavities, recesses, and voids.

A general characteristic of convex shapes, particularly fibers, is that, although diffuse, they still have their peak reflectance in the forward or specular direction, especially for low grazing angles. Concave shaped surfaces have the opposite characteristic, which is also characteristic of the moon, exhibiting much greater scatterback than forward specular reflectance.

For a rough surface, the casual employment of Fresnel reflection laws gives poor agreement with experimental data because of the inherent multiple reflections involved. Although Fresnel laws remain valid at a microscopic interface and are capable of simultaneously describing the directional and polarimetric reflectance characteristics, these laws are rarely employed to obtain a directional photometric function because of the complexity of multiple reflection ray tracings.

## LOW GRAZING ANGLES - ABSENCE OF LIMB DARKENING

At low grazing angles, every smooth plane surface displays a high specular reflectance. Many surfaces which diffuse radiation at normal incidence reflect specularly or appear smooth at low grazing angles within a degree of the surface ( $89^\circ < \psi < 90^\circ$ ). If, at these low grazing angles, (1) the projected features of the surface become smaller than one wavelength of the incident radiation, and (2) the features that protrude the most are essentially parallel to the gross surface, then high specular reflectance is observed, and the surface behaves as a smooth surface. At very low grazing angles, a rough convex surface will become smooth; a rough concave surface, however, is prevented from doing so by failure to satisfy condition (2).

At full moon, limb darkening is absent; consequently, for low grazing angles on the moon, high specular reflectance just does not occur. This strongly suggests that the lunar surface, in addition to being highly porous, is predominately concave in microdetail. Hapke<sup>2</sup> has made the astute observation from experimental photometric tests that, for a material to backscatter light as strongly as the moon does, it must be extremely porous and composed of interconnected cavities that open to the surface.

## SIGNIFICANT LUNAR PHOTOMETRIC CONTRIBUTIONS

Significant photometric contributions toward understanding the nature of the lunar surface have been made in recent years by Van Diggelen<sup>3</sup> and Hapke<sup>4</sup>. Excellent summaries of the significant lunar photometric knowledge has appeared in recent years by M. Minnaert<sup>5</sup>, Z. Kopal<sup>6</sup>, and C. A. Pearse<sup>7</sup>. Russian astronomers have been quite active in the field of observational and interpretive lunar photometry, the most notable contributors being N. P. Barabascheff<sup>8</sup>, V. A. Fedorets<sup>9</sup>, V. G. Fesenkova<sup>10</sup>, A. V. Markov<sup>11</sup>, N. S. Orlov<sup>12</sup>, N. N. Sytinskaya<sup>13</sup>, and V. V. Sharonov<sup>14</sup>. Russian and American investigators in recent years have been largely at odds concerning the interpretation and emphasis on lunar photometric data, with the Russian favoring a surface composed of a light porous froth of volcanic slag and the American favoring a meteoric dust surface. Both groups agree on a high-porosity surface. At yet, no one has succeeded in constructing a satisfactory physical model capable of predicting from theory the observed lunar surface directional reflectance and polarization characteristics accurately.

## PHOTOMETRIC FUNCTION

A lunar photometric function, developed by the writer<sup>15</sup> in 1964, describes with good accuracy the directional reflectance characteristics of the lunar surface. This photometric function is programmed readily on a computer, and will accurately describe the reflected solar radiation incident upon an object located on the lunar surface or in a lunar orbit. This photometric function was developed primarily by an empirical approach, together with a certain amount of mathematical theory. We undertook the task of representing accurately in functional form the three-dimensional photometric characteristics of the



moon as it exists. The technique that was employed might be called "Multi-dimensional analytical function development." A one-dimensional function,  $g(\alpha)$  was developed for equatorial lunar reflectance using certain special cases ( $\beta = 0$ ,  $\beta = \alpha$ , etc). This function  $g(\alpha)$  was combined with a mixed function  $y(\alpha, \beta)$ . The mixed function was developed to satisfy certain symmetry relations. The result was a two-dimensional equatorial photometric function that fit well the equatorial observational data of M. Minnaert<sup>15</sup> (1961). His data had been summarized and averaged previously by N. S. Orlova<sup>12</sup> (1956). The original measurements were made by Fedoretz<sup>9</sup> (1952) and by Sytinskaya and Sharonov<sup>14</sup> (1952). The developed two-dimensional expression was then expanded into a three-dimensional photometric function.

### TWIN COORDINATE SYSTEMS

To describe lunar reflectance, it has proved convenient to employ two different types of coordinate systems. An earth-based observational coordinate system is defined in Figure 2a. These coordinates consist of a solar phase angle,  $\alpha$ , a pair of lunar surface coordinates, a lunar surface longitude,  $\beta$ , and a lunar surface latitude,  $\gamma$ , where  $\gamma = 0$  is the illumination equator and  $\beta$  is measured from the sub-earth point. For operations on the lunar surface, we will employ a set of lunar surface coordinates. Such a set of coordinates is defined in Figure 2b; these consist of (1) zenith angle,  $\psi$ , of the incident flux relative to the gross surface normal, (2) zenith angle,  $\phi$ , of the exit ray (observer direction) and (3) azimuth angle,  $\theta$ , of the exit ray measured in the plane of the gross lunar surface. This angle is measured relative to the plane of incidence. The included angle between the incident and exit ray is  $\alpha$ , precisely the solar phase angle employed in the earth-based coordinate system. In the lunar-based coordinate system, an important reversible relation exists between the azimuth angle,  $\theta$ , and the phase angle,  $\alpha$ .

$$\cos \alpha = \cos \psi \cdot \cos \phi + \sin \psi \cdot \sin \phi \cdot \cos \theta \quad (1.a)$$

This relationship is obtained from the dot product of the incident and exit unit vectors. The significance and usefulness of this expression lies in the fact that once  $\psi$  and  $\phi$  are chosen,  $\theta$  determines  $\alpha$ , and vice versa.

$$\cos \theta = \frac{\cos \alpha - \cos \psi \cdot \cos \phi}{\cos(\psi - \phi) - \cos \psi \cdot \cos \phi} \quad (1.b)$$

Because the lunar photometric function depends so strongly upon the phase angle,  $\alpha$ , we chose to utilize as the set of 3 independent lunar-based variables  $\psi$ ,  $\phi$ , and  $\alpha$  rather than  $\psi$ ,  $\phi$ , and  $\theta$ . A transition between the two viewpoints may be effected by either equation (1.a) or (1.b).

A second and third relation may be derived similarly by taking dot products of the appropriate unit vectors.

$$\cos \phi = \cos \beta \cdot \cos \gamma \quad (2)$$

$$\cos \psi = \cos(\alpha - \beta) \cdot \cos \gamma \quad (3)$$

Taken as a triplet of equations, (1), (2), and (3) provide the means for making a general transition between an earth-based observational coordinate system of the moon ( $\alpha, \beta, \gamma$ ) and a lunar-surface-oriented system ( $\psi, \phi, \theta$ ). In making a transition from a terrestrial ( $\alpha, \beta, \gamma$ ) viewpoint to a lunar ( $\psi, \phi, \alpha$ ) viewpoint, we will require only equations (2) and (3).

#### PHOTOMETRIC SIMPLIFICATIONS UPON THE ILLUMINATION EQUATOR

For points being observed on the lunar equator,  $\gamma = 0$ , equations (2) and (3) simplify, so that:

$$\cos \phi = \cos \beta \quad \phi = \pm \beta \quad (2.a)$$

$$\cos \psi = \cos (\alpha - \beta) \quad \psi = \pm (\alpha - \beta) \quad (3.a)$$

Instead of using three independent variables ( $\psi, \phi, \alpha$ ), two independent variables ( $\alpha, \beta$ ) will suffice to describe the observed photometric function for the lunar equator. Once a two-dimensional equatorial photometric function has been obtained, this may be converted with relative ease into a three-dimensional function in ( $\psi, \phi, \alpha$ ) by utilizing symmetry relation in  $\psi$  and  $\phi$ .

Figure 3, is a plot of the observed two-dimensional photometric function of the moon as presented by M. Minnaert<sup>5</sup>, with some minor alterations which we made after re-examining the data of N. S. Orlova<sup>12</sup>.

Figure 3 serves as the graphical representation of the actual lunar equatorial reflectance characteristics. The two-dimensional equatorial photometric function that we developed as our best analytical function fit of these data is:

$$F_{2d}(\alpha, \beta) = \frac{\cos(\alpha - \beta)}{\cos\left(\frac{\alpha}{2} - \beta\right) \cdot \left(1 + \sin\frac{\alpha}{2}\right)^2} \sqrt{\frac{1 - \sin\frac{\alpha}{2}}{\cos\frac{\alpha}{2}}} \quad (4)$$

#### DEVELOPMENT OF LUNAR PHOTOMETRIC FUNCTION

Several well known observational results may be formalized into a set of general lunar statements. Consistent with the following statements, we develop first a two-dimensional Equatorial Photometric Function,  $F_{2d}(\alpha, \beta)$  and then subsequently expand this into a three-dimensional Photometric Function, which is presented in three different forms.

$$F_{3d}(\psi, \phi, \alpha) \text{ and } F_{3d}(\psi, \phi, \theta) \text{ and } F_{3d}(\alpha, \beta, \gamma).$$

- I. At full moon, the lunar surface is uniformly bright across its face, except for relatively minor albedo variations. This fact will be expressed functionally by the condition that at zero phase angle ( $\alpha = 0$ ), both the two-dimensional equatorial photometric function,

$F(\alpha, \beta)$  and the more general three-dimensional photometric function,  $F(\alpha, \beta, \gamma)$  are both unity, irrespective of the value of  $\beta$  and  $\gamma$ .

$$F_{2d}(0, \beta) = 1, \quad -\frac{\pi}{2} < \beta < \frac{\pi}{2} \quad (5)$$

$$F_{3d}(0, \beta, \gamma) = 1, \quad 0 < \gamma < \frac{\pi}{2} \quad (5.a)$$

II. The integrated flux from the moon peaks sharply at full moon, with a steep rise prior and up to full moon, and a steep descent immediately after full moon. The trace of  $F(\alpha, \beta)$  for a fixed value of  $\beta$  displays a sharp apex with a slope discontinuity at  $\alpha = 0$ .

$$\frac{dF(0_+, \beta)}{d\alpha} \neq \frac{dF(0_-, \beta)}{d\alpha} \quad (6)$$

III. The photometric function is always positive or zero; and, except under rare conditions, it is confined to an upper limit of one.

$$0 < F_{2d}(\alpha, \beta) \lesssim 1 \quad (7)$$

$$0 < F_{3d}(\alpha, \beta, \gamma) \lesssim 1 \quad (7.a)$$

IV. At a non-zero lunar phase angle ( $\alpha \neq 0$ ), the moon is not full, so that part of the lunar surface facing the earth is not directly illuminated by the sun. Treating the moon as a sphere, there exists a boundary between the illuminated and the non-illuminated portions of the moon. For  $\alpha > 0$ , this illuminated boundary is defined by the simple equation,  $\beta = \alpha - \frac{\pi}{2}$ , where  $\beta$  is the lunar surface illumination longitude defined in Figure 2a. At other than full moon, there exists a darkened terminator. The photometric function assumes a value of zero at the darkened terminator and for all points on the non-illuminated portion of the moon.

$$F_{2d}(\alpha, \beta) = 0, \quad -\frac{\pi}{2} \leq \beta \leq \alpha - \frac{\pi}{2} \quad (8)$$

$$F_{3d}(\alpha, \beta, \gamma) = 0, \quad -\frac{\pi}{2} \leq \beta \leq \alpha - \frac{\pi}{2} \quad (8.a)$$

V. All points that have been observed on the lunar surface possess a similar photometric function. The two types of lunar features, Maria (plains) and Terrae (highlands), which present the greatest visual contrast, possess virtually identical reflectance characteristics. Generally, the highlands possess a greater data scatter than the flatter region on the moon. Large-feature shadowing problems exist in rough terrain at low grazing angles, but otherwise, one photometric function serves to describe the directional reflectance characteristics of the entire lunar surface. As a consequence of the above statement, certain symmetry conditions will exist between different observed points on the lunar surface. A phase angle,  $\alpha$  and longitude,  $\beta$  symmetry condition requires that

$$F_{2d}(-\alpha, \beta) = F_{2d}(\alpha, -\beta) \quad (9)$$

$$F_{3d}(-\alpha, \beta, \gamma) = F_{3d}(\alpha, -\beta, \gamma) \quad (9.a)$$

where  $\alpha$  and  $\beta$  may be either positive or negative numbers.  
A latitude symmetry condition requires that

$$F_{3d}(\alpha, \beta, \gamma) = F_{3d}(\alpha, \beta, -\gamma) \quad (10)$$

For non-equatorial points, combining relations 9.a and 10 produce four points on the lunar surface (at two different phase angles) for which the value of the photometric function under these different conditions will be identical.

VI. A reciprocity law involving symmetry in  $\psi$  and  $\phi$  states that  $F_{3d}(\psi, \phi, \alpha)/\cos \psi = h(\psi, \phi, \alpha)$  must be symmetric in  $\psi$  and  $\phi$ .

$$h(\psi, \phi, \alpha) = h(\phi, \psi, \alpha) \quad (11)$$

#### SELECTION OF AN APPROPRIATE SET OF INGREDIENTS

The initial effort of this study was directed toward developing a satisfactory algebraic-trigonometric expression for the lunar equatorial photometric function,  $F_{2d}(\alpha, \beta)$ . It was noted that Statement IV would be satisfied by use of the factor  $\cos(\alpha - \beta)$  in the numerator of the expression for  $F_{2d}(\alpha, \beta)$ . This factor,  $\cos(\alpha - \beta)$  has the characteristic that it is zero at the terminator or whenever  $\beta = \alpha \pm \frac{\pi}{2}$  since  $\cos \frac{\pi}{2} = 0$ .

The choice for a first ingredient,  $\cos(\alpha - \beta)$ , appears to have been a judicious one because it also prepared the way for the easy satisfaction of Statement VI.

Statements I and IV, which define when the function is one and zero, respectively, are elemental to the functional development. Both of these statements are satisfied simultaneously by an expression of the form:

$$F(\alpha, \beta) = \left[ \frac{\cos(\alpha - \beta)}{\cos(a\alpha - \beta)} \right]^n \cdot g^*(\alpha) \quad (12)$$

where  $g^*(\alpha)$  is a phase angle dependent function having the characteristic  $g^*(0) = 1$ , where  $n > 0$ , and "a" must be a number between 0 and 1, such that  $\cos(a\alpha - \beta)$  does not assume the value of zero in the range for which  $F(\alpha, \beta)$  is to be defined.

Equation 12 will satisfy statement VI, for  $n = 1$  and  $a = 1/2$ , because on the lunar equator we have:

$$\begin{aligned} \cos(\alpha - \beta) &= \cos \psi \\ \cos\left(\frac{\alpha}{2} - \beta\right) &= \cos \frac{\psi + \phi}{2} \end{aligned} \quad \text{symmetric in } \psi \text{ and } \phi$$

Statements I, IV and VI are all satisfied by two-dimensional functions of the form:

$$F_{2d}(\alpha, \beta) = y(\alpha, \beta) \cdot g(\alpha) \quad (13)$$

where

$$y(\alpha, \beta) = \frac{\cos(\alpha - \beta)}{\cos \frac{\alpha}{2} - \beta}$$

The following expression provides an alternate means of satisfying Statement I and IV.

$$F(\alpha, \beta) = [\cos(\alpha - \beta)]^{b\alpha} \cdot g_2^*(\alpha) \quad (14)$$

where  $g_2^*(\alpha)$  is a different function of  $\alpha$ .

Expressions of the form shown in equation (14) were examined but were rejected primarily because of their inability to functionally satisfy (reciprocity) statement VI.

Equation 13 actually satisfies only the first part of Statement IV: that pertaining to the terminator boundary. This is easily remedied for positive values of  $\alpha$  by letting:

$$F_{2d}(\alpha, \beta) = \begin{cases} \frac{\cos(\alpha - \beta)}{\cos \left( \frac{\alpha}{2} - \beta \right)} \cdot g(\alpha), & 0 < |\alpha - \beta| < \frac{\pi}{2} \\ 0, & \frac{\pi}{2} < |\alpha - \beta| < \pi \end{cases} \quad (15)$$

For negative values of phase angle,  $\alpha$ , Equation 9 of statement V will be used to define the function. The  $y(\alpha, \beta)$  portion of equation 15, already satisfies statement V. Hence,  $F_{2d}(\alpha, \beta)$  will satisfy it as long as  $g(\alpha)$  is symmetric about  $\alpha = 0$ .

$$g(\alpha) = g(-\alpha) \quad (16)$$

#### PHASE ANGLE DEPENDENT FUNCTION, $g(\alpha)$

The  $\alpha, \beta$  shaping function,  $y(\alpha, \beta) = \frac{\cos(\alpha - \beta)}{\cos \left( \frac{\alpha}{2} - \beta \right)}$ , which we have selected, possesses the following characteristics

when

$$\alpha = 0 \quad y(\alpha, \beta) = 1, \quad -\frac{\pi}{2} < \beta < \frac{\pi}{2} \quad (\text{Statement I})$$

$$\beta = \alpha - \frac{\pi}{2} \quad y(\alpha, \beta) = 0, \quad (\text{Statement IV})$$

$$\beta = 0 \quad y(\alpha, 0) = \frac{\cos \alpha}{\cos \frac{\alpha}{2}}, \quad 0^\circ < \alpha < 90^\circ$$

$$\begin{aligned}
\beta = \frac{\alpha}{2} \quad y(\alpha, \frac{\alpha}{2}) &= \cos \frac{\alpha}{2}, \quad 0^\circ < \alpha < 180^\circ \\
\beta = \frac{3\alpha}{4} \quad y(\alpha, \frac{3\alpha}{4}) &= 1, \quad 0^\circ < \alpha < 120^\circ \\
\beta = \alpha \quad y(\alpha, \alpha) &= \frac{1}{\cos \frac{\alpha}{2}}, \quad 0^\circ < \alpha < 90^\circ
\end{aligned}$$

Since  $F(\alpha, \beta) = y(\alpha, \beta) \cdot g(\alpha)$ , we may use the above information to define  $g(\alpha)$  from  $g(\alpha) = \frac{f(\alpha, \beta)}{y(\alpha, \beta)}$  for specific  $\beta(\alpha)$  curves. This results in

$$g(\alpha) = \begin{cases} g_1(\alpha) = \frac{\cos \frac{\alpha}{2}}{\cos \alpha} \cdot f(\alpha, 0), & \text{for } \beta = 0 \text{ and } 0^\circ < \alpha < 90^\circ \\ g_2(\alpha) = \frac{1}{\cos \frac{\alpha}{2}} \cdot f(\alpha, \frac{\alpha}{2}), & \text{for } \beta = \frac{\alpha}{2} \text{ and } 0^\circ < \alpha < 180^\circ \\ g_3(\alpha) = f(\alpha, \frac{3\alpha}{4}), & \text{for } \beta = \frac{3\alpha}{4} \text{ and } 0^\circ < \alpha < 120^\circ \\ g_4(\alpha) = \cos \frac{\alpha}{2} \cdot f(\alpha, \alpha), & \text{for } \beta = \alpha \text{ and } 0^\circ < \alpha < 90^\circ \end{cases} \quad (17)$$

Using the experimental photometric curve, figure 3, we can select the required values for  $F(\alpha, \beta)$  to define  $g(\alpha)$ . Note that  $g(\alpha)$  is being defined redundantly on all but the range,  $120^\circ < \alpha < 180^\circ$ . This will be of assistance in eliminating experimental scatter.

In Figure 4 and in Table I, we presented a plot and a tabulation, respectively, of the resulting values of  $g_1(\alpha) \dots g_4(\alpha)$ . These different  $g_i(\alpha)$  are generally in good agreement, which serves to indicate that the functional choice of  $y(\alpha, \beta) = \cos(\alpha - \beta) / \cos(\frac{\alpha}{2} - \beta)$  was a very good choice. Also, presented for comparison purposes are tabular values of the analytical expression  $g(\alpha)$ , which has been developed to fit these experimental  $g_1(\alpha) \dots g_4(\alpha)$  data. It is noted in Figure 4 that  $g(\alpha)$  is a monotonically decreasing function such that  $g(0) = 1$  and  $g(\pi) = 0$ . The analytical expression that we developed to best fit the experimental data for  $g(\alpha)$  has the form:

$$g(\alpha) = \frac{1}{(1 + \sin \frac{\alpha}{2})^2} \sqrt{\frac{1 - \sin \frac{\alpha}{2}}{\cos \frac{\alpha}{2}}}, \quad \alpha \geq 0 \quad (18)$$

This function was concocted as follows:

1. The trigonometric function,  $\sin \frac{\alpha}{2}$ , was selected as a suitable monotonic function from which to algebraically build  $g(\alpha)$ . It is positive and defined for  $\alpha$  on the interval  $(0, \pi)$ . It is monotonic and assumes the values 0 and 1 at the end points of the interval.
2. Different algebraic combinations of  $\sin \frac{\alpha}{2}$  and 1 were tried, until a very good match with the experimental data was attained with the combination:

$$g(\alpha) = \frac{1}{\left(1 + \sin \frac{\alpha}{2}\right)^2} \cdot \sqrt[4]{\frac{1 - \sin \frac{\alpha}{2}}{1 + \sin \frac{\alpha}{2}}}, \quad \alpha \geq 0 \quad (19)$$

We are now in a position to assemble the developed two-dimensional lunar equatorial photometric function.

For positive  $\alpha$ , the function assumes the form previously announced in equation 4.

$$F_{2d}(\alpha, \beta) = \frac{\cos(\alpha - \beta)}{\left(\cos \frac{\alpha}{2} - \beta\right)} \cdot \frac{1}{\left(1 + \sin \frac{\alpha}{2}\right)^2} \cdot \sqrt[4]{\frac{1 - \sin \frac{\alpha}{2}}{\cos \frac{\alpha}{2}}}$$

In Figure 5 the developed analytical curve,  $F_{2d}(\alpha, \beta)$  is plotted versus  $\beta$  as solids lines for  $\alpha = 0^\circ, 10^\circ, 20^\circ \dots 170^\circ$  and compared with experimental data points. For a two-dimensional functional representation, the agreement is thought to be very good.

#### NEGATIVE PHASE ANGLES

We have determined earlier (equation 16) that in order to satisfy statement V we must satisfy  $g(\alpha) = g(-\alpha)$ . Up to this point in our development of  $g(\alpha)$  and  $F_{2d}(\alpha, \beta)$ , we have been dealing only with positive values of phase angle  $\alpha$ . In the event that we need to define  $F_{2d}(\alpha, \beta)$  for negative  $\alpha$ 's, we should use:

$$g(\alpha) = \frac{1}{\left(1 + \sin \left|\frac{\alpha}{2}\right|\right)^2} \cdot \sqrt[4]{\frac{1 - \sin \left|\frac{\alpha}{2}\right|}{1 + \sin \left|\frac{\alpha}{2}\right|}} \quad (20)$$

Incidentally, the use of the absolute value sign around  $\alpha$  creates a slope discontinuity at  $\alpha = 0$ , and permits satisfaction of statement II. Although the three-dimensional lunar photometric function,  $F_{3d}(\psi, \phi, \alpha)$ , which we are developing, is concerned only positive  $\alpha$ 's, the occasion will arise to define  $F_{3d}(\alpha, \beta, \gamma)$  for both positive and negative phase angle  $\alpha$ 's. The more general form of the two-dimensional lunar photometric function, defined for  $-\pi < \alpha < \pi$  and  $-\frac{\pi}{2} < \beta < \frac{\pi}{2}$  is:

$$F_{2d}(\alpha, \beta) = \frac{\cos(\alpha - \beta)}{\cos\left(\frac{\alpha}{2} - \beta\right)} \cdot \frac{1}{\left(1 + \sin \left|\frac{\alpha}{2}\right|\right)^2} \cdot \sqrt[4]{\frac{1 - \sin \left|\frac{\alpha}{2}\right|}{1 + \sin \left|\frac{\alpha}{2}\right|}} \quad (21)$$

A quick rundown of statements I - VI reveals that each of these statements is satisfied by the above two-dimensional lunar photometric function (equation 21). However, in much of the presentation that follows we will actually use

the slightly simpler results (equation 4), whenever the situation may be fully described by  $\alpha > 0$ .

Comparison of Figures 3 and 5 reveal a greater degree of limb brightening in the analytical curve, Figure 5, than is indicated in Figure 3. However, it should be realized that good extreme limb experimental data are difficult to obtain with photocell detectors because of sensor angular resolution problems. Very little data exist in the literature for  $\beta > 65^\circ$ . Experimentally, using a 30X telescope and with the eye as a sensor, the author has determined that a considerable amount of extreme limb brightening does occur for  $85^\circ < \beta < 90^\circ$  for the phase angle range  $10^\circ < \alpha < 50^\circ$ . This is a region for which some authors, for example M. Minnaert<sup>5</sup>, have apparently made the mistake of indicating darkening on the extreme limb near full moon.

More recently, Pearse<sup>7</sup>, Herriman, Washburn, and Willingham<sup>10</sup> show, as we do, a limb brightening for all values of  $\alpha \neq 0$ . A replot of Figure 5 versus the projected longitude,  $\sin \beta$ , rather than the actual longitude,  $\beta$ , reveals, in Figure 6, the limb brightening predicted by  $f(\alpha, \beta)$  as it would be observed across the equatorial region of the moon. What has been observed experimentally at various phase angles, using the eye as a detector, appears to be consistent with the degree of extreme limb brightening shown in Figure 6.

#### INTEGRATED - TWO-DIMENSIONAL LUNAR INTENSITY

By making the fairly good assumption that the lunar brightness is the same everywhere along a lunar longitude line as it is on the equator at that longitude, the equatorial photometric function,  $F_{2d}(\alpha, \beta)$  may be integrated over the face of the moon to produce a good approximation of the actual integrated lunar intensity. This integration of  $F_{2d}(\alpha, \beta)$  will be symbolized by  $I_{2d}(\alpha)$ .

$$I_{2d}(\alpha) = \frac{1}{A} \int F_{2d}(\alpha, \beta) dA, \quad dA = \frac{\pi r^2}{2} d(\sin \beta) \quad (22)$$

Table II shows this in tabular form, compared with experimental results of Bullrich 1948. Even for this analytical approximation, the results are rather good. There is quite good agreement for  $0 < \alpha < 60^\circ$ , moderately good agreement in the range  $60^\circ < \alpha < 120^\circ$  and poor agreement in the range  $120^\circ < \alpha < 180^\circ$ . However, the fact of these approximate analytical results differing from the experimental results by more than a factor of 2.5 in the range where  $I_{2d}(\alpha)$  is very low would not be at all apparent in examining a linear plot of  $I_{2d}(\alpha)$  such as is shown in Figure 7; here the agreement looks rather good. However this situation is noticed in Table II. The analytical integrated two-dimensional lunar intensity curve shown in Figure 7 may also be considered a plot of the areas under the individual curves in Figure 6.



# DEVELOPMENT OF A 3D PHOTOMETRIC FUNCTION, $f_{3d}(\psi, \phi, \alpha)$

The most difficult aspect of developing a three-dimensional photometric function was the development of a two-dimensional expression which accurately described the equatorial photometric function  $f(\alpha, \beta)$ .

$$f(\alpha, \beta) = \frac{\cos(\alpha - \beta)}{\cos\left(\frac{\alpha}{2} - \beta\right)} \cdot \frac{1}{\left(1 + \sin\frac{\alpha}{2}\right)^2} \cdot \sqrt{\frac{1 - \sin\frac{\alpha}{2}}{\cos\frac{\alpha}{2}}} \quad (23)$$

The conversion of this 2D photometric function in  $\alpha$  and  $\beta$  into a 3D photometric function in  $\psi$ ,  $\phi$ , and  $\alpha$ , with the requisite symmetry conditions involving  $\psi$  and  $\phi$ , proved not to be very difficult. There exists a finite and fairly small number of ways in which the equatorial identities:

$$\beta = \pm \psi \text{ and } \alpha - \beta = \pm \psi$$

can be substituted into equation (6).

The combinations investigated were:

$$\alpha \rightarrow \alpha, \pm(\psi - \phi), \frac{\alpha + \psi - \phi}{2}, \frac{\alpha - (\psi - \phi)}{2}$$

$$\alpha - \beta \rightarrow \pm \psi, \alpha \pm \phi, \frac{\alpha + (\psi - \phi)}{2}, \frac{\alpha - (\psi - \phi)}{2}$$

$$\frac{\alpha}{2} - \beta \rightarrow \pm \psi - \frac{\alpha}{2}, \frac{\alpha}{2} \pm \phi, \pm \frac{\psi + \phi}{2}, \pm \frac{\psi - \phi}{2}$$

The function  $f(\phi, \psi, \alpha)$ , when divided by  $\cos \psi$ , must be symmetric in  $\phi$  and  $\psi$ ; so it appeared plausible to assume that

$$\cos(\alpha - \beta) \rightarrow \cos \psi$$

Two combinations for  $\cos(\alpha - \beta)$  display the required symmetry in  $\psi$  and  $\phi$ :

$$\begin{aligned} \cos\left(\frac{\alpha}{2} - \beta\right) &\rightarrow \cos \frac{\psi + \phi}{2} \\ &\rightarrow \cos \frac{\psi - \phi}{2} \end{aligned}$$

The most apparent substitution for  $\alpha$  is  $\alpha$  itself. For substitutions into  $(1 - \sin\frac{\alpha}{2})$  and  $(1 + \sin\frac{\alpha}{2})^2$ , no other substitution shows the required symmetry properties. However for substitution into  $\cos\frac{\alpha}{2}$ ,  $\cos\left(\frac{\psi - \phi}{2}\right)$  is also a possibility.

Symmetry considerations reduced to four the possible ways in which the equatorial photometric function  $f(\alpha, \beta)$  might be extended into a three-dimensional photometric function. These possible functional forms for  $f(\psi, \phi, \alpha)$  are:

$$f_1(\psi, \phi, \alpha) = \frac{\cos \psi}{\cos \frac{\psi - \phi}{2}} \cdot \frac{1}{\left(1 + \sin \frac{\alpha}{2}\right)^2} \cdot \sqrt{\frac{1 - \sin \frac{\alpha}{2}}{\cos \frac{\psi - \phi}{2}}} \quad (24)$$

$$f_2(\psi, \phi, \alpha) = \frac{\cos \psi}{\cos \frac{\psi + \phi}{2}} \cdot \frac{1}{\left(1 + \sin \frac{\alpha}{2}\right)^2} \cdot \sqrt{\frac{1 - \sin \frac{\alpha}{2}}{\cos \frac{\psi - \phi}{2}}} \quad (25)$$

$$f_3(\psi, \phi, \alpha) = \frac{\cos \psi}{\cos \frac{\psi + \phi}{2}} \cdot \frac{1}{\left(1 + \sin \frac{\alpha}{2}\right)^2} \cdot \sqrt{\frac{1 - \sin \frac{\alpha}{2}}{\cos \frac{\alpha}{2}}} \quad (26)$$

$$f_4(\psi, \phi, \alpha) = \frac{\cos \psi}{\cos \frac{\psi - \phi}{2}} \cdot \frac{1}{\left(1 + \sin \frac{\alpha}{2}\right)^2} \cdot \sqrt{\frac{1 - \sin \frac{\alpha}{2}}{\cos \frac{\alpha}{2}}} \quad (27)$$

Selection of one from this set of four possible extended three-dimensional photometric functions was accomplished by computer programming the resulting intensities in a fine  $\beta, \gamma$  grid and drawing the lunar isophotes for two phase angles,  $34^\circ$  and  $96^\circ$ , for which lunar observational isophotes are recorded in the literature<sup>5</sup>. The final selection of a three-dimensional lunar photometric function was  $f_3(\psi, \phi, \alpha)$ , which henceforth will be written as  $F_{3d}(\psi, \phi, \alpha)$

$$F_{3d}(\psi, \phi, \alpha) = \frac{\cos \psi}{\cos \frac{\psi + \phi}{2}} \cdot \frac{1}{\left(1 + \sin \frac{\alpha}{2}\right)^2} \cdot \sqrt{\frac{1 - \sin \frac{\alpha}{2}}{\cos \frac{\alpha}{2}}} \quad (28)$$

It is important to realize that this 3 dimensional lunar photometric function does resemble, yet is distinctly different from, the photometric function which would result from taking the values of the equatorial 2 dimensional lunar photometric function and assuming that the brightness remains constant along the illumination longitude lines. Lunar photometry is a potential tool for remotely mapping the lunar surface. Under certain viewing and illumination conditions, it becomes very important to use the 3D and not a 2D photometric function, because these functions may differ by as much as a factor of 3, for slopes typical of the lunar surface.

### 3D PHOTOMETRIC FUNCTION, $F_{3d}(\psi, \phi, \theta)$

Computer programming of the three-dimensional lunar directional reflectance characteristics,  $F(\psi, \phi, \theta)$  from a lunar point of view assumed the following form:

$$F_{3d}(\psi, \phi, \theta) = \frac{\cos \psi}{\cos \frac{\psi + \phi}{2}} \cdot \frac{1}{\left(1 + \sin \frac{\alpha}{2}\right)^2} \cdot \sqrt{\frac{1 - \sin \frac{\alpha}{2}}{\cos \frac{\alpha}{2}}}$$

where

$$\sin \frac{\alpha}{2} = \sqrt{\frac{1 - \cos \alpha}{2}}, \quad \cos \frac{\alpha}{2} = \sqrt{\frac{1 + \cos \alpha}{2}}$$

and

$$\cos \alpha = \cos \psi \cdot \cos \phi + \cos \theta \sqrt{(1 - \cos^2 \psi)(1 - \cos^2 \phi)}$$

with

$$\cos \frac{\psi + \phi}{2} = \sqrt{\frac{1 + \cos \phi \cdot \cos \psi - \sqrt{(1 - \cos^2 \phi)(1 - \cos^2 \psi)}}{2}}$$

Note that this formulation, although more complicated algebraically, has completely eliminated the need for use of the series trigonometric routines. This expression is in a form such that  $\cos \psi$ ,  $\cos \phi$ , and  $\cos \theta$  will serve as the three independent input variables. The results from equation (29) were plotted in three-dimensional form and photographed. Figure 8 reveals the three-dimensional directional reflectance characteristics of  $F_{3d}(\psi, \phi, \theta)$  for three angles of incidence  $\psi = 15^\circ$ ,  $\psi = 45^\circ$  and  $\psi = 75^\circ$ .

### 3D PHOTOMETRIC FUNCTION, $F_{3d}(\alpha, \beta, \gamma)$

Computer programming the three-dimensional lunar directional reflectance characteristics,  $F(\alpha, \beta, \gamma)$  from an earth-based point of view, assume the following form:

$$F_{3d}(\alpha, \beta, \gamma) = \frac{\cos \psi}{\cos \frac{\psi + \phi}{2}} \cdot \frac{1}{\left(1 + \sin \frac{\alpha}{2}\right)^2} \cdot \sqrt{\frac{1 - \sin \frac{\alpha}{2}}{1 + \sin \frac{\alpha}{2}}}$$

where

$$\cos \frac{\psi + \phi}{2} = \sqrt{\frac{1 + \cos \phi \cdot \cos \psi}{2}}$$

$$= \sqrt{\frac{1 + \cos \phi \cdot \cos \psi - \sqrt{(1 - \cos^2 \phi)(1 - \cos^2 \psi)}}{2}}$$

and  $\cos \phi = \cos \beta \cdot \cos \gamma$

$$\cos \psi = \cos(\alpha - \beta) \cdot \cos \gamma$$

$$= [\cos \alpha \cdot \cos \beta + \sqrt{(1 - \cos^2 \alpha)(1 - \cos^2 \beta)}] \cdot \cos \gamma$$

with

$$\cos \alpha = 1 - 2 \sin^2 \frac{\alpha}{2}$$

(30)

This formulation is also complicated algebraically, however it permits the computation to be performed without using the trigonometric and inverse trigonometric routines. This expression is now in a form such that  $\sin \frac{\alpha}{2}$ ,  $\cos \beta$  and  $\cos \gamma$  will serve as the three independent input variables.

### 3D INTEGRATED LUNAR INTENSITY, $I(\alpha)$

An integration of  $F_{3d}(\alpha, \beta, \gamma)$  two-dimensionally over the face of the moon for various phase angles,  $\alpha$ , produces the three-dimensional integrated relative intensity  $I_{3d}(\alpha)$  curve for the moon.

$$I_{3d}(\alpha) = \frac{\int F_{3d}(\alpha, \beta, \gamma) \cdot dA}{\int dA} \quad (31)$$

$$I_{3d}(\alpha) = \frac{\int_0^{\frac{\pi}{2}} \int_{-\frac{\pi}{2}}^{\frac{\pi}{2}} F_{3d}(\alpha, \beta, \gamma) \cdot \cos \beta \cdot \cos^2 \gamma \cdot d\beta d\gamma}{\int_0^{\frac{\pi}{2}} \int_{-\frac{\pi}{2}}^{\frac{\pi}{2}} \cos \beta \cdot \cos^2 \gamma \cdot d\beta d\gamma} \quad (32)$$

This expression is most readily evaluated, numerically by converting it into a double summation over evenly-spaced values of  $\cos \beta \cdot d\beta = d(\sin \beta)$  and  $\cos^2 \gamma d\gamma$

$$I_{3d}(\alpha) = \frac{\sum_{j=1}^m \sum_{k=1}^n F_{3d}(\alpha, \beta_j, \gamma_k)}{m \cdot n} \quad (33)$$

The analytical results,  $I_{3d}(\alpha)$ , from this evaluation are shown in Table III and Figure 9, where they are compared with the experimental results of Rougier<sup>18</sup>, 1933. The analytical results  $I_{3d}(\alpha)$  are in excellent agreement with the experimental results of Rougier<sup>18</sup>, 1953; whereas the approximate expression  $I_{2d}(\alpha)$  ran low, typically by a factor of about three in the phase angle range,  $90^\circ < \alpha < 180^\circ$ . Comparison of the analytical results for  $I_{2d}(\alpha)$  and  $I_{3d}(\alpha)$  leads to the conclusion that the higher results of  $I_{3d}(\alpha)$  as compared to those of  $I_{2d}(\alpha)$  must be due to polar brightening, since on the equator  $F_{2d}(\alpha, \beta) = F_{3d}(\alpha, \beta, \gamma)$ .

## EARTH BASED OBSERVATIONS

The developed lunar photometric function,  $F_{3d}(\psi, \phi, \alpha)$ , has been expressed in the earth-based observational form,  $F_{3d}(\alpha, \beta, \gamma)$  and the lunar surface form,  $F_{3d}(\psi, \phi, \theta)$ . The transition between these two primary viewpoints is readily achieved by using the simpler expression  $F_{3d}(\psi, \phi, \alpha)$  as a common element in each formulation. Comparison between experimental or observational results and the predicted results of the developed three-dimensional lunar photometric function is most easily accomplished using the earth-based observational form,  $F_{3d}(\alpha, \beta, \gamma)$ .

Figures 10 through 13 have been prepared to show the predicted relative brightness of various regions of the moon at various phase angles. These data are presented in Figures 10 through 13 as lunar isophotes, lines of constant brightness plotted across the face of the moon, at the phase angle,  $\alpha = 34^\circ$ ,  $65^\circ$ ,  $96^\circ$ ,  $127^\circ$ , respectively. Also shown in these figures is a set of ten lunar craters which are more or less evenly spaced over the face of the moon that is seen from the earth. Because of latitude symmetry about  $\gamma = 0$ , isophotes are drawn only for  $\gamma > 0$ . Consistent with this situation, lunar features that are actually in the 4th and 3rd quadrants are shown in the 1st and 2nd quadrants respectively, along with those that actually are in the 1st and 2nd quadrants.

Figures 14 through 23 show the predicted brightness,  $F_{3d}(\alpha, \beta, \gamma)$  versus phase angle,  $\alpha$  for ten different lunar craters: Vendelinus, Cleomedes, Posidonius, Albategnius, Archimedes, Clavis, Copernicus, Gassendi, Schikhard and Grimaldi. Shown on each of these curves are comparative experimental results of a least one of the following observers, Blagg and Muller<sup>19</sup>, Bennett<sup>20</sup>, Markov and Sharonov<sup>21</sup> and Fedoretz<sup>3</sup>. These experimental values were taken from Van Diggeln's paper<sup>3</sup>. The latitude coordinates for two of the ten lunar features were noted to be recorded incorrectly in reference 3. We corrected the longitude values of Posidonius (Figure 16) and Schikhard (Figure 22) to correspond with values read from the lunar atlas. Good agreement between experimental observation and the analytical evaluation of  $F_{3d}(\alpha, \beta, \gamma)$  occurred for all ten lunar features over the full range of phase angles. After obtaining very good agreement between earth-based experimental results and our proposed three-dimensional lunar photometric function, it was decided to shift viewpoints to the lunar surface and see what the relative brightness of the moon's surface looked like to an individual standing on the lunar surface. Figure 24 through 30 were prepared to show how the brightness of the lunar surface varies in different directions. Isophotes, which are lines of constant brightness, have been plotted versus the pair of directional angles  $(\phi, \theta)$  defined in Figure 2b. Isophotes of  $F_{3d}(\psi, \phi, \theta)$  are shown in Figures 24 through 30 for angle of incidence  $\psi = 0^\circ, 15^\circ, 30^\circ, 45^\circ, 60^\circ, 75^\circ$  and  $85^\circ$ .

The horizontal base of each of these hemispheres corresponds to observational data taken along the illumination equator, and represents the directions in the plane containing the surface normal and the incident flux vector. For someone standing on the lunar surface, the outermost hemisphere at  $\phi = 90^\circ$  corresponds to the horizon. The single point denoted as  $\bullet$  is that point at which scatterback is occurring in the direction opposite to that of the incident flux.

## STRANGE LUNAR REFLECTANCE EFFECTS

Some rather strange visual effects will be seen on the lunar surface. When the sun is at a zenith angle,  $\psi = 45^\circ$ , with respect to the lunar surface, the brightest direction on the lunar surface will be in the direction away from the sun, looking down  $45^\circ$  below the horizon. Standing and looking at this bright spot, you will see the shadow of your head masking the brightest zone. The direction at which the bright direct scatterback is occurring is denoted by  $\odot$  on Figures 24-30. The brightness will fall off from this, brightest spot in a pattern resembling eccentric concentric rings. For zenith angles greater than  $45^\circ$  there will also exist a darkest region in the general vicinity of the specular direction. Superimposed on this effect will be shadows due to gross surface irregularities, and brightness variation due to surface orientation.

When the sun is directly overhead, Figure 24, the contrast between the brightest nadir point and the darker horizon will only be a factor of 3. The contrast between the brightest and darkest direction upon the lunar surface increases with increasing zenith angle. At a zenith angle of  $60^\circ$ , Figure 28, the brightness ratio between the darkest and brightest region will be about seven.

For large zenith angles, such as shown in Figure 30 where  $\psi = 85^\circ$  and the sun is but slightly above the lunar horizon, the brightness contrast, even on the smoothest areas of the lunar surface, will be extreme, differing by a factor of 50. The brightest spot reflectance on the lunar surface will have shifted from  $5^\circ$  below the horizon in the direction opposite the sun, up to the horizon in this same azimuth direction. This effect should be most prominent on the lunar maria, where the effect will not be obscured by the variation in slope of the gross surface features. The information contained in the lunar directional isotopes, Figures 24-30, have by no means been exhaustively described; however, it is hoped that a sufficient description has been provided to develop an appreciation for the information contained and to acquaint the reader with this 3-D lunar photometric function.

## HEMISPHERICAL REFLECTANCE OF THE LUNAR SURFACE

Hemispherical reflectance is that portion of the incidence reflected in all directions from a surface. The hemispherical reflectance of the lunar surface to solar radiation is dependent upon the angle of incidence, which is the solar zenith angle,  $\psi$  for a horizontal surface. The hemispherical reflectance can be evaluated by performing an integration of the directional reflectance  $A_{fm} F_{3d}(\psi, \phi, \theta)$  over all hemispherical angles. Employing the appropriate weighting function,  $\cos \phi$ , to account for the projected area of the surface in various directions, the expression for the hemispherical reflectance is:

$$R_{\odot}(\psi) = A_{fm} \int_0^{2\pi} \int_0^{\frac{\pi}{2}} F_{3d}(\psi, \phi, \theta) \sin \phi \cos \phi \, d\phi \, d\theta \quad (34)$$

Because of variation in full moon albedo,  $A_{fm}$ , at various locations on the lunar surface, it is convenient to introduce the concept of the directional hemispherical reflectance function,  $F_{\Delta}(\psi)$ , defined as  $F_{\Delta}(\psi) = R_{\Delta}(\psi)/A_{fm}$ .

Numerical evaluation of this double integral  $F_{\Delta}(\psi)$  is greatly simplified by selecting the angles  $\theta$  at which to evaluate  $F_{3d}(\psi, \phi, \theta)$  so that they are evenly spaced in  $\theta$ , and by selecting the angles  $\phi$  such that the values of  $\sin^2\phi$  are evenly placed.

The double integral under these conditions reduces to an accumulative average of the values of the lunar photometric function  $F_{3d}(\psi, \phi, \theta)$ , evaluated at a prechosen  $\phi, \theta$  grid of angles.

$$F_{\Delta}(\psi) = \frac{\sum_{j=1}^m \sum_{k=1}^n F_{3d}(\psi, \phi, \theta)}{m \cdot n}, \quad R_{\Delta}(\psi) = A_{fm} F_{\Delta}(\psi) \quad (35)$$

Figure 31 shows the plot of  $F_{\Delta}(\psi)$  resulting from the computerized numerical evaluation of this double integral. This directional hemispherical reflectance  $R_{\Delta}(\psi)$  is needed to derive an accurate lunar surface temperature from a radiation heat balance statement.

It should be noted that the hemispherical reflectance  $R_{\Delta}$  for all incident angles,  $\psi$ , remains less than one seventh the full moon albedo. As a consequence, the lunar surface absorptance,  $\alpha_s = 1 - R_{\Delta}(\psi)$ , to solar radiation is typically only a few percent less than unity.

	<u><math>A_{fm} = 0.05</math></u>			<u><math>A_{fm} = 0.10</math></u>		<u><math>A_{fm} = 0.20</math></u>	
	$F_{\Delta}(\psi)$	$R_{\Delta}(\psi)$	$\alpha_s(\psi)$	$R_{\Delta}(\psi)$	$\alpha_s(\psi)$	$R_{\Delta}(\psi)$	$\alpha_s(\psi)$
0	0.1015	0.0051	0.9949	0.0102	0.9898	0.0203	0.9797
15°	0.1063	0.0053	0.9947	0.0106	0.9894	0.0213	0.9798
30°	0.1178	0.0059	0.9941	0.0118	0.9882	0.0236	0.9764
45°	0.1312	0.0066	0.9934	0.0131	0.9869	0.0262	0.9738
60°	0.1380	0.0069	0.9931	0.0138	0.9862	0.0276	0.9724
75°	0.1175	0.0059	0.9941	0.0118	0.9882	0.0235	0.9765
85°	0.0612	0.0031	0.9969	0.0061	0.9939	0.0122	0.9878
90°	0.0000	0.0000	1.0000	0.0000	1.0000	0.0000	1.0000

The directional reflectance effects from the lunar surface have an influence on both the deduced lunar surface temperatures and upon an equilibrium surface temperature of objects located on a lunar surface environment. To achieve surface temperature predictions with accuracy greater than 5%,  $\pm 25^\circ\text{F}$  at  $500^\circ\text{R}$ , in a lunar environment, these directional reflectance effects and object shadowing effects need to be considered. A detailed evaluation of these effects for spherical and cylindrical shapes located on the lunar surface will be reserved for another paper, which deals specifically with lunar cryogenic storage tanks.

## CONCLUSION AND RECOMMENDATIONS

A three-dimensional lunar photometric function has been developed in this paper that does an excellent job of describing the visible reflectance characteristics of the moon's surface. For ten craters floors distributed over the face of the moon, very good agreement has been demonstrated between the predicted results and experimental observations at all phase angles. The predicted brightness of the entire moon,  $I_{3d}(\alpha)$  versus phase angle is also in excellent agreement with experimental results. The isophote pattern lies essentially along the lunar longitude and agrees well with observations. The developed photometric function is recommended for use in performing accurate engineering evaluations for the temperature of objects in a lunar and near lunar orbital environment.



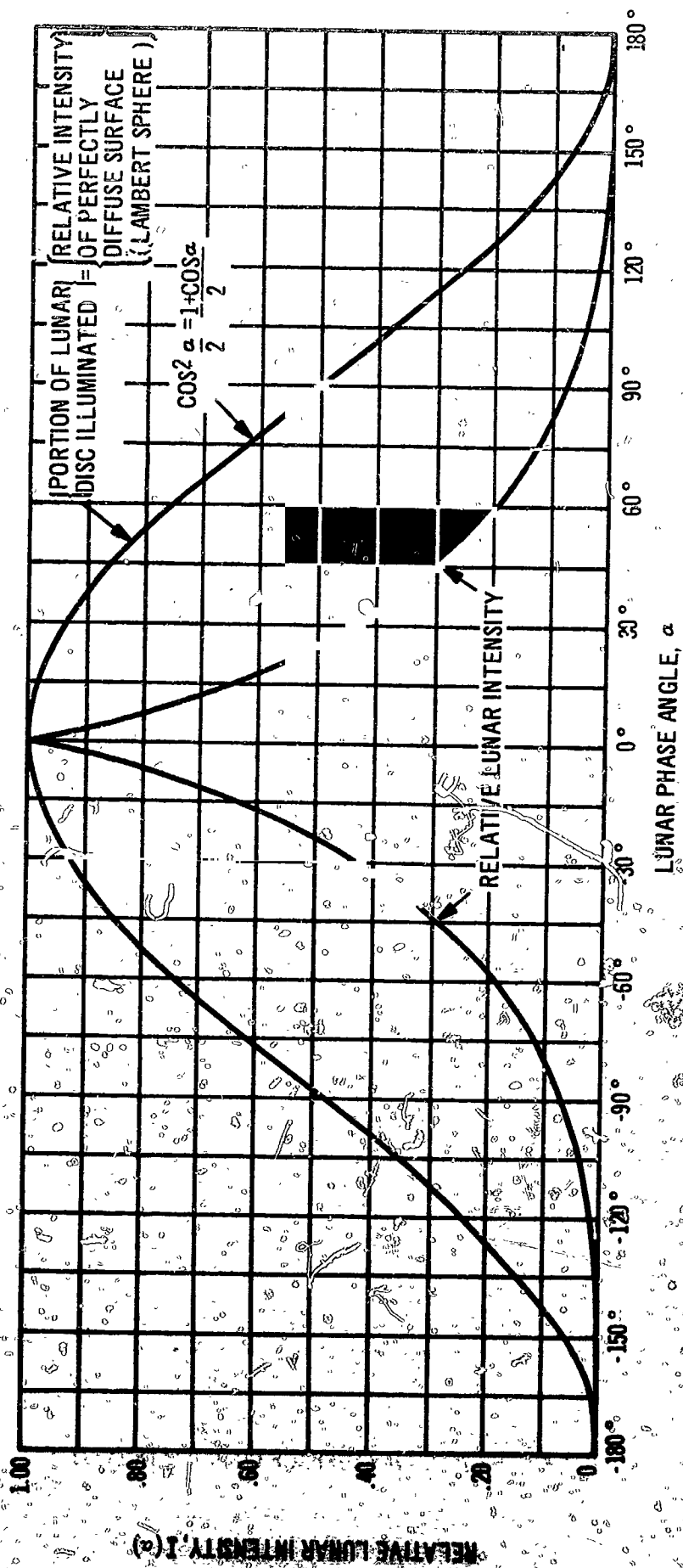


FIGURE 1 LUNAR REFLECTANCE CHARACTERISTICS COMPARED TO A LAMBERT SURFACE

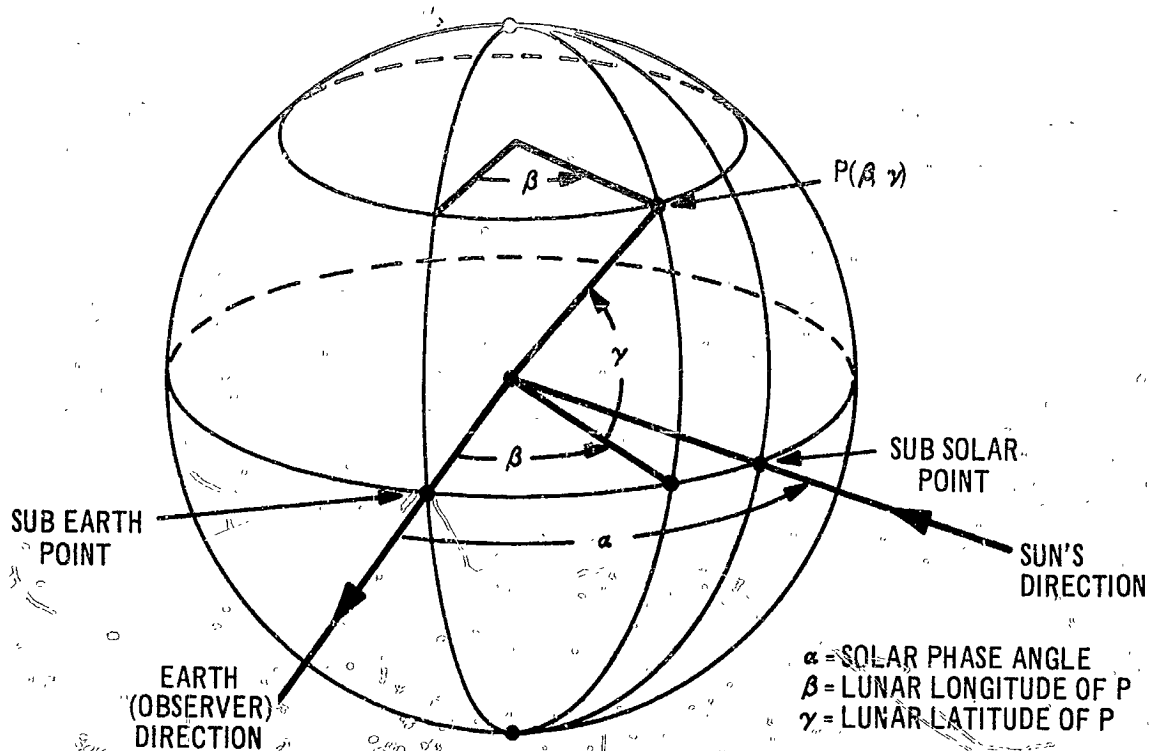


FIGURE 2a MOON COORDINATES OBSERVED FROM EARTH

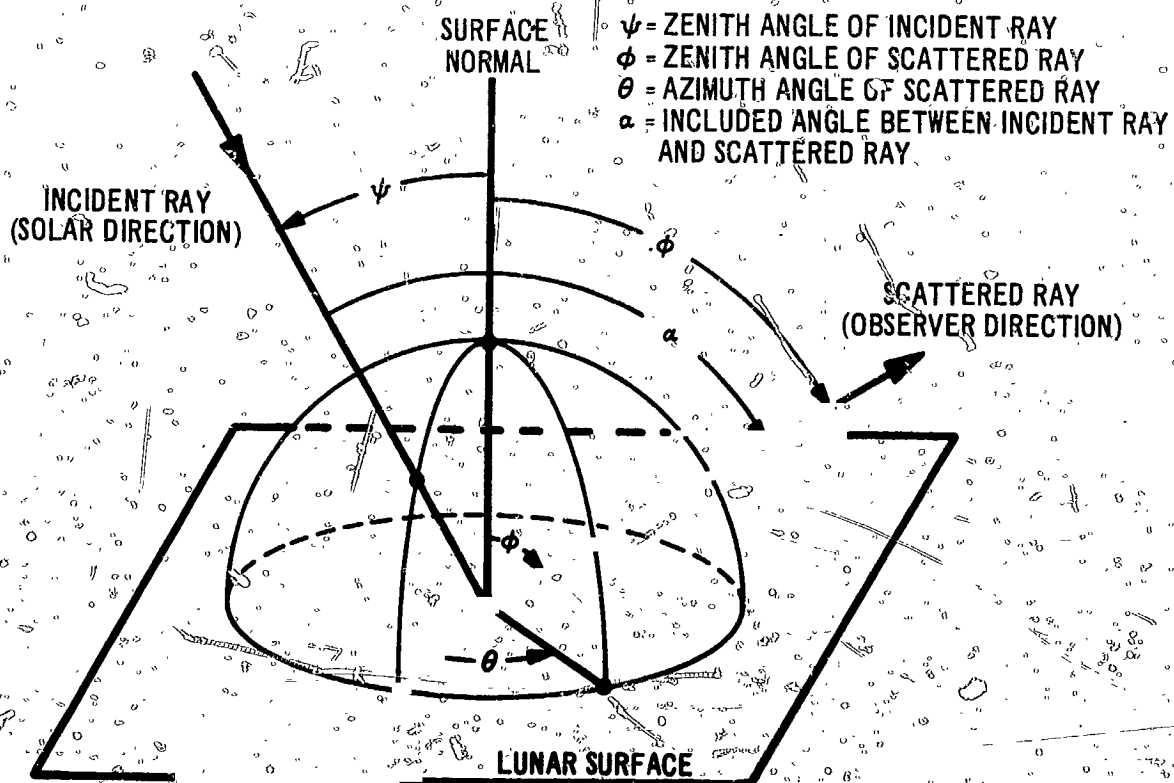


FIGURE 2b LUNAR SURFACE COORDINATE SYSTEM

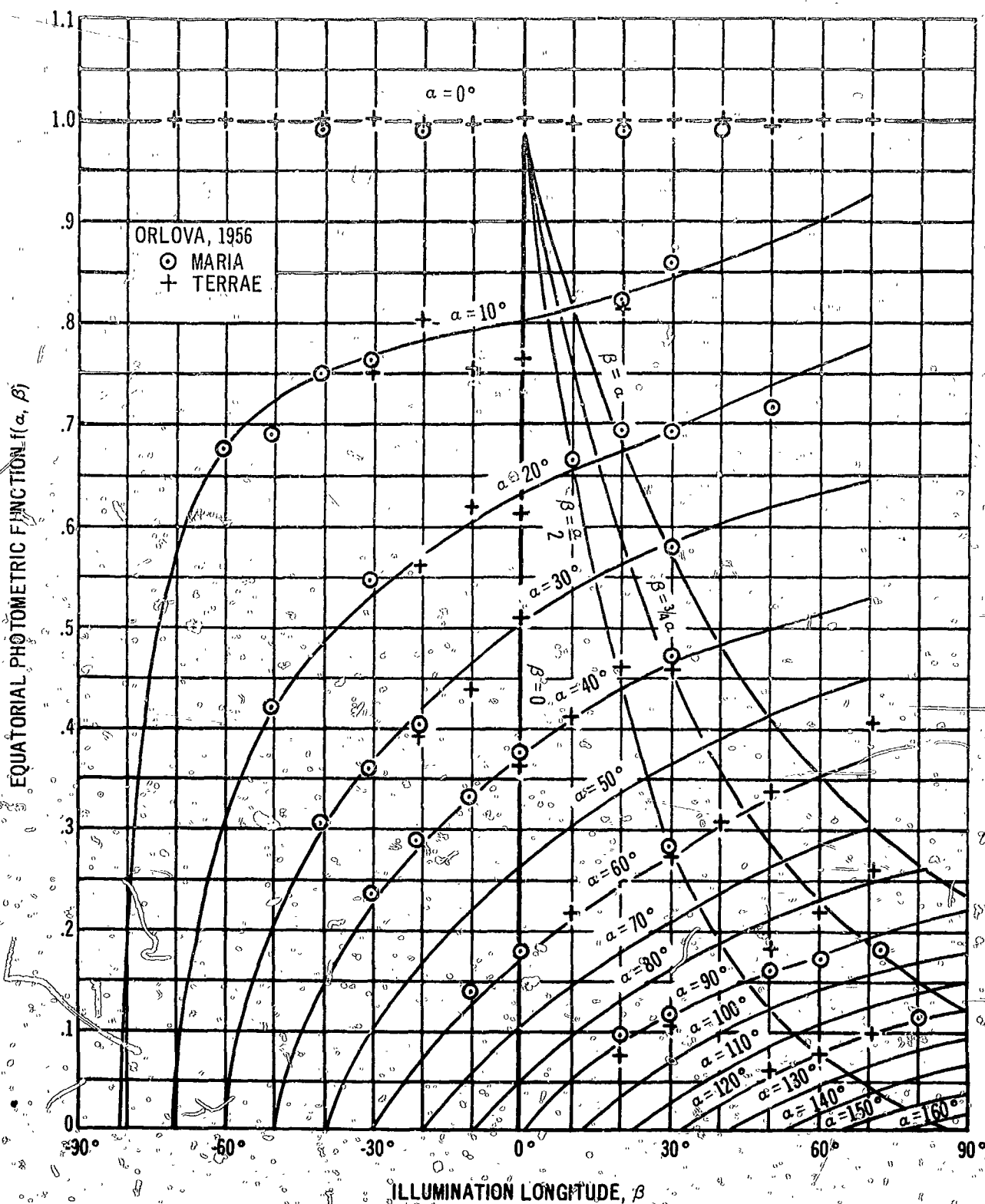


FIGURE 3. EXPERIMENTAL LUNAR EQUATORIAL PHOTOMETRIC FUNCTION

PHASE ANGLE DEPENDENT FUNCTION,  $g(\alpha)$

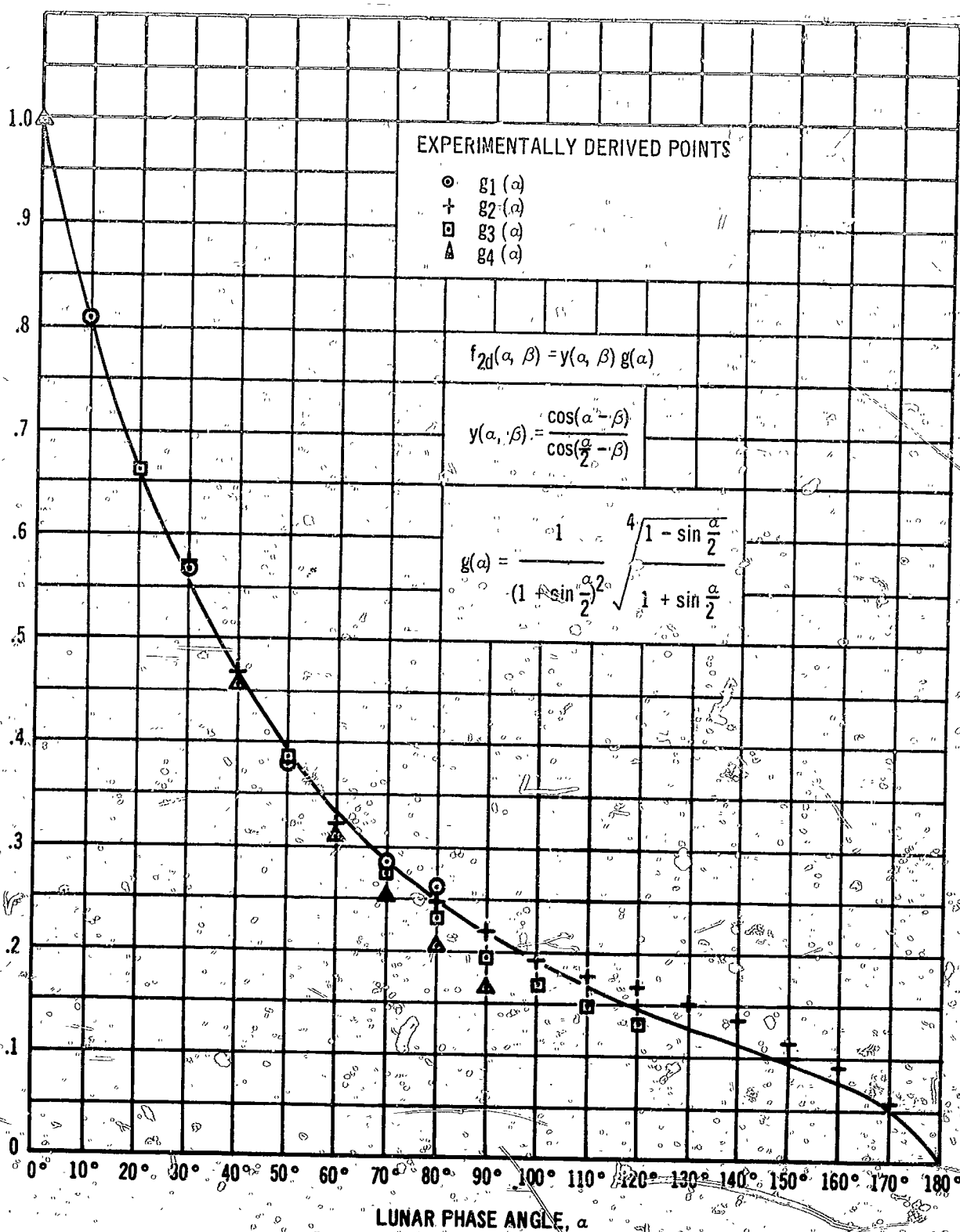


FIGURE 4 PHASE ANGLE DEPENDENT FUNCTION,  $g(\alpha)$

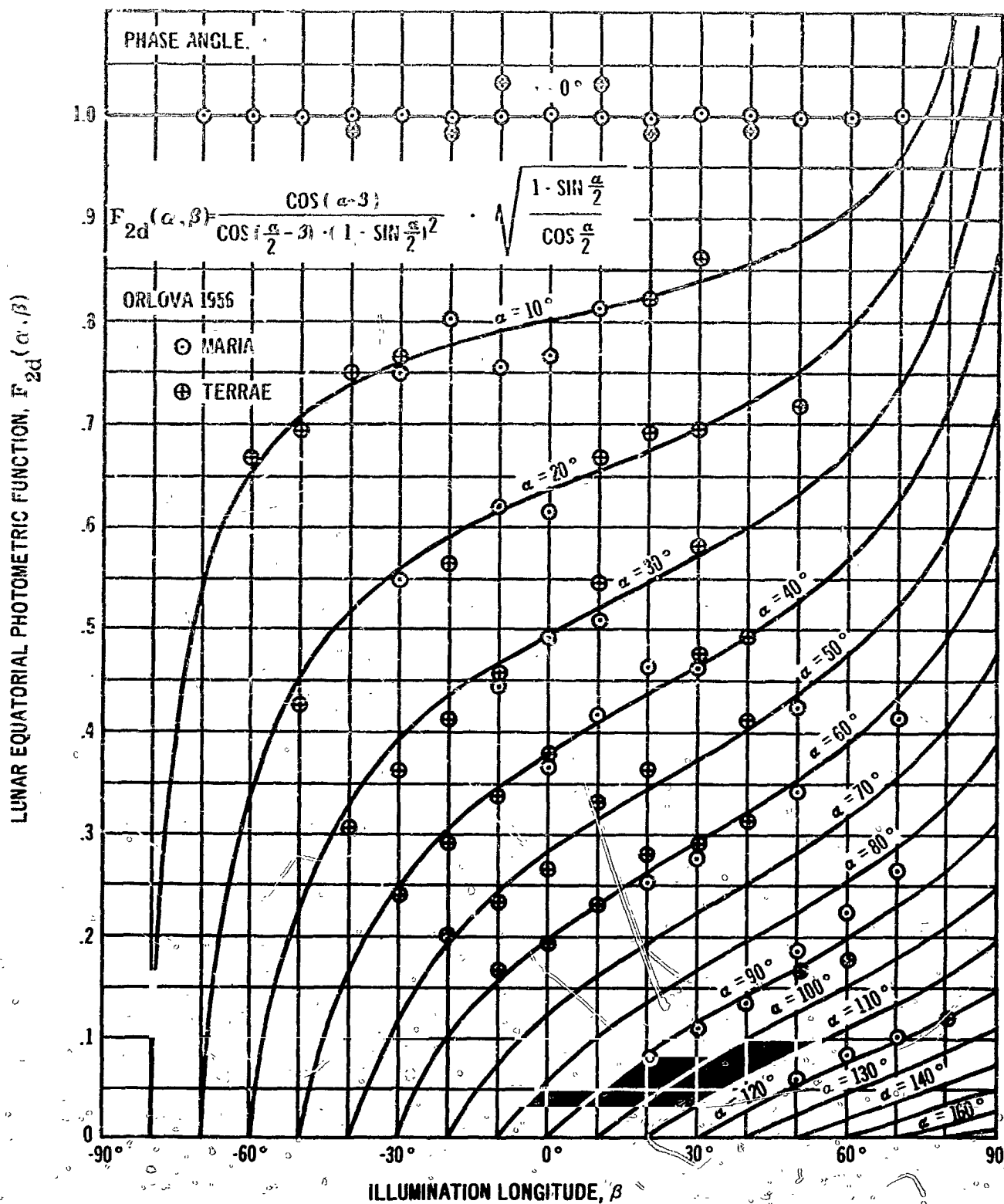


FIGURE 5 LUNAR EQUATORIAL PHOTOMETRIC FUNCTION FOR  $\gamma = 0$

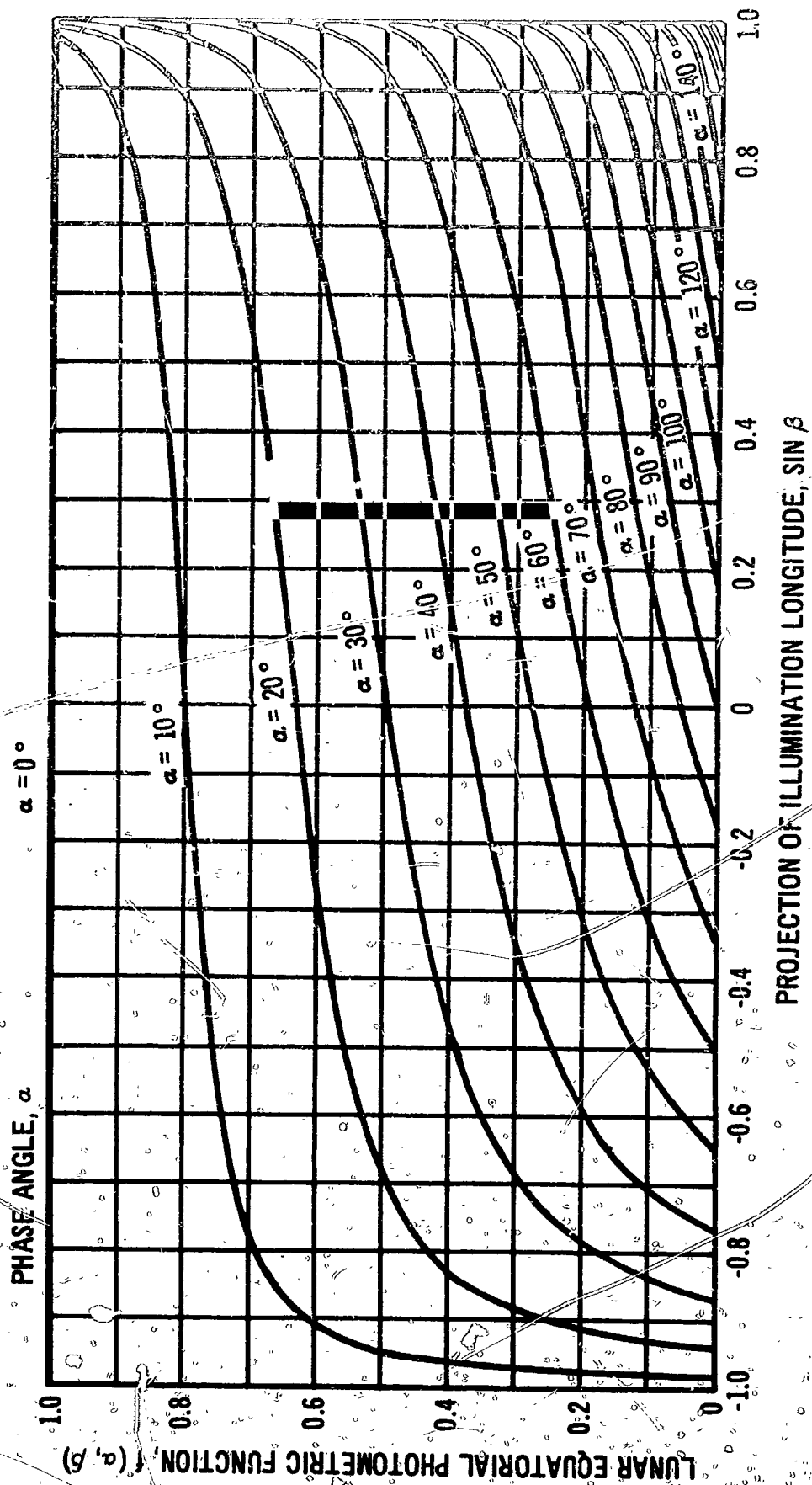


FIGURE 6 RELATIVE BRIGHTNESS OF LUNAR EQUATOR ( $\gamma = 0$ )

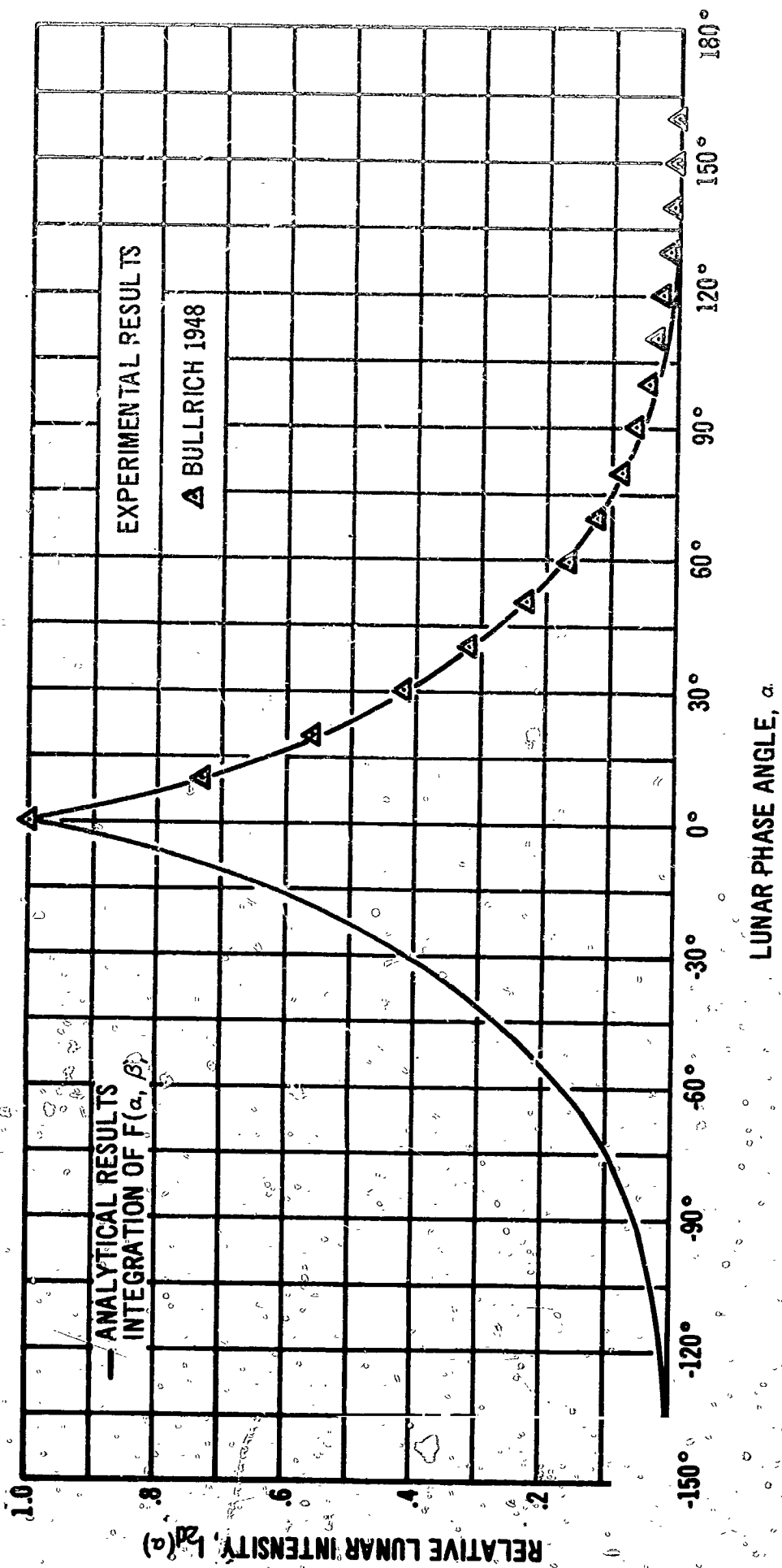
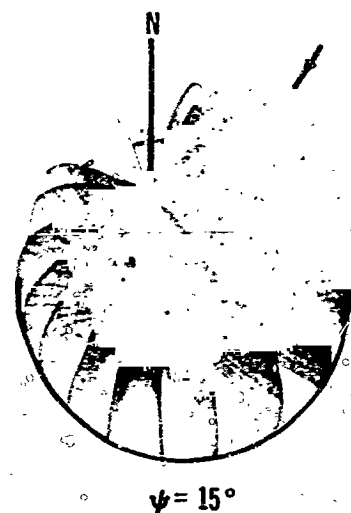
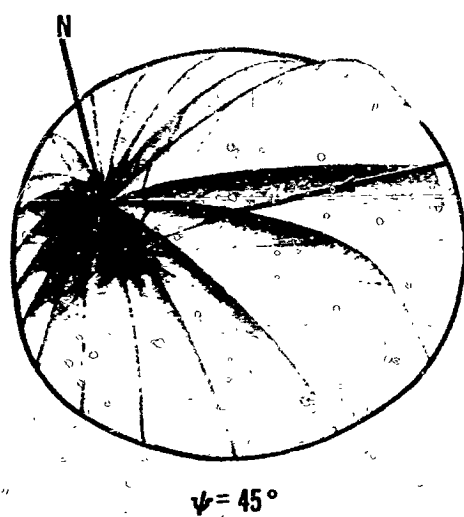
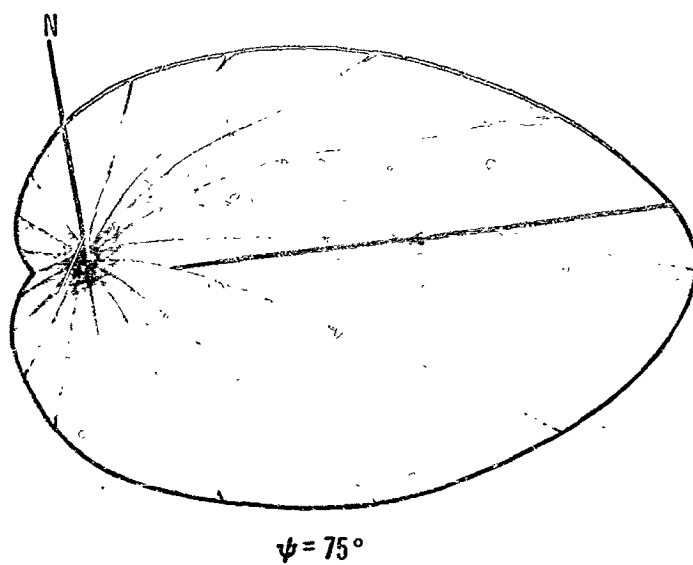


FIGURE 7 2D INTEGRATED LUNAR INTENSITY,  $I_{2D}(\alpha)$  COMPARED WITH EXPERIMENTAL RESULTS



**FIGURE 8 LUNAR REFLECTION CHARACTERISTICS**



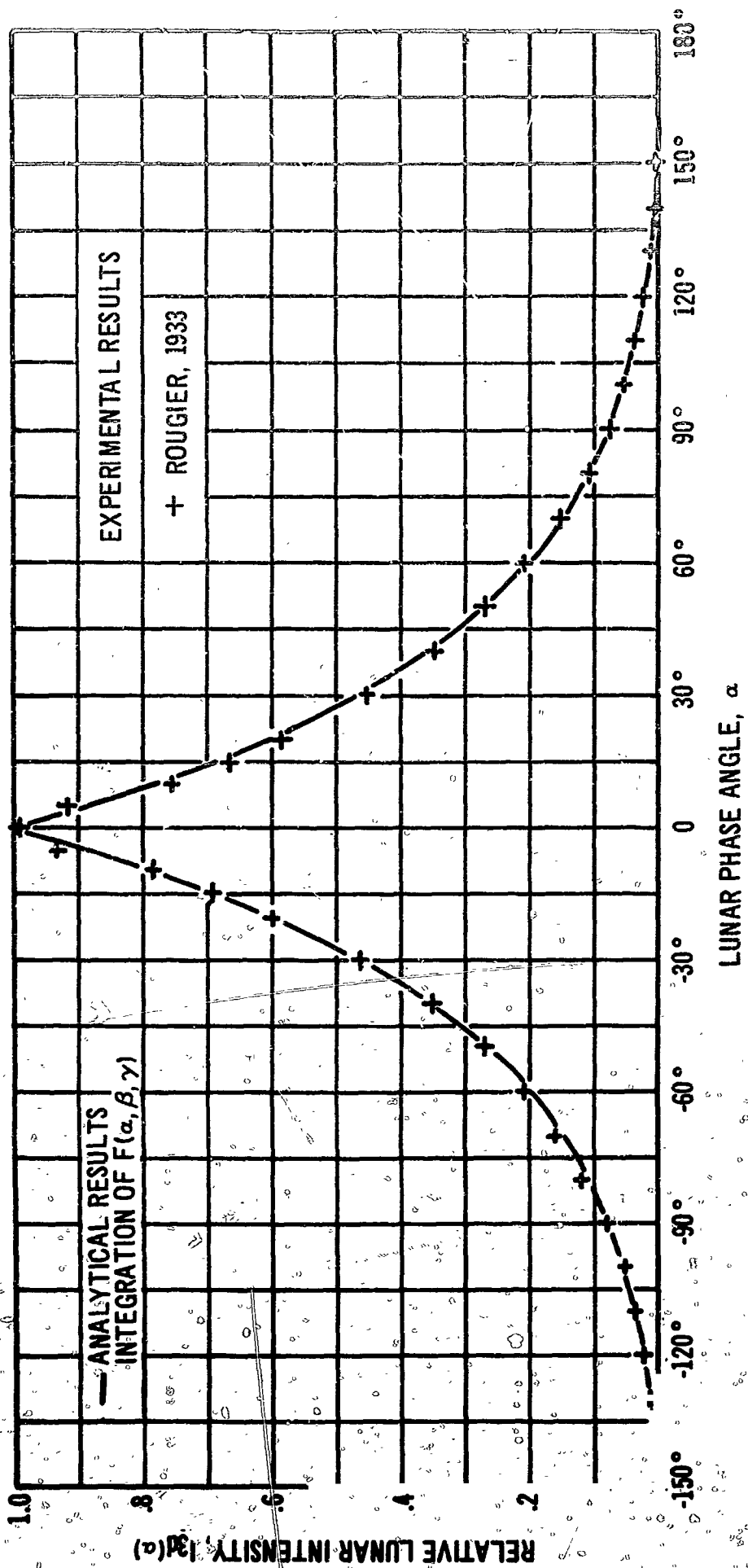


FIGURE 9 3D LUNAR INTENSITY,  $I_{3D}(\alpha)$  COMPARED WITH EXPERIMENTAL RESULTS

PHASE ANGLE,  $\alpha = 34^\circ$   
 ILLUMINATION LONGITUDE,  $\beta$   
 ILLUMINATION LATITUDE,  $\gamma$

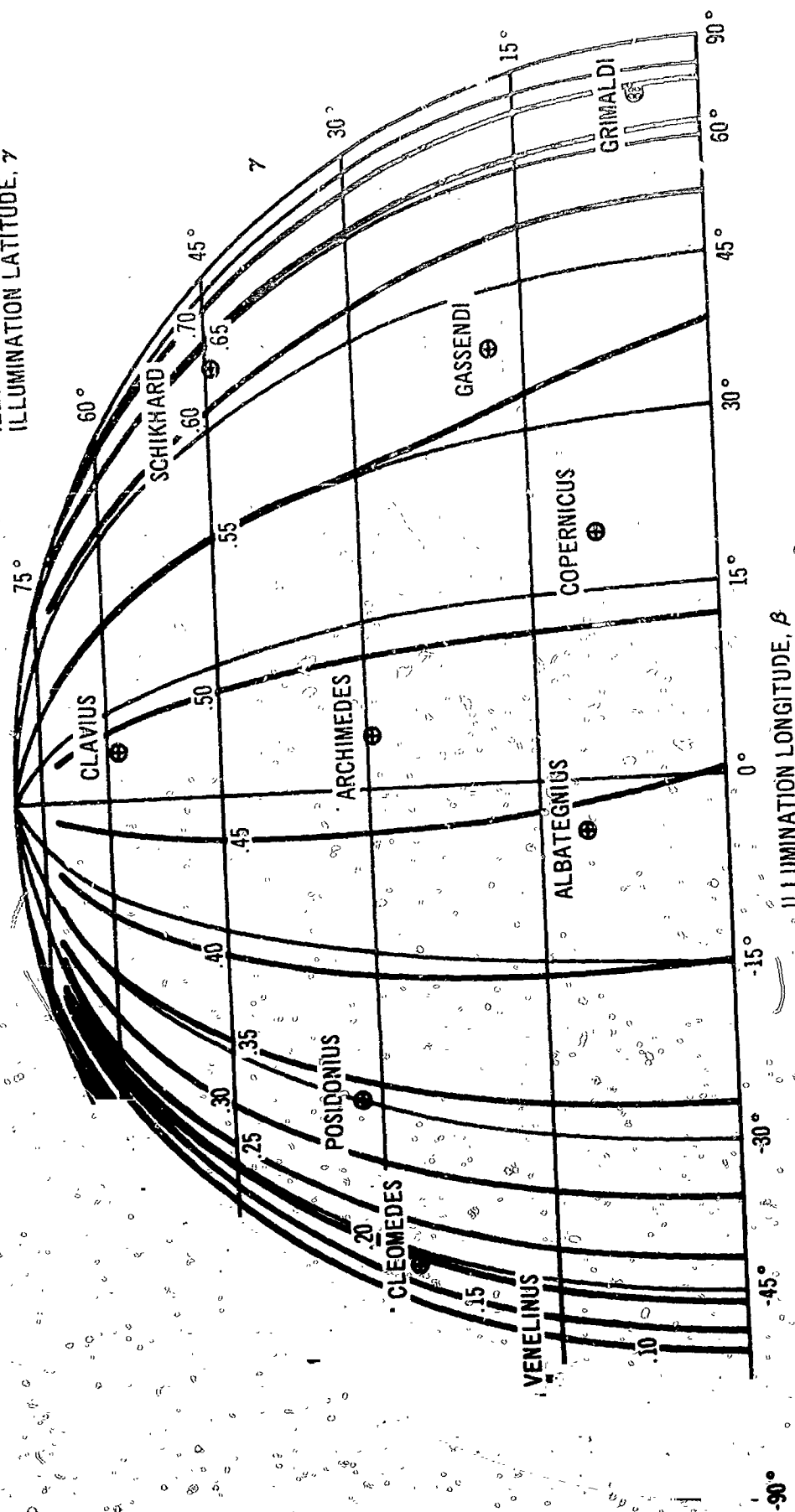


FIGURE 10 PREDICTED LUNAR ISOPHOTES  $\alpha = 34^\circ$

PHASE ANGLE,  $\alpha = 65^\circ$   
 ILLUMINATION LONGITUDE,  $\beta$   
 ILLUMINATION LATITUDE,  $\gamma$

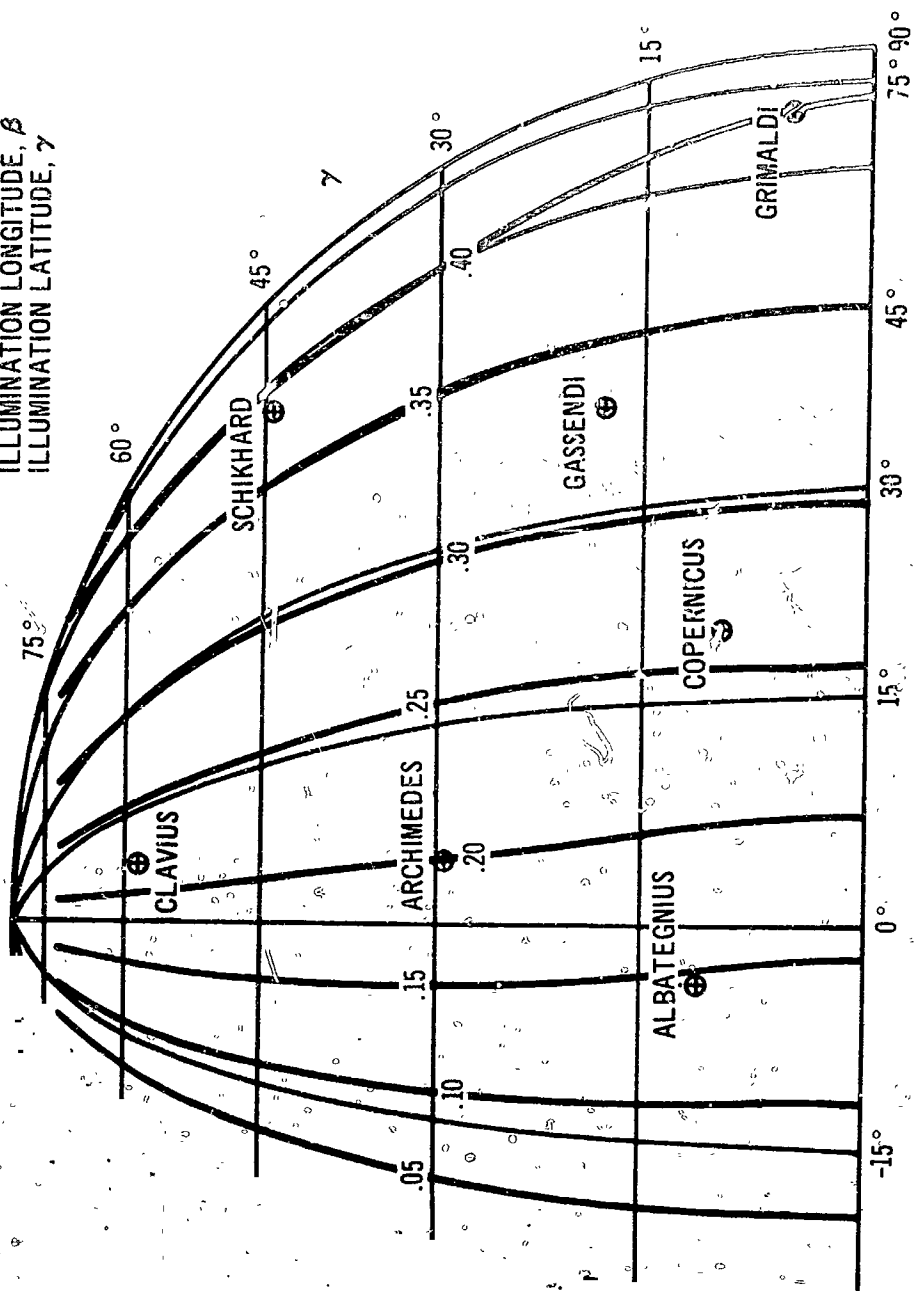


FIGURE 11 PREDICTED LUNAR ISOPHOTES,  $\alpha = 65^\circ$

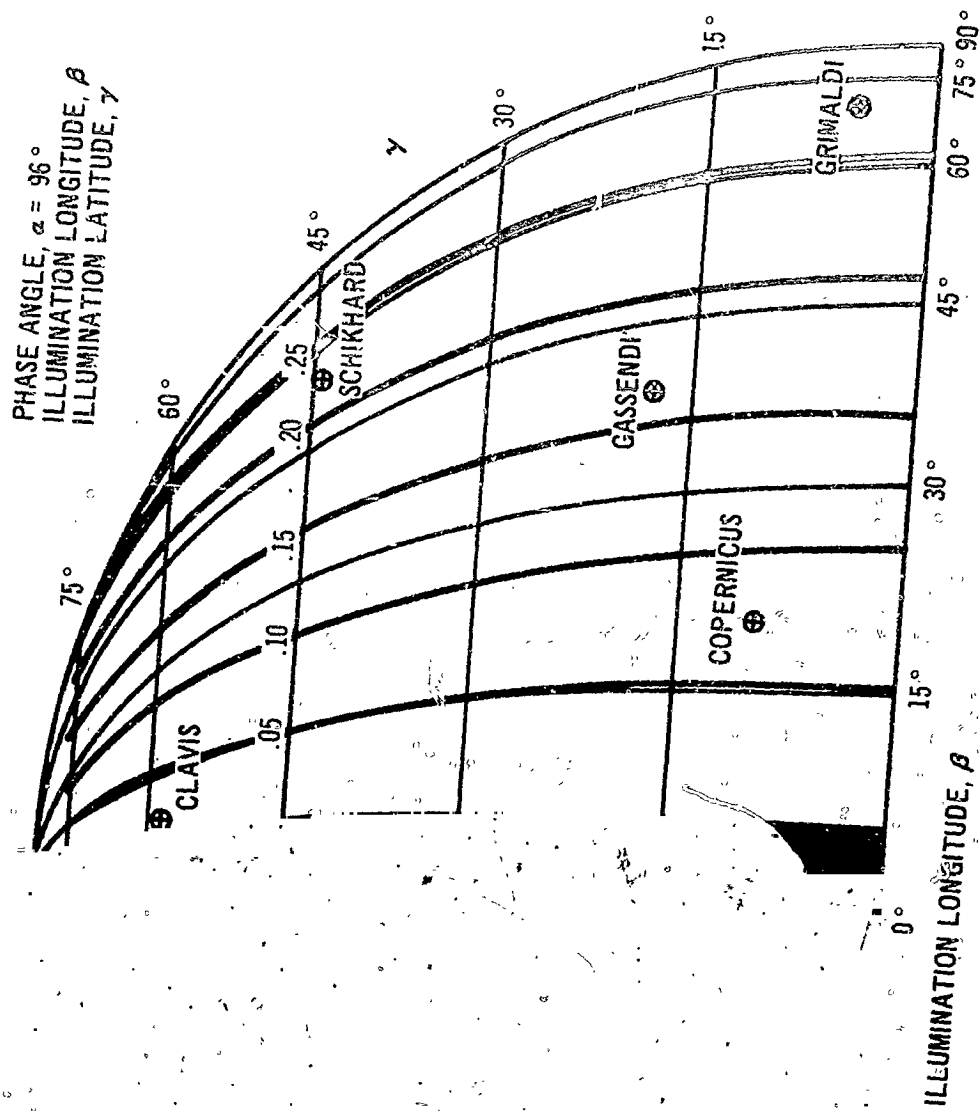
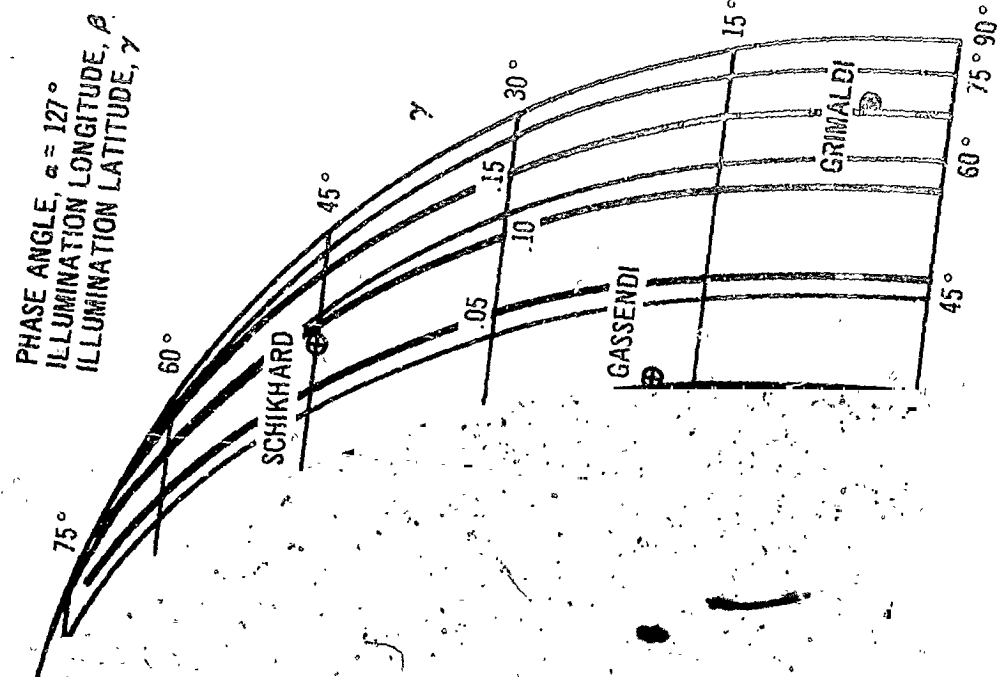


FIGURE 12 PREDICTED LUNAR ISOPHOTES,  $\alpha = 96^\circ$



MOON AS VIEWED  
FROM THE EARTH

ILLUMINATION LONGITUDE,  $\beta$   
FIGURE 13 PREDICTED LUNAR ISOPHOTES,  $\alpha = 127^\circ$

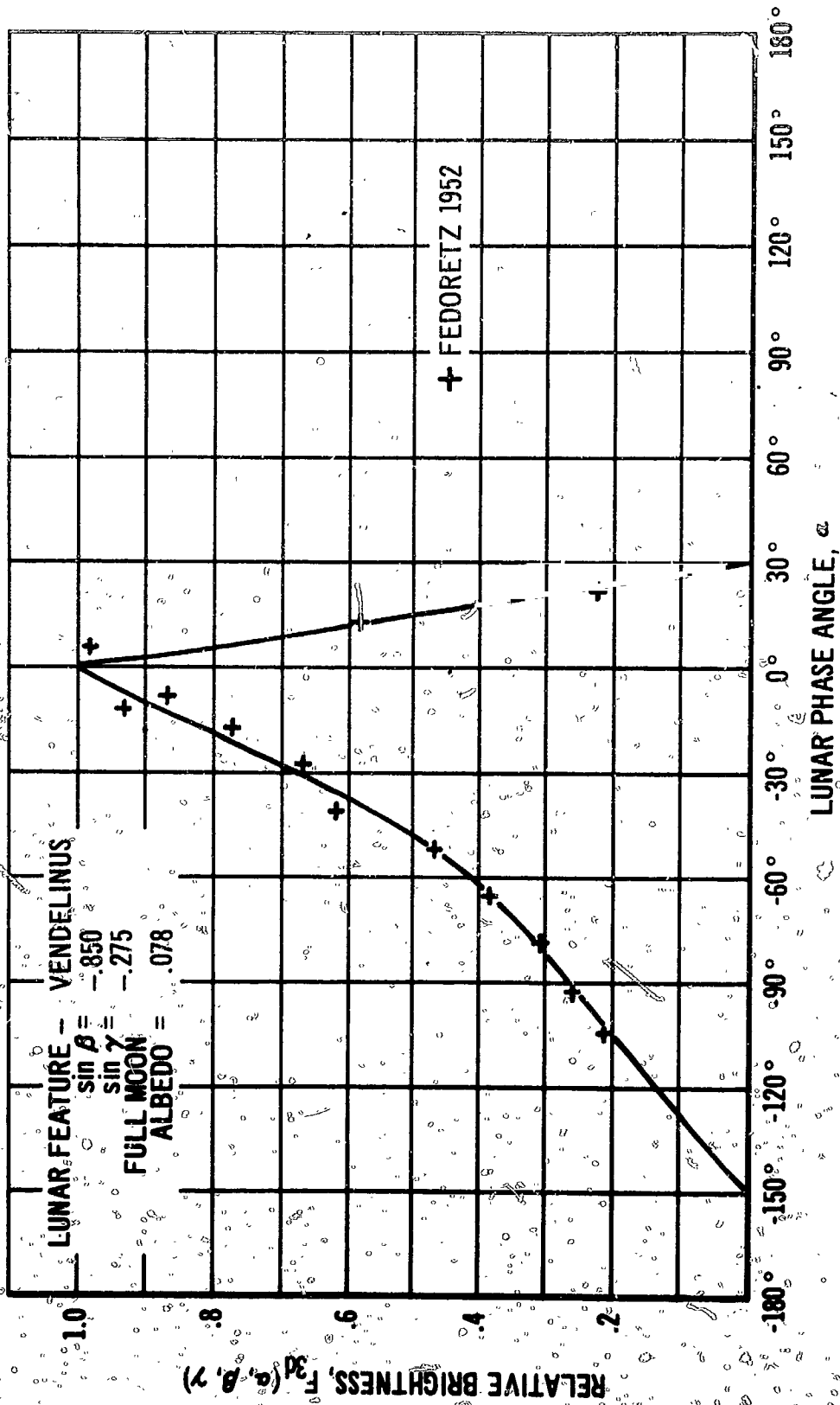


FIGURE 14 PREDICTED RELATIVE BRIGHTNESS OF VENDELINUS COMPARED WITH EXPERIMENTAL RESULTS

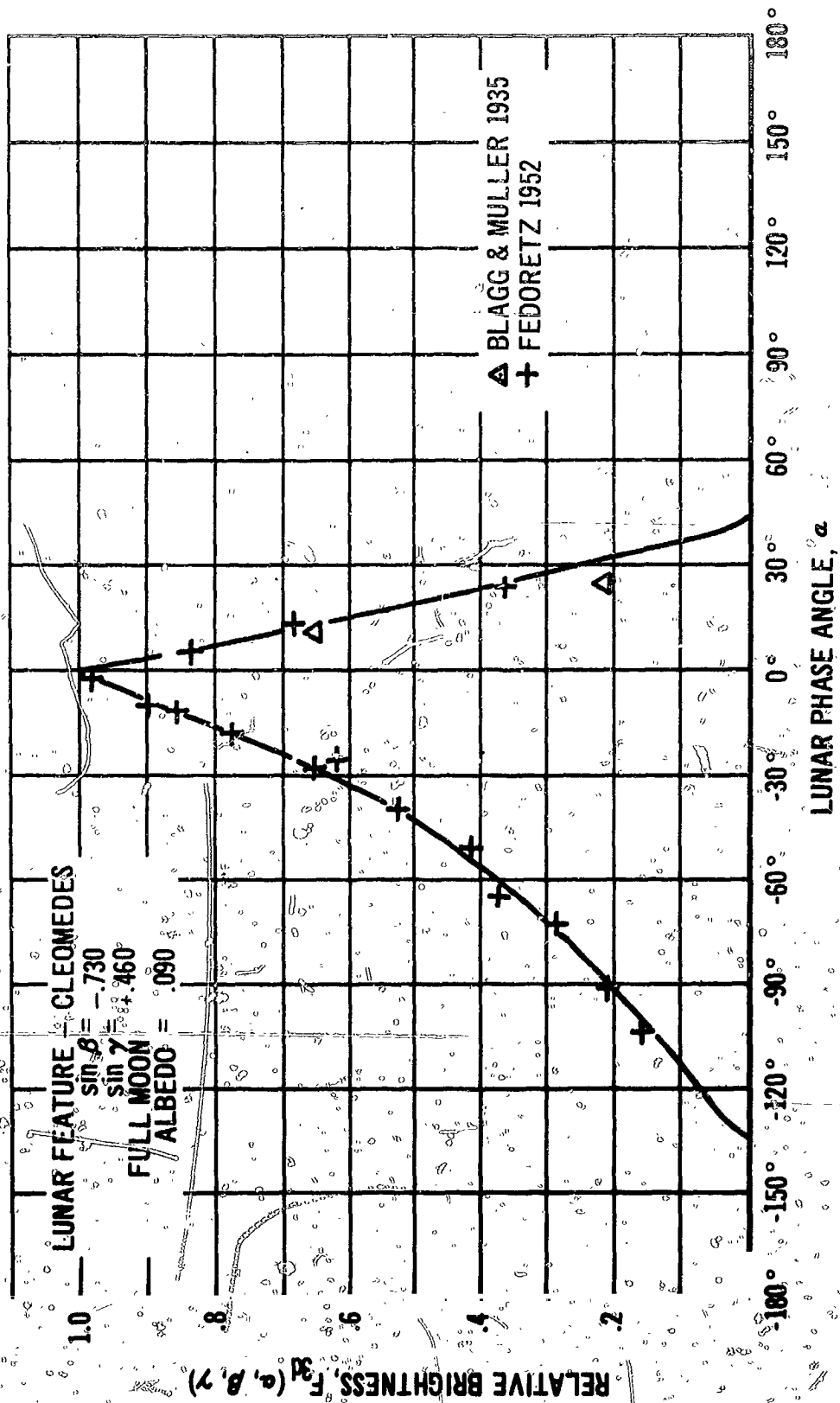


FIGURE 15 PREDICTED RELATIVE BRIGHTNESS OF CLEOMEDES COMPARED WITH EXPERIMENTAL RESULTS

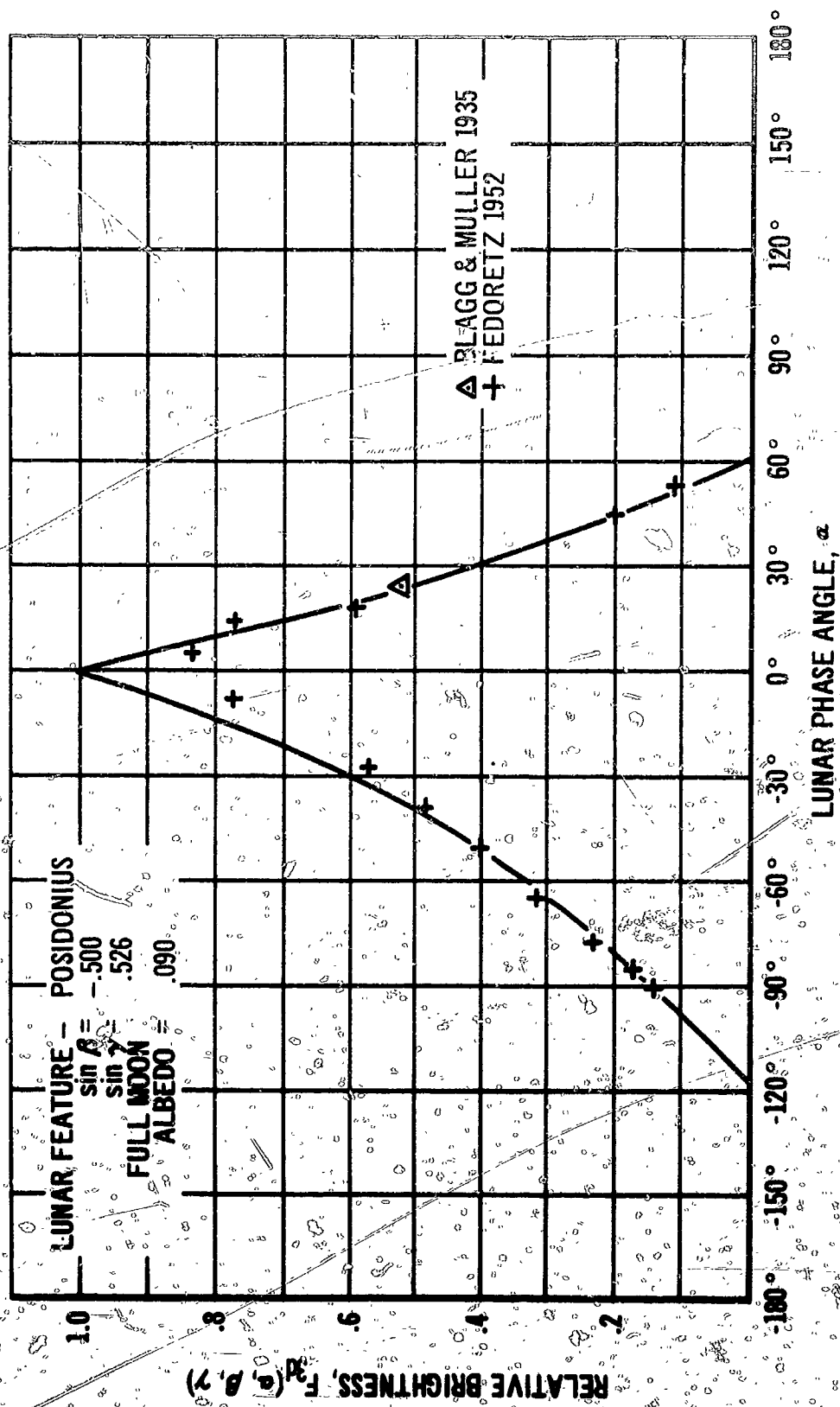


FIGURE 16 PREDICTED RELATIVE BRIGHTNESS OF POSIDONIUS COMPARED WITH EXPERIMENTAL RESULTS



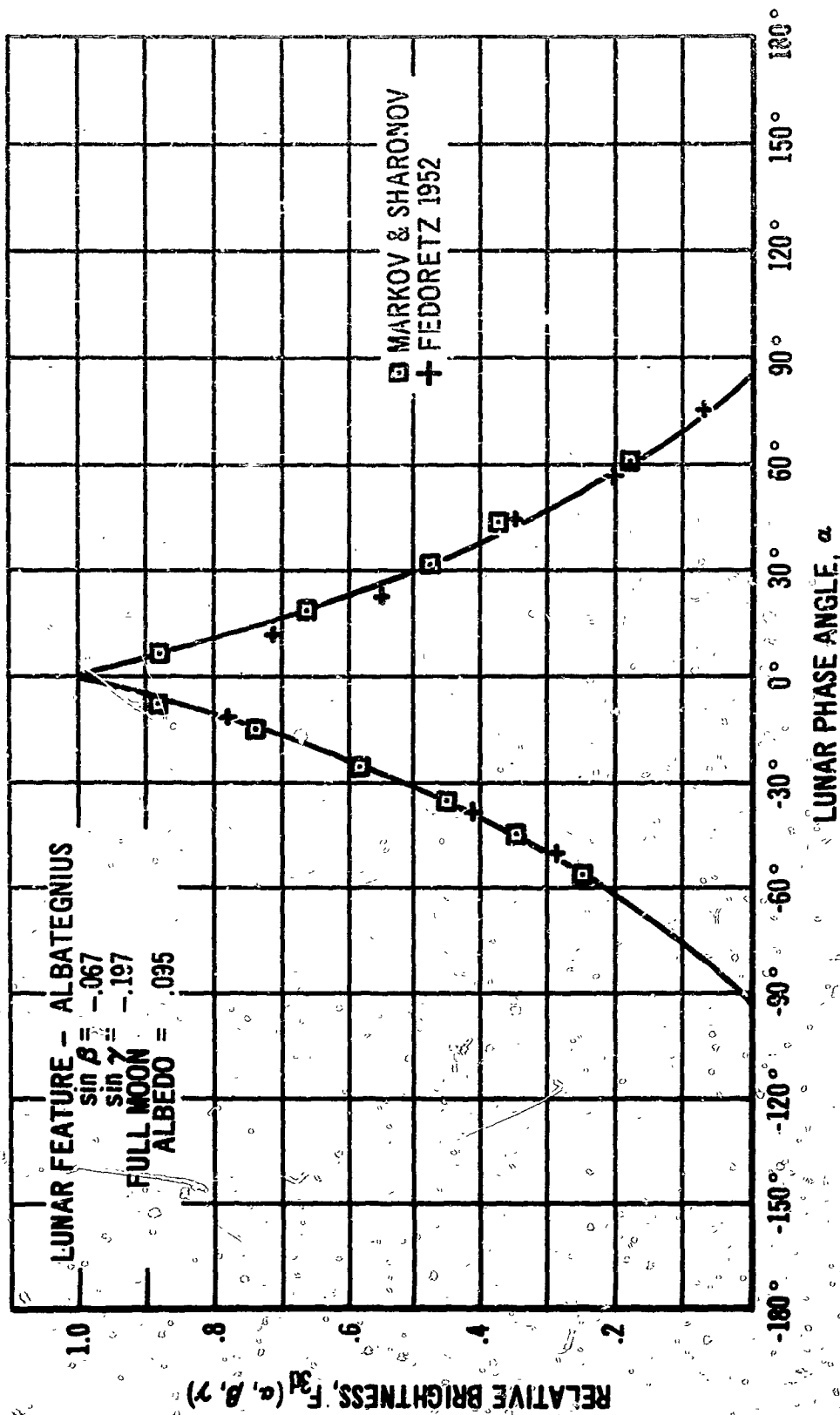


FIGURE 17. PREDICTED RELATIVE BRIGHTNESS OF ALBATEGNIUS COMPARED WITH EXPERIMENTAL RESULTS

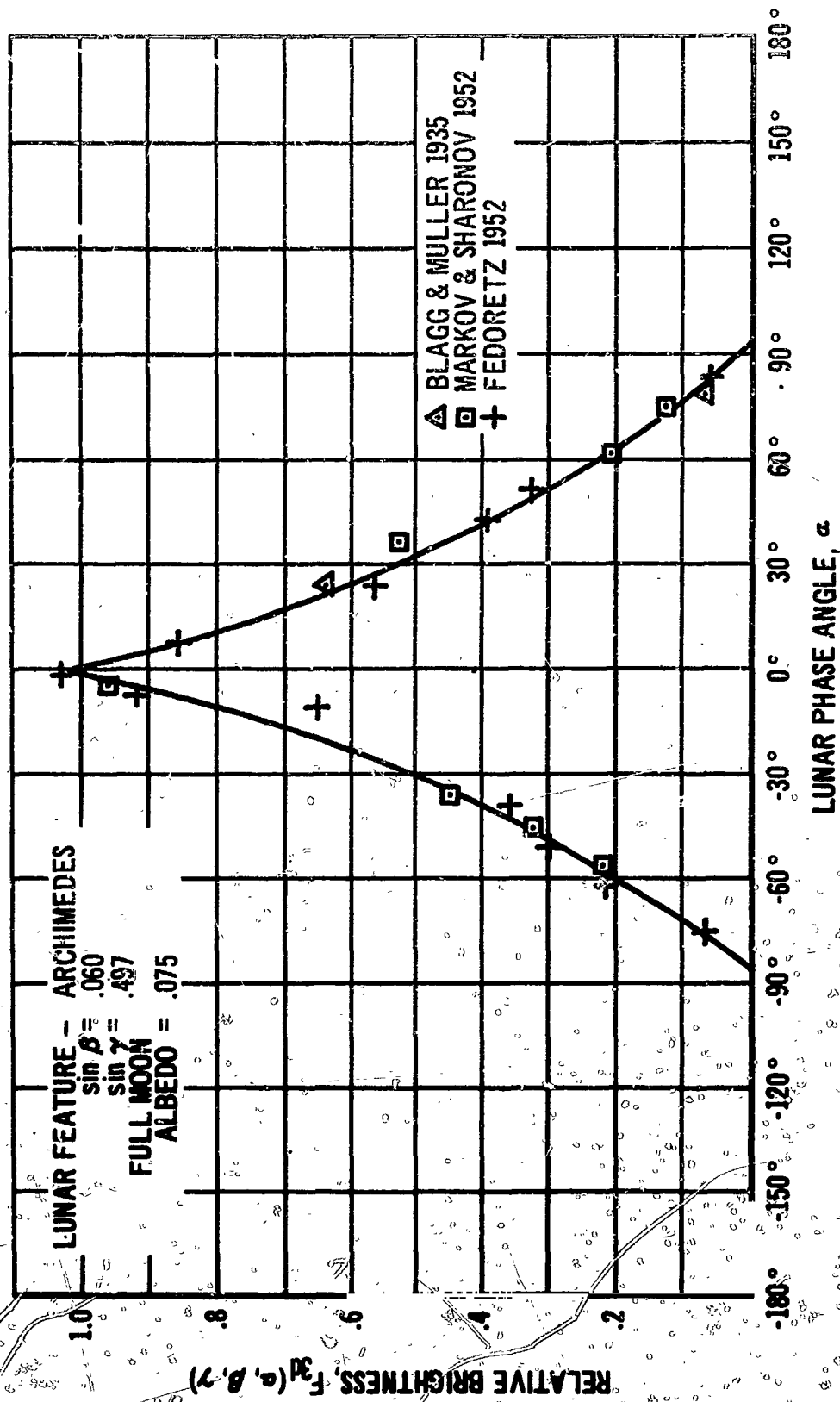


FIGURE 18 PREDICTED RELATIVE BRIGHTNESS OF ARCHIMEDES COMPARED WITH EXPERIMENTAL RESULTS

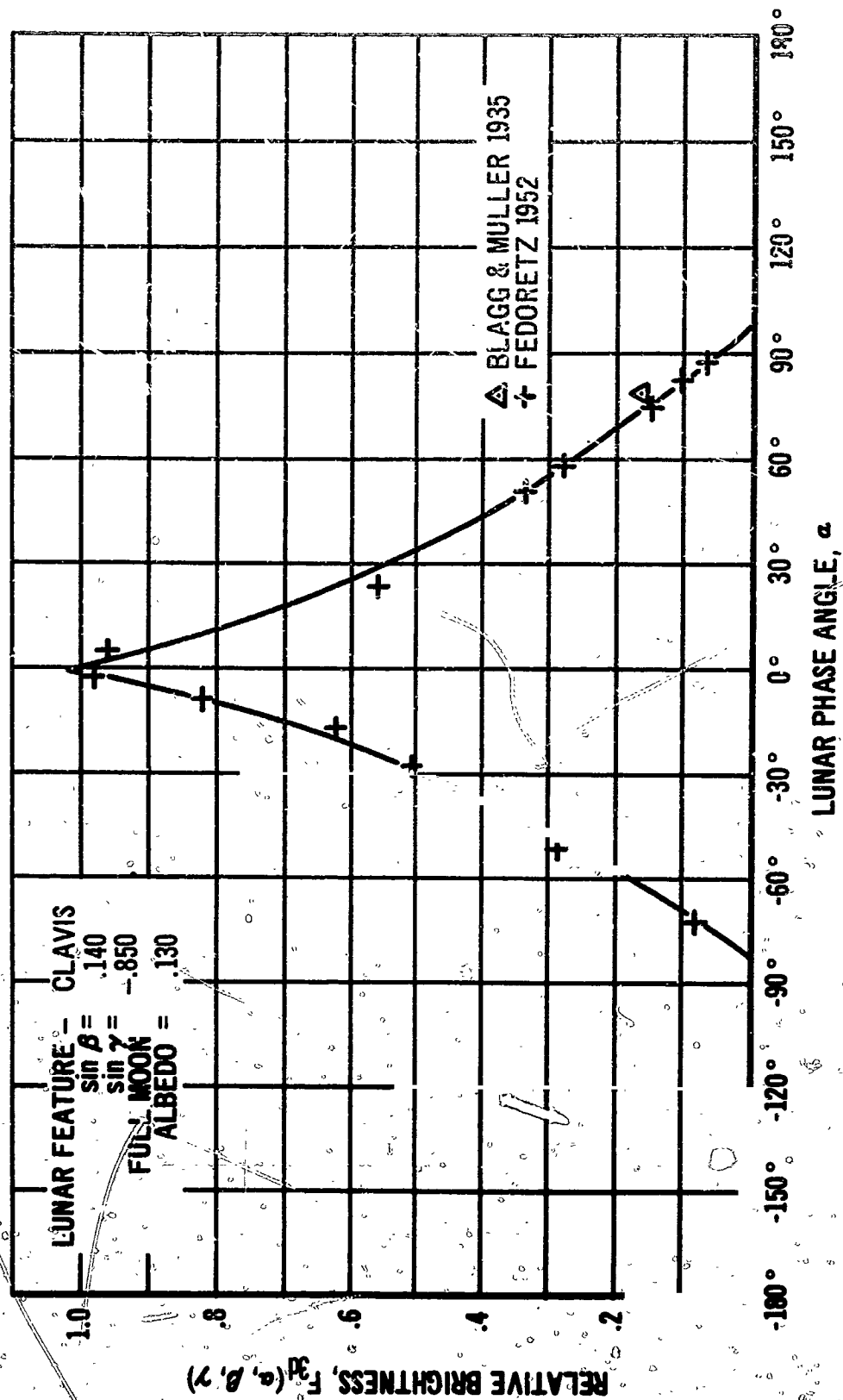


FIGURE 19 PREDICTED RELATIVE BRIGHTNESS OF CLAVIS COMPARED WITH EXPERIMENTAL RESULTS

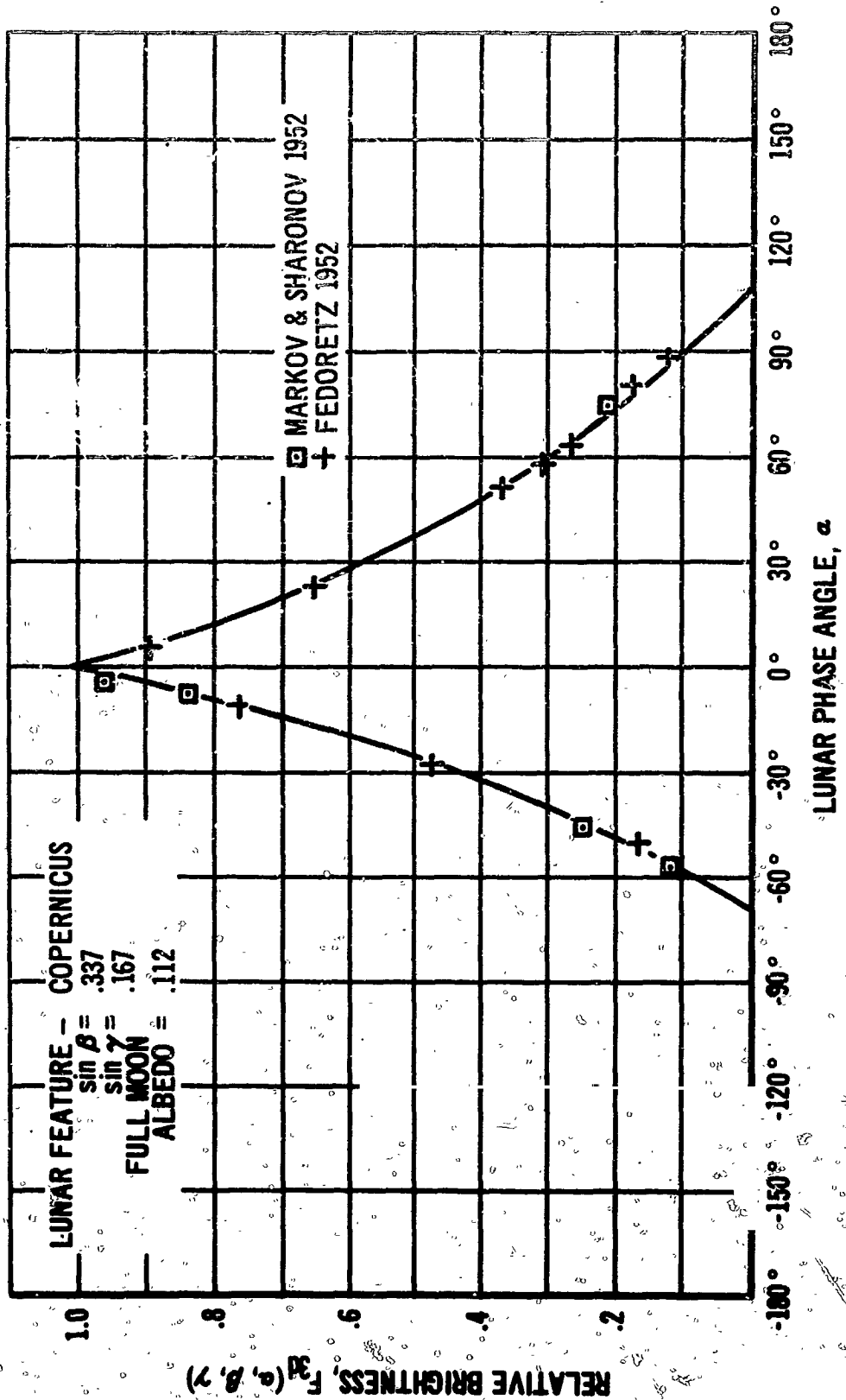


FIGURE 20 PREDICTED RELATIVE BRIGHTNESS OF COPERNICUS COMPARED WITH EXPERIMENTAL RESULTS

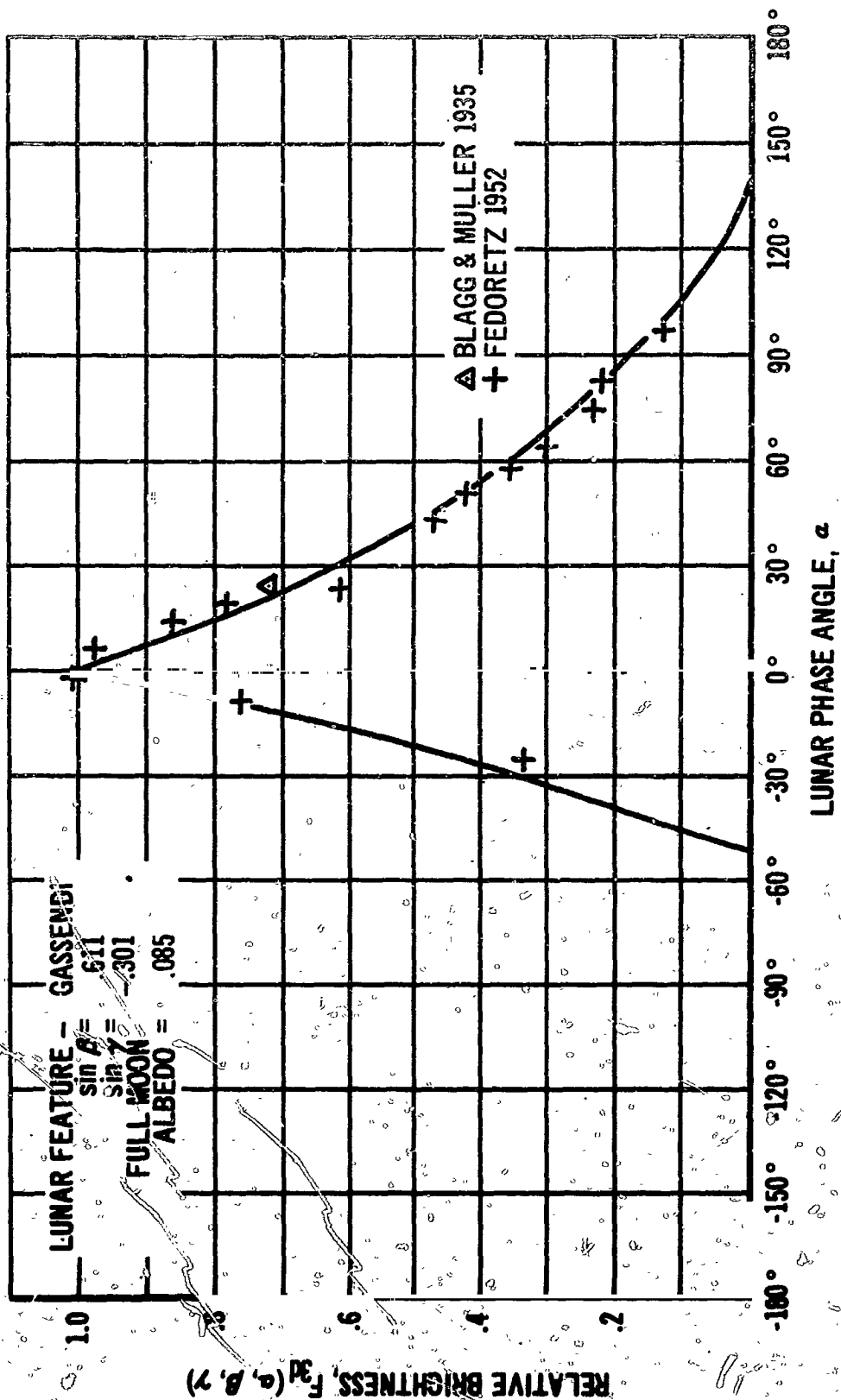


FIGURE 21 PREDICTED RELATIVE BRIGHTNESS OF GASSENDI COMPARED WITH EXPERIMENTAL RESULTS

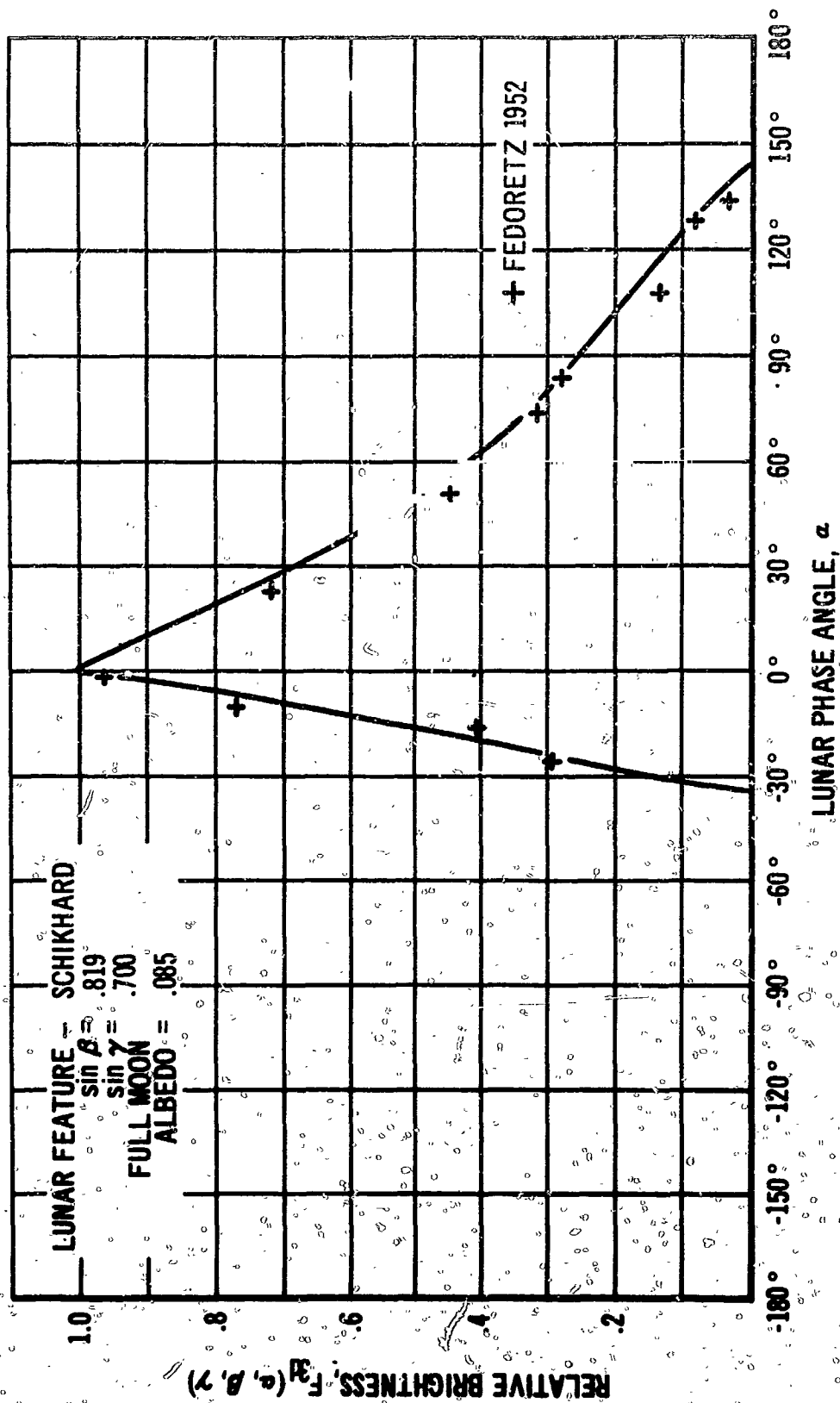


FIGURE 22 PREDICTED RELATIVE BRIGHTNESS OF SCHIKHARD COMPARED WITH EXPERIMENTAL RESULTS

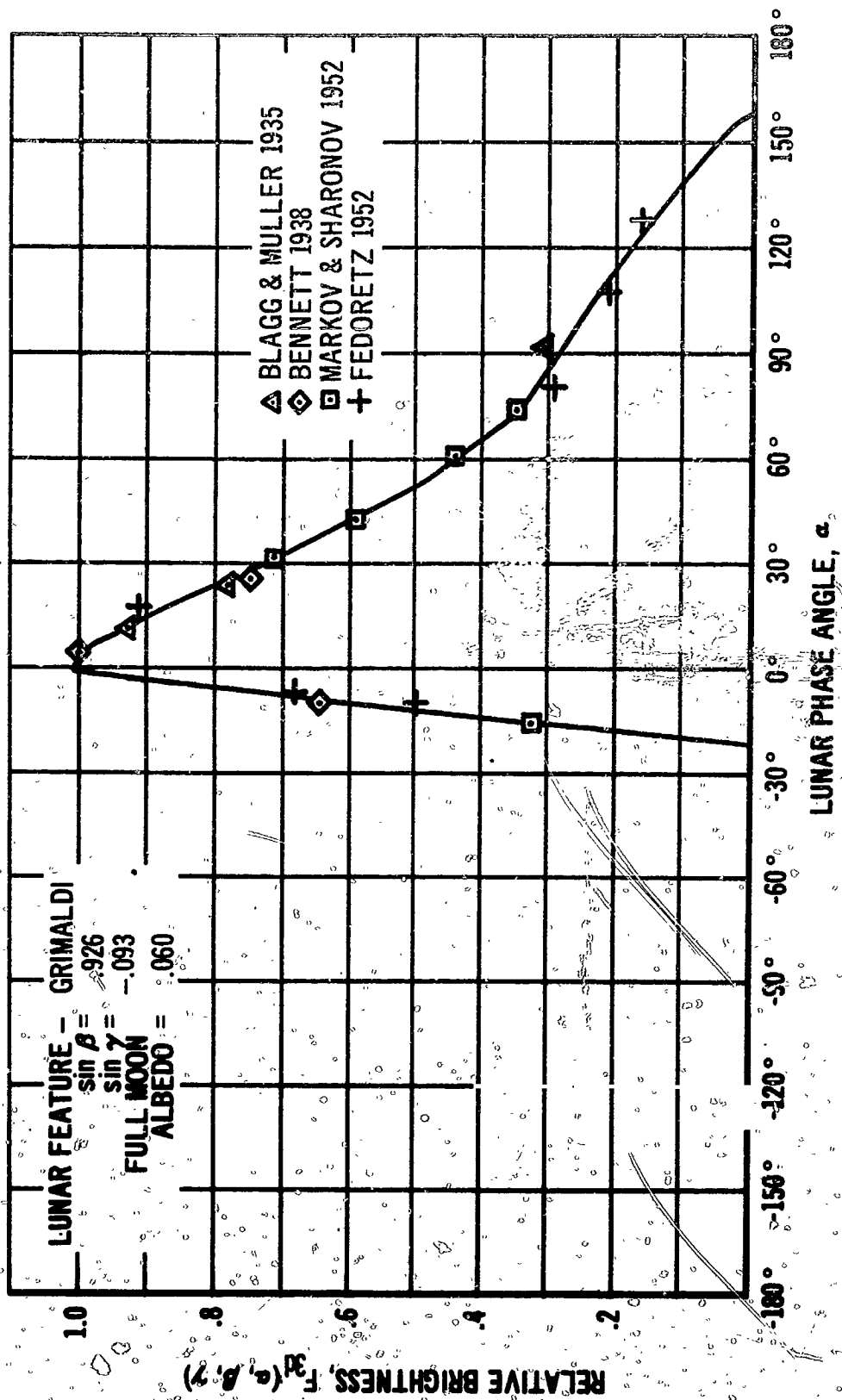


FIGURE 23 PREDICTED RELATIVE BRIGHTNESS OF GRIMALDI COMPARED WITH EXPERIMENTAL RESULTS

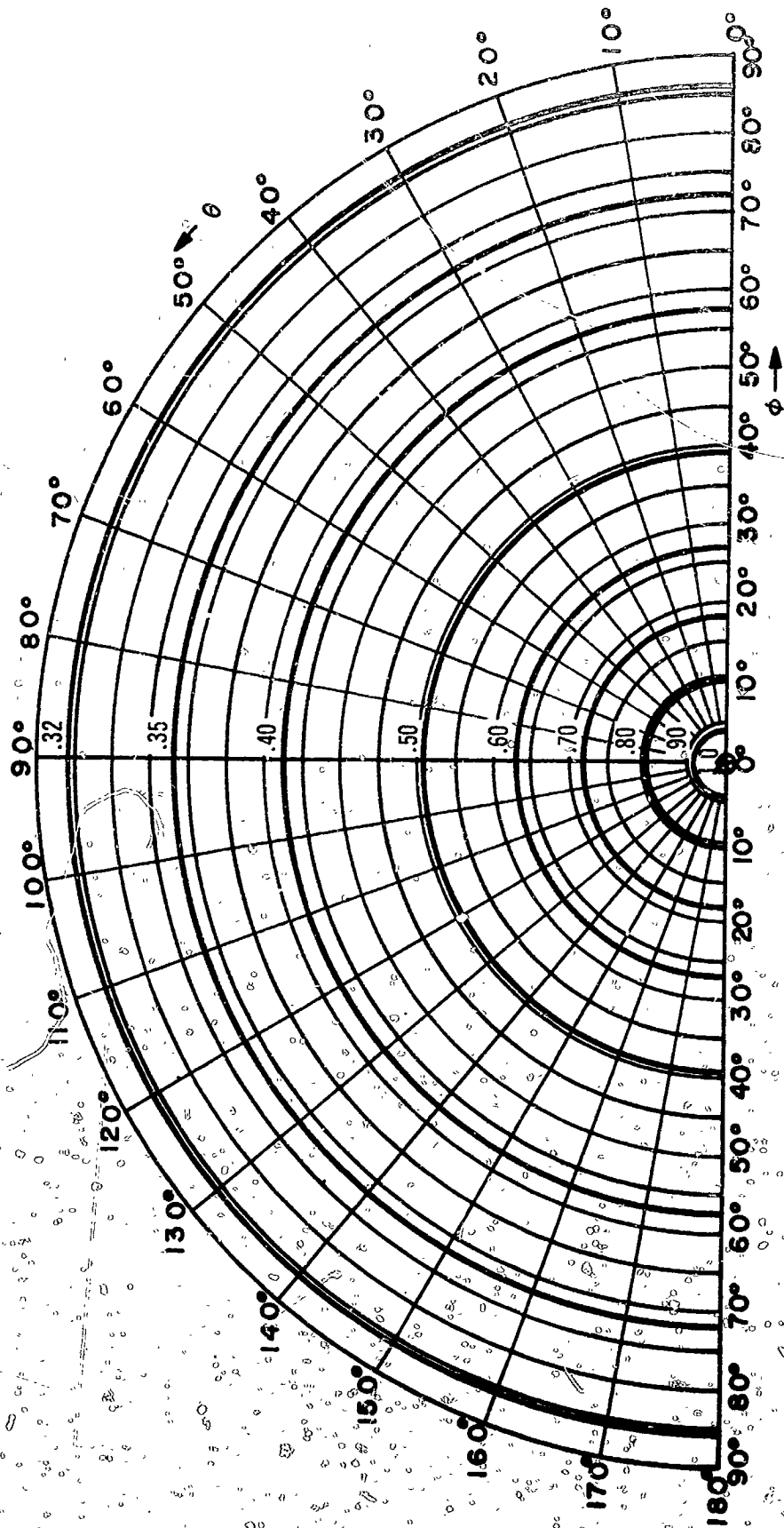


FIGURE 24 LUNAR SURFACE DIRECTIONAL REFLECTANCE ISOPHOTES,  $\psi = 0$



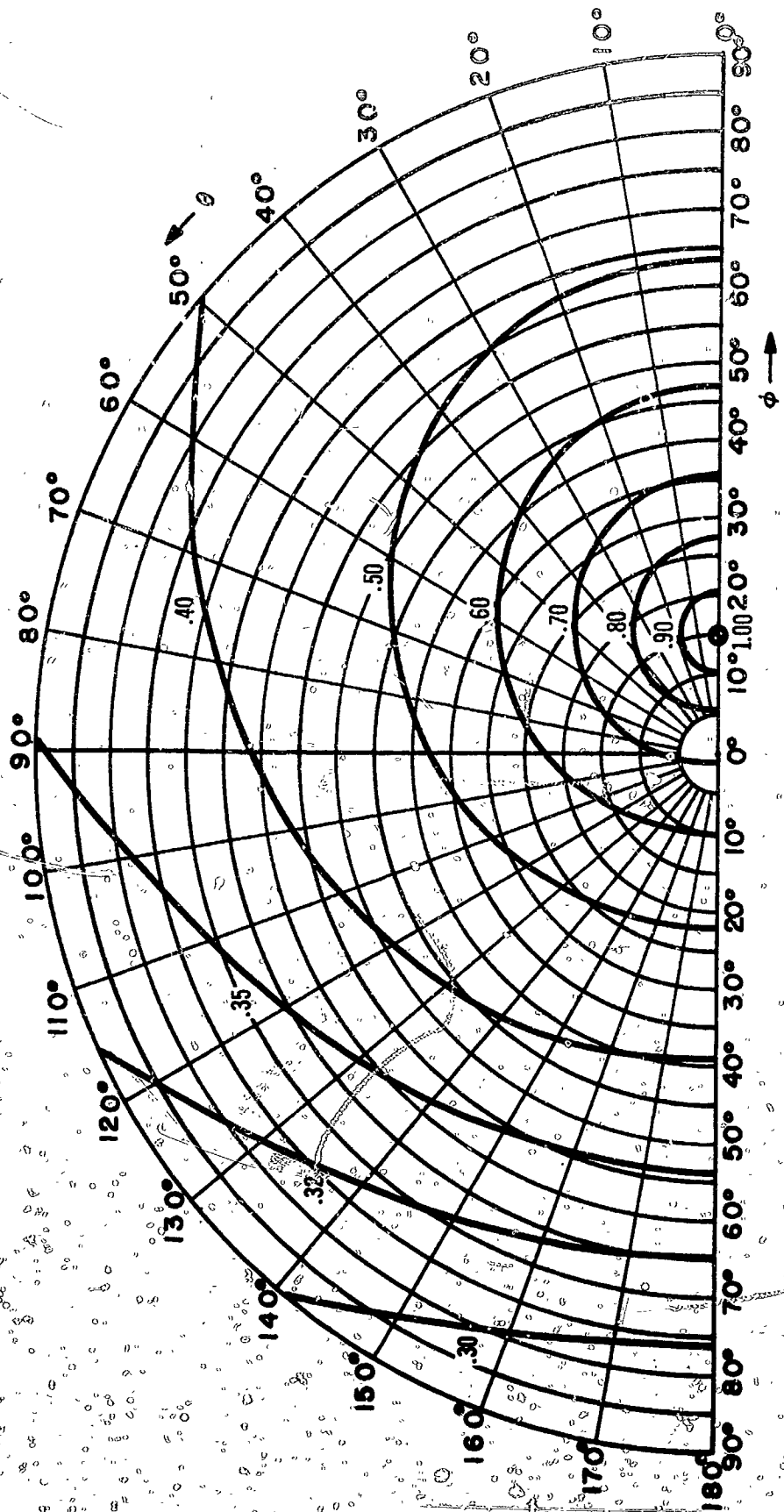


FIGURE 25 LUNAR SURFACE DIRECTIONAL REFLECTANCE ISOPHOTES,  $\psi = 15^\circ$

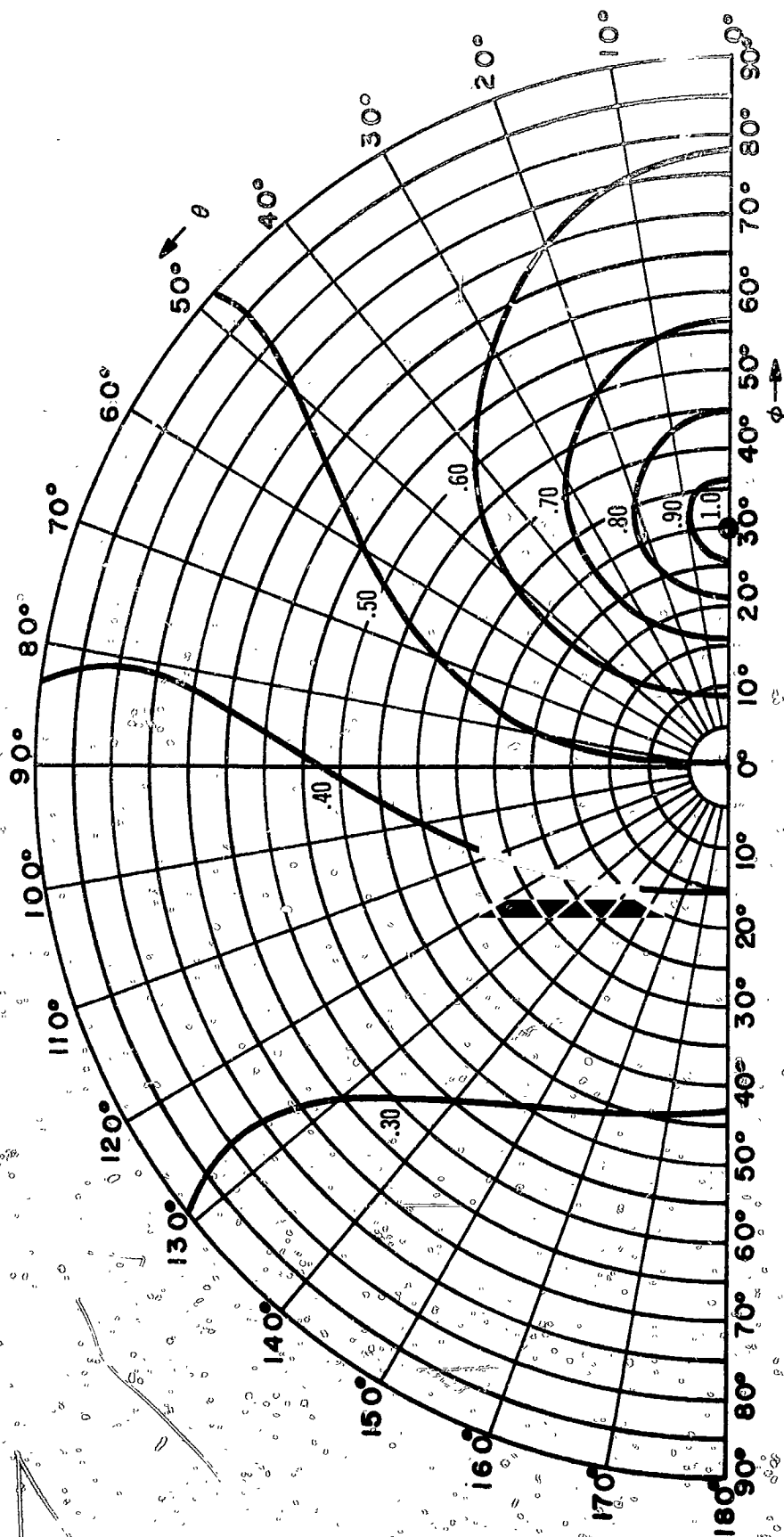


FIGURE 26 LUNAR SURFACE DIRECTIONAL REFLECTANCE ISOPHOTES,  $\psi = 30^\circ$

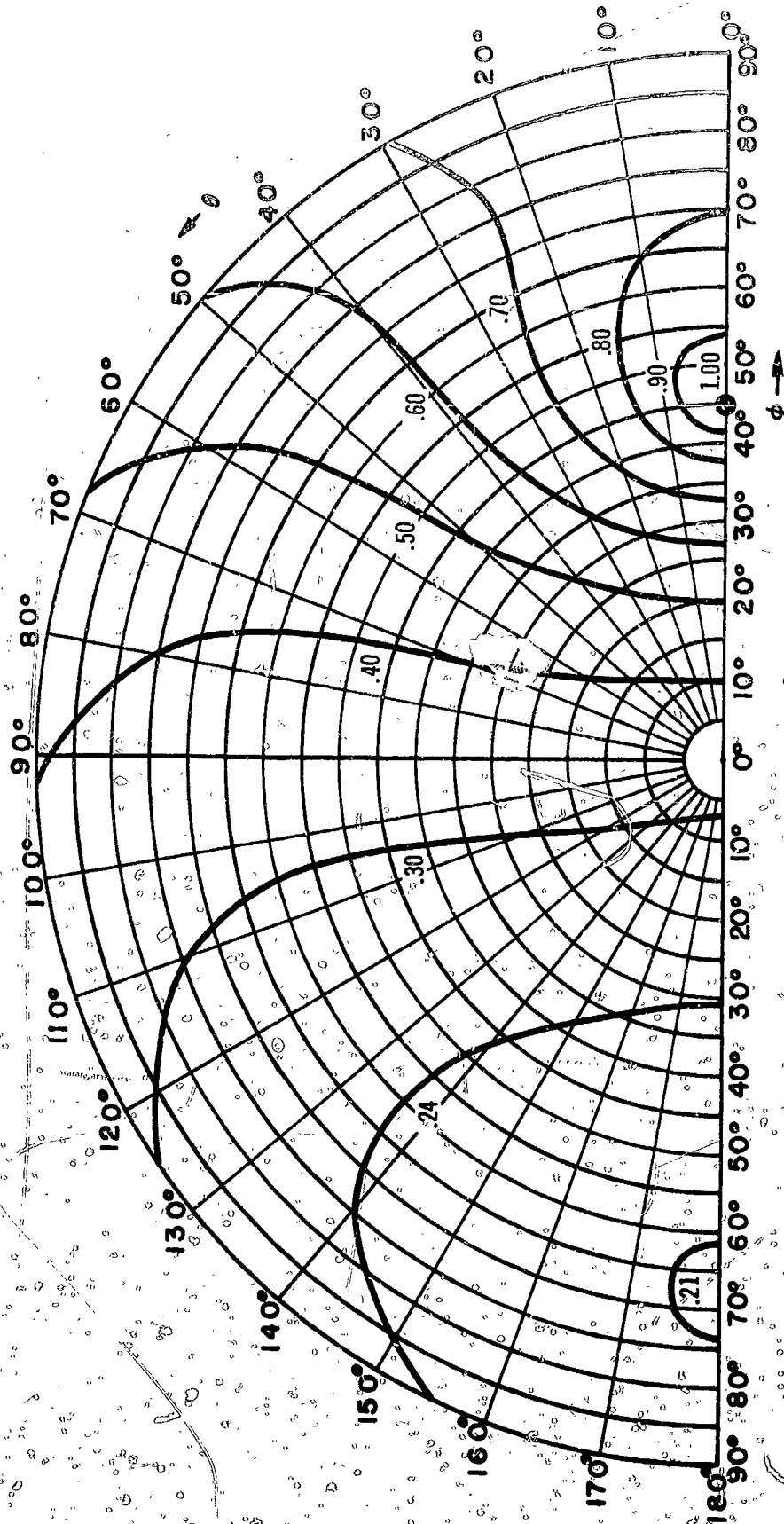


FIGURE 27 LUNAR SURFACE DIRECTIONAL REFLECTANCE ISOPHOTES,  $\psi = 45^\circ$

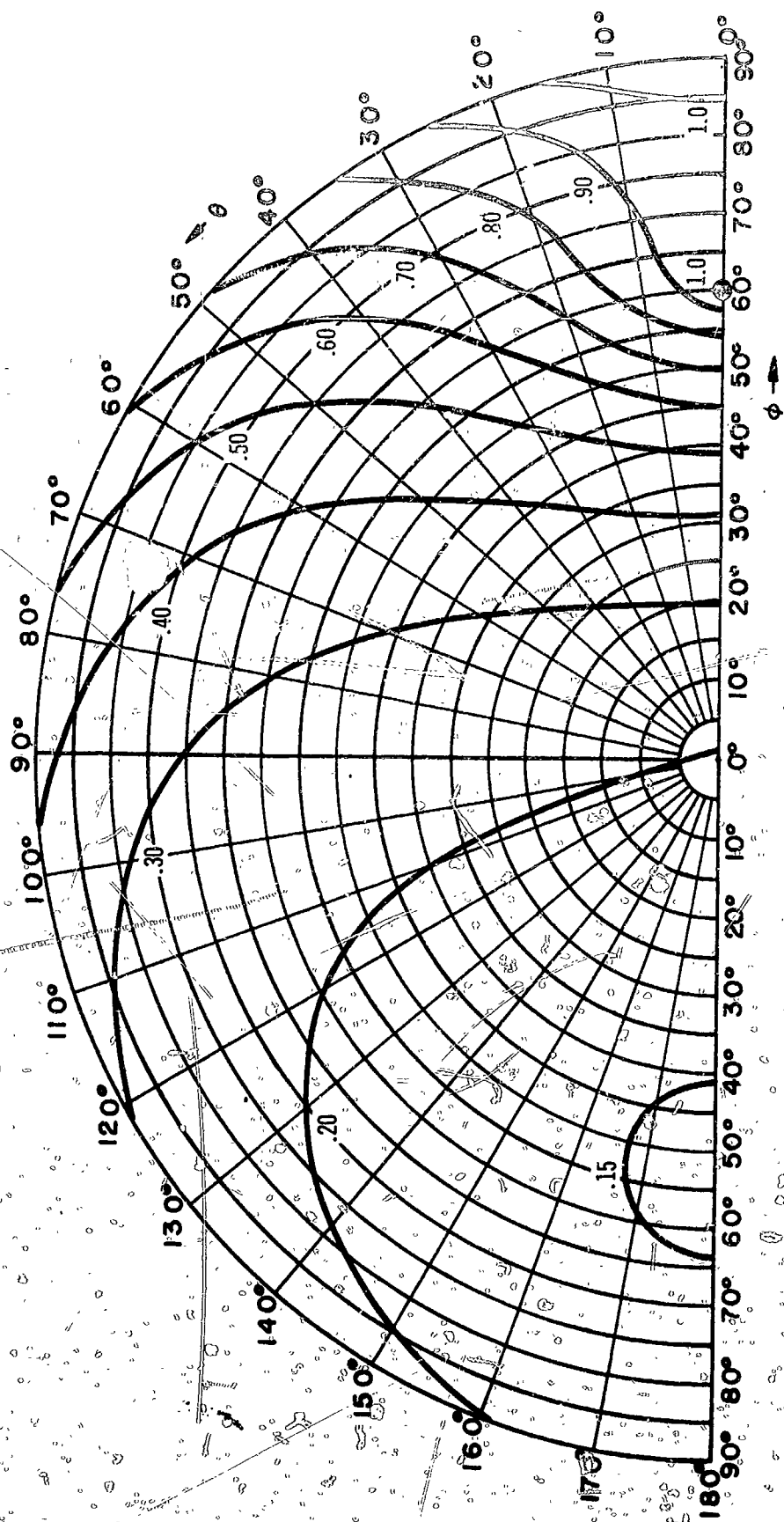


FIGURE 28 LUNAR SURFACE DIRECTIONAL REFLECTANCE ISOPHOTES,  $\psi = 60^\circ$

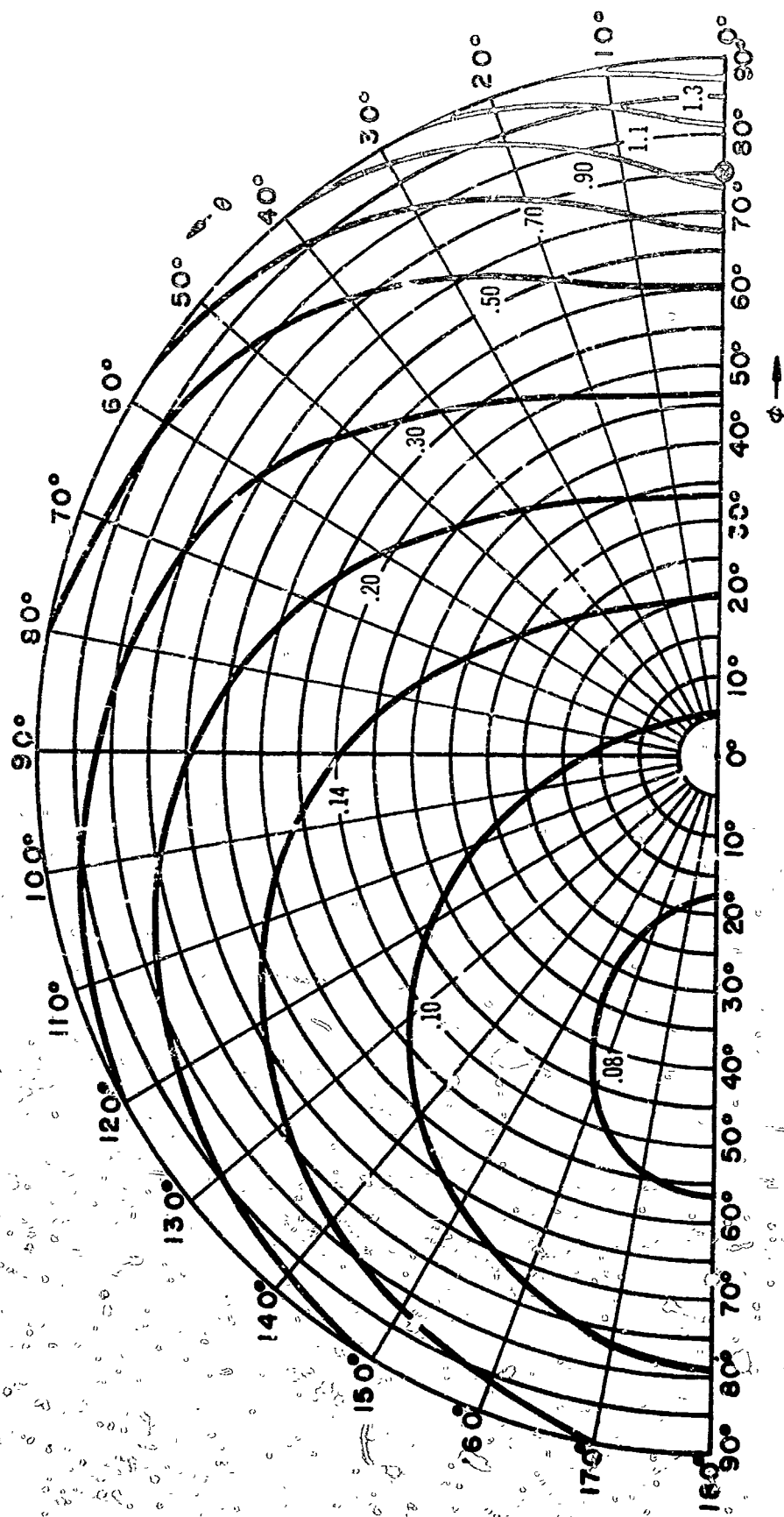


FIGURE 29 LUNAR SURFACE DIRECTIONAL REFLECTANCE ISOPHOTES,  $\psi = 75^\circ$

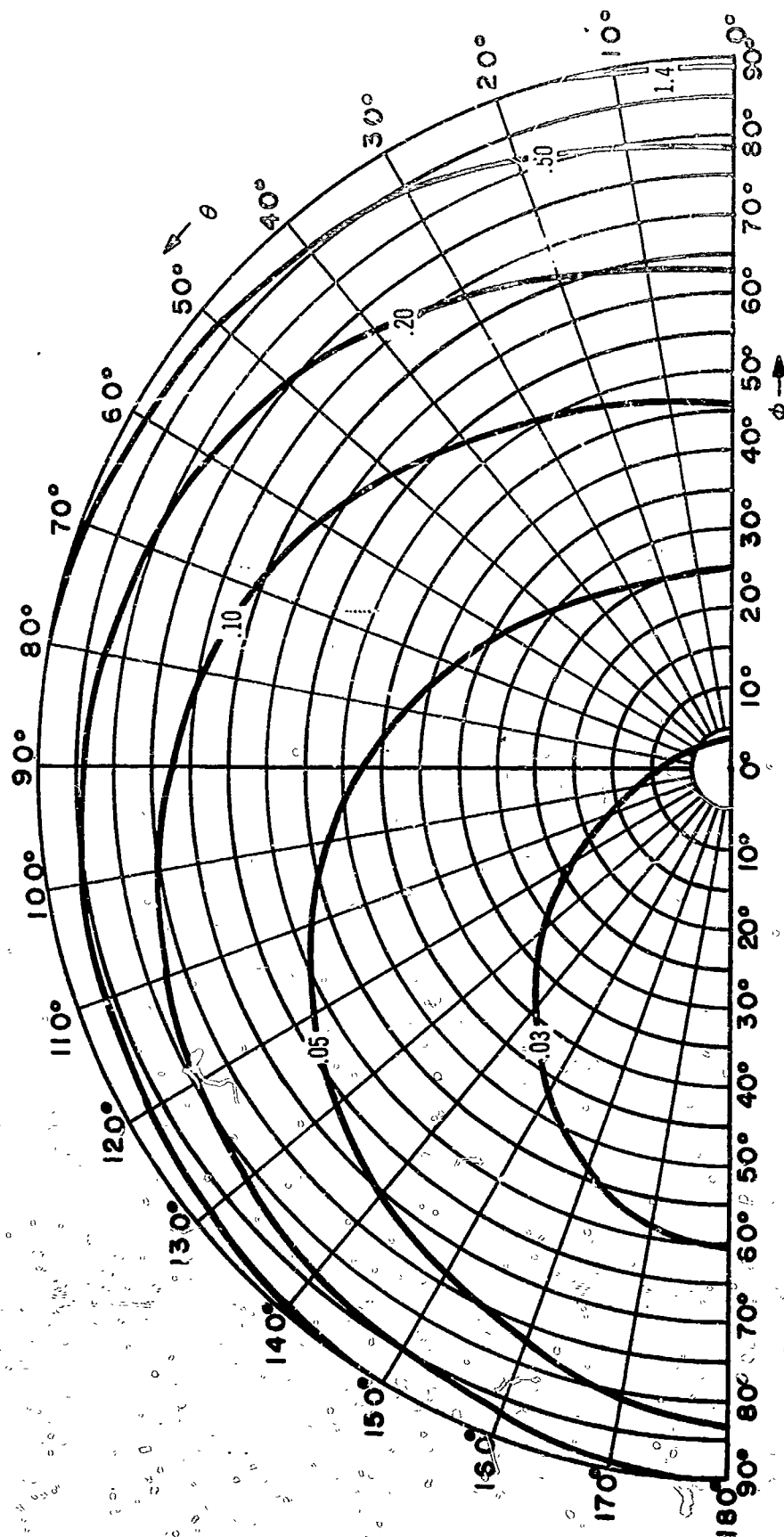


FIGURE 30 LUNAR SURFACE DIRECTIONAL REFLECTANCE ISOPHOTES,  $\psi = 85^\circ$

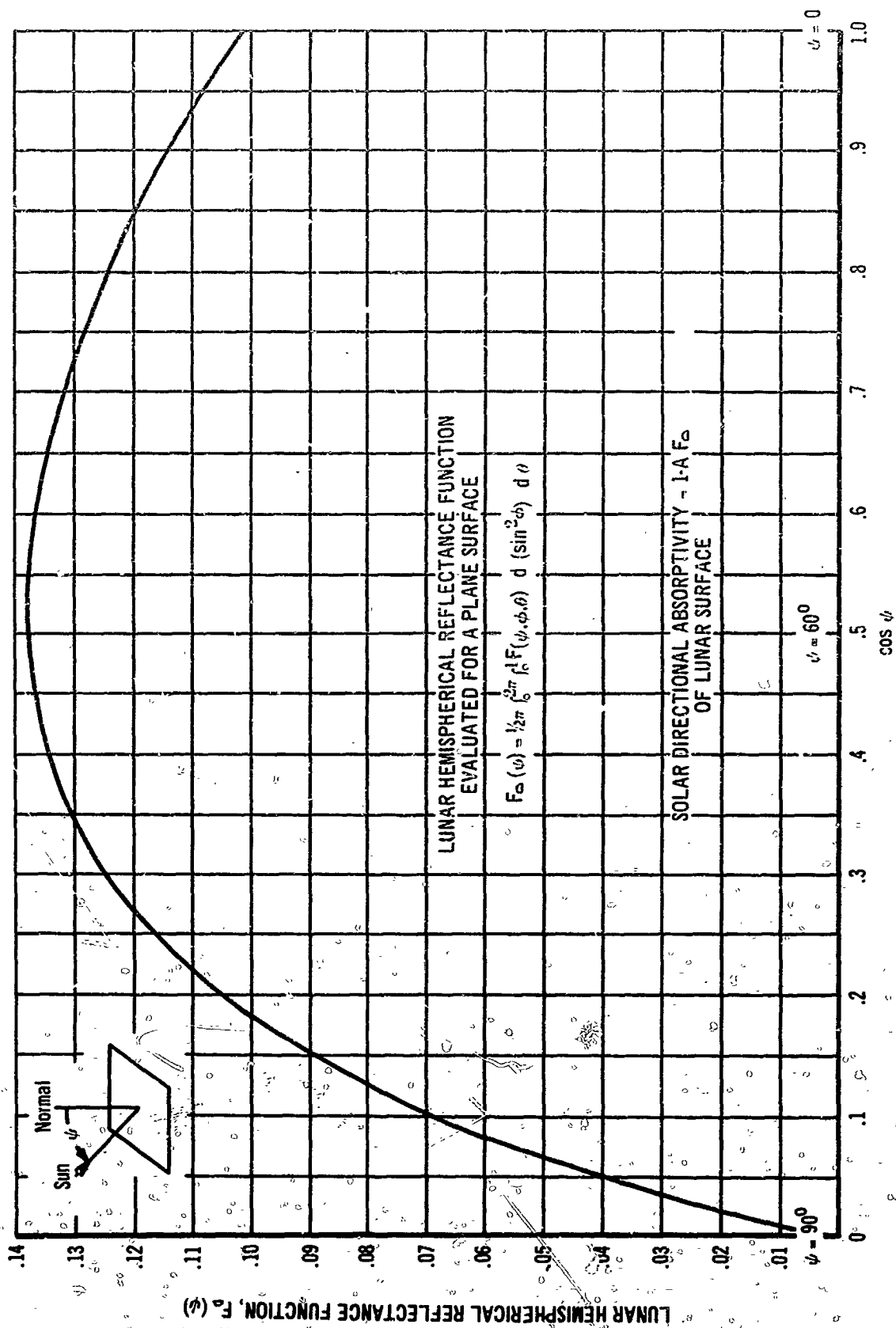


FIGURE 31. LUNAR HEMISPHERICAL REFLECTANCE FUNCTION,  $F_0$ , VERSUS ZENITH ANGLE OF ILLUMINATION,  $\psi$

TABLE I

Phase Angle Dependent Function,  $g(\alpha)$ . Tabular value of experimentally based curves  $g_1(\alpha)$ ,  $g_2(\alpha)$ ,  $g_3(\alpha)$  and  $g_4(\alpha)$  compared with the developed analytical expression for  $g(\alpha)$

$\alpha$	$g_1(\alpha)$	$g_2(\alpha)$	$g_3(\alpha)$	$g_4(\alpha)$	$g(\alpha)$
0°	1.000	1.000	1.000	1.000	1.000
10°	.809	.813	.809	.812	.803
20°	.666	.665	.665	.665	.662
30°	.569	.574	.572	.570	.556
40°	.460	.466	.467	.455	.463
50°	.381	.386	.388	.38	.392
60°	.303	.323	.324	.312	.336
70°	.287	.281	.275	.254	.292
80°	.264	.248	.233	.207	.250
90°	-	.221	.196	.166	.219
100°	-	.194	.170	-	.192
110°	-	.178	.150	-	.167
120°	-	.168	.133	-	.149
130°	-	.154	-	-	.130
140°	-	.143	-	-	.112
150°	-	.116	-	-	.095
160°	-	.092	-	-	.074
170°	-	.057	-	-	.051
180°	-	.000	-	-	.000

FROM FIGURE 3

$$g_1(\alpha) = \frac{\cos \frac{\alpha}{2}}{\cos \alpha} \cdot F(\alpha, 0)$$

 $F(\alpha, 0)$ 

$$g_2(\alpha) = \frac{1}{\cos \frac{\alpha}{2}} \cdot F\left(\alpha, \frac{\alpha}{2}\right)$$

 $F\left(\alpha, \frac{\alpha}{2}\right)$ 

$$g_3(\alpha) = F\left(\alpha, \frac{3\alpha}{4}\right)$$

 $F\left(\alpha, \frac{3\alpha}{4}\right)$ 

$$g_4(\alpha) = \cos \frac{\alpha}{2} \cdot F(\alpha, \alpha)$$

 $F(\alpha, \alpha)$ 

$$g(\alpha) = \frac{1}{\left(1 + \sin \frac{\alpha}{2}\right)^2} \cdot \sqrt{\frac{1 - \sin \frac{\alpha}{2}}{\cos \frac{\alpha}{2}}}$$



TABLE II

An approximate integrated lunar brightness,  $I_{2d}(\alpha)$  is obtained for various phase angles,  $\alpha$ , by assuming that the brightness of the moon assumes an equatorial value everywhere along an illumination longitude line and then integrating the equatorial brightness  $F_{2d}(\alpha, \beta)$  over the projected area of the moon. These analytical results  $I_{2d}(\alpha)$  are compared with earlier results of Rougier 1933 and more recent results of Bullrich 1948

2D INTEGRATED LUNAR BRIGHTNESS,  $I_{2d}(\alpha)$ 

PHASE ANGLE $ \alpha $	EXPERIMENTAL RESULTS ROUGIER	ANALYTICAL RESULTS $I_{2d}(\alpha)$	EXPERIMENTAL RESULTS BULLRICH
$0^\circ$	1.000	1.0000	1.000
$10^\circ$	.725	.7212	.732
$20^\circ$	.578	.5446	.560
$30^\circ$	.437	.4144	.423
$40^\circ$	.339	.3136	.320
$50^\circ$	.263	.2338	.233
$60^\circ$	.208	.1703	.167
$70^\circ$	.166	.1204	.124
$80^\circ$	.115	.0819	.087
$90^\circ$	.080	.0532	.067
$100^\circ$	.056	.0325	.047
$110^\circ$	.039	.0185	.036
$120^\circ$	.025	.0095	.024
$130^\circ$	.016	.0044	.012
$140^\circ$	.009	.0017	.009
$150^\circ$	.004	.0005	.004
$160^\circ$	.002	.0001	.002
$170^\circ$	-	-	-
$180^\circ$	.000	.0000	.000

where

$$I_{2d}(\alpha) = \frac{\int_{-\frac{\pi}{2}}^{\frac{\pi}{2}} F_{2d}(\alpha, \beta) \cdot \cos \beta \cdot d\beta}{\int_{-\frac{\pi}{2}}^{\frac{\pi}{2}} \cos \beta \cdot d\beta}$$

TABLE III

The integrated lunar brightness,  $I_{3d}(\alpha)$  at various phase angles, obtained by integrating  $F_{3d}(\alpha, \beta, \gamma)$  for  $\beta, \gamma$  points on the lunar surface over the projected lunar surface area, and then comparing this analytical result with the modern experimental results of Rougier, 1933

3D INTEGRATED LUNAR BRIGHTNESS,  $I_{3d}(\alpha)$ 

PHASE ANGLE $ \alpha $	EXPERIMENTAL RESULTS ROUGIER $\alpha \leq 0$	ANALYTICAL RESULTS $I_{3d}(\alpha)$	EXPERIMENTAL RESULTS ROUGIER $\alpha \geq 0$
0°	1.0000	1.0000	1.0000
5°	.938	.8921	.920
10°	.787	.7887	.757
15°	.692	.6952	.667
20°	.603	.6109	.586
30°	.466	.4679	.453
40°	.356	.3555	.350
50°	.275	.2682	.273
60°	.211	.2310	.211
70°	.161	.1495	.1556
80°	.120	.1102	.1107
90°	.0824	.0800	.0780
100°	.0560	.0568	.0581
110°	.0377	.0390	.0405
120°	.0249	.0256	.0261
130°	.0151	.0153	.0158
140°	-	.0088	.0093
150°	-	.0042	.0046
160°	-	.0015	-
170°	-	.0002	-
180°	.0000	.0000	.0000

where

$$I_{3d}(\alpha) = \frac{\int_0^{\frac{\pi}{2}} \int_{-\frac{\pi}{2}}^{\frac{\pi}{2}} F_{3d}(\alpha, \beta, \gamma) \cdot \cos \beta \cdot \cos^2 \gamma \, d\beta \, d\gamma}{\int_0^{\frac{\pi}{2}} \int_{-\frac{\pi}{2}}^{\frac{\pi}{2}} \cos \beta \cdot \cos^2 \gamma \cdot d\beta \, d\gamma}$$

NOTE: Advantage has been taken of the symmetry in  $F_{3d}(\alpha, \beta, \gamma)$  about  $\gamma = 0$ , when selecting the integration limits for  $I_{3d}(\alpha)$ .

# BIBLIOGRAPHY

1. Rougier, Gilbert, TOTAL PHOTOELECTRIC PHOTOMETRY OF THE MOON (PHOTOMETRIE PHOTOELECTRIQUE GLOBALE DE LA LUNE), Observatoire de Strasbourg, Annales, Vol. 2, fasc. 3, pp. 205-339, 1933 (in French).
2. Hapke, Bruce W., PHOTOMETRIC & OTHER LABORATORY STUDIES RELATING TO THE LUNAR SURFACE Cornell University, Center for Radiophysics and Space Research. Ithaca, New York, "THE LUNAR SURFACE LAYER" Proceeding of the Lunar Surface Materials Conference, edited by Salisbury J. W. and Glaser, P. E., New York & London, Academic Press, 1964, pp. 323-344.
3. Van Diggelen, J., PHOTOMETRIC PROPERTIES OF LUNAR CRATER FLOORS, Observatoire d'Utrecht, Recherches Astronomiques, Vol. 14, No. 2, pp. 1-114, 1960.
4. Hapke, Bruce W. and Van Horn, Hugh, PHOTOMETRIC STUDIES OF COMPLEX SURFACES, WITH APPLICATIONS TO THE MOON, Cornell University, Center for Radiophysics and Space Research, Ithaca, New York, February 1963, Report No. CRSR 139, NASA Contract Grant NSA-119-61; Journal of Geophysical Research, Vol. 68, No. 15, pp. 4545-4586, 1 August 1963.
5. Minnaert, M., PHOTOMETRY OF THE MOON, Utrecht Observatory, "Planets and Satellites," Chicago and London, University of Chicago Press, 1961, pp. 213-248.
6. Kopal, Zdenek (editor), PHYSICS AND ASTRONOMY OF THE MOON, New York, New York, Academic Press, 1962.
7. Pearse, C. A., PHOTOMETRY AND POLARIMETRY OF THE MOON AND THEIR RELATIONSHIP TO PHYSICAL PROPERTIES OF THE LUNAR SURFACE, Washington, D. C., Bellcom, Inc., 1963.
8. Barabashov, N. P., INDICATRICES OF REFLECTION OF INDIVIDUAL SECTIONS OF THE LUNAR SURFACE, Akademiya Nauk, SSSR, Komissiya po fizike planet, Izvestiya, No. 2, pp. 65-72, 1960; translated in "News of the Commission of Planetary Physics," FTD-TT-62-1514, AD-295 436.
9. Fedorets, V. A., PHOTOGRAPHIC PHOTOMETRY OF THE LUNAR SURFACE, Gorkiy State University, Kharkov Astronomicheskaya Observatoriya, Trudy, Vol. 2, No. 10, pp. 49-172, 1952; (in Russian).
10. Fesenkov, V. G., PHOTOMETRIC PECULIARITIES OF THE MOON (PHOTO-METRICHESKIE OSOBENNOSTI LUNY), Astrophysical Institute, Academy of Sciences, Ka SSR, Soviet Astronomy-AJ, Vol. 4, No. 3, pp. 468-472, November-December 1960; translated from Astronomicheskii Zhurnal, Vol. 37, No. 3, pp. 496-500, May-June 1960.

11. Markov, A. V., POLARIZATION PROPERTIES OF THE LUNAR SURFACE, "The Moon - A Russian View," Chicago and London, University of Chicago Press, 1962, pp. 156-175.
12. Orlova, N. S., PHOTOMETRIC RELIEF OF THE LUNAR SURFACE, Astronomical Observatory, Leningrad State University, *Astronomicheskii Zhurnal*, Vol. 33, No. 1, pp. 93-100, 1956; translated in "Selected Articles on Light Scattering and Photometric Relief of the Lunar Surface," NASA TT-F-75, September 1962, and by K. N. Trirogo and Z. Jakubske in STL-TR-61-5110-13, Space Technology Laboratories, Inc., Los Angeles, California, March 1961, AD-264 169.
13. Sytinskaya, N. N., NEW DATA ON THE METEORIC-SLAG THEORY OF THE FORMATION OF THE OUTER LAYER OF THE LUNAR SURFACE, Main Astronomical Observatory, Academy of Sciences, USSR, *Soviet Astronomy - Astronomy Journal*, Vol. 3, No. 2, pp. 310-314, 1959; translated from *Astronomicheskii Zhurnal*, Vol. 36, No. 2, pp. 315-321, 1959.
14. Sytinskaya, N. N. and Sharonov, V. V., INVESTIGATION OF REFLECTIVITY OF THE LUNAR SURFACE, Leningrad State University, *Astronomicheskaya Observatoriya, Trudy*, Vol. 16, pp. 114-154, 1952, (in Russian).
15. Snyder, E. F., Parametric thermal studies of Saturn IB and Payloads. Fourth Informal Progress Report. Internal Document of Chrysler Corporation Space Division Huntsville Operation Research Section 4/15/64.
16. Herrington, A. G., Washburn, H. W. and Willingham, D. E. Jet Propulsion Laboratory Report No. 32-384 (Rev.) California Institute of Technology 1963.
17. Bullrich, K. *Berichts Deutsch Wetterd U. S. Zone* No. 4, 1948.
18. Rougier, G. *Annales de l'Observatoire de Strasbourg* Vol. 2 pp. 319, 1933.
19. Blagg, M. A. and Muller, K. *Named Lunar Formations*, I.A.U. London 1935.
20. Bennett, A. L. A Photo-visual Investigation of the Brightness of 59 Areas on the Moon, *Astrophysical Journal* Vol. 88 No. 1 pp. 1-26 July 1938.
21. Markov, A. *Bull. Abastumani*, No. 11, 107, 1950.

For a more extensive bibliography in this general area we highly recommend Shenk, C. F., Eckstein, H. P., and McNutt, N. P., *Lunar Thermophysics (Bibliography)*, Redstone Scientific Information Center, RSIC-419, June 1965.

# ANALYSIS AND CORRELATION OF THERMODYNAMIC CYCLES FOR SPACE APPLICATIONS

By

D. M. Adams  
Thiokol Chemical Corporation

## ABSTRACT

N67-24273

Quantitative prediction and correlation of performance factors, thermal efficiencies, and optimum cycle design requirements for any thermodynamic cycle or any individual process in the cycle was possible by the introduction of the concept of maximum cycle irreversibility and the utilization of the principles of the Second Law of Thermodynamics. Optimization of the thermal efficiency to cycle specific weight ratio was analyzed and example problems were included to illustrate the practical applications of the concepts presented. The study concentrated on the analysis and design requirements of thermodynamic cycles intended for use as power systems in space where power output to specific weight ratio must be optimized.

## NOMENCLATURE

$c_p$	- Specific heat of gas, Btu/lbm $^{\circ}$ R
$h$	- Enthalpy, Btu/lbm
$I_{act}$	- Actual irreversibility of cycle, Btu/lbm
$I_{max}$	- Maximum irreversibility of cycle, Btu/lbm
$m_s$	- Specific weight of cycle equipment,
	$m_t/Q_a$ - lbmhr/Btu
$m_t$	- Total weight of cycle equipment, lbm
$Q_a$	- Total energy transferred to cycle, Btu/hr
$Q_r$	- Total energy rejected from cycle, Btu/hr
$s$	- Entropy, Btu/lbm $^{\circ}$ R
$T_h$	- Heat source temperature, $^{\circ}$ R
$T_l$	- Heat sink temperature, $^{\circ}$ R
$T_o$	- Surrounding temperature, $^{\circ}$ R
$W_{net}$	- Net power output of cycle, Btu/hr

### Greek Letters

$\Delta$	- $\eta/\eta_c$
$(\Delta s_{isol})_n$	- Entropy change of a process in the cycle and the surroundings, Btu/lbm $^{\circ}$ R
$\eta$	- Thermal efficiency of cycle
$\eta_c$	- Thermal efficiency of a Carnot cycle

## INTRODUCTION

With the advent of large space boosters and vehicles, large orbiting space platforms or manned installations on other bodies such as the moon or Mars are feasible but require large output, light weight, and efficient internal power systems. To satisfy these requirements, thermodynamic cycles such as the Rankine cycle may be employed.

One of the most important performance parameters considered in the design of cycles for space applications is the ratio of the power output of the cycle,  $W_{net}$ , to the total equipment weight,  $m_t$ . The power output is related to the thermal efficiency of the cycle by

$$\eta = \frac{W_{net}}{Q_a}$$

where  $Q_a$  is the total energy transferred to the cycle. The ratio  $W_{net}/m_t$  reduces to  $\eta/m_s$  where  $m_s = m_t/Q_a$ , the specific equipment weight. The ultimate selection of the type and design of the cycle depends on the following criteria:

1. Analysis and understanding of the performance of the complete cycle and individual cycle processes and the relationship to the thermal efficiency of the cycle.
2. Design requirements for the complete cycle and individual processes such that the thermal efficiency to specific weight ratio may be optimized.
3. Correlation of performance and efficiency characteristics corresponding to various types of cycles.

Thermodynamic cycle analyses have almost entirely been based on concepts of the First Law of Thermodynamics and, as a result, the above criteria cannot be satisfactorily evaluated. This study presents a unique approach that relates, on the basis of the Second Law of Thermodynamics, efficiency and irreversibility quantitatively for any type of cycle (or process) from which significant understanding of the above criteria may be determined. The concept of maximum cycle irreversibility,  $I_{max}$ , is introduced and shown to occur when the ideal intended energy conversion does not take place (heat converted to work) and/or all internal and external irreversibilities are maximized.

## ANALYSIS

Consider a closed thermodynamic system operating in a cycle between a constant high temperature heat source at  $T_h$  and a constant low temperature heat sink at  $T_l$ . The temperature-entropy diagram,  $T - s$ , is shown on Figure 1, where

$n$  = number of processes in the cycle,

$dQ_a$  = differential quantity of energy transferred to each process in system (cycle) from heat source at  $T_h$ ,

$dQ_r$  = differential quantity of energy rejected from each process in system to heat sink at  $T_l$ ,

$W_{net}$  = net power output of cycle, and

$T_o$  = surrounding temperature (not necessarily equal to  $T_l$ ).

The Inequality of Clausius shows that

$$\oint \frac{dQ}{T} \leq 0,$$

$$\sum_{n=1}^n \left( \int \frac{dQ}{T} \right)_n \leq 0,$$

and

$$\sum_{n=1}^n \left( \frac{Q_a}{T_h} + \frac{Q_r}{T_l} \right)_n \leq 0$$

for a reversible or irreversible cycle of  $n$  processes operating between constant temperature reservoirs (Ref 1). When the total energy transferred in the processes,  $Q_a$  and  $Q_r$ , is referred to the heat source and heat sink, the above equation becomes

$$\sum_{n=1}^n \left( \frac{Q_a}{T_h} + \frac{Q_r}{T_l} \right)_n \geq 0 \tag{1}$$

where the summation is equal to zero for reversible cycles and greater than zero for irreversible cycles. Irreversibilities associated with the cycle may be classified in nature as:



1. External to System: energy transfer between the system and surrounding across a finite temperature difference and frictional shear work crossing system boundaries.
2. Internal to System: molecular friction, sudden expansion, diffusion, combustion, nuclear reactions, and hysteresis effects.

A reversible cycle must be internally and externally reversible.

The Principle of Increase of Entropy (Ref 2) yields

$$\begin{aligned}\Delta s_{\text{isol}} &= \Delta s_{\text{system}} + \Delta s_{\text{surroundings}} \\ &= \Delta s_{\text{system}} + \Delta s_{\text{source}} + \Delta s_{\text{sink}} \geq 0\end{aligned}$$

where  $\Delta s_{\text{isol}}$  = the increase of entropy when the system (cycle) and surroundings (external heat source and heat sink) are considered as an isolated system,

$$\Delta s_{\text{system}} = \sum_{n=1}^n (\Delta s_n) = \text{the summation of entropy changes for each process in the cycle} = 0,$$

$$\Delta s_{\text{source}} = \sum_{n=1}^n \left( \frac{Q_a}{T_h} \right)_n = \text{entropy change of external source, and}$$

$$\Delta s_{\text{sink}} = \sum_{n=1}^n \left( \frac{Q_r}{T_l} \right)_n = \text{entropy change of external sink.}$$

The irreversibility of the cycle,  $I_{\text{act}}$ , may be given as (Ref 2):

$$\begin{aligned}I_{\text{act}} &= T_o \Delta s_{\text{isol}} \\ \text{Then, } I_{\text{act}} &= T_l \left( \cancel{\Delta s_{\text{system}}}^o + \Delta s_{\text{source}} + \Delta s_{\text{sink}} \right), \quad (2) \\ &= T_l \sum_{n=1}^n \left( \Delta s_n + \frac{Q_a}{T_h} + \frac{Q_r}{T_l} \right)_n \geq 0,\end{aligned}$$

and

$$I_{act} = T_1 \sum_{n=1}^n \left( \frac{Q_a}{T_h} + \frac{Q_r}{T_1} \right) \geq 0. \quad (3)$$

Thus, the cycle irreversibility,  $I_{act}$ , is the product of the heat sink temperature  $T_1$  and the Inequality of Clausius (Equation 1). If the interaction of each individual process in the cycle with the surrounding is considered separately, then Equation (2) becomes

$$I_{act} = T_1 \sum_{n=1}^n \left( \Delta s_{isol} \right)_n = T_1 \sum_{n=1}^n \left( \Delta s_{source} + \Delta s_{sink} \right)_n \quad (4)$$

where  $(\Delta s_{isol})_n = \Delta s_n + \Delta s_{surrounding}$

= net increase of entropy of each individual process.

The maximum irreversibility,  $I_{max}$ , of the cycle occurs when

1. The ideal intended energy conversion does not take place, and/or
2. All internal and external irreversibilities are maximized.

Consequently, cycle irreversibilities are so large that no energy transferred to the system is converted to work and the heat transferred to the cycle

$$\sum_{n=1}^n Q_a$$

is rejected to the heat sink across the largest temperature difference,  $T_h - T_1$ . From the First Law of Thermodynamics,

$$W_{net} = \sum_{n=1}^n Q_a + \sum_{n=1}^n Q_r = 0 \quad (5)$$

and Equation (3) becomes

$$I_{max} = T_1 \sum_{n=1}^n \left( \frac{Q_a}{T_h} \right)_n \left( 1 - \frac{T_h}{T_1} \right)$$

and 
$$I_{\max} = -T_1 \Delta s_{\text{source}} \left( \frac{T_h - T_1}{T_1} \right). \quad (6)$$

The thermal efficiency,  $\eta$ , of the closed cycle may be defined as

$$\eta = \frac{W_{\text{net}}}{\sum_{n=1}^n Q_a} = \frac{\sum_{n=1}^n Q_a + \sum_{n=1}^n Q_r}{\sum_{n=1}^n Q_a} = 1 + \frac{\sum_{n=1}^n Q_r}{\sum_{n=1}^n Q_a}. \quad (7)$$

The thermal efficiency,  $\eta_c$ , of a reversible cycle (Carnot cycle, for example) operating between the same reservoir temperatures,  $T_h$  and  $T_1$ , is given as

$$\eta_c = 1 - \frac{T_1}{T_h}. \quad (8)$$

Combining Equations (7) and (8) and defining  $\alpha = \eta/\eta_c$  yields

$$\alpha = \frac{\eta}{\eta_c} = \frac{1}{\eta_c} \left( 1 + \frac{\sum_{n=1}^n Q_r}{\sum_{n=1}^n Q_a} \right). \quad (0 \leq \alpha \leq 1.0)$$

Adding  $\eta_c$  and subtracting  $(1 - T_1/T_h)$  gives

$$\alpha = \frac{1}{\eta_c} \left( 1 + \frac{\sum_{n=1}^n Q_r}{\sum_{n=1}^n Q_a} + \eta_c + \frac{T_1}{T_h} - 1 \right),$$

$$\begin{aligned}
&= \frac{1}{\eta_c} \left[ \eta_c + \frac{T_1}{T_h} \left( \frac{\sum_{n=1}^n \frac{Q_a}{T_h} + \sum_{n=1}^n \frac{Q_r}{T_1}}{\sum_{n=1}^n \frac{Q_a}{T_h}} \right) \right], \\
&\text{and} \quad = 1 + \frac{\sum_{n=1}^n \left( \frac{Q_a}{T_h} + \frac{Q_r}{T_1} \right)}{\left( \frac{T_h - T_1}{T_1} \right) \sum_{n=1}^n \left( \frac{Q_a}{T_h} \right)}. \quad (9)
\end{aligned}$$

Combining Equations (9), (6), (3), and (4) gives

$$\alpha = 1 + \frac{\sum_{n=1}^n (\Delta s_{\text{isol}})_n}{\left( \frac{T_h - T_1}{T_1} \right) \Delta s_{\text{source}}} \quad (10)$$

$$\text{or} \quad \alpha = 1 - \frac{I_{\text{act}}}{I_{\text{max}}}. \quad (11)$$

Thus, Equations (10) and (11) relate the irreversibility of each individual process in the cycle to the maximum cycle irreversibility, and to the ratio of the cycle thermal efficiency to that of a reversible engine operating between the same reservoir temperatures,  $T_h$  and  $T_1$ . The magnitude and significance of the losses in efficiency corresponding to each individual process in the cycle may be evaluated or the over-all loss in efficiency may be determined directly from combining Equations (4) and (10) to give

$$\alpha = 1 + \frac{\sum_{n=1}^n (\Delta s_{\text{source}} + \Delta s_{\text{sink}})_n}{\left( \frac{T_h - T_1}{T_1} \right) \Delta s_{\text{source}}}$$

$$\text{or} \quad \alpha = 1 + \left( \frac{T_1}{T_h - T_1} \right) \left( 1 + \frac{\Delta s_{\text{sink}}}{\Delta s_{\text{source}}} \right). \quad (12)$$

Figure 2 shows a plot of Equation (10). Calculations of  $\alpha$  and  $I_{\text{act}}/I_{\text{max}}$  for all thermodynamic cycles must lie on the same straight line.

## DISCUSSION

It was assumed that the temperature of the heat source and heat sink processes,  $T_h$  and  $T_1$ , were constant but, in general, they may vary as shown on Figure 1 (dotted processes). Under these conditions, Equations (10), (11), and (12) refer to constant temperature source and sink processes corresponding to the maximum and minimum temperatures of the cycle,  $T_h$  and  $T_1$ . The number of processes in the cycle must include the variable temperature source and sink processes in

$$\sum_{n=1}^n (\Delta s_{\text{isol}})_n.$$

Although the irreversibilities between the source processes and sink processes do not actually occur, they are inherent in the system and represent a loss in efficiency which cannot be prevented unless the reservoir processes occur at constant temperature. For example, suppose the thermodynamic cycle shown on Figure 1 operates completely reversibly between the variable temperature heat source and sink processes. The thermal efficiency of the cycle,  $\eta$ , cannot equal that of the Carnot cycle; i. e.,  $\alpha < 1$ , due to the inherent irreversibilities between the heat source processes with constant and variable temperatures and between the heat sinks processes with constant and variable temperatures. This concept is demonstrated in an example given later.

In the design of any thermodynamic cycle, the total irreversibility of the cycle must be reduced to increase the thermal efficiency ratio,  $\alpha$ , as seen from Equations (10) and (11); i. e., the irreversibilities of one or more of the processes must be reduced. If the irreversibility in a process is generated by heat transfer across finite temperature differences, larger surface areas can be used to reduce the temperature differences required to transfer the same amount of energy. However, internal irreversibilities may increase as a result of increased surface friction effects. An optimum point usually occurs where the total irreversibility (external + internal) is minimized.

However, reduction in cycle irreversibility to increase the thermal efficiency,  $\eta$ , may be associated with an increase in equipment specific

weight,  $m_s$  (ratio of equipment weight to total energy transferred to cycle), which is undesirable for space applications. Process redesign to reduce irreversibilities may not appreciably affect the weight of the equipment such as in the redesign of flow passageways to reduce separation losses, turbulence, and frictional effects or in the redesign of combustion chambers to promote better combustion efficiency. The ultimate design criterion is the ratio of thermal efficiency to specific weight,  $\eta/m_s$ , which was shown earlier to be equal to the ratio of the power output of the cycle to total cycle equipment weight,  $W_{\text{net}}/m_t$ .

Although it is not the purpose of this study to present design data for  $\eta/m_s$ , the method of design to optimize  $\eta/m_s$  for the cycle may be generalized. Figure 3 shows the qualitative effect of reducing the irreversibility  $[T_1 (\Delta s_{\text{isol}})_n / I_{\text{max}}]$  of a heat exchange process on the specific weight of the heat exchanger,  $(m_s)_n$ . The corresponding increase in the thermal efficiency,  $\eta$ , evaluated from Equation (10), is included. The maximum in  $\eta/(m_s)_n$ , if one exists, indicates the optimum heat exchanger design. A similar analysis for all processes in the cycle can be conducted to yield a maximum  $\eta/m_s$  for the cycle.

From Figure 3, it can be seen that

$$\frac{d \left( \frac{\eta}{m_s} \right)}{d \left( \frac{T_1 \sum_{n=1} (\Delta s_{\text{isol}})_n}{I_{\text{max}}} \right)} = 0$$

to give a maximum for the entire cycle. Substituting  $\alpha = \eta/\eta_c$  in Equation (11) and dividing by  $m_s$  yields

$$\frac{\eta}{m_s} = \frac{\eta_c}{m_s} \left( 1 - \frac{I_{\text{act}}}{I_{\text{max}}} \right) = f \left( \frac{I_{\text{act}}}{I_{\text{max}}}, m_s, \eta_c \right)$$

where

$$m_s = g \left( \frac{I_{\text{act}}}{I_{\text{max}}} \right).$$

Assuming  $T_h$  and  $T_l$  constant gives  $\eta_c = \text{constant}$ , and letting  $x = I_{\text{act}}/I_{\text{max}}$ , the above equation becomes

$$\frac{\eta}{m_s} = \frac{\eta_c (1 - x)}{g(x)}$$

and 
$$\frac{d^2 (\eta/m_s)}{dx} = \eta_c \frac{[-g(x) - (1-x) g'(x)]}{g(x)^2} = 0$$

which gives a maximum when  $x$  satisfies

$$g(x) = -(1-x) g'(x)$$

or 
$$\frac{[g'(x)]}{g(x)} = -\frac{1}{1-x}.$$

Since  $x = \frac{I_{act}}{I_{max}} = \frac{T_1 \sum_{n=1}^n (\Delta s_{isol})_n}{I_{max}}$ ; the above equation yields

$$\frac{g'\left(\frac{T_1 \sum_{n=1}^n (\Delta s_{isol})_n}{I_{max}}\right)}{g\left(\frac{T_1 \sum_{n=1}^n (\Delta s_{isol})_n}{I_{max}}\right)} = -\frac{1}{\left(1 - \frac{I_{act}}{I_{max}}\right)} = -\frac{\eta_c}{\eta} \quad (13)$$

and the maximum  $\eta/m_s$  results when the individual processes are re-designed such that the function

$$g\left(\frac{T_1 \sum_{n=1}^n (\Delta s_{isol})_n}{I_{max}}\right)$$

satisfies Equation (13), if possible. Of course, the function must necessarily be obtained analytically or experimentally for each process in the cycle.

The same analysis may be conducted for various types of cycles and the ultimate selection of the type of cycle for space applications necessarily dictates that  $\eta/m_s$  be a maximum.

## EXAMPLE PROBLEMS

To illustrate the practical usage of the above concepts and to get a better understanding of their significance towards cycle analysis and design, the following example problems were considered:

A. Rankine cycle steam power system installed in an orbiting space platform. Figure 4a shows a schematic diagram of the power system and Figure 4b depicts the corresponding temperature-entropy,  $T - s$ , diagram. Gases, heated within the nuclear reactor (external heat source), are cycled through the boiler and transfer energy to the boiler. Thereafter, the gases pass through the superheater, reheater, and economizer before returning to the reactor. To improve the thermal efficiency, a superheater, reheater, economizer, and two extraction feedwater heaters were included in the basic Rankine cycle. The energy rejected in the cycle is accomplished by the use of a radiative type condenser where the earth is considered as the external heat sink. Refer to Table I for system data and values of enthalpy and entropy at each point in the cycle. Entropy changes for the constant pressure gas process were calculated from

$$s_e - s_i = \frac{m_g}{m_b} c_p \ln \frac{T_e}{T_i}$$

Neglecting kinetic energies, the temperature changes of the gases were determined from

$$(T_e - T_i) = \frac{Q_{rn} m_b}{c_p m_g}$$

where  $Q_{rn}$  is the energy transferred from the gases to each respective process in the cycle.

The losses in thermal efficiency of the cycle resulting from irreversibilities generated in each process of the cycle were evaluated from Equation (10)

$$\alpha = 1 - \frac{\sum_{n=1}^{12} (I_{act})_n}{I_{max}} = 1 - \frac{T_1 \sum_{n=1}^{12} (\Delta s_{isol})_n}{I_{max}}$$

and are given in Table II. It is noted that  $\alpha = \eta/\eta_c = 46.25\%$ ; i. e., the losses in efficiency amounted to 53.75% for the 12 processes in the cycle. The most significant losses result in the following processes:



1. Boiler process--13.14% loss primarily due to external heat transfer across a finite temperature difference.
2. Condenser process--4.61% loss resulting from irreversible radiation energy exchange with the heat sink (earth). Generally, this loss will be larger for applications in areas of space void of mass where the effective heat sink temperature approaches absolute zero; i. e.,  $T_1 = T_0 = 0^{\circ}\text{R}$ .
3. Superheater process--8.06% loss due to external heat transfer irreversibilities.
4. Gas-nuclear reactor process--external heat transfer irreversibilities yield 8.54% losses.
5. Turbine c process--8.23% losses resulting from internal frictional irreversibilities produced because of inefficient turbine design (turbine blade design, for example).
6. Low pressure feedwater extraction process--4.98% loss resulting from external heat transfer irreversibilities.

Other losses were individually small. Cycle redesign criteria may be determined by knowing the types of irreversibilities produced and how to eliminate them. Optimization of  $\eta/m_s$  may be ascertained from methods given previously. It is important to note that redesign of individual processes may affect the performance of other processes in the cycle. Thus, optimization of each process in the cycle must be interrelated to each other to insure optimum performance of the complete cycle.

To determine the maximum value of  $\alpha$  for the cycle, it was assumed that the Rankine cycle operates completely reversibly between the variable temperature heat source process,  $T_h \rightarrow T_{ec}$ , and constant temperature heat sink process,  $T_1$ . From Table II,

$$\begin{aligned}
 \alpha_{\max} &= 100 - \frac{I_{\text{act}} \text{ (minimum)}}{I_{\max}} \\
 &= \left( 100 - \frac{I_{\text{act}}_{n=1} + \sum_{n=2}^{12} (I_{\text{act}})_{n=2}^{\circ}}{I_{\max}} \right) \% \\
 &= (100 - 8.54)\% = 91.46\%
 \end{aligned}$$

which yields a loss of 8.54% due to external irreversibilities in the gas-nuclear reactor process. In addition, suppose that the nuclear reactor was eliminated and that gases at temperature  $T_h$  were continually supplied to the heat source process,  $T_h \rightarrow T_{ec}$ , from some gas supply (combustion process, for example). Calculations showed that the loss in efficiency was 8.54%, the same as with a constant temperature heat source at  $T_h$ . Thus, inherent irreversibilities result from the use of variable temperature heat sources (and sinks). The equivalent heat source temperature is considered constant at  $T_h$  and the gas heating process,  $R_i \rightarrow R_o$ , does not actually occur but must be effectively considered as the reverse of process  $T_h \rightarrow T_{ec}$  and included as an additional process in the cycle (identical to conditions in example above).

Although the Rankine cycle shown on Figure 4a is typical of modern power systems on earth, some of the components tending to reduce  $\eta/m_s$  (feedwater heaters, economizer) resulting from excessive equipment weight must be eliminated for use of the cycle in space applications.

B. Thermodynamic cycles involving combustion processes have commonly been approximated by the air-standard cycle (Ref 2). An example of this is the Otto cycle shown on Figure 5 where the combustion process is replaced by energy transferred to the system from a heat source at  $T_h$  and the cycle is considered closed (no change in composition). The temperature and volume limits correspond to maximum power conditions of modern internal combustion engines (410 hp). Assuming the cycle to be internally reversible, an analysis similar to above yielded  $\alpha = \eta/\eta_c = 0.673$ . To account for deviations from air-standard approximations and irreversibilities such as heat transferred to the surroundings,  $Q_r$ , in processes (1  $\rightarrow$  2), (2  $\rightarrow$  3), and (3  $\rightarrow$  4), internal frictional irreversibilities, and external friction in bearings and reciprocating components ( $W_{friction} = Q_{r4}$ , energy dissipated to the surroundings), the actual  $W_{net}$  output of the cycle is given by.

$$W_{net} \text{ (actual)} = e_b W_{net} \text{ (ideal)}$$

where  $e_b \cong 0.65$  = Mechanical efficiency of a well-constructed engine.

Thus, the actual value of  $\alpha$  is

$$\alpha = \alpha e_b = 0.438.$$

To include these effects in Equation (10),

$$\alpha = \frac{\eta}{\eta_c} = 1 - \left( \frac{T_1 \sum_{n=1}^4 (\Delta s_{isol})_n + \frac{\eta Q_a (1 - e_b)}{T_1}}{I_{max}} \right)$$

where processes  $n = 1$  to  $n = 4$  may consider the actual internally and externally irreversible processes occurring in the cycle ( $\alpha < 0.673$ ). In this case,  $e_p$  includes only external frictional irreversibilities.

From Figure 3, it is seen that  $\alpha = 0.438$  is less than  $\alpha = 0.4625$  for the Rankine cycle. However, the thermal efficiency to specific weight ratio,  $\eta/m_s = \alpha \eta_c/m_s$ , is higher for the Otto cycle.

Applications of the above concepts may be extended to processes since cycles are merely specialized processes. Detailed analyses for processes and other cycles such as gas-particle processes in rocket nozzles and combustion driven Brayton cycles have been conducted, respectively.

It was shown that the relation  $\alpha = f(1 - I_{act}/I_{max})$  can be used for any process ( $\alpha$  redefined for processes), including thermodynamic refrigeration cycles. For the latter,

$$\alpha = \frac{\beta}{\beta_c} = \frac{1}{\sum_{n=1}^n (\Delta s_{isol})_n} = \frac{1}{\left(1 - \frac{I_{act}}{I_{max}}\right)} \cdot \frac{1}{1 - \left(\frac{T_h}{T_h - T_l}\right) \frac{\Delta s_{source}}{\Delta s_{source}}}$$

where  $\beta = Q_a/W_{net}$  = coefficient of performance and  $I_{max} = -(T_l/T_h) I_{max}$ .

Concepts of availability of energy were interrelated with the analysis given herein. The applications and results will be presented in later studies.

Ackeret (Ref 3) presented a historical background of entropy and other examples of the role of entropy in the aerospace sciences.

## CONCLUSIONS

Significant conclusions of the analysis were:

1. The concept of maximum cycle irreversibility interrelated with the actual irreversibility of the cycle, reflected in Equations (10) and (11), successfully determine cycle performance and thermal efficiency design criteria quantitatively for any thermodynamic cycle.
2. The performance and efficiency/specific weight of any thermodynamic cycle may be quantitatively determined, compared, and correlated. Graphical representation of Equation (10) is

shown on Figure 2 which relates efficiency and irreversibility of all cycles. Results (Table II) for the Rankine cycle shown on Figure 4a, and those corresponding to an air-standard Otto cycle (Figure 5) are included.

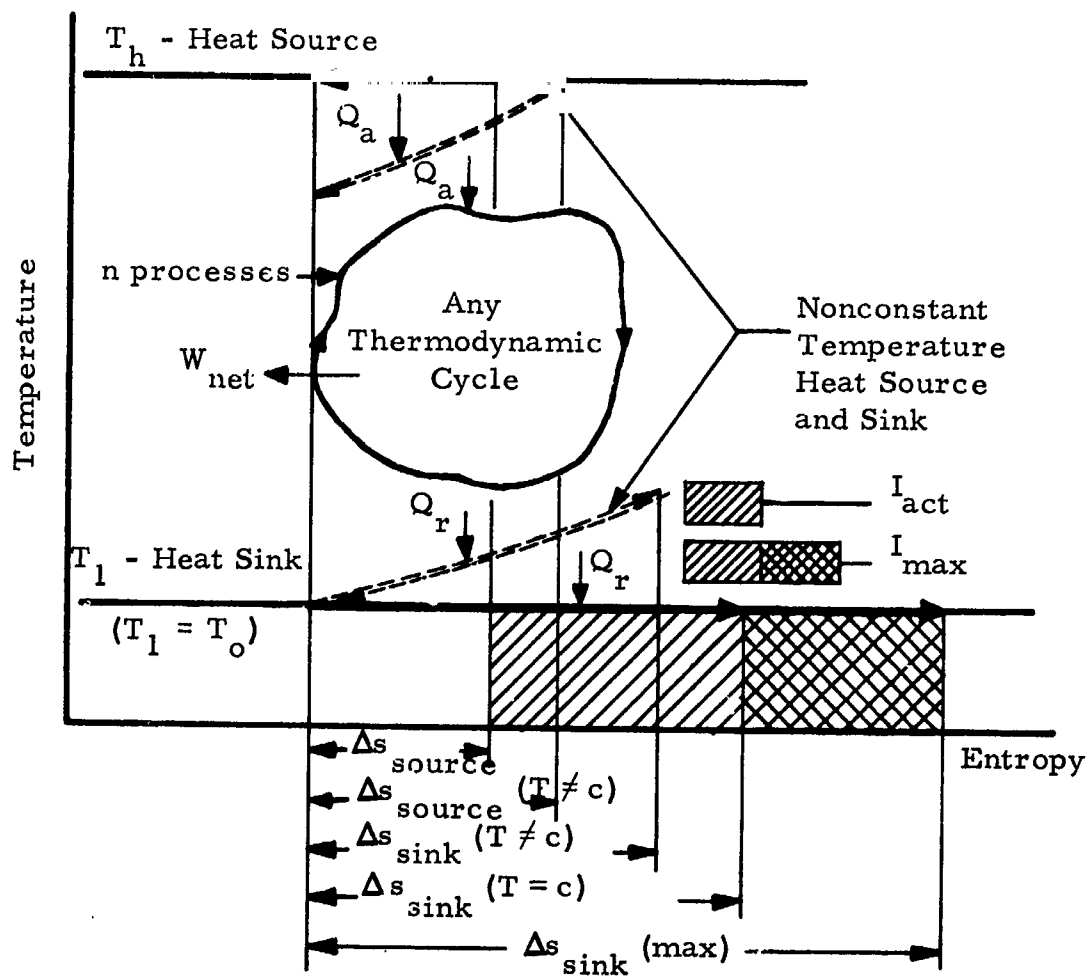


Figure 1. Temperature-Entropy Diagram

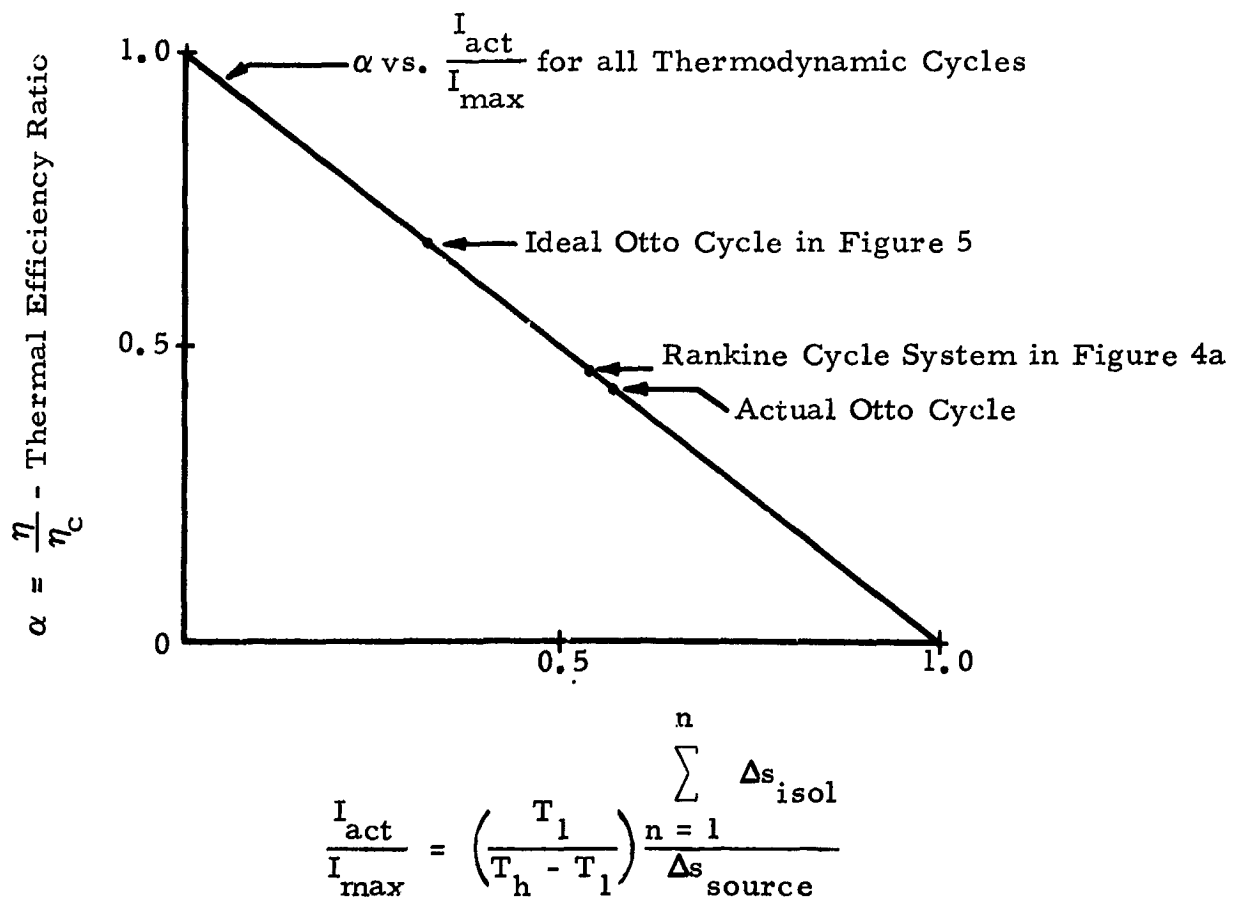


Figure 2. Efficiency-Irreversibility Correlation for Thermodynamic Cycles

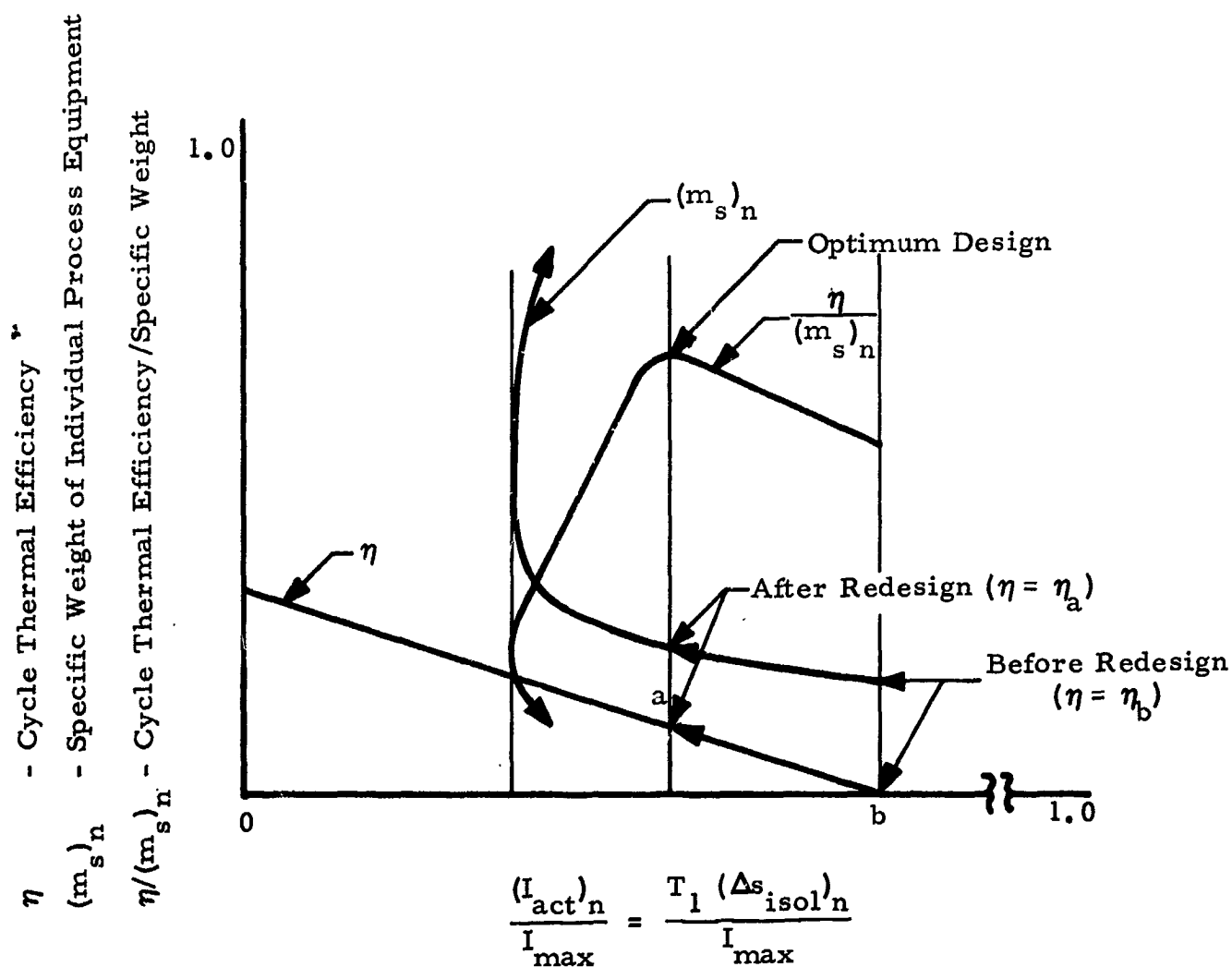


Figure 3. Irreversibility, Efficiency, and Specific Weight Characteristics of a Heat Exchanger Utilized in a Thermodynamic Cycle

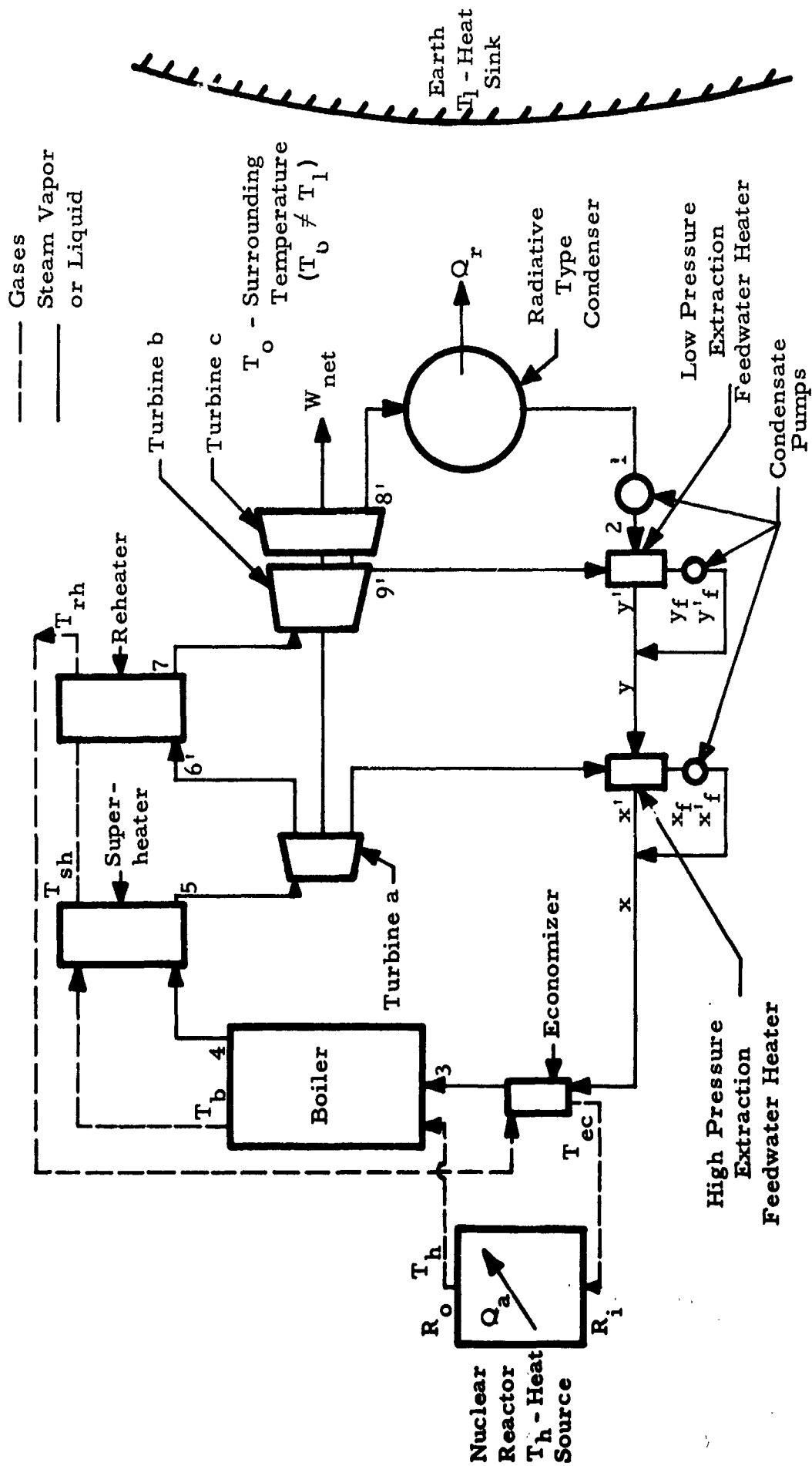


Figure 4a. Rankine Cycle Power System



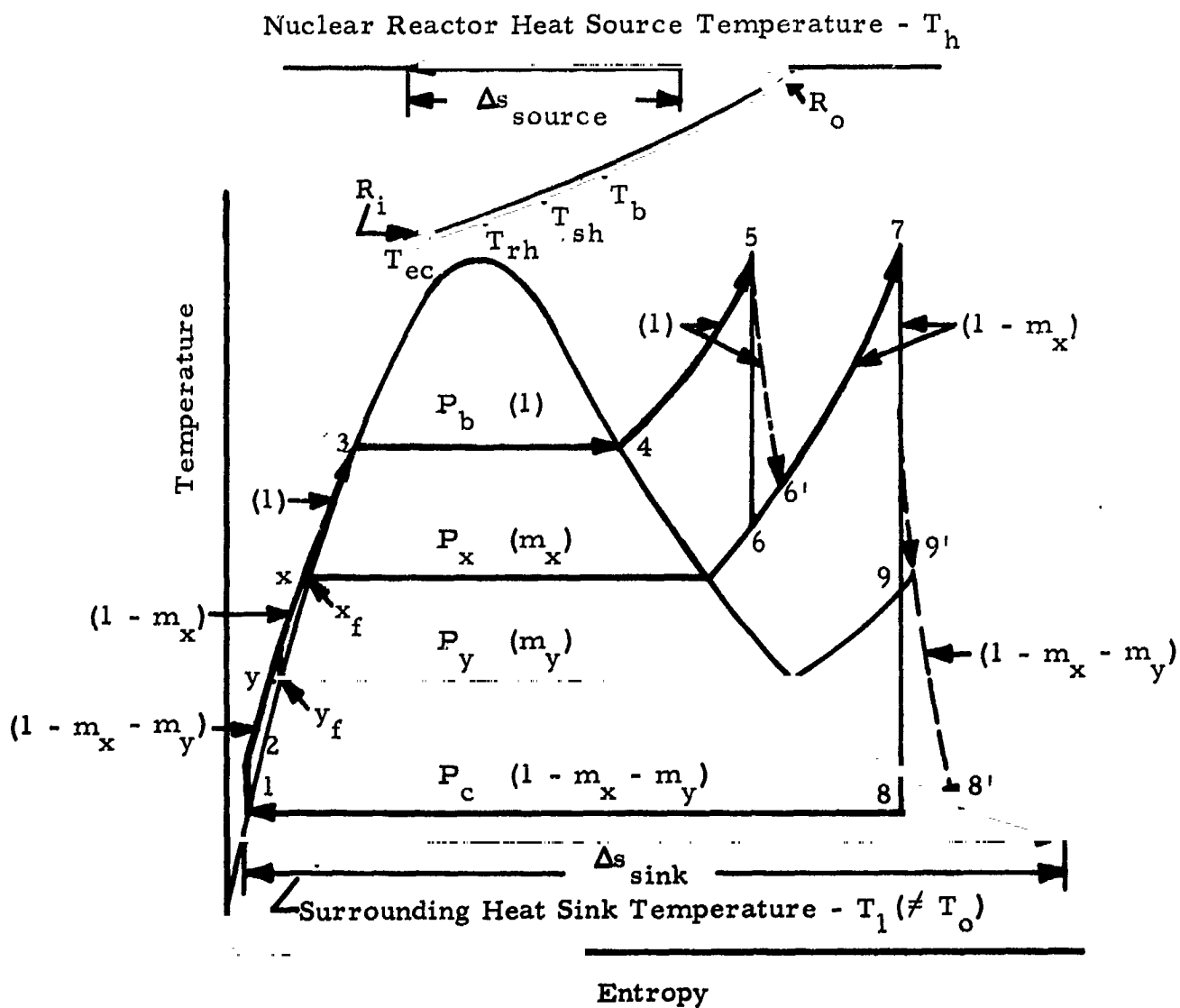


Figure 4b. Temperature Entropy Diagram of Rankine Cycle Power System

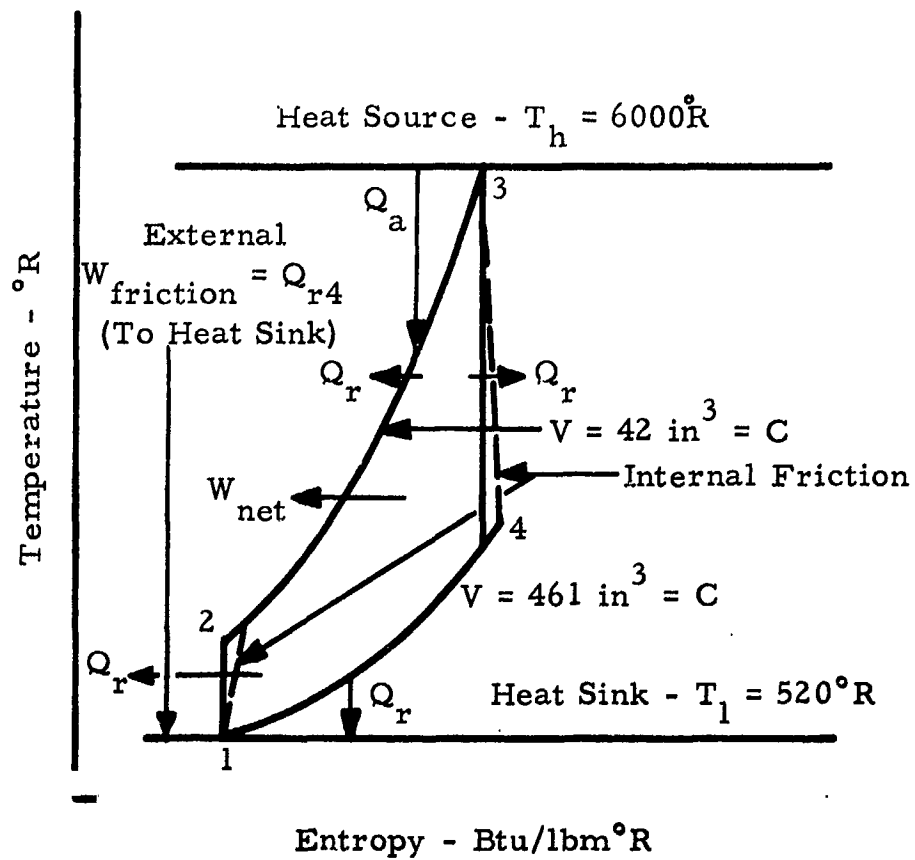


Figure 5. Temperature Entropy Diagram for Air-Standard Otto Cycle

TABLE I  
RANKINE CYCLE POWER SYSTEM PROPERTIES

DATA

$P_b$	- Boiler Pressure = 2400 psia
$P_c$	- Condenser Pressure = 2 in. hg. abs.
$P_{rh}$	- Reheater Pressure = 1200 psia
$P_x$	- Feedwater Extraction Pressure = 1200 psia
$P_y$	- Feedwater Extraction Pressure = 600 psia
$T_h$	- Temperature of Nuclear Reactor Heat Source = 3310°R
$T_1$	- Temperature of Heat Sink (earth) = 520°R
$T_5$	- Exit Superheater Temperature = 1460°R
$T_7$	- Exit Reheater Temperature = 1460°R
$e_i$	- Internal Efficiencies of Turbines a, b, and c = 0.8
$c_p$	- Specific Heat of Gases = 0.27 Btu/lbm°F
$m_g/m_b$	- lbm of Gas per lbm of Steam Generated in Boiler = 2.0
$m_x$	- Mass of Steam Extracted at $P_x$ = 0.107 lbm/lbm (boiler)
$m_y$	- Mass of Steam Extracted at $P_y$ = 0.263 lbm/lbm (boiler)

Condensate pump processes assumed reversible. All results are referred to 1.0 lbm<sub>b</sub> of steam generated in boiler. Interconnecting line losses were neglected.

TABLE I  
(CONTINUED)

<u>State Point</u>	<u>h-Enthalpy Btu/lb</u>	<u>s-Entropy Btu/lbm<sup>°</sup>R</u>
1	69.1	0.1316
2	76.27	0.1316
y' ( $y \cong y'$ )	472.0	0.666
y <sub>f</sub>	471.6	0.672
x' ( $x \cong x'$ )	570.0	0.765
x <sub>f</sub>	571.7	0.7711
3	718.4	0.9023
4	1101.1	1.2434
5	1461.7	1.5335
6	1371.0	1.5335
6'	1389.2	1.5485
7	1499.2	1.6293
8	909.1	1.6293
8'	1027.2	1.8556
9	1401.0	1.6293
9'	1420.8	1.646

TABLE II

## CALCULATED RESULTS FOR RANKINE CYCLE POWER SYSTEM

Process in Cycle		$(Q_a \text{ or } Q_r)_n$ Heat Transfer in Process Btu/lbm <sub>b</sub>	$\Delta s_n$ Entropy Change of Process Btu/lbm <sub>b</sub> °R	$\Delta s_{sn}$ Entropy Change of Source or Sink Btu/lbm <sub>b</sub> °R	$(\Delta s_{isol})_n = \Delta s_n + \Delta s_{sn}$ Net Entropy Change of Process Btu/lbm <sub>b</sub> °R	$T_1 (\Delta s_{isol})_n$ I <sub>max</sub> Percent Loss in Efficiency %
1. Gas in Reactor ( $R_1 \rightarrow R_0$ )		990.	.4361	-.299	.1371	8.54
2. Boiler ( $3 \rightarrow 4$ )		382.7	.3411	-.13	.2111	13.14
3. Superheater ( $4 \rightarrow 5$ )		360.6	.2901	-.1608	.1293	8.06
4. Reheater ( $6' \rightarrow 7$ )		98.2	.0722	-.054	.0182	1.13
5. Turbine a ( $5 \rightarrow 6'$ )		0	.0150	0	.0150	0.935
6. Turbine b ( $7 \rightarrow 9'$ )		0	.0149	0	.0149	0.929
7. Turbine c ( $9' \rightarrow 8'$ )		0	.132	0	.132	8.23
8. Condenser ( $8' \rightarrow 1$ )		-604.	-1.088	1.162	.074	4.61
9. Condensate Pumps ( $1 \rightarrow 2, y_f \rightarrow y_f', x_f \rightarrow x_f'$ )		0	0	0	.0	0.0
10. Extraction - P <sub>x</sub> ( $6' \rightarrow x_f'$ )		-87.3	-.083	.0885 ( $y \rightarrow x'$ )	.0054	0.34
11. Extraction - P <sub>y</sub> ( $9' \rightarrow y_f'$ )		-224.	-.256	.3360 ( $2 \rightarrow y'$ )	.080	4.98
12. Economizer ( $x \rightarrow 3$ )		148.4	.1373	-.0913	.046	2.86
$I_{n,act} = -T_1 \left( \frac{T_h - T_1}{T_1} \right) \Delta s_{source}$						
$I_{max} = T_1 (1.605) \text{ Btu/lbm}_b \text{ °R}$						
$\alpha = \left( 100 - \frac{I_{act}}{I_{max}} \right) \%$						
$\eta = \left( 1 - \frac{T_1}{T_h} \right) \alpha$						
$\eta = \left( 1 - \frac{520}{3310} \right) 46.25\% = 38.8\%$						
$\frac{I_{act}}{I_{max}} = \frac{\sum_{n=1}^{12} (I_{act})_n}{I_{max}} = \frac{T_1 \sum_{n=1}^{12} (\Delta s_{isol})_n}{I_{max}} = \frac{53.75\%}{1} = 53.75\%$						

## REFERENCES

1. Fermi, E., Thermodynamics, Dover Publications, Inc., New York, 1936.
2. Van Wylen, G., Thermodynamics, John Wiley & Sons, Inc., New York, 1959.
3. Ackeret, J., "The Role of Entropy in the Aerospace Sciences," J. of Aerospace Sciences, Vol. 28, No. 2, February, 1961.

# MATHEMATICAL ADVANCES IN THE THEORY OF ONE DIMENSIONAL FLOW (

By

Ervin Y. Rodin  
Wyle Laboratories

## SUMMARY

**N67-24274**

This paper contains the derivation of a Burgers' equation, as a definite approximation of high order, from the one dimensional Riemann pair of equations (with a viscous term) which is a description of the motion of waves of finite amplitude. The solution of the Cauchy problem for Burgers' equation is presented, together with a discussion of solutions by means of infinite products.

## INTRODUCTION

The ambitious plans of the free world in space travel are predicated to a large extent on the ability of scientists and engineers to cope with a demand for knowledge that is rising in an exponential manner. The recent great strides in this field are ascribable to two important factors: one, the development of large and accurate thrusters and two, the appropriate miniaturization of much of the component and support equipment. These, in turn, were made possible by basic scientific studies performed earlier in this century.

There is, however, a very practical limitation both to miniaturization and to largeness of rockets. Thus, in order to continue the rapid advance in this field, it is necessary to refine many of the existing techniques or theories. For instance, much of the lifting capacity of a thruster today is used to put into orbit a considerable mass of ignorance - many call it a safety factor - which is necessary; because all calculations used in design and operation are approximations of varying exactness. Thus, approximations of higher order will reduce this dead mass and refine the processes and equipment used.

Basically, this is the subject of the present paper. In the hierarchy of approximations used for describing various phenomena, such as acoustics of waves of finite amplitude, properties of highly conducting gases, etc., exact solutions of the governing equations are available only in highly specialized and idealized cases. One uses these exact solutions as stepping stones, from which solutions of more real problems can be obtained approximately. Thus, the higher in this hierarchy one is able to obtain exact solutions, the better the further approximations are.

One of the more important of these stepping stones is the model equation, proposed in 1940 by J.M. Burgers, whose general solution was obtained in 1950 and 1951 by E. Hopf and J. Cole. This nonlinear partial differential equation, while being a descriptor of phenomena only in one space dimension, still includes an important nonlinear feature and also takes into consideration effects of dissipation and diffusion. The functional form of the equation was shown to be extremely useful in many fields; see the Bibliography.

The only important boundary/initial value problem solved so far in connection with this equation is the one describing the decay of a pattern existing at some initial time. It is of great importance, however, to know the behavior of a system with excitation conditions described at one of the physical boundaries; the solution of this "Cauchy Problem" is one of the subjects of this paper.

The general solution of Burgers' Equation has, usually, the form of the quotient of two infinite series of rather complicated terms. Thus, it is not easily adaptable to a qualitative analysis, and is very cumbersome quantitatively also.

In order to cope with this problem, the second part of this paper obtains some of these solutions in the form of a single infinite series. The approach is through infinite products; a mathematical object which has been used in practice but very little; but one which could have an importance in the solution of nonlinear problems that is comparable to the utility of infinite series in the theory of linear differential equations.



The first section of this paper contains a derivation of Burgers' Equation. It consists essentially of the justification for the reduction of a pair of one dimensioned coupled equations to the one used and comes from the theory of nonlinear acoustics. This is followed by a description of the properties of Burgers' equation and of its solution, which is a prelude necessary for the next section, containing the solution of the Cauchy Problem. Finally, the last section of the paper contains solutions by means of an infinite product approach.

## THE EQUATIONS FROM NONLINEAR ACOUSTICS

One interpretation of the equations

$$(1) \quad v_t + vv_x + \frac{2}{\gamma-1} aa_x = \epsilon v_{xx}$$

$$(2) \quad a_t + a_x v + \frac{\gamma-1}{2} av_x = 0$$

is that they describe the propagation of plane sound waves of finite amplitude in a dissipative fluid (see Lighthill). Here  $v$  is the particle velocity,  $a$  a quantity proportional to the local speed of sound,  $\gamma$  the ratio of specific heats of the medium and  $\epsilon$  is a dissipation constant. The subscripts, as usual, denote partial differentiations with respect to the letter involved. The system (1) - (2) is a classical Riemannian one when  $\epsilon = 0$ ; it is then solvable by means of its characteristics. In its fullness, the pair (1) - (2) has not been solved. We shall now present, however, an argument which reduces (1) - (2) to the simple equation

$$v_t + vv_x = \delta v_{xx} ,$$

where  $\delta$  is also a constant.

The substitution

$$a = a_0 \left( \frac{\rho}{\rho_0} \right)^{\frac{\gamma-1}{2}}$$

reduces (1) - (2) to the system

$$(3) \quad v_t + vv_x + k^2 \rho^{\gamma-2} \rho_x = \epsilon v_{xx}$$

$$(4) \quad \rho_t + (\rho v)_x = 0$$

where

$$k^2 = a_0^2 \rho_0^{1-\gamma}$$

is a non-negative quantity.

Let us introduce a stream function  $\phi$ , defined by

$$(5) \quad \rho = \phi_x , \quad v = -\phi_t / \phi_x .$$

Then equation (4) is satisfied identically by  $\phi$ ; there remains to satisfy (3).

To this end, we shall assume that  $\phi$  satisfies the equation

$$(6) \quad \phi_t = c_1 \phi_{xx}$$

for some  $c_1 > 0$ . This, of course, also means that  $\rho$  satisfies the same equation:

$$(7) \quad \rho_t - c_1 \rho_{xx} = \phi_{xt} - c_1 \phi_{xxx} = 0$$

In fact, we can write for  $v$ , from (5), (6), and (7):

$$(8) \quad v = -\frac{\phi_t}{\phi_x} = -c_1 \frac{\phi_{xx}}{\phi_x} = -c_1 \frac{\rho_x}{\rho}$$

Let us use this value of  $v$  in (3); the substitution and subsequent simplifications follow:

$$-c_1 \frac{\rho \rho_{xt} - \rho_x \rho_t}{\rho^2} + c_1^2 \frac{\rho_x}{\rho} \frac{\rho \rho_{xx} - \rho_x^2}{\rho^2} + k^2 \rho^{\gamma-2} \rho_x = -\epsilon c_1 \frac{\rho^2 \rho_{xxx} - 3 \rho \rho_x \rho_{xx} + 2 \rho_x^3}{\rho^3}$$

$$\rho^2 \rho_{xt} - \rho \rho_x \rho_t - c_1 \left( \rho \rho_x \rho_{xx} - \rho_x^3 \right) - \frac{k^2}{c_1} \rho^{\gamma+1} \rho_x = \epsilon \left( \rho^2 \rho_{xxx} - 3 \rho \rho_x \rho_{xx} + 2 \rho_x^3 \right)$$

$$\rho^2 \left( \rho_{xt} - \epsilon \rho_{xxx} \right) - \rho \rho_x \left( \rho_t + (c_1 - 3\epsilon) \rho_{xx} \right) + (c_1 - 2\epsilon) \rho_x^3 - \frac{k^2}{c_1} \rho^{\gamma+1} \rho_x = 0$$

$$(9) \quad (c_1 - \epsilon) \rho^2 \rho_{xxx} - (2c_1 - 3\epsilon) \rho \rho_x \rho_{xx} + (c_1 - 2\epsilon) \rho_x^3 = \frac{k^2}{c_1} \rho^{\gamma+1} \rho_x$$

The cases

$$c_1 = \frac{n}{2} \epsilon, \quad n = 0, 1, 2, 3, 4$$

lead to special situations, corresponding to various physical restraining assumptions; we shall not consider them here.

By assumption (6), we have that  $p$  satisfies

$$p_{xt} = c_1 p_{xxx} \quad , \quad c_1 > 0$$

Let us recall that, for increasing values of  $c_1$ , the solutions of the heat equation approach bounded values in a manner which is usually of the exponentially damped type. Furthermore, derivatives  $p_x$  of the solution approach 0 for increasing  $c_1$ .

With this in mind, let us write (9) in the form

$$(10) \quad p^2 p_{xxx} - \frac{2c_1 - 3\epsilon}{c_1 - \epsilon} p p_x p_{xx} + \frac{c_1 - 2\epsilon}{c_1 - \epsilon} p_x^3 = \frac{k^2}{(c_1 - \epsilon)} p^{2+\alpha} p_x$$

and consider the effect of letting  $c_1$  increase. Clearly, since by the preceding argument the numerator of the right hand side of (10) is bounded, it becomes very small for  $c_1$  large; in fact, it is of the order  $o(c_1^\alpha)$ , where  $\alpha < 2$ . Therefore, choosing

$$(11) \quad c_1 = \delta > \left[ 1; \epsilon; k^2 M^{\gamma+1} M_x \right] \quad ,$$

where

$M = \max p$  in some region  $R$

$M_x = \max p_x$  in the same region

we reduce (10) to

$$(12) \quad p^2 p_{xxx} - 2 p p_x p_{xx} + p_x^3 = 0$$

This expression can be integrated; using the letter  $p$  for the upcoming functions (of  $t$ ) of integration, we obtain

$$p p_{xx} - p_x^2 = p p_1(t) \quad ,$$

or

$$(13) \quad p \left( \frac{p_x}{p} \right)_x = p_1(t) \quad .$$

Letting now

$$p = e^u$$

(13) becomes

$$u_x u_{xx} = p_1(t) e^{-u} u_x$$

which can again be integrated:

$$\frac{1}{2} u_x^2 = -p_1(t) e^{-u} + p_2(t)$$

and thus

$$(14) \quad \frac{u_x}{\sqrt{p_2(t) - p_1(t) e^{-u}}} = \sqrt{2}$$

One more integration, and a transformation from  $u$  back to  $p$  gives us

$$(15) \quad p = \frac{p_1(t)}{p_2(t)} \sin^2 \left[ \frac{\sqrt{-p_2(t)}}{2} (\sqrt{2} x + p_3(t)) \right]$$

where we must have  $p_1(t) < 0$  and  $p_2(t) < 0$

This function then is the justification for the assumptions made on  $p$  a priori, for an appropriate choice of the arbitrary functions  $p_i(t)$ . In particular, let us note that  $p$ , as given by (15), is a non-negative function; a fact which will further corroborate the appropriateness of our choice of  $p$  as a solution of the heat equation in later developments.

Our conclusion, however, is the following: if  $p$  satisfies

$$p_{xt} = \delta p_{xxx}$$

with  $\delta$  given by (11), and

$$v = -\delta \frac{p_x}{p}$$

then equation (4) is satisfied identically. Furthermore,  $v$  then satisfies the equation

$$v_t + 2v v_x = \delta v_{xx}$$

(as will be shown in the next section); while the magnitude of the error in using an approximation for equation (3) is

$$E = \left| \frac{v^2}{2} + \frac{k^2}{\gamma-1} \exp \left[ -\frac{\gamma-1}{\delta} \int v \, dx \right] + (\delta - \epsilon) v_x + G(t) \right| ,$$

where  $G$  may be freely chosen. Furthermore, we have shown that  $E$  is negligible for a  $\delta$  chosen large enough, in some region of interest  $R$ .

Our task, then, is to solve the equation

$$v_t + 2v v_x = \delta v_{xx} ;$$

and it will turn out that the most general solution is

$$v = -\delta \frac{\theta_x}{\theta}$$

where  $\theta$  is any (positive) solution of the heat equation.

## BURGERS EQUATION; INITIAL VALUE PROBLEM

The crucial step in the developments of the previous section was the assumption that  $p$  satisfies a third order heat equation. However, in order to make that assumption, it was necessary to know that its consequences will be desirable ones. In this section we are going to show how the heat equation enters the picture independently of any other considerations.

We shall start with Burgers' equation in a slightly more general form:

$$(16) \quad v_t + \beta v v_x = \delta v_{xx}$$

where  $\beta$  and  $\delta$  are constants.

In order to give a measure of physical judgement to this equation, let us multiply it by  $v$  and integrate on the interval  $(x_1, x_2)$ , to obtain

$$(17) \quad \frac{1}{2} \int_{x_1}^{x_2} \frac{\partial}{\partial t} (v^2) dx + \frac{\beta}{3} \left\{ v^3(x_2, t) - v^3(x_1, t) \right\} =$$

$$= \delta \left\{ v(x_2, t) \frac{\partial v}{\partial x}(x_2, t) - v(x_1, t) \frac{\partial v}{\partial x}(x_1, t) - \int_{x_1}^{x_2} \left( \frac{\partial v}{\partial x} \right)^2 dx \right\}$$

Going in order from term to term, we can interpret this equation as one stating that the total rate of change of kinetic energy in the system, plus the net flux of this energy out across the boundaries, exactly balances the rate at which work is done at the boundaries, less the total dissipation present.

We now proceed to find the solution of (16); following, substantially, Cole. First, we return to the stream function of (5), letting  $v = \phi_x$  and integrating (16). If we take the constant of integration as 0, we arrive at

$$(18) \quad \phi_t + \frac{\beta}{2} \phi_x^2 = \delta \phi_{xx}$$

Let us now assume that  $\phi = f(h)$ ; i.e., that  $\phi$  depends on the single function  $h$  (of the variables  $x$  and  $t$ ). Then (18) can be written in the form

$$(19) \quad f' \left( h_t - \delta h_{xx} \right) + h_x^2 \left( \frac{\beta}{2} (f')^2 - \delta f'' \right) = 0$$

If we now assume that  $h$  satisfies the heat equation,

$$h_t = \delta h_{xx} ,$$

then  $f$  has to be a solution of

$$(20) \quad (f')^2 = \frac{2\delta}{\beta} f'' ;$$

which means that

$$\phi = f = - \frac{2\delta}{\beta} \ln(h + c_1) + c_2 ,$$

with  $c_1$  and  $c_2$  arbitrary. Thus,

$$(21) \quad v = \phi_x = - \frac{2\delta}{\beta} \frac{h_x}{h}$$

is the solution of (16). The constant  $c_2$  disappeared and  $c_1$  was incorporated in the solution of the heat equation.

Let us remark at this point that no rigorous mathematical proofs are included in this paper; however, we shall make a precise statement at each point. Thus, in this case we have

**Theorem 1:** The following two statements are equivalent:

- A {
- i.)  $v$  is a solution of (16) in an open rectangle  $R$  of the  $x, t$  plane
  - ii.)  $v, v_x$ , and  $v_{xx}$  are continuous in  $R$

i.) For  $t > 0$ , there exists a function  $h$  of the form

$$h = C(t) \exp \left[ - \frac{\beta}{2\delta} \int v(x, t) dx \right] ,$$

such that

- B {
- ii.)  $h > 0$  and  $h, h_x, h_{xx}, h_{xxx}$  are continuous in  $R$
  - iii.)  $h_t = \delta h_{xx}$  in  $R$ .



It is interesting to note how the constant  $\beta$ , representing finite amplitude effects, is balanced by the viscosity constant  $\delta$ :

$$(21) \quad v = - \frac{2\delta}{\beta} \frac{h}{h_x}$$

What we have achieved so far is to reduce the general solution of a nonlinear equation to that of a well known linear one. A question that immediately arises is how the initial values are related. From (21) we have

$$(22) \quad C(t) \exp \left[ - \frac{\beta}{2\delta} \int v(x,t) dx \right] = h(x,t)$$

so that, if

$$v(x,0) = f(x)$$

we obtain the relation

$$(23) \quad h(x,0) = C_0 \exp \left[ - \frac{\beta}{2\delta} \int f(x) dx \right]$$

as the initial condition to be used in the solution of the heat equation. However, we shall not pursue this any further, for this question has been studied quite extensively both by Cole and by Hopf. Instead, we shall investigate the question of how to relate the condition given on a line  $x = \text{constant}$  for  $v$  to  $h$ .

# SOLUTION OF CAUCHY PROBLEM

The problem we shall solve in this section is the following: find a twice continuously differentiable solution  $v$  of the equation

$$v_t + \beta v v_x = \delta v_{xx} , \quad \delta, \beta, > 0 .$$

satisfying the Cauchy conditions

$$(24) \quad v(x_0, t) = a(t)$$

$$v_x(x_0, t) = b(t)$$

Clearly, no generality will be lost if we take  $\beta = 1$  and  $x_0 = 0$ .

We know that  $v$  is given by

$$v(x, t) = -2\delta \frac{h_x(x, t)}{h(x, t)}$$

where  $h$  satisfies

$$h_t = \delta h_{xx} .$$

Let us assume a solution  $h$  of the heat equation that is of the form

$$(25) \quad h(x, t) = \sum_{n=0}^{\infty} \frac{\omega^{(n)}(t)}{\delta^n} \frac{x^{2n}}{(2n)!} + \sum_{n=0}^{\infty} \frac{\psi^{(n)}(t)}{\delta^n} \frac{x^{2n+1}}{(2n+1)!} ;$$

where  $w$  and  $\psi$  are arbitrary functions of  $t$  and where

$$\Omega^{(n)}(t) \equiv \frac{d^n \Omega}{dt^n} , \quad \Omega^{(0)}(t) = \Omega(t)$$

for any function  $\Omega$ . It can be easily seen that

$$\begin{aligned} h(0, t) &= \omega(t) , \\ h_x(0, t) &= \psi(t) , \end{aligned}$$

$$h_{xx}(0,t) = \frac{1}{\delta} \omega'(t)$$

Thus

$$(26) \quad v(0,t) = -2\delta \frac{h_x(0,t)}{h(0,t)} = -2\delta \frac{\psi(t)}{\omega(t)}$$

and

$$(27) \quad v_x(0,t) = -2\delta \left[ \frac{h_{xx}(0,t)}{h(0,t)} - \left( \frac{h_x(0,t)}{h(0,t)} \right)^2 \right] = -2\delta \left[ \frac{\omega'(t)}{\delta \omega(t)} - \left( \frac{\psi(t)}{\omega(t)} \right)^2 \right]$$

In order to satisfy the conditions (24), we therefore must have

$$-2\delta \frac{\psi(t)}{\omega(t)} = a(t)$$

and

$$-2\delta \left[ \frac{\omega'(t)}{\delta \omega(t)} - \left( \frac{\psi(t)}{\omega(t)} \right)^2 \right] = b(t)$$

Thus

$$\frac{\omega'(t)}{\omega(t)} = \frac{1}{4\delta} (a^2(t) - 2\delta b(t))$$

so that

$$(28) \quad \omega(t) = \exp \left[ \frac{1}{4\delta} \int (a^2(t) - 2\delta b(t)) dt \right]$$

$$(29) \quad \psi(t) = - \frac{a(t)}{2\delta} \omega(t)$$

Therefore we see that the conditions (24) "translate" to the heat equation in the form of (28) and (29). The precise statement follows.

**Theorem 2.** Suppose that each of  $a(t)$ ,  $b(t)$  is analytic for  $t > 0$ . Then

$$(30) \quad v = \frac{-2\delta \sum_{n=1}^{\infty} \frac{K^{(n)}(t)}{\delta^n} \frac{x^{2n-1}}{(2n-1)!} + \sum_{n=0}^{\infty} \frac{[a(t) K(t)]^{(n)}}{\delta^n} \frac{x^{2n}}{2n!}}{\sum_{n=0}^{\infty} \frac{K^{(n)}(t)}{\delta^n} \frac{x^{2n}}{2n!} - \frac{1}{2\delta} \sum_{n=0}^{\infty} \frac{[a(t) K(t)]^{(n)}}{\delta^n} \frac{x^{2n+1}}{(2n+1)!}}$$

where  $K(t) = \exp \left[ \frac{1}{46} \int (a^2(t) - 26b(t)) dt \right] ,$

is a solution of

$$v_t + vv_x = \delta v_{xx}$$

such that, for  $t > 0, -\infty < x < \infty ,$

- i.)  $v, v_x$  and  $v_{xx}$  are continuous
- ii.)  $v(0,t) = a(t), v_x(0,t) = b(t)$
- iii.)  $v$  is unique.

As an illustration of the solution (30), we shall give a steady state solution of (30), obtainable by letting

$$v(0,t) = a_0, \quad v_x(0,t) = b_0, \quad a_0, b_0 \text{ constants.}$$

Under such conditions we find that

$$(31) \quad v = a_0 c_1 \frac{c_1 \sinh c_2 x + \cosh c_2 x}{\sinh c_2 x + c_1 \cosh c_2 x}$$

where the significant parameters  $c_1$  and  $c_2$  are given by

$$c_1 = - \sqrt{\frac{46 a_0^2 - 26 b_0}{a_0^2}}$$

$$c_2 = - \frac{a_0}{26} c_1$$

which characterizes the highly nonlinear nature of the solution.

## UTILIZATION OF INFINITE PRODUCTS

The solution given by (30) is quite typical for Burgers' equation: one infinite series divided by another. There are only a very few cases where such an expression can be analyzed without further approximations. Therefore, in this section we shall discuss how to improve such approximations and how, in many cases, to obtain a single series representation for the solution  $v$ .

Our approach is going to utilize a simple property of infinite products. Thus, let

$$(32) \quad h(x, t) = \prod_{n=1}^{\infty} (1 + f_n(x, t))$$

with the condition

$$\sum_{n=1}^{\infty} f_n^{-2}(x, t) < \infty$$

to insure that the product converges. Let us note that the logarithmic derivative of (32) is given by

$$(33) \quad \frac{h_x(x, t)}{h(x, t)} = \sum_{n=1}^{\infty} \frac{[f_n(x, t)]_x}{1 + f_n(x, t)}$$

This can be seen either by taking the logarithm of both sides of (32) and differentiating, or by a factor by factor differentiation of the right hand side of (32), followed by division.

The functional form of the left hand side of (33) is exactly that of the solution of Burgers' equation. The question we have to discuss is therefore the following: how can one represent the solution of the heat equation as an infinite product? In answering this question we have to remember that only positive solutions of the heat equation need be considered (see Theorem 1).

Let us assume that in the process of solving Burgers' equation, we reached the point where we already have the solution of the associated heat equation; let this be  $h(x, t)$ . To find  $v$ , we now have to form the quotient

$$v = -2\delta \frac{h_x(x, t)}{h(x, t)}.$$

However, since  $h(x,t) > 0$ , in many cases it is possible to write  $h$  in the form

$$(34) \quad h(x,t) = \exp \left[ \sum v_n(x,t) \right]$$

where the series (which can be finite or infinite) is a real one. In such a case, our infinite product is

$$(35) \quad \prod_{n=0}^{\infty} (1 + f_n(x,t)) = \prod_{n=0}^{\infty} \left[ 1 + \left( e^{v_n(x,t)} - 1 \right) \right]$$

and the solution  $v$  is given by

$$(36) \quad v = -2\delta \sum_{n=0}^{\infty} \frac{\partial}{\partial x} v_n(x,t) .$$

The situation is not so simple in the general case. Nevertheless, the approach through infinite products is possible in many other cases. If the solution  $h$  of the associated heat equation can be factored at all, then the method applies. Also, in many cases, it is much easier - and one obtains much better results - if instead of trying to approximate the quotient of two series, one approximates the solution of the heat equation. This can be done, for instance, by using the approximation theorem of Weierstrass, according to which a function, analytic on an interval, can be approximated to any degree of accuracy - on that interval - by a polynomial. This polynomial then can be factored and the method applied.

In addition, one can use Hadamard's factorization theorem for the direct splitting of  $h$  into its factors; although, to be sure, it does not apply in every case.

Finally, let us note that one can tackle this problem in yet another way. To see this, we begin the solution of our problem all over again.

We wish to find a simple series solution of

$$v_t + v v_x = \delta v_{xx}$$

We shall let  $v = -2\delta \phi_x$  and integrate:

$$(37) \quad \phi_t - \delta \phi_x^2 = \delta \phi_{xx}$$

Let now

$$(38) \quad \phi = \ln \sum v_n(x, t) .$$

Then, in abbreviated form,

$$\frac{\sum_t}{\sum} - \delta \left( \frac{\sum_x}{\sum} \right)^2 = \delta \left[ \frac{\sum_{xx}}{\sum} - \left( \frac{\sum_x}{\sum} \right)^2 \right]$$

so that

$$\sum_t = \delta \sum_{xx}$$

or

$$(39) \quad \sum \frac{\partial}{\partial t} v_n(x, t) = \delta \sum \frac{\partial^2}{\partial x^2} v_n(x, t)$$

We can now proceed to find the solution of (39) in terms of easily factorizable eigenfunctions  $v_n$ ; use this in (38) to arrive at

$$\phi = \ln \sum v_n(x, t) = \sum \ln f_n(x, t)$$

and obtain the solution  $v$  as

$$v = -2\delta \phi_x = -2\delta \sum \frac{[f_n(x, t)]_x}{f_n(x, t)} .$$

## BIBLIOGRAPHY

1. Cole, J.D. (1951) *Quart. Appl. Math.* 9, 225
2. Hopf, E. (1950) *Commun. Pure Appl. Math.* 3, 201
3. Widder, D.V. (1956) *Annali di Matematica*, 42, 279



# LOW FREQUENCY RADIO ASTRONOMY IN SPACE

By

N. F. Six ( /  
Brown Engineering Company  
and  
G. R. Lebo and A. G. Smith /  
University of Florida

## ABSTRACT

**N67-24275**

Radio astronomical observations made from the surface of the Earth are restricted at the high frequency end of the RF spectrum by the troposphere and at the low frequency end by the ionosphere. Artificial Earth satellites provide the means for eliminating these restrictions, but low frequency studies require large antennas, so a large stable platform is desirable. The surface of the Moon meets this requirement.

In order to study the sources (Sun, Jupiter, radio stars, cosmic background, and perhaps Earth and Saturn) over the frequency range from 30 kHz to 10 MHz, the radiometer should be able to measure intensity, apparent position, apparent size, temporal variation, and polarization. The order of experiments will most likely be determined by the antenna system complexity and size. Early experiments on the lunar surface probably will employ simple broadband "pencil-beam" antennas. Man will be necessary for antenna installation and initial calibration.

## INTRODUCTION

Over the past three decades a vast amount of astronomical information has been gained from observations in the radio frequency portion of the electromagnetic spectrum. Earth-bound investigations are restricted at the high frequency end of the RF spectrum by the troposphere and at the low frequency end by the ionosphere. Artificial Earth satellites provide the means for eliminating these restrictions, but low frequency studies require large antennas, so a large stable platform is desirable.

In general, the scientific objectives of low frequency (30 kHz - 10 MHz) radio astronomy in space will be to make observations of all possible sources of emission and to derive from these data new knowledge concerning source mechanisms and factors influencing the propagation of the radio waves. The known sources of low frequency nonthermal radio emission are the Sun, Jupiter, the discrete galactic and extragalactic sources, and the cosmic background. Perhaps Saturn and Earth will also fall in this category. The types of measurements to be considered are 1) calibrated intensity, 2) apparent position, 3) apparent size, 4) polarization, and 5) temporal variation. These studies will require large antennas, and man will participate in their erection. The order of experiments will be determined by the antenna system complexity and size.

Such investigations should result in a better understanding of the magnetospheric systems of Jupiter, Earth, and perhaps Saturn; of the distribution of plasma clouds in interplanetary space; and of the structure of our galaxy. Very likely many of the results will be unsuspected.

The author wishes to acknowledge the suggestions and encouragement of Drs. A. G. Smith, G. R. Lebo, and T. D. Carr of the Department of Physics and Astronomy, University of Florida. Some of the material

presented herein is the result of studies performed under NASA Contract NASR-176 with the University of Florida concerning the development of an orbital receiver for the reception of low frequency radio energy from the planet Jupiter.

## ATMOSPHERIC LIMITATIONS

The astronomer is interested in obtaining new knowledge about extraterrestrial bodies. The information he obtains at ground level arrives in the form of particles or waves and almost none escapes interaction with the earth's atmospheric envelope. The difficulties involved in sorting out the atmospheric influences are in many cases insurmountable. So, the astronomer confines himself to making observations in narrow regions of the electromagnetic spectrum where the atmospheric interactions are minimal. These regions have been aptly referred to as "windows", and are shown in Figure 1.

Those parts of the electromagnetic spectrum which can be advantageously examined from beyond the sea of gases which encircle our planet are, in order of increasing wavelength, cosmic ray, gamma ray, x-ray, ultraviolet, visible, infrared, and radio. In the radio region of the spectrum, earth-based measurements are confined to the window between about 5 MHz and 60,000 MHz. At the low frequency end of this window, the ionosphere becomes opaque to radio wave transmission. The critical frequency for normal incidence, or the plasma frequency of the most dense layer of electrons,<sup>1</sup> depends on the time of day, season, sunspot cycle and other variables, but usually ranges from 3 to 12 MHz. Figures 2 and 3 illustrate respectively the variation of plasma frequency with altitude in the ionosphere and in the magnetosphere. The high frequency boundary of the radio astronomy window is caused by tropospheric absorption. This absorption is associated with the rotational energy of the oxygen and water vapor molecules and occurs strongly in certain frequency bands. Between these bands, radio noise is a serious problem. Even in the spectral region where the earth's atmosphere is transparent to radio waves, there are other effects which are a nuisance to radio astronomers. The troposphere and the ionosphere cause refraction of radio waves resulting in an apparent displacement of the source. Drifting ionospheric irregularities or clouds of ionization produce scintil-

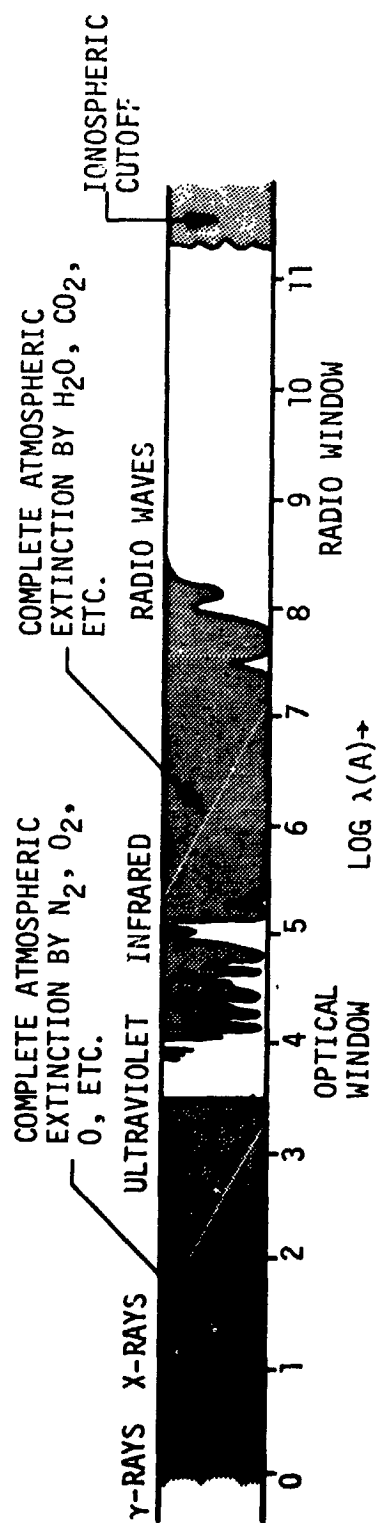


Figure 1. Atmospheric Windows in the Electromagnetic Spectrum (Aller)

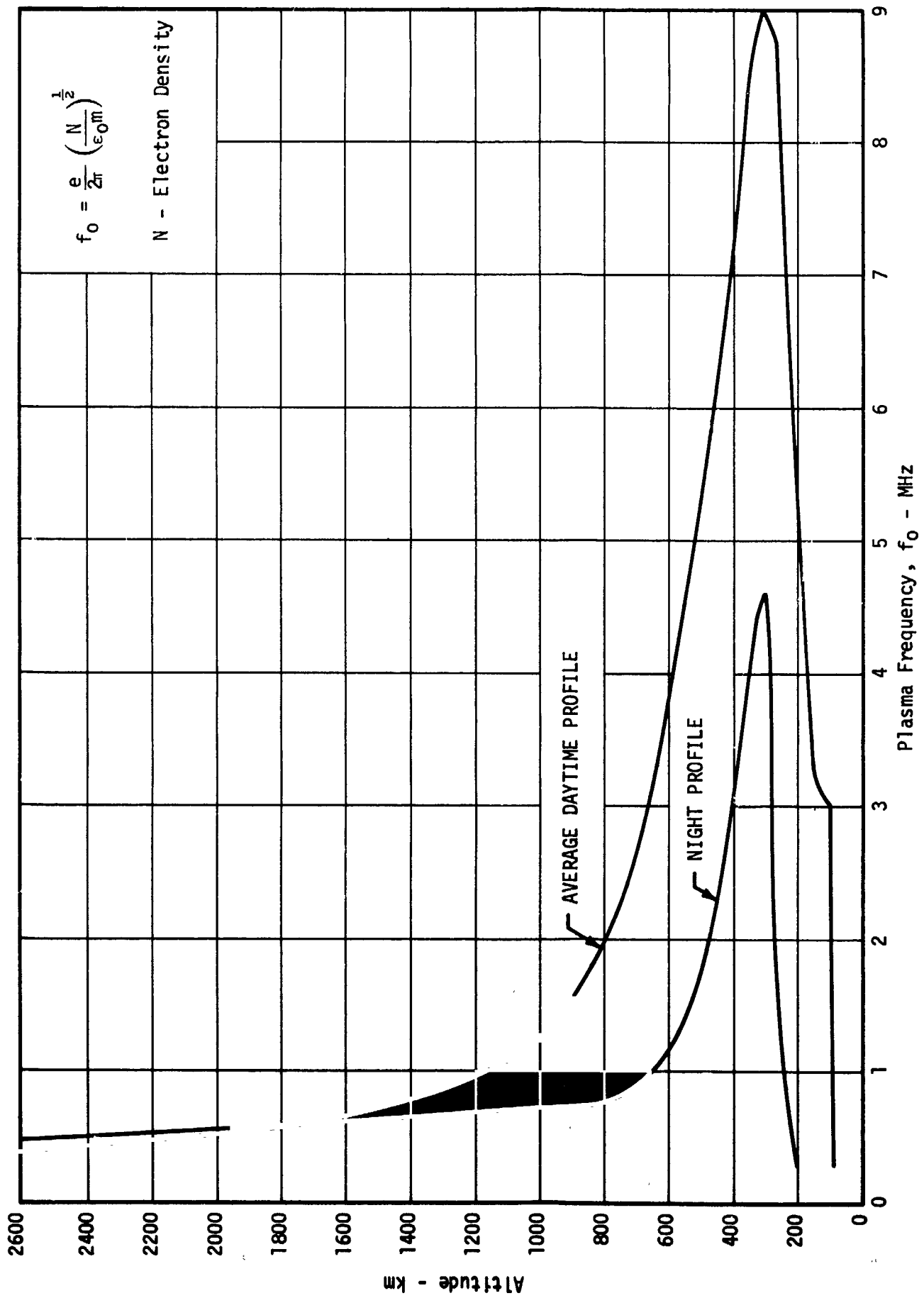


Figure 2. Plasma Frequency as a Function of Altitude from Electron Density Profiles in the Ionosphere at Mid Latitudes (Reference 1)

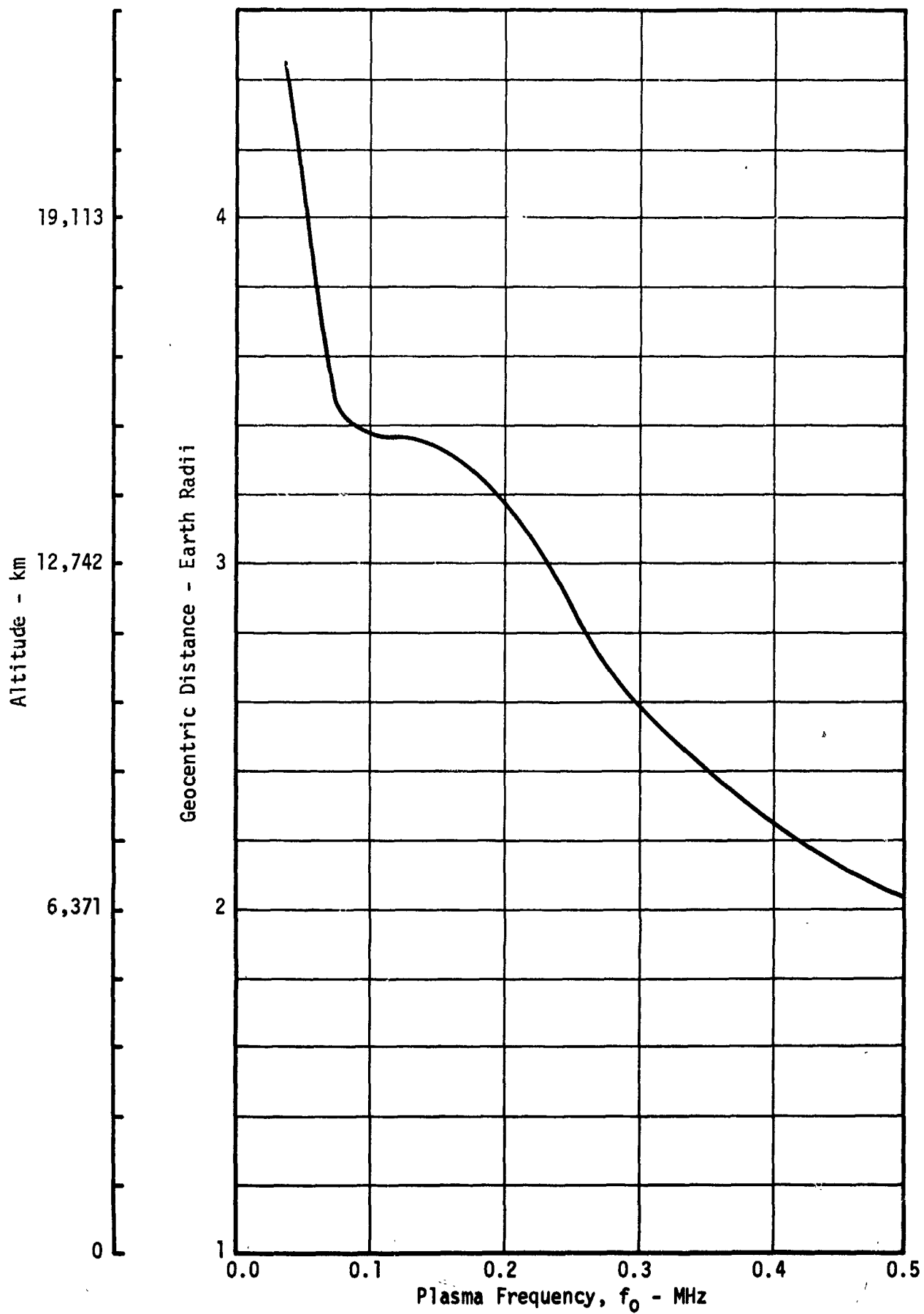


Figure 3. Plasma Frequency as a Function of Altitude from the Equatorial Profile of Magnetospheric Electron Density (Reference 2)

lations or rapid variations in the intensity of received signals. The patchy ionosphere acts like an optical grating, producing a diffraction pattern on the ground. The smaller the angular size of the source, the more pronounced are the focusing and interference phenomena. Electrical storms produce radio static and, at low frequencies, these natural disturbances as well as man-made interference are reflected off the ionosphere and compete with the desired signals. For these reasons the lowest frequencies are accessible only between midnight and dawn when the electron density in the ionosphere is at a minimum. By judicious choice of the observing station location - high altitude and low humidity - atmospheric absorption effects can be reduced considerably.

### LOW FREQUENCY SPECTRUM

The present discussion will concern only one part of the radio region of the spectrum - those electromagnetic waves having frequencies between 30 kHz and 10 MHz, or wavelengths between 30 and 10,000 meters. This part of the radio spectrum will be referred to as the low frequency region. Very low frequencies ( $f < 30$  kHz) and high frequencies ( $f > 10$  MHz) are outside the scope of the present endeavor.

The atmospheric limitations at low frequencies can be avoided by making measurements from high earth orbits or from the moon. With no ionosphere to contend with, observations can be performed on down into the kHz range. At frequencies below the critical frequency in the  $F_2$  region of the ionosphere, observations can be made neglecting natural electrical disturbances, associated with thunderstorms, and man-made interference, for these will be confined in the ionosphere-earth cavity.

### SOURCES

The sources of low frequency radio emission that we know about are the following: the sun, Jupiter, "radio stars", and the cosmic background. There are reasons to believe that Saturn might also belong in



this group. The radiation belts which encircle the earth probably provide magnetic Bremsstrahlung emissions which also could be detected from an orbital or lunar radio astronomy package.

### Sun

The radio spectrum of the sun is one of enormous complexity with at least five different types of transient outbursts in addition to the steady thermal emission. Study of these outbursts has increased our knowledge of the solar atmosphere and, in particular, has led to a better understanding of centers of activity. Figure 4 shows the dynamic spectra of solar radio bursts - electromagnetic phenomena associated with chromospheric flares.

Type I bursts which accompany noise storms are not shown on Figure 4. These narrow-band (1% of center frequency), short-duration (few tenths of a second) bursts occur in the frequency range 50 - 300 MHz and are found superimposed on a broad continuum. All of the noise storm radiation, continuum and bursts, is strongly circularly polarized. Its most notable characteristic is its long duration; a typical storm lasts about one day.

Type II bursts are the most intense. They are characterized by one or more narrow bands about 50 MHz wide which drift slowly from high to low frequencies. When two Type II bursts occur together, as in Figure 4, the features are duplicated in two frequency ranges suggesting a fundamental and second harmonic. Type II bursts are rarer, but longer lasting than Type III bursts. Some time structure has been detected.

Type III bursts last only a few seconds, are very intense, and often occur in groups. The individual burst appears as a sharp line tilted slightly towards the right. The emission at each moment occurs in a narrow frequency band some MHz wide, which quickly drifts toward long wavelengths. Both Type II and III bursts are associated with fast moving disturbances in the corona.

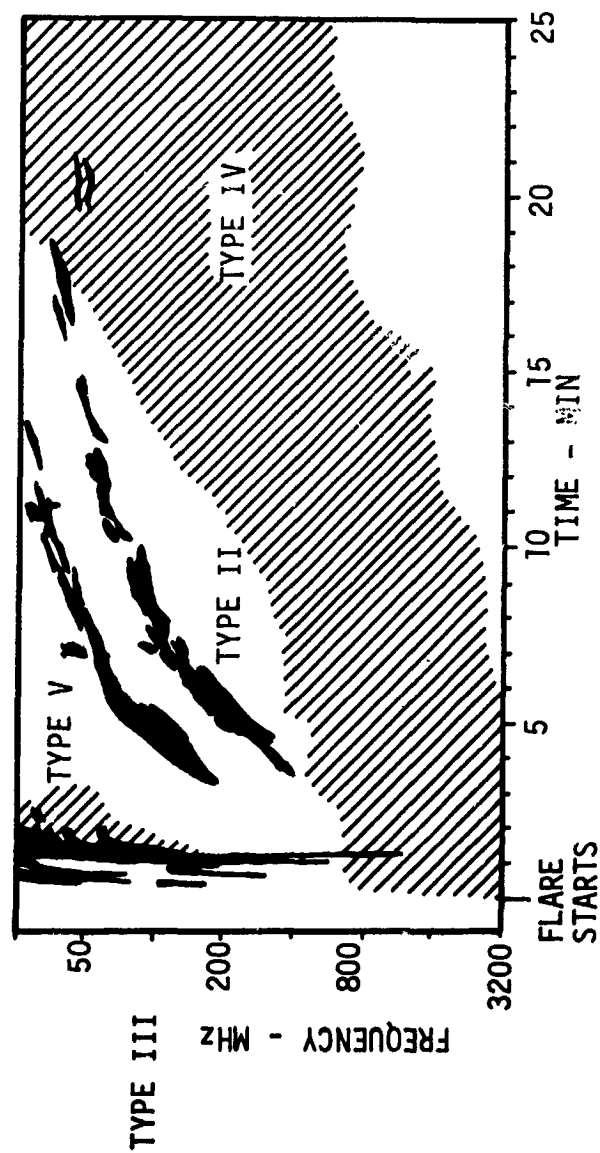


Figure 4. Dynamic Spectra of Solar Radio Bursts (Piddington)

Type IV radiation has a broad spectrum and great steadiness. This radiation, called continuum because of its wide frequency spread, follows Type II bursts and may persist for several hours. It is often circularly polarized.

Type V bursts follow Type III. This is also continuum radiation, but its spectrum is not as broad as Type IV. It appears only at wavelengths greater than a few meters, and no fine structure can be seen.

Since the solar radio spectrum is continuously changing, attempts to extend measurements into the low frequency region which borders the top of Figure 4 should be designed to fully reveal the characteristics of the bursts in the frequency time domain. The experiment should be capable of tuning over a wide range of frequencies in a fraction of a second and recording the intensity of the radiation at each frequency.

Occultation experiments - monitoring the emission from discrete sources as they pass behind the solar corona - can provide information on the heliocentric distribution of plasma in interplanetary space. Low frequencies would be especially advantageous here since it is believed that the scattering effects of plasma clouds scale as  $\lambda^2$ .

### Jupiter

Excepting the sun, Jupiter is the only confirmed nonthermal source of radio frequency emission in the solar system. The sporadic bursts at dekameter wavelengths are strongly correlated with Jovian longitude and with the position of the satellite Io indicating that the sources of radiation are linked to the disk of the planet. Whether the mechanism responsible is a surface phenomenon or occurs in the exosphere and is coupled to the planet through its magnetic field has not yet been determined. Another nonthermal component of emission which occurs in the microwave part of the spectrum is believed to originate in Jovian Van Allen belts where trapped electrons radiate by the synchrotron process. Figure 5 shows

the spectral distribution of the average planet-wide flux density from Jupiter.<sup>3</sup> The spectral index varies between -5 and -8 over the observable dekametric range, suggesting that the bulk of the radiation may actually lie in the low-frequency tail, which is unobservable from the ground because of ionospheric cutoff. Furthermore, the apparent structure of the Jovian radio sources changes radically at frequencies below 15 MHz, and the pulse structure of the emission is unquestionably altered by the terrestrial ionosphere.

Observations of the giant planet at frequencies below 5 MHz could establish the spectral distribution of the emission, i. e., extend the curve of Figure 5 to the left. Such information is vital to theories concerning the origin of the radiation - total energy involved, particle densities required, and efficiency of the conversion mechanism. An examination of the pulse structure, unaltered by the terrestrial ionosphere could yield information about Jupiter's ionosphere. Dynamic spectra (frequency versus time plots) and polarization studies at these low frequencies might unravel the mysteries of the planet's magnetic field. Long-term monitoring would undoubtedly yield evidence of propagation effects in interplanetary space, correlation with sunspot activity, and increase our knowledge of another magnetospheric system, perhaps much like our own but on a larger scale.

### Saturn

There have been reports of possible emissions from Saturn at low frequencies.<sup>4,5</sup> These do not, at present, constitute hard evidence. Since modern theories tend to associate a planet's magnetic field with its rate of rotation, Saturn might be expected to emit because of its similarity to Jupiter in this respect. The fact that no confirmed nonthermal radiation from the ringed planet has been detected could be the fault of listening at the wrong frequencies. Here again, monitoring at low frequencies, un-hindered by an ionosphere and atmospheric and man-made interference, could solve the riddle.

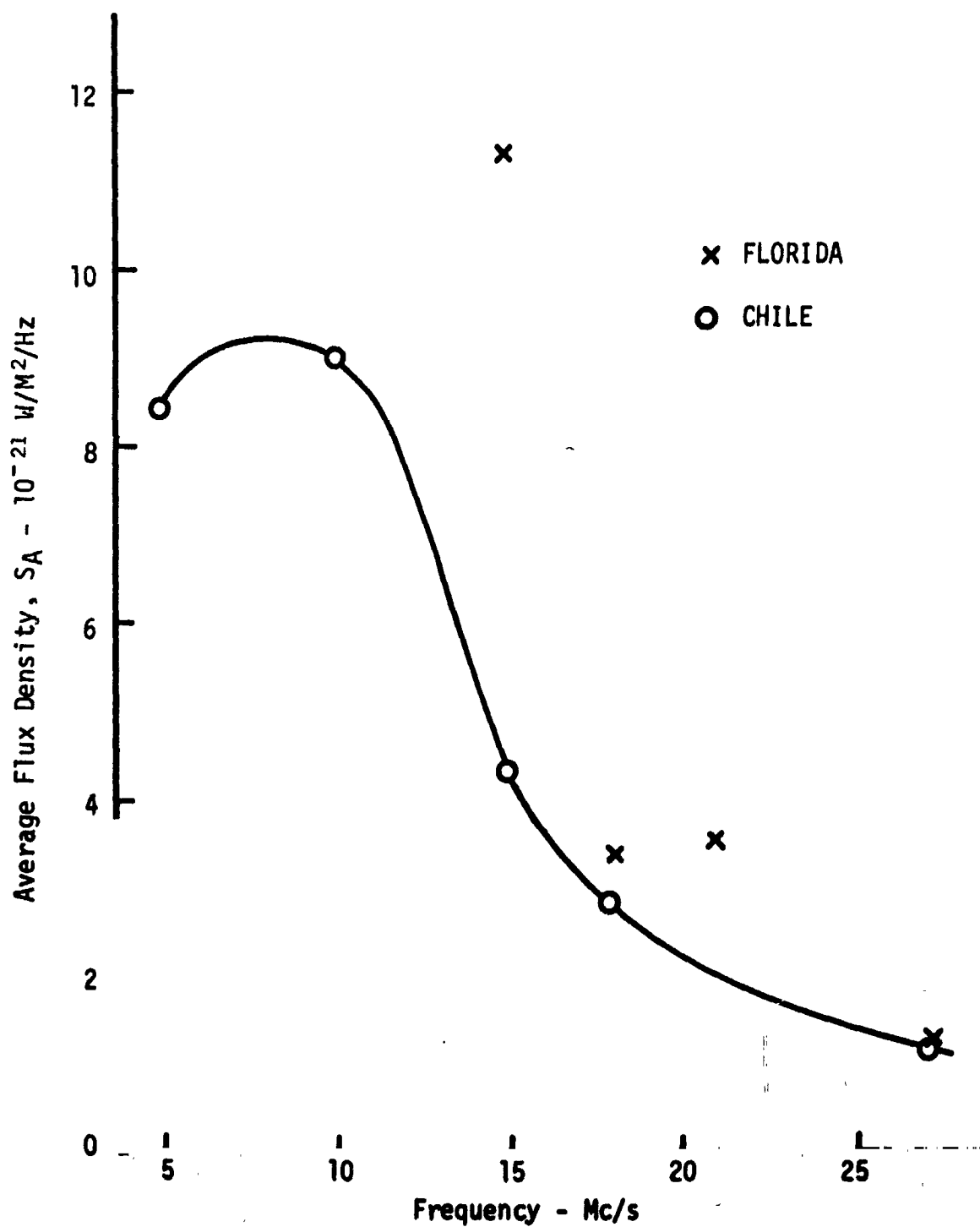


Figure 5. Spectral Distribution of the Average Planet-Wide Flux Density from Jupiter

## Radio Stars

There are numerous discrete sources on the celestial sphere, and these have been dubbed "radio stars" because of their small extent. Actually they are not stars, but nebulae, and their emission is continuous in time. They can be classed as galactic or extragalactic, thermal or nonthermal. Only the discrete sources of our own galaxy exhibit typical thermal emission spectra. These sources (galactic, thermal) are thought to be clouds of ionized gas - the coronas surrounding bright, hot stars in the spiral arms, and are referred to as H-II sources. A typical example is the source Cygnus X. All of the galactic, nonthermal sources are believed to be remnants of supernovae - catastrophic explosions of stars. The Crab Nebula is an example and emission is by the synchrotron process. All of the extragalactic discrete sources, which constitute the vast majority of "radio stars", are characterized by nonthermal spectra, i. e., the radiation increases in intensity with wavelength. Again, the synchrotron mechanism offers a reasonable explanation of this emission. These extragalactic sources which have an isotropic distribution in space are classified as "normal" and "peculiar". The normal sources are bright, nearly spiral galaxies with radio outputs of approximately  $10^{28}$  kw, i. e., the same total power as the Milky Way. The classic example is the Great Nebula in Andromeda. The peculiar sources are much more intense. For example, the source Cygnus A, believed to be two galaxies in collision, has a radio output of  $10^{34}$  kw.

All of the discrete radio sources emit a fairly smooth continuum of radio frequency energy. Measurements of the intensity of these sources at low frequencies will provide additional spectral evidence which has a bearing on the stability of the emission mechanism and on the energy spectrum of the particles responsible. Surveys at frequencies below 5 MHz showing the positions in space of the discrete sources would be valuable additions to the information now in hand.<sup>6</sup> This mapping, along with individual source studies to ascertain angular dimensions and intensity

distributions, will require high resolution and narrow beamwidth. Such investigations are vital to attempts at optical identification of the radio sources.

### Galactic Background

By background radiation, we mean the emission that has a continuous spatial distribution as opposed to the discrete sources. Most of this radiation comes from our own galaxy and two types can be distinguished, the galactic continuum and the hydrogen-line emission. Since the emphasis here is on the scientific worth of extending the radio astronomy spectrum to lower frequencies, the 1420 MHz emission from neutral hydrogen will not be discussed.

Galactic continuum surveys or maps of radiation intensity show the following: average intensity varies over the celestial sphere but appears to be constant for a given direction; intensity is greater in the galactic plane and is a maximum toward the center of the galaxy; surveys at different frequencies indicate that both thermal and nonthermal processes are operative. The bright band of emission in the galactic plane is thermal emission from clouds of ionized hydrogen (H-II regions). The extended component of the background emission is synchrotron radiation by cosmic ray electrons in the galactic corona which is spherical about the galactic center. This emission is most intense at lower frequencies as indicated in Figure 6. There is synchrotron emission from the galactic disk also, but it is absorbed by H-II regions. At long wavelengths (dekameter and longer) where the nonthermal emission predominates, galactic observations permit a study of the structure of these regions in absorption.

The points in Figure 6 show the measurements of the galactic background noise. One group of experimenters believes in a rather drastic decrease in intensity between 3 and 1 MHz. Another group sees a leveling off in this region.

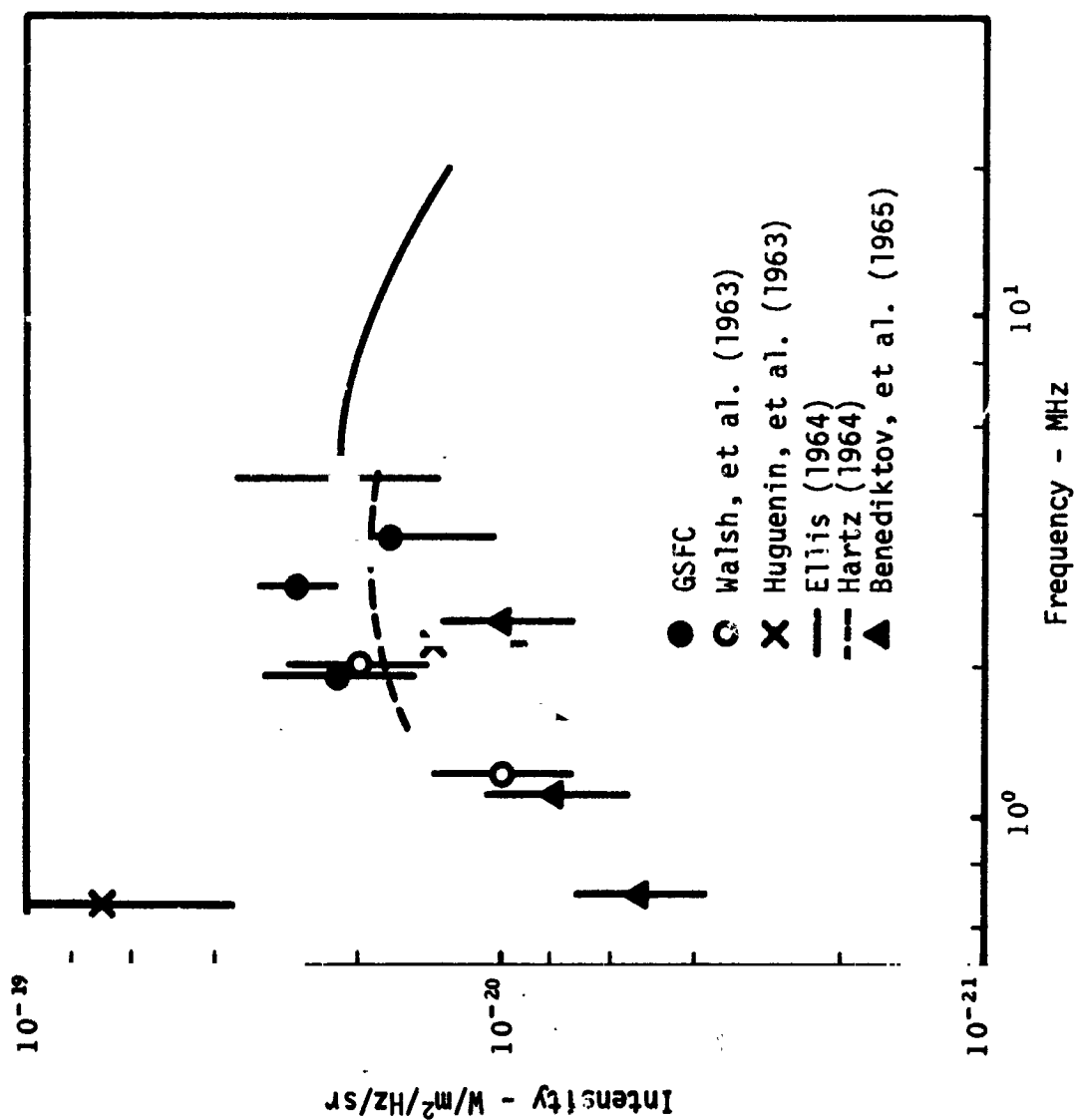


Figure 6. Observed Cosmic Noise Intensities Below 10 MHz



The intensity values reported by Benediktov, et al. at 0.7 MHz are an order of magnitude smaller than the values reported by Huguenin, et al. Perhaps what is being sampled is earth noise. This might be expected to possess large, order of magnitude, variations whereas the cosmic background would not. Measurements made outside of the magnetosphere could perhaps resolve this enigma and give a true reading of the intensity of cosmic radio emission below 2 MHz.

The shape of the spectrum of the galactic continuum at low frequencies has consequences on other lines of endeavor. If the intensity of the emission levels off or increases, it will be difficult to detect other sources above this interference. On the other hand, if the emission falls off, the detection of weak signals in this part of the spectrum will be possible. Whatever the shape, the spectrum definition will provide input to questions of energetics - populations of cosmic ray electrons, and accelerating mechanisms. The spatial distribution of galactic radiation at low frequencies will undoubtedly lead to a clearer delineation of the spiral structure of the Milky Way.

#### Earth and Interplanetary Medium

The Van Allen radiation zones probably provide magnetic Bremsstrahlung emissions which could be detected from the moon. Occultation experiments with the aim of detecting propagation effects caused by the interposition of the earth's ionosphere or magnetosphere between the source and the receiver can yield valuable data on the terrestrial environment.

It is presumed that interplanetary space contains filaments or blobs of plasma that have been spewed out of the sun. From the moon it should be possible to ascertain the distribution of these solar plasma clouds by monitoring celestial sources at low frequencies over a time span of one year and scrutinizing the data for propagation effects such as the scattering of radio waves by irregularities in electron density. The moon is well

suited for such an investigation for, besides providing a large platform for low frequency observations, it is outside of the terrestrial magnetosphere a majority of the time and thus enables a distinction between propagation effects in interplanetary space and those operative at the magnetospheric boundary.

### TYPES OF MEASUREMENTS

Certain types of measurements are possible utilizing the techniques of radio astronomy. These are intensity, apparent source position, apparent source size, temporal variation and polarization. Intensity measurements at fixed frequencies will extend source spectra into the region inaccessible to earth-based radio telescopes. Swept frequency measurements will yield dynamic spectra, i. e., how the frequency of emission drifts with time. Measurements of source positions or "mapping" will be a definite asset to studies of galactic and extragalactic structure. Source size is a clue to the mechanism of emission. Synoptic observations will provide data for time variation investigations, correlation with other space parameters, and cause and effect analyses. From this standpoint, unattended operation of the experiments would be desirable to provide a long time span. Polarization data is necessary to infer the character of magnetic fields existing at the source and certain propagation effects.

### INSTRUMENTATION

A radio astronomy package designed for the space environment should include antenna, receiver, calibration source, and programming circuitry. Figure 7 shows the relationship of these essential components. Power supply and telemetry are considered supporting equipment. The calibration source and programming circuitry are standard items. Various types of receivers have been developed for low frequency experiments in space. The greatest effort will be required in the field of antenna design. In the detection of relatively weak and small sources, very large antennas

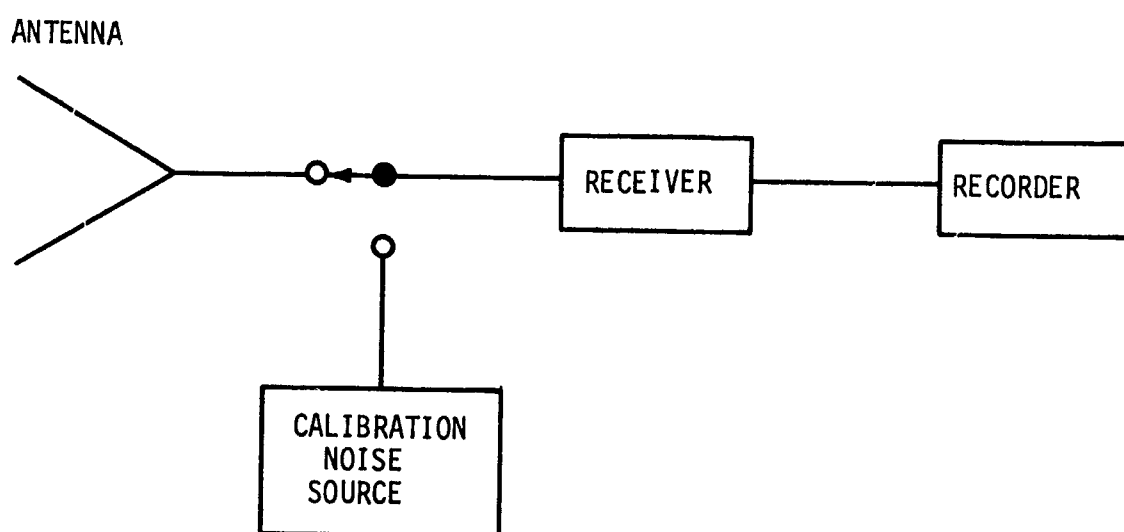


Figure 7. Essential Components of a Radio Telescope

will be required. There are two reasons for this. First, the effective area must be sufficiently large to capture enough energy to be measurable. Second, because of diffraction, the angular resolution of a radio telescope improves with each increase in the ratio of the aperture to the wavelength. When the antenna is swept across a point radio source, radiation is received over an angle of approximately  $\lambda/D$  radians, where  $D$  is the effective width of the antenna. Two small sources will appear as a single source if their angular separation is much less than  $\lambda/D$ , and they cannot be resolved.

At low frequencies, cosmic noise exceeds the receiver noise and becomes the factor which limits the sensitivity of a radio telescope. Figure 6 shows the increase in cosmic noise intensity with decreasing frequency. High resolving power (paid for in terms of large antenna size) is necessary to insure that the integrated cosmic noise does not drown out the desired signal from some discrete source.

### TYPICAL EXPERIMENTS

Advances in science usually await advances in instrumentation. It is only natural that the capability to leave the earth and its atmospheric envelope be exploited to extend the frontiers of science. Low frequency radio observations of extraterrestrial sources can be performed from above the ionosphere, that is, from earth-orbiting platforms at altitudes greater than 2000 km and from lunar bases. Earth-orbiting platforms are less expensive, thus early efforts will be in this direction. However, for even moderate resolution at these long wavelengths, the antenna arrays become quite large. There are limitations to the size and stability of antenna systems deployed in space. When these limitations are too severe for the experiment being considered, then the lunar base becomes attractive.

#### Earth-Orbiting Observatories

Low frequency radio experiments are planned for the Orbiting Geophysical Observatory (OGO) and the Radio Astronomy Explorer (RAE) series. Both are unmanned, so the experiments are entirely automatic.

The OGO spacecraft is designed to accommodate about twenty different experiments on each flight. Two classes of orbits are planned - one circular, polar with apogee of 1000 km, the other elliptical,  $31^\circ$  inclination, with apogee of 133,000 km. For the reception of low frequency radio signals from extraterrestrial sources, the latter class of orbits is more desirable since both the outer ionospheric electron density and the magnetospheric electron density decrease with altitude. Experimenters at the University of Michigan intend to measure the dynamic spectrum of solar noise bursts using a swept frequency radiometer and a dipole antenna. The radio astronomy group at the University of Florida hopes to determine the spectrum and pulse structure of Jupiter's low frequency emission on one of the later OGO flights. The receiving system for this experiment is a four-channel superheterodyne total power radiometer and the antenna is a 240-foot dipole. Figure 8 shows the antenna patterns at the four operating frequencies: 4, 2, 1, and 0.5 MHz. This simplest type of antenna provides very little directivity.

The Radio Astronomy Explorer satellites will go one step further in antenna directivity. Using two 750-foot VEE antennas, observations of terrestrial and celestial noise will be made from a 6000-km circular orbit. At this altitude, the satellite will be within the magnetosphere, but observations should still extend down to 0.5 MHz, the local plasma frequency. Figure 9 shows the satellite configuration.

The high-altitude Apollo flights (synchronous orbit) provide the capability for the next advance in low frequency radio astronomy. The addition of man to the experiment makes it possible to employ large directive antenna arrays and guide them. By extravehicular maneuvers, the astronaut can assemble these more complex antennas and point them in preferred directions using the spacecraft control system. Figure 10 shows a large log-periodic array sensitive over a frequency decade. The availability of man also permits maintenance and alteration of system parameters based on the results obtained, thus making the experiment more reliable and more flexible.

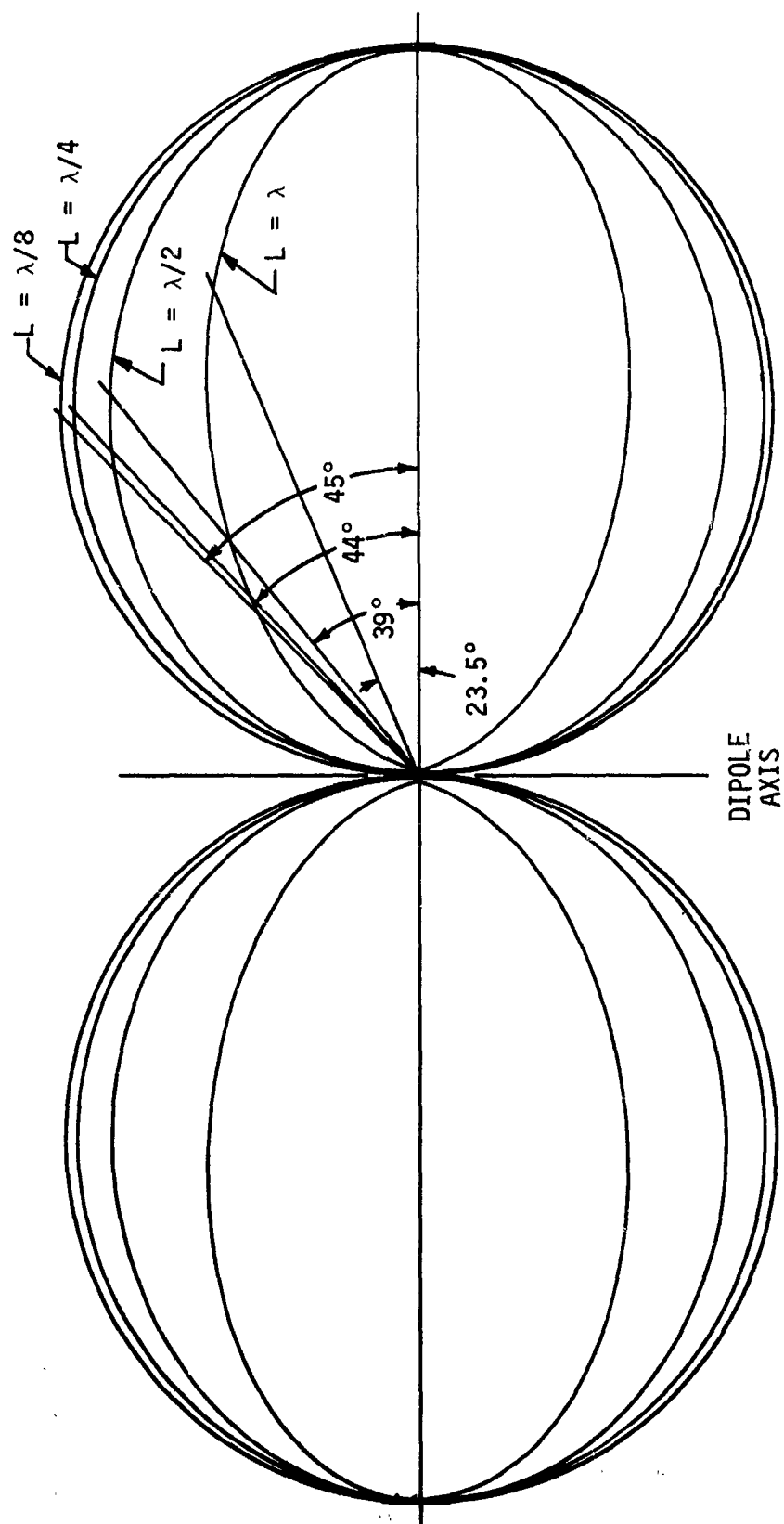


Figure 8. Antenna Patterns for a Free Space Dipole of Length  $L$



Figure 9. Radio Astronomy Explorer Satellite



Figure 10. Unfurlable Log Periodic Antenna for the Frequency Range 0.7 - 7.0 MHz



## Lunar Observatory

Knowing the advantages that a high altitude manned orbiting platform provides, why attempt radio astronomical measurements from the moon? The lunar surface affords the advantages of a large stable platform. Very large antennas can be deployed from a roving vehicle and orientation of the antenna beam can be accomplished electronically. Once the lunar base is a reality, maintenance will be less unfamiliar under lunar gravity than under the zero-g conditions of an earth-orbiting spacecraft. For those experiments demanding high resolution, the lunar horizon can be used as an occulting edge, allowing the precise positioning of the sources of low frequency radio emission. On earth, the atmosphere rules out this possibility, and the guidance of an artificial occulting disc in proximity to an earth-orbiting spacecraft would be extremely difficult.

In order to design a flexible system with research capabilities in many of the areas mentioned earlier, the characteristics of the essential elements of a radio telescope must be considered. For the antenna, these characteristics are bandwidth, beamwidth, gain, and steerability. Since we are interested in a wide range of frequencies (30 kHz - 10 MHz) the antenna should be broadband. This can be accomplished by constructing the array of broadband elements. The beamwidth should be reasonably narrow, allowing the resolution of closely spaced sources. This is determined by the length of the array. Narrow beam implies high gain or the ability to detect weak sources. The antenna beam should be steerable in elevation so that a large portion of the celestial sphere can be monitored. For a broadband array, this can be accomplished using delay line techniques. To measure intensity, it is best to use a large but simple antenna; however, such an antenna does not give the position and diameter with high accuracy. Interferometers are best from this standpoint, but they cannot make reliable measurements of intensity due to the overlap of the interference fringes of neighboring sources. Single beam antennas provide the best plots of distributed radiation, i. e., a general survey of the sources and the background radiation.

There are many different types of radio receivers, and these will not be discussed here. Briefly, fixed frequency channels are better for absolute intensity and pulse structure measurements, while swept frequency receivers provide information in the frequency-time domain and are better for locating sources of interference.

The radio telescope shown in Figure 11 is a compromise which will achieve many of the objectives mentioned earlier. It is designed to operate over the frequency decade 0.2 - 2.0 MHz. The resolution of this array is  $10^\circ$  at 0.2 MHz. At higher frequencies the "pencil beam" becomes narrower, but there are sidelobes. At frequencies below 0.2 MHz the beamwidth is greater than  $10^\circ$ . A multichannel receiver at the center of the array can perform fixed and swept frequency observations. The east-west baseline is 10.5 km long and contains 22 dipoles each a half wavelength at 0.2 MHz ( $\lambda/2 = 750$  m). The north arm is 6 km long and contains 7 dipoles. The spacing between the dipoles can be less than 750 m since the lunar surface is assumed to be a lossy medium. Such a medium cuts down on sidelobes and makes the antenna more broadbanded. The array has been deployed on the moon by a roving vehicle. Surface irregularities up to a tenth of a wavelength can be tolerated. To change the elevation of the beam, switches are activated which insert delay lines between the separate elements and the receiver. The astronaut will be needed primarily for the initial installation. Operation of the experiment will be automatic and should collect data for a period of at least one year. Proximity of the antenna to the Emplaced Scientific Station will facilitate use of the latter's data storage, power, and telemetry systems.

With such a radio telescope, we can expect to learn more about the structure of our galaxy, the distribution of plasma clouds in interplanetary space, the magnetospheric systems of Jupiter, earth, and perhaps Saturn, and source mechanisms in general. Later experiments will involve larger, more complex antenna systems for finer directional

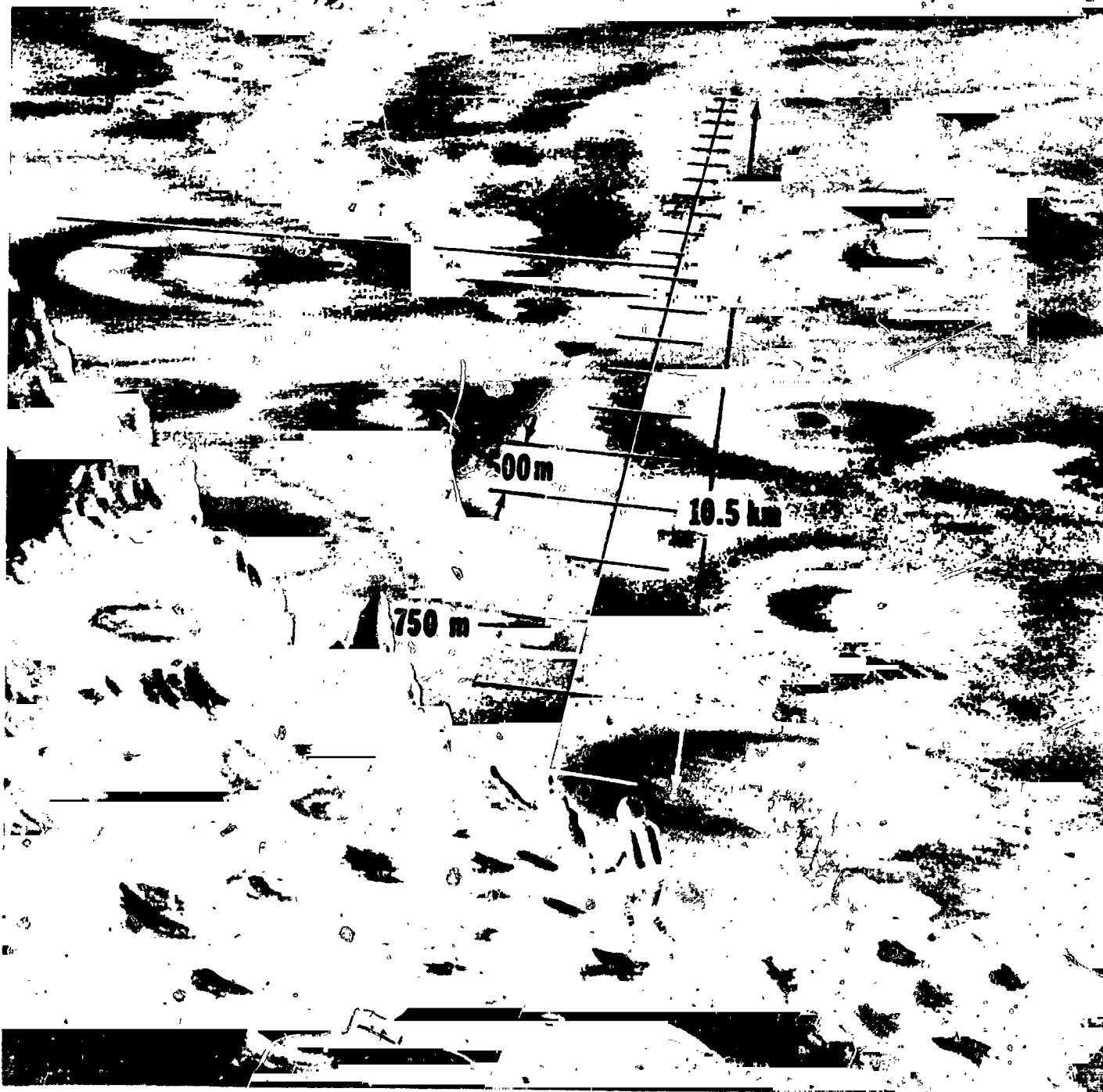


Figure 11. Pencil-Beam Array for Low Frequency Radio Astronomy from the Moon.

resolution and for polarization measurements. Besides the experiments described, there are other worthwhile areas of investigation which have been omitted for the sake of brevity. These include millimeter observations, beacon transmissions between the earth and the moon, lunar ionosphere sounding, point-to-point communication on the moon, and electromagnetic probing of the lunar surface and subsurface.

## REFERENCES

1. Bourdeau, R. E., "Electron Distribution in the Ionosphere", NASA-Goddard, X-615-64-29, January 1964
2. Carpenter, D. L., Proc. of the 14th URSI General Assembly, 1963
3. Lebo, G. R., Decameter-Wavelength Radio Observations of the Planets in 1962, Ph.D. Dissertation, University of Florida, 1964
4. Carr, T. D., et al., "Recent Decameter-Wavelength Observations of Jupiter, Saturn, and Venus", *Astrophys. J.* 134, 105, (1961)
5. Smith, A. G., et al., "Decameter-Wavelength Observations of Jupiter: The Apparitions of 1961 and 1962", *Astrophys. J.* 141, 457, (1965)
6. Alexander, J. K. and R. G. Stone, "Rocket Measurements of Cosmic Noise Intensities Below 5 Mc/s", *Astrophys. J.* 142, 1327, (1965)

## GENERAL REFERENCES

- Aller, L. H., Astrophysics, Ronald Press Company, New York, 1963, 2nd ed.
- Piddington, J. H., Radio Astronomy, Harper & Brothers, New York, 1961
- Smith, A. G. and T. D. Carr, Radio Exploration of the Planetary System, Van Nostrand, Princeton, New Jersey, 1964
- Steinberg, J. L. and J. Lequeux, Radio Astronomy, McGraw-Hill Book Company, Inc., New York, 1963

# REMOTE SENSING WITH OPTICAL CROSS-CORRELATION METHODS

By

F. R. Krause (

Aero-Astroynamics Laboratory

and

M. J. Fisher )

| Illinois Institute of Technology Research Institute,

## ABSTRACT

N67-24276

Our basic concept is to employ the cross correlation of two narrow light beams for remote sensing. The problem with most optical methods such as schlieren, shadowgraph systems or spectrometers is that the received signal is always integrated along the line of sight. However, we want information for a particular spot along the line of sight. To this purpose we adjust a second beam to intersect the first at the point of interest. The integration along the two beams is then eliminated by a cross correlation of the detected fluctuations. This paper indicates how this new concept of combining standard spectroscopy with a statistical cross correlation analysis might be used for dynamic and kinematic studies such as the formation and motion of water vapor or dust clouds, the dynamics and production of the ozone layers, and the generation and motion of radiation belts.

The concept has been demonstrated successfully by measuring the turbulent fluctuations in subsonic jets. The main problems in AAP applications are formulated in terms of questions, such that the background information becomes apparent which is needed to establish the feasibility of particular experiments.

## INTRODUCTION

The cross correlation of optical signals has been used for remote sensing in jet shear layers [1]. Concentration fluctuations of a water vapor fog could be resolved with good accuracy in space and time [2]. In principle, the method should also work on an atmospheric scale. Experimental investigations about the generation and motion of atmospheric constituents such as clouds, nuclear debris, ozone, radiation belts, etc., offer an exciting challenge. We will now give a simplified version of our new remote sensing concept and outline some of the problems, which one would have to overcome in atmospheric applications.

### THE CROSSED BEAM CONCEPT

Remote sensing of distant light sources like planets is based on a fundamental theorem of geometrical optics, which states that the spectral radiance,  $I$ , of a source and its image are equal, if one neglects light extinction and emission along the line of sight. The spectral radiance of a distant source is therefore accessible through the spectral radiance of its image on the exit slit of a monochromator, as shown in fig. 1. Source area,  $\Delta A$ , and wave length interval,  $\Delta\lambda$ , are set by the optical filter. The solid angle,  $\Delta\vartheta$ , into which the exit slit radiates, is set by the photodetector. Therefore, the received radiative power is directly proportional to the spectral radiance,  $I$ , of the distant source:

$$I(\vec{x} \rightarrow -\infty, t, \lambda) = I_s(t, \lambda) = \frac{w(\vec{x} \rightarrow +\infty, t, \lambda)}{\Delta A \Delta\vartheta \Delta\lambda} = I_d. \quad (1)$$

However, if the line of sight goes through the atmosphere, the detected spectral radiance  $I_d(t, \lambda)$  is changed due to the light extinction or emission in the detector's field of view. In the two limiting cases of dominant extinction or dominant emission, the change in spectral radiance

$$I_d(t, \lambda) = I(\vec{x} \rightarrow +\infty, t, \lambda) = I_s(t, \lambda) e^{-\int_{-\infty}^{+\infty} K(\vec{x}, t, \lambda) dx} \quad (2)$$

may be expressed by integrating the extinction or emission coefficient

$$K(\vec{x}, t, \lambda) = \frac{1}{I} \frac{\partial I}{\partial x} = K(\vec{x}, \lambda) + k(\vec{x}, t, \lambda). \quad (3)$$

In astronomy and optical communication, these effects are a nuisance. From an atmospheric science point of view, they can be used to study the thermodynamic properties of the atmosphere, since the extinction coefficient  $K$  is uniquely determined by the thermodynamic properties.

The problem with local measurement of atmospheric properties is how to retrieve the local information, that is buried in the integrated signal. A solution is only possible by repeating the remote sensing as a function of the remaining independent variables, such that some mathematical transformation can be used to extract the local extinction coefficient.

Several authors [3 - 8] used the remaining space variables  $y$  and  $z$  and had to assume axial symmetry. This assumption can be made in the study of single rocket exhaust and flames but not in the atmosphere. Another group [9 - 15] used the dependence on optical wave length  $\lambda$ . They subdivide the line of sight into as many zones as there are isolated molecular bands, and need some advance knowledge about the spatial distribution of temperatures and concentrations. The method worked on a package of controlled burners [16]. In the atmosphere, a larger number of isolated bands which are free from scattering, and the advance knowledge are hard to find. However, the "zonal approximation" should be considered as a backup of our cross correlation method, since it does give mean value information, which we cannot obtain.

We use the time aspect to retrieve the local information. Consider the experimental arrangement on fig. 2. Two lines of sight intersect in an atmosphere-fixed point. These lines define a plane which we shall call "turbulence wave front" and a normal in the intersection point  $(x, y, z)$  which is called the wave normal. We then measure the spectral radiance  $I(t, \lambda)$  (radiative power/solid angle, area, and wave length interval) along both fields of view, split off the time average signal,  $\bar{I}$ , cross correlate the fluctuations,  $i(t)$ , and calculate the quantity,  $G$ , as described in fig. 2. Let us assume that the two detecting telescopes have been aligned to the  $y$  and  $z$  axis of a Cartesian, atmosphere-fixed coordinate system. Each line of sight is denoted by an  $y$  or  $z$  subscript and each point on the line of sight by the distances  $\eta$  or  $\zeta$  relative to the intersection point. The quantity  $G$  is then equal to



$$G(\vec{x}, \lambda) = \frac{\overline{i_z(t, \lambda) i_y(t, \lambda)}}{\overline{I_y} \cdot \overline{I_z}}. \quad (4)$$

The interpretation of the measured quantity  $G$  follows by relating it to the local fluctuations,  $k$ , of the extinction coefficient. We have shown that  $G$  is equal to an area integral over the space time correlation function [17],

$$G(\xi, \tau, \lambda)_{\vec{x}} = \iint_{-\infty}^{+\infty} \overline{k(x, y, z+\xi, t, \lambda_1) k(x+\xi, y+\eta, z, t+\tau, \lambda_2)} d\eta d\xi, \quad (5)$$

provided that the following assumptions are met:

1. The number of statistically independent atmospheric disturbances is small enough to avoid a cancellation of the integrated fluctuation.
2. The integrated fluctuation of the extinction coefficient is small enough to permit linearization.
3. The light source fluctuations and the atmospheric fluctuations are statistically independent.
4. The fluctuations of the two light sources are uncorrelated.
5. Either extinction or emission dominates the change of the detected radiative power.

The first assumption is not very restrictive since the integrated mean value would still be large. Furthermore, the local fluctuation,  $k$ , does not have to be small; only the integral over statistically independent fluctuations is assumed to be linearized. In the very few cases where these weak restrictions are not met, one can possibly choose another wave length,  $\lambda$ , where the second assumption is met. The other assumptions can

mostly be met by a suitable experimental arrangement. Therefore, the result of equation 5 appears to be sufficiently general for atmospheric applications.

Two important conclusions can be derived from equation 5:

1. For a pair of statistically independent light sources, the source characteristics do not have to be known. The method would work for any source, such as ground beacons, the sun, or reflected sunlight.
2. The random nature of turbulent fluctuations assures that integrand drops to zero over distances which are comparable to a typical eddy size. This explains, qualitatively, why the cross correlation partially eliminates the usual optical integration along a line of sight.

According to equation 5, the crossed beam correlation works whenever the wanted signal is common to both lines of sight. The way in which the wanted signal is then pulled out of the integrated signal may be described best by splitting each of the integrated signals in two parts. The first describes the contribution of the "correlated volume" where the integrand of equation 5 does not vanish. The second part describes the rest of the integrated signal. Multiplying the fluctuations of the two integrated signals then leads to four products. Three of these change between positive and negative values in a random fashion. If we now average these products over time, their mean value will go to zero, whereas the deviation from the mean will increase with the square root of time.

The fourth product describes the contribution of the correlated volume, which is common to both lines of sight. The associated product is always positive and its summation over time should increase linearly with time. Therefore, it will be the dominant one, if one goes on adding long enough. Even small contributions at the beam intersection can be pulled out provided (1) the integrated signals show detectable fluctuations and (2) the combination of light source fluctuations, shot noise and instrument noise is not orders of magnitudes larger than the root mean square value of the integrated signal.

#### MEASURABLE TURBULENCE PARAMETERS

The optical integration is restricted to the wave front. Along the wave normal, no integration takes place and local information inside a correlated volume may be obtained by repeating the crossed beam experiment for several beam separations along the normal as shown in fig. 3. The space separation,  $\xi$ , describes the minimum beam distance, which defines the wave normal. Also a time separation is introduced electronically by a time delay unit. As will be discussed later, the measured signal,  $G$ , then approximates a two-point product mean value, which would have been measured by point probes on the wave normal.

$$\frac{G(\xi, \tau, \lambda)_{\vec{x}}}{G(0, 0, \lambda)_{\vec{x}}} = \frac{\overline{i_z(t) i_y(t+\tau)}}{(\overline{i_z(t) i_y(t)})_{\xi=0}} \cdot \frac{(\overline{i_y})_{\xi=0}}{(\overline{i_y})_{\xi \neq 0}}$$

$$\approx \frac{\overline{k(x, y, z, t, \lambda) k(x+\xi, y, z, t+\tau, \lambda)}}{\overline{k(x, y, z, t, \lambda) k(x, y, z, t, \lambda)}} \quad (6)$$

The position of these imaginary point probes is indicated on fig. 3 by two dots. Thus, all turbulent properties, which are commonly derived from two-point product mean values, may also be approximated with the crossed beam method.

The local integral scale of turbulence is defined by averaging the area under the covariance curve  $G(\xi, \tau=0)$  and its graphical evaluation is illustrated on fig. 3.

Plotting the beam correlation coefficient against the time separation instead of the space separation, fig. 4, allows bulk convection speeds to be read. For a given space separation, the correlation will reach a maximum at the time that the turbulent eddies need to travel from the upstream to the downstream beam. The time lag,  $\tau_M$ , which is indicated by the maximum is therefore a direct measure of convection speeds.

Power spectra and cross power spectra are defined by a Fourier transform of the measured autocorrelation,  $\xi = 0$ , and cross correlation  $\xi \neq 0$ , curves. They may be calculated using the digital computer programs, developed for the analysis of mechanical vibrations [18].

A study of the envelope to the time correlations,  $r(\tau)_\xi$  provides a measure of the temporal rate of decay of turbulent eddies as seen by an observer moving with the convection speed. Therefore, the decay of this correlation curve to  $1/e$  of its original value is used to define the average eddy lifetime. The Fourier transform of this envelope would indicate the dominant frequencies which are felt by the moving observer.

Summarizing the graphical evaluations sketched in figures 3 and 4, we find that the crossed beam method remotely senses integral scales of turbulence, convection speeds, eddy lifetimes and spectra for arbitrarily chosen atmosphere-fixed points at which a beam intersection can be achieved.

The above turbulent properties are only approximations, since the optical integration over the wave front does catch fluctuations which are not felt by the point probe on the wave normal. However, our experiments in a subsonic jet have shown that weighting of contributions close to the wave normal is sufficiently strong to yield a good spatial resolution. One may thus expect a good spatial resolution on a wide range of other turbulent motions which are of practical interest.

The absorption (or emission) spectrum of extinction coefficients is commonly used to find species concentrations and temperatures of both stagnant gases and small scattering particles. Adjusting the optical wave length of the crossed beams to chosen atomic lines and/or molecular bands, one might therefore extend the spectroscopic methods from stagnant media to inhomogeneous turbulent flows and study multicomponent or two-phase flow phenomena.

### EXPERIMENTAL VERIFICATIONS

The most revealing and instructive test of the crossed beam concept is to compare the optical approximation of point measurements with known hot-wire measurements. The initial portion of an axisymmetric free shear layer was chosen for the experiments since (1) the turbulence is anisotropic and inhomogeneous and (2) convection speeds, turbulence scales and eddy lifetimes are well documented in the literature.

All measurements were taken in a subsonic ( $M = 0.2$ ) air jet exhausting through a one-inch diameter nozzle into the atmosphere (fig. 5). Light extinction was achieved by spraying a small amount of liquid nitrogen into the settling chamber. This produces small water droplets in the exhaust flow which attenuate the crossed beams by scattering. Later, the nitrogen injection was replaced with water spray which offers a better control of the tracer concentration.

A diagram of the optical and electronic hardware is also shown in fig. 5. A plane mirror and a spherical mirror collect the light from a powerful mercury arc and transmit it as a parallel beam through the jet. A similar mirror combination projects the arc image on the entrance slit of a grating spectrograph. The aperture stop in front of the spectrograph is set at a beam diameter of 2 mm. The photomultiplier then scans the first order spectrum of the grating. In this way, the wave length interval  $\Delta\lambda$  and the wavelength  $\lambda$  are adjusted by the width of the monochromator slit and the rotation of the grating, respectively. By exchanging light sources, gratings, and photodetectors, the system is able to cover the spectrum from the vacuum ultraviolet ( $\lambda = 1200\text{\AA}$ ) to the infrared ( $\lambda = 25 \mu$ ).

The above light source and detector arrangement is used to generate two beams, one in a horizontal and one in a vertical direction (fig. 5). A lathe bed provides a mechanical support which allows us to align the beams parallel to the nozzle exit plane. A beam separation in the stream-wise direction gives the longitudinal turbulence scales and convection speeds. Transport of the whole system allows us to repeat the measurements for all axial and radial traverses of the jet.

A typical sample of optically measured two-point product mean values is shown in fig. 6. The beam intersection was adjusted to the center of the free shear 1.5 to 3 exit diameters downstream of the nozzle exit. The general appearance of the temporal correlation functions is indistinguishable from published hot-wire results. The turbulent convection process is clearly indicated by the displaced maxima for finite beam separation. The monotonic decay of the envelope shows the decay of the moving eddies. Measuring the time delay for which this curve falls to  $1/e$  of its initial value yields a value of 880 microseconds. This is in excellent agreement with the hot-wire data of Ref. 19 from which we estimate that the value of the time scale for our experimental conditions should be 920 microseconds.

Fig. 7 shows the same experiment under different conditions. The initial intersection point of the beams was six diameters from the jet exit, (i.e., at  $x/D = 6.0$ ) instead of at  $x/D = 3.0$ . Instead of using liquid nitrogen to generate a water droplet fog tracer, a small nozzle was mounted in the jet settling tank which sprayed water droplets into the flow to form the tracer fog. The curves do appear to fall onto or close to an envelope as required. Unfortunately, the range of beam separations used is not sufficient to merit the extrapolation of the curve to  $1/e$  of its initial value. Therefore, the moving axis autocorrelation curve has been obtained from the hot-wire data of Ref. 19 and is shown as the dotted line superimposed on the measured cross correlation curve.

The spatial resolution of the crossed beam method seems very encouraging, considering that the envelope from the hot-wire data exactly matches the individual curves from the crossed beam method. For the moving frame, the optically measured autocorrelation agreed with the hot-wire curves, regardless of whether nitrogen or water spray was used as a tracer.

A quantitative comparison of individual cross correlation curves  $G(\tau)_r$  has been based on the indicated convection velocities. These velocities have been evaluated graphically following the procedure of fig. 4. To increase the accuracy, we have always used more than one

curve. The chosen set of beam separations was plotted as a function of the time lag values  $t_M$ , which were indicated by the common tangent of envelope and individual cross-correlation curve. The result is a straight line which is shown in the upper part of fig. 7. The desired convection speed follows from the slope of this line.

The results of all convection velocity determinations made using the crossed beam correlation system to date are summarized on fig. 8, where they are also compared with hot-wire data from Reference 19. It is shown that in the outer portion of the shear layer ( $\eta > 0$ ) the convection velocity determinations agree within experimental accuracy. For  $\eta < 0$ , however, the crossed beam results tend to follow the mean velocity profile ( $U/U_0$ ) rather than attain the constant maximum value observed for hot-wire data. This was not an unexpected result. All convection velocity results presented in Reference 19 were taken at axial stations where the potential core still exists. At these positions, the large difference between the mean velocity and convection velocity has not been completely explained. However, Davies [20] has discussed the subject recently, and it does appear that the closer correspondence between mean and convection velocity observed here is to be expected when a measuring technique other than the hot-wire anemometer is being used, and/or the potential core no longer exists.

The optically measured results in fig. 8 were only 0.2 inch apart. This is much smaller than the geometrical shear layer thickness ( $\approx 8''$ ) which is indicated by the hot-wire results. Thus, convection speeds have been resolved inside a correlated volume by moving the intersection point.

#### REMOTE SENSING FROM LOW AND HIGH EARTH ORBITS

The concept of remote sensing through cross correlation of optical signals is not restricted by scale and the method should, at least in principle, work also over atmospheric distances. Mounting the two photodetectors on satellites instead of on the ground or on airplanes has the advantages of a larger field of view, quicker scanning, and avoiding vibration problems. In addition to these benefits, which were discussed during the recent remote sensing symposium, the satellite detector can use reflected sunlight, whereas the ground detector is restricted to scattered sunlight. The orbital detector can thus use absorption spectroscopy for a detailed study of atmospheric and ionospheric constituents, whereas the ground detector is restricted to refractive index fluctuations, the interpretation of which is very difficult.

Sometimes the fluctuations of atmospheric constituents may be detectable with the radiative power, which is provided by reflected and scattered sunlight or by emission inside the detector's field of view. In such a case, the optical hardware which would be needed for the crossed beam method is quite similar to that which is developed for the photographic surveys of the earth and the moon. Both applications require a diffraction-limited telescope coupled with an optical filter which selects the ultraviolet, visible, and infrared regions of the spectrum. The main difference consists in replacing the camera with a sensitive phototube and to fly two satellites instead of one.

Two orbital detectors could adjust their lines of sight to intersect on an atmosphere-fixed spot, by continuously turning the telescope during the fly-by. Remote sensing of disturbances around the intersection might be feasible for both the lower and the upper atmosphere. Typical lines of sight are sketched on figures 9 and 10.

We suggest to study the feasibility of remote sensing in the lower atmosphere with respect to the following AAP experiments:

1. The generation and motion of nuclear debris using emitted radiation during the night cycle.
2. The motion or generation of clouds, dust, and iodine using reflected sunlight (fig. 9).

Remote sensing in the upper atmosphere is intriguing, if the use of ground beacons can be avoided. The optical path between the upper atmosphere and the orbital telescope is then short. Also, oxygen has extremely high absorption peaks in the ultraviolet, such that the motion of very diluted oxygen might still be detectable. We suggest to study the feasibility of remote sensing the upper atmosphere and ionosphere with respect to the following AAP experiments:

1. The motion or generation of ozone using direct or scattered sunlight, fig. 5.
2. The motion or generation of radiation belts using the emitted electromagnetic radiation. Both vertical and horizontal motions might be studied using the same arrangement sketched for the upper atmosphere (fig. 10).

## PROBLEMS

The main problems with the crossed beam method are as follows:

1. To find an atmospheric constituent that produces detectable fluctuations of the integrated signal along accessible lines of sight.
2. To reduce light source fluctuations, shot noise and instrument noise to root mean square levels, which have the same order of magnitude as the integrated signal.
3. To have the lines of sight intersect on an atmosphere-fixed spot for an observation time, which is sufficiently long to pull the local signal out of the integrated signal and the combined light source noise, shot noise and instrument noise.

These problems are formidable and they may prohibit some of the applications that were outlined in the previous section. However, since we can pick the detected radiation from any region of the electromagnetic spectrum and since the orientation of the lines of sight may be chosen arbitrarily, we believe that there is at least one interesting AAP experiment where the above problems may be overcome through special test arrangements. Such an experiment presents an exciting challenge, since the dynamic behavior of the atmosphere, or radiation belts could be added to the "static" mapping on oceanic, geographic, and atmospheric surveys.

Several facts about atmospheric constituents and optical AAP hardware must be collected before we could decide the feasibility of particular experiments. These facts have been identified in the previous discussions and may be summarized by the following questions:

1. Which constituents of the lower atmosphere, such as clouds, dust and nuclear debris, produce detectable fluctuations within a response time of 0.1 second along a line of sight which traverses the entire atmosphere?
2. Do the usual constituents of the upper atmosphere and ionosphere such as ozone produce detectable fluctuations along a line of sight which traverses the outer portions of the upper atmosphere.



3. Do reflected or scattered sunlight and/or radiation belts put enough radiative power into the orbital detector's field of view to reduce the shot noise below the expected signal levels, considering the telescopes and optical filters which are developed for other AAP missions?
4. Does the continuous motion of the detector's field of view lead to fluctuations of the reflected sunlight that are comparable to the signal fluctuations?
5. For which observation time is it possible to have the narrow fields of view intersect at a fixed point on the lower and the higher atmosphere and what are the beam diameters and pointing accuracies?
6. Is it possible to extend these applications to the complete day and night cycle by using ground beacons besides reflected and scattered sunlight?

## REFERENCES

1. Fisher M. J., F. Krause, "Local Measurements in Turbulent Flows through Cross-Correlation of Turbulent Fluctuations," NASA TMX 53295, dated April 1, 1965.
2. Fisher, M. J., and T. H. Black, "Optical Measurements with High Temporal and Spatial Resolution," IITRI progress report M6114-18, contract NAS8-11258, dated December 1965.
3. Nestor, O. H., and H. N. Olsen, SIAM Rev. 2,200 (1960).
4. Freeman, M. P. and S. Katz, J. Opt. Soc. Am. 50,826 (1960).
5. Bockasten, K., J. Opt. Soc. Am. 51,943 (1961).
6. Barr, W. L., J. Opt. Soc. Am. 52,885 (1962).
7. Herlitz, S. I., Arkiv Vysik 23, 571 (1963).
8. Paquette, D. R. and W. L. Wiese, Appl. Opt. 3, 291 (1964).
9. Howard, J. N., D. E. Burch, and D. Williams, J. Opt. Soc. Am. 46, 186, 237, 242, 334, 452, (1956).
10. Burch, D. E., and D. Williams, Appl. Opt. 1, 473 (1962).
11. Burch, D. E., D. Gryvnak, E. B. Singleton, W. L. France and D. Williams, Air Force Cambridge Research Labs., Report AFCRL-62-698 (1962).
12. Edwards, D. K., J. Opt. Soc. Am. 50, 617 (1960).
13. Plass, G. N., J. Opt. Soc. Am. 48, 690, 1958.
14. Plass, G. N., J. Opt. Soc. Am. 50, 868, 1960.
15. Plass, G. N., J. Opt. Soc. Am. 49, 821, 1959.
16. Tourin, H. and B. Krakow, Appl. Opt. 4, 237, 1965.
17. Krause, F. R., and M. J. Fisher, "Optical Integration over Correlation Areas in Turbulent Flows," 5th International Congress on Acoustics, Paper K65, Liège, Belgium, September 7 to 14, 1965.
18. NASA, Geo. C. Marshall Space Flight Center, The Vibration Manual, (1 ed) 1964.

REFERENCES (Continued)

19. Davies, P. O. A. L., M. J. Fisher, and M. T. Barrat, J. Fluid Mech., Vol. 15, pp. 337-367.
20. Davies, P. O. A. L., "Near-Field Generation by Intense Turbulence," 5th International Congress of Acoustics, Liège, Belgium, paper L53.

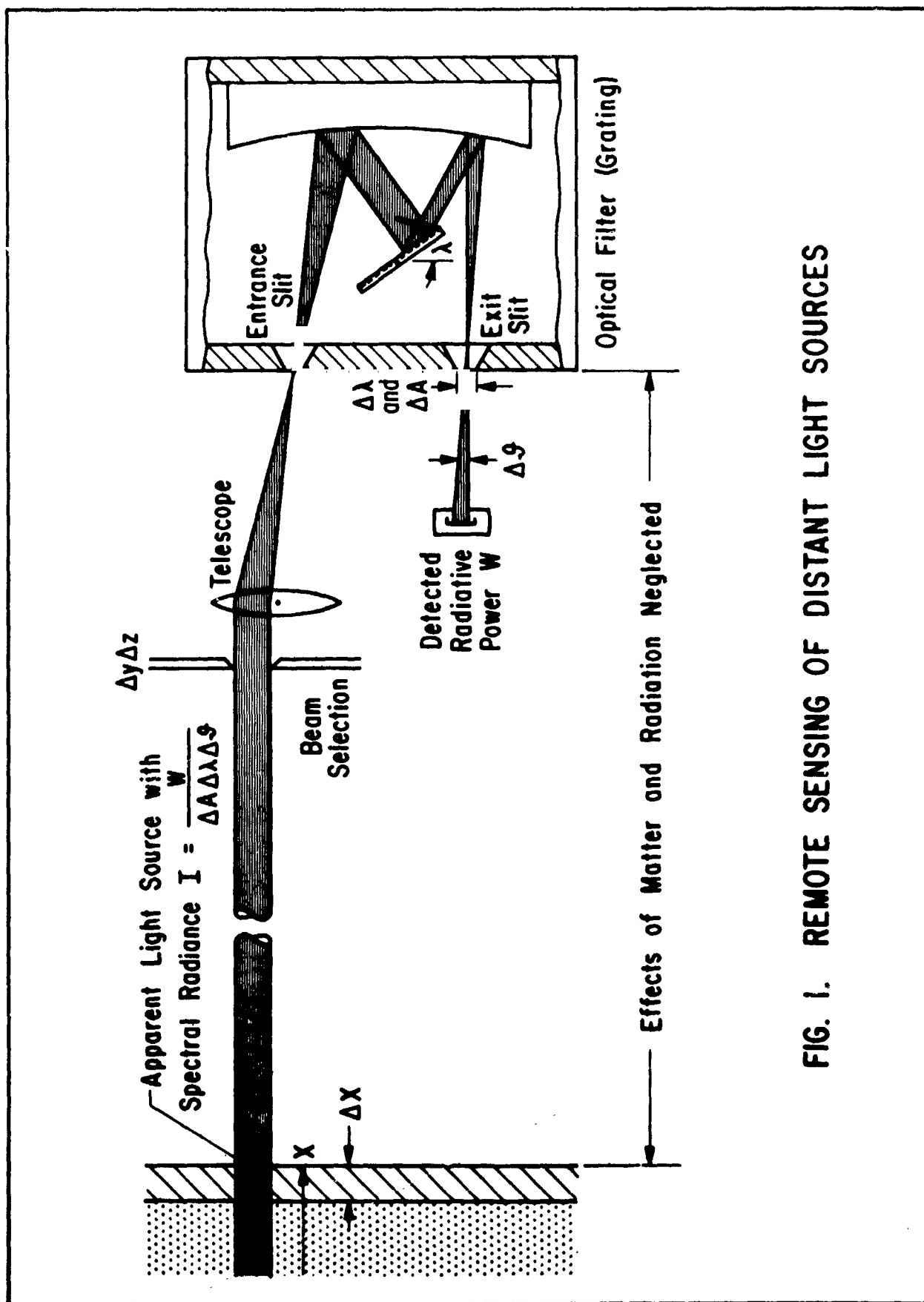
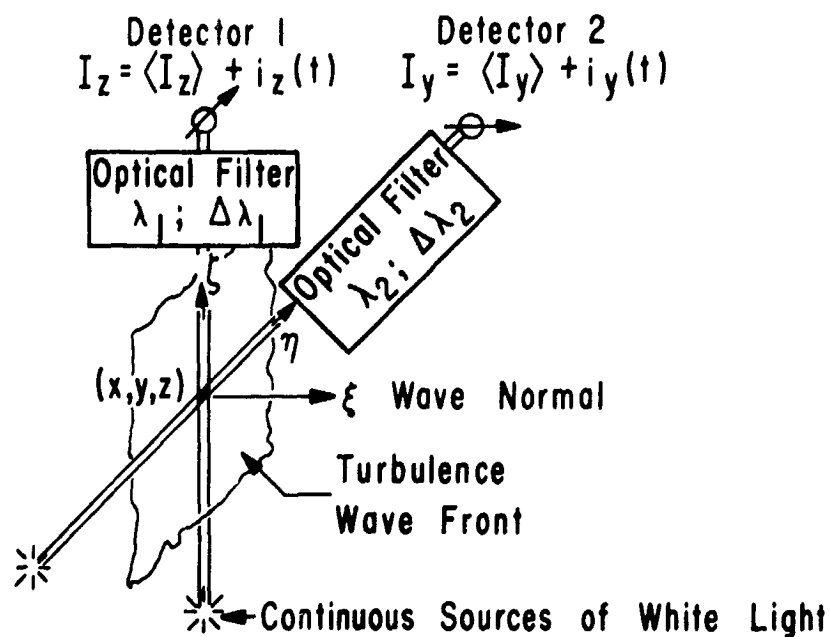


FIG. 1. REMOTE SENSING OF DISTANT LIGHT SOURCES



The Crossed Beam Technique Area Integrates the Cross Correlation Function of Light Extinction Coefficients,

$$K = \bar{K} + k$$

$$\frac{\langle i_z(t) i_y(t+\tau) \rangle}{\langle I_z \rangle \langle I_y \rangle} = G(\xi, \tau, \lambda) = \int_{-\infty}^{+\infty} \int_{-\infty}^{+\infty} k(x, y, z + \zeta, t, \lambda_1) k(x + \xi, y + \eta, z, t + \tau, \lambda_2) d\eta d\zeta$$

FIG. 2. REMOTE SENSING OF LOCAL TURBULENCE THROUGH CROSS CORRELATION OF OPTICAL SIGNALS

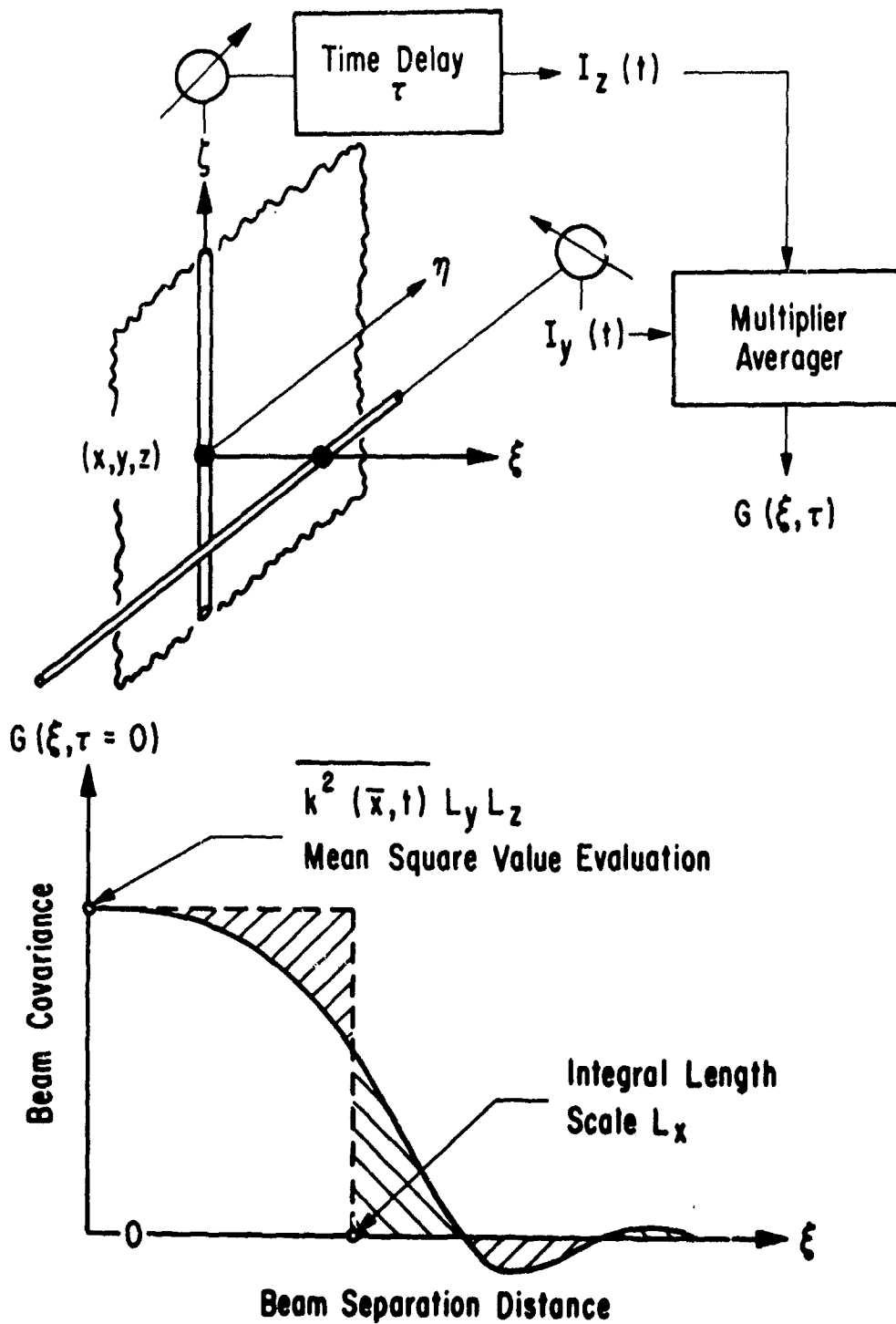


**FIG. 3. TURBULENCE SCALES AND INTENSITIES FROM CROSSED BEAM COVARIANCE MEASUREMENTS**

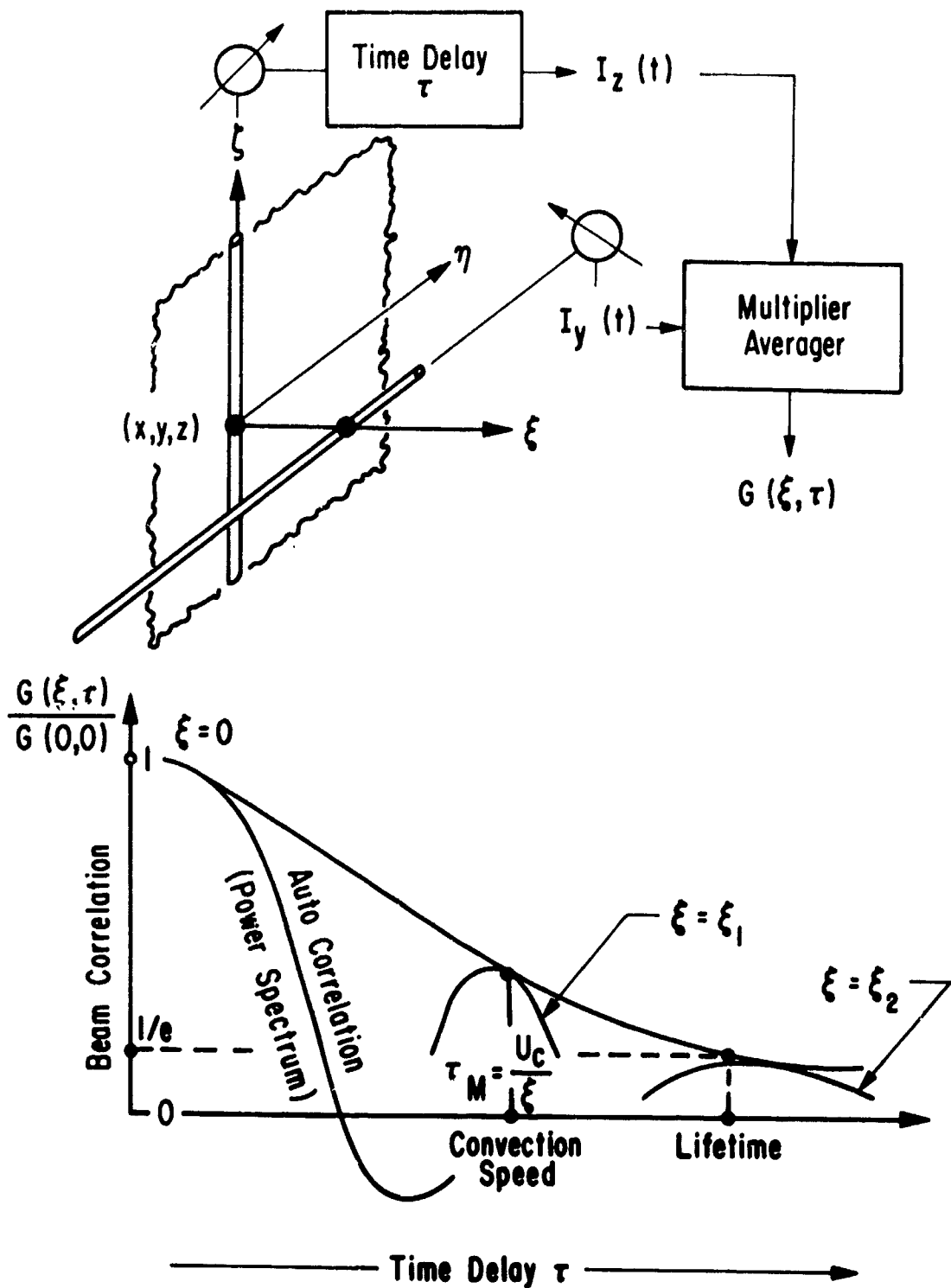


**FIG. 4. LOCAL POWER SPECTRA CONVECTION SPEEDS AND EDDY LIFETIMES FROM CROSSED BEAM CORRELATION MEASUREMENTS**

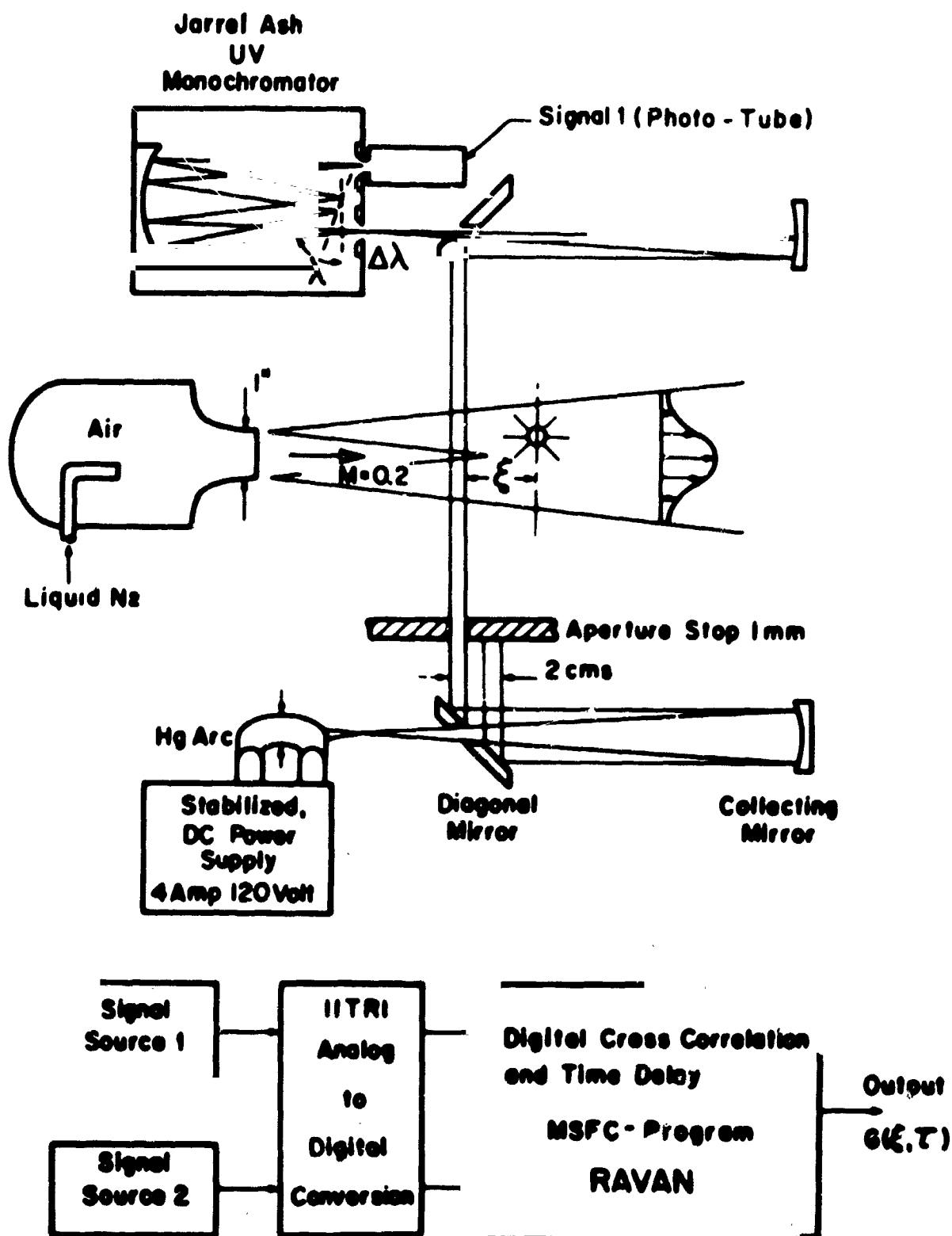


**Fig.5 THE FIRST CROSSED BEAM CORRELATOR**



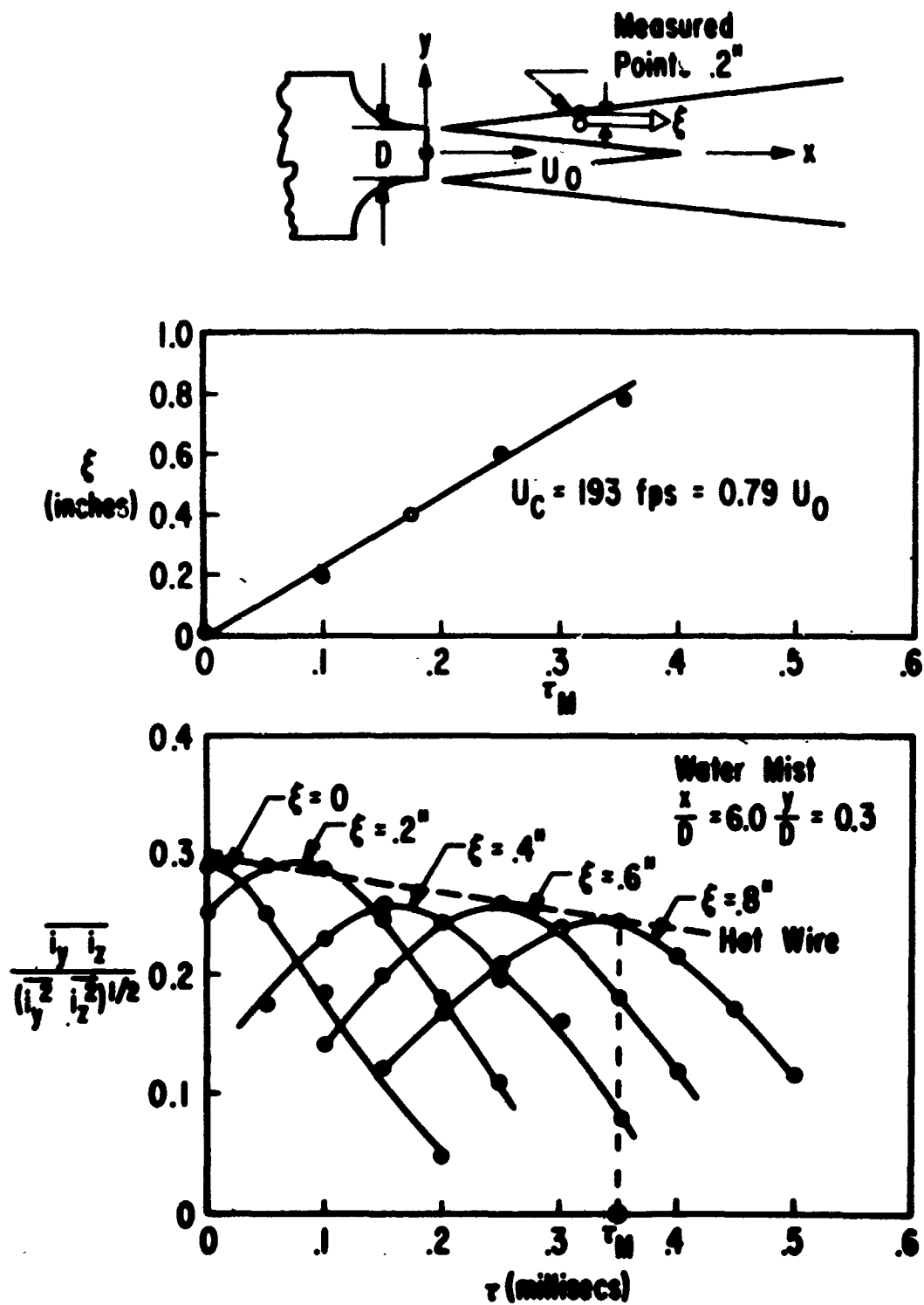


FIG. 6 CROSS CORRELATION  
WITH DOWNSTREAM BEAM SEPARATION

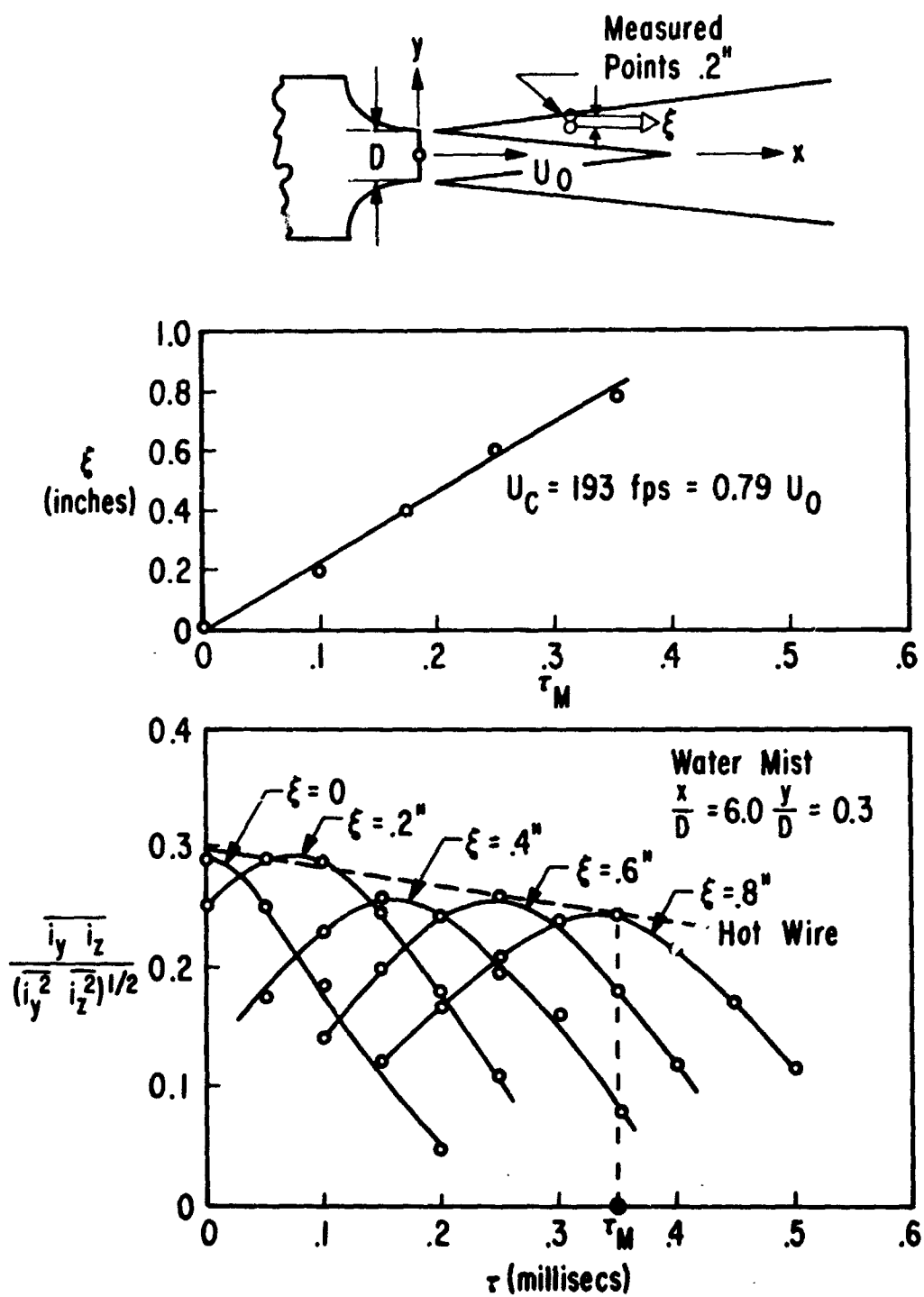


FIG. 7. CROSS CORRELATION  
WITH DOWNSTREAM BEAM SEPARATION

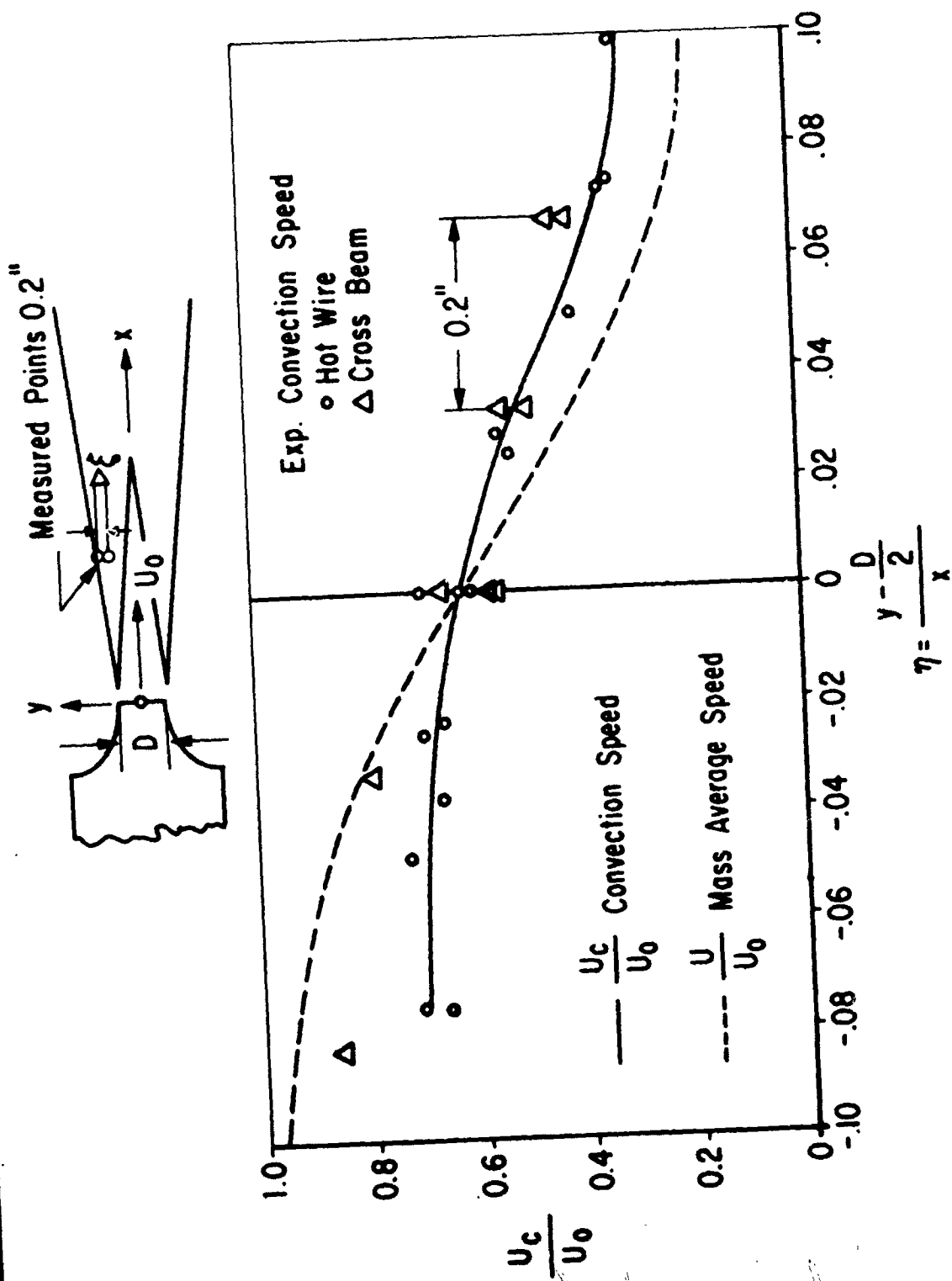


FIG. 8. VELOCITY PROFILES FROM HOT WIRE AND CROSS BEAM METHODS

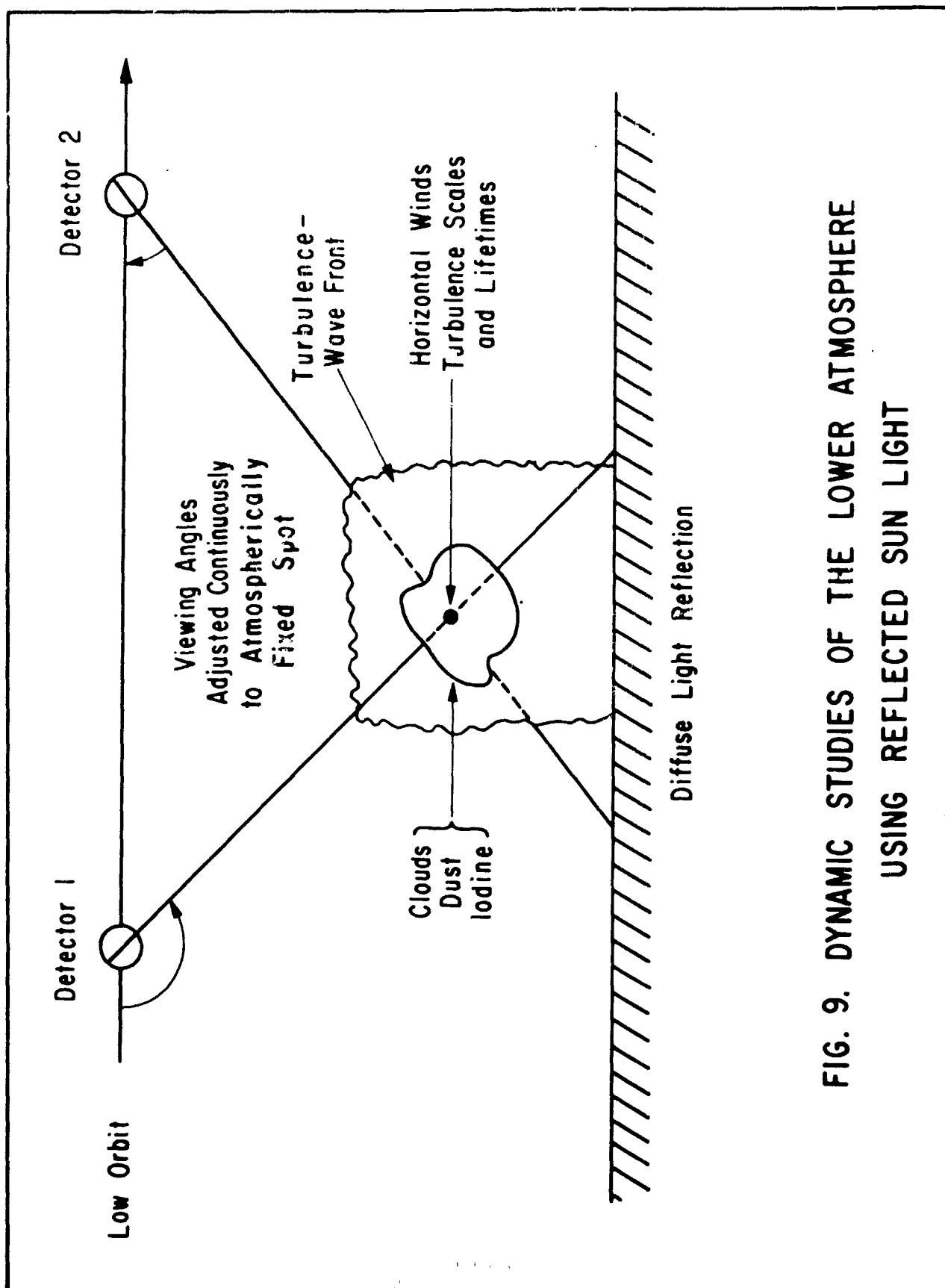
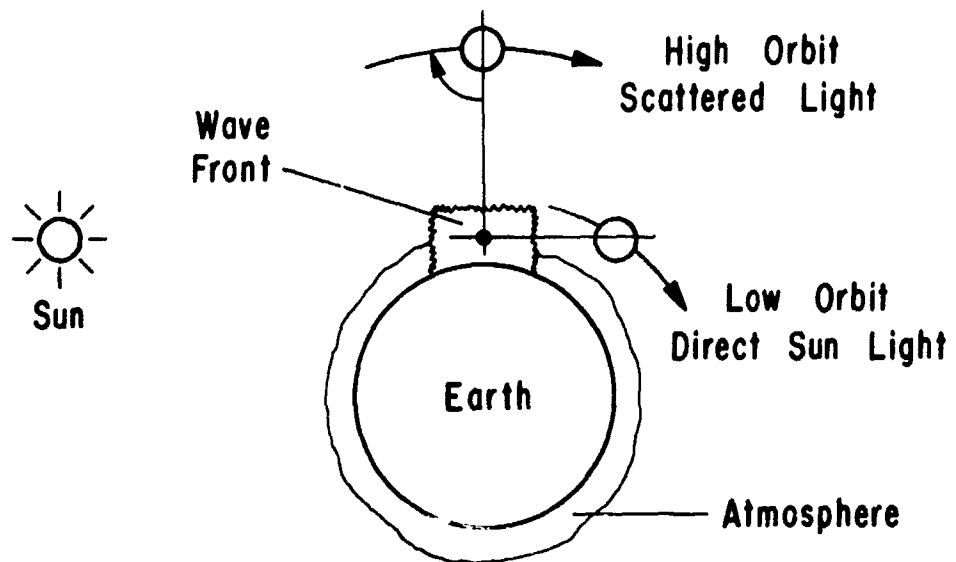
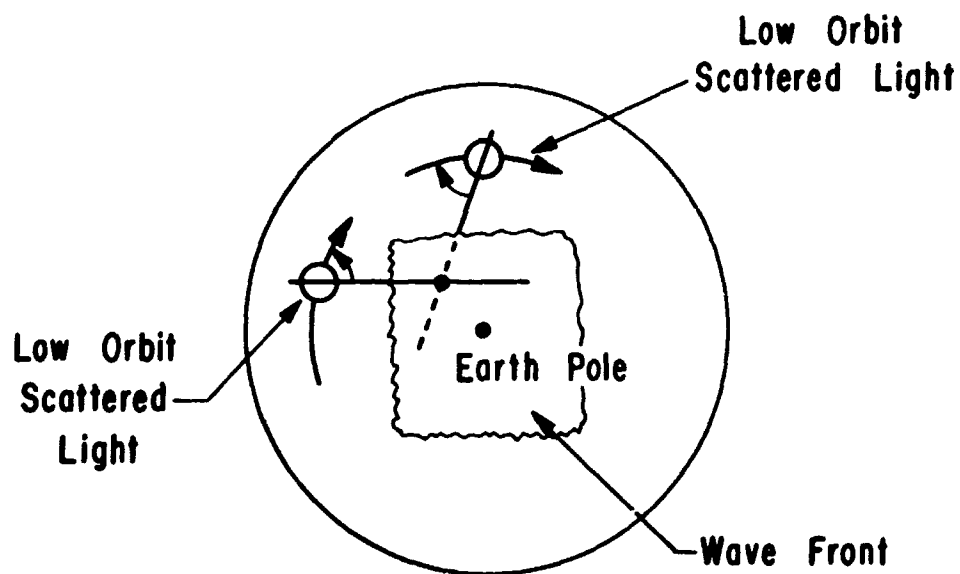


FIG. 9. DYNAMIC STUDIES OF THE LOWER ATMOSPHERE  
USING REFLECTED SUN LIGHT



a. HORIZONTAL MOTION



b. VERTICAL MOTION

FIG. 10. DYNAMIC STUDIES IN THE UPPER ATMOSPHERE

# SOME CONCEPTS FOR AN EMPLACED SCIENTIFIC STATION ON THE LUNAR SURFACE

By

{ Russell D. Shelton }  
/ Marshall Space Flight Center }

## INTRODUCTION

**N67-24277**

The concept for an emplaced scientific station (ESS) has been studied at the Marshall Space Flight Center for the past year and at the Westinghouse Corporation under contract NAS8-20245. The figures used in the following discussion were taken from the Westinghouse Final Report,\* and the concepts discussed resulted from a joint study effort.

The ESS concept was based on the following general scientific objectives (emphasizing that observations were to be made for a year):

1. To acquire data on the lunar interior by means of seismic detectors and probe measurements
2. To monitor the lunar atmosphere
3. To measure fluxes of nuclear and meteoroid particles
4. To study the moon as a possible base for improved planetary and stellar astronomy

The physical requirements of the ESS are such that it can be stored in a volume of  $0.6 \text{ m}^3$ , weigh 290 kg, or less, and packaged suitably for astronaut deployment. For seismic purposes, the ESS array would consist of 4 stations: a central station for communications with the earth as well as for experimentation and three identical satellite stations deployed at  $120^\circ$ -arc intervals on a circle of 8-km radius.

The central and satellite stations would be a standardized package designed to make possible a wide latitude in the selection of experiments and to support a variety of scientific instruments.

---

\*Westinghouse group directed by Vernon B. Morris under Contract No. NAS8-20245.

This particular philosophy seems desirable in a situation in which data are being acquired continuously, instrumentation is being improved, and new ideas are evolving.

The packages would use local signal conditioning and passive thermal control to conserve power. The central station would include an orientable platform for a number of observations. The general appearance of the deployed central and satellite stations of the ESS related experiments are shown in Figs. 1 and 2.

The design of the ESS was based on the considerable interest in the measurement of physical quantities which vary in time and on experiments which depend on simultaneous readings from points widely separated on the lunar surface. Considerable emphasis was given to the discussions held at Woods Hole and Falmouth, Massachusetts in the summer of 1965 [1, 2]. The satellite stations transmit data to the central station where it is stored for subsequent transmittal to earth. Astronauts will deploy the central and satellite stations; therefore, their safety and work limitations must be considered. Presumably, the ESS will use man's capabilities to obtain effective data for applications in future mission planning with a minimum of effort.

Experiments yielding information on the lunar atmosphere and surface rank high in priority with emphasis on the experiments which might possibly suffer from contamination by radioactive materials or exhaust gases from landing rockets. An attempt will be made to study the lunar subsurface by active and passive seismic techniques and the surface structure by radiometric and probe techniques.

There are a number of observations of the earth which can be made effectively from a lunar base, particularly of phenomena which are seasonal and which cover a large part of the surface of the earth



FIGURE 1 - DEPLOYMENT OF THE CENTRAL SCIENTIFIC STATION





FIGURE 2 - DEPLOYMENT OF A SATELLITE STATION

at one time. Examples of such phenomena would be ionospheric disturbances, atmospheric activity, oceanographic properties, and items of geodesic interest. It is possible also that a number of observations of interplanetary space, the sun, and the planets could be made more effectively from the moon.

It is probably true that no disciplines of the physical sciences have been able to do more with small clues than astronomy, cosmology, and astrophysics. Consequently, it could be of great interest to continue on a long-term basis the improved stellar, interstellar, galactic, and intergalactic observations possible from the lunar surface.

Naturally, by the time an emplaced scientific station on the lunar surface is possible, there will be considerably more added to the background of instruments available for space measurements. It is a widely accepted axiom that maximum use should be made of proven instruments which, if man-operated, can give the largest amount of significant data at the lowest cost. Instrument groupings which provide redundancy, continuity, and inter-related measurements are of course desirable. Naturally, the planning for any experiment involves some estimate of weight, size, power, and environmental control. Operational constraints such as pointing or handling, instrument sensitivity to RFI and environmental changes, command and control requirements, etc., must also be considered.

## RADIATION MEASUREMENTS

There are a number of radiation experiments which can be done on the lunar surface. Of almost universal interest is the total radiation dosimeter which provides an indication of the astronauts' exposure.

The vibrating-reed ionization chamber is probably a good choice for such an instrument. The nuclear emulsion, which would be returned with the astronauts, still provides one of the most reliable means of identifying many particles and establishing their energy and directional distribution. Other instruments of interest on the lunar surface would include: 1) a magnetometer, which is highly developed at the present time; 2) an electric field meter, which presently is the subject of much discussion; and 3) a VLF meter, which could measure some of the interactions of the solar wind with the moon.

### LUNAR BODY MOTIONS

The lunar body motions can be studied by means of a three-axis passive seismometer, by geophone, tidal gravimeter, or UV telescope. The lunar surface can be studied from the viewpoint of radiometers, borehole temperature probes, and perhaps lasers for mapping and ranging.

The seismic studies will benefit from the largest possible baseline array for information on direction, distance, and depth of lunar tremors. Although a central station and two satellite stations may appear to be sufficient from a theoretical viewpoint, it is felt that, from the viewpoint of reliability and ease of data interpretations, three satellite stations are needed. The stations should be roughly 8 km apart, as shown in Fig. 3.

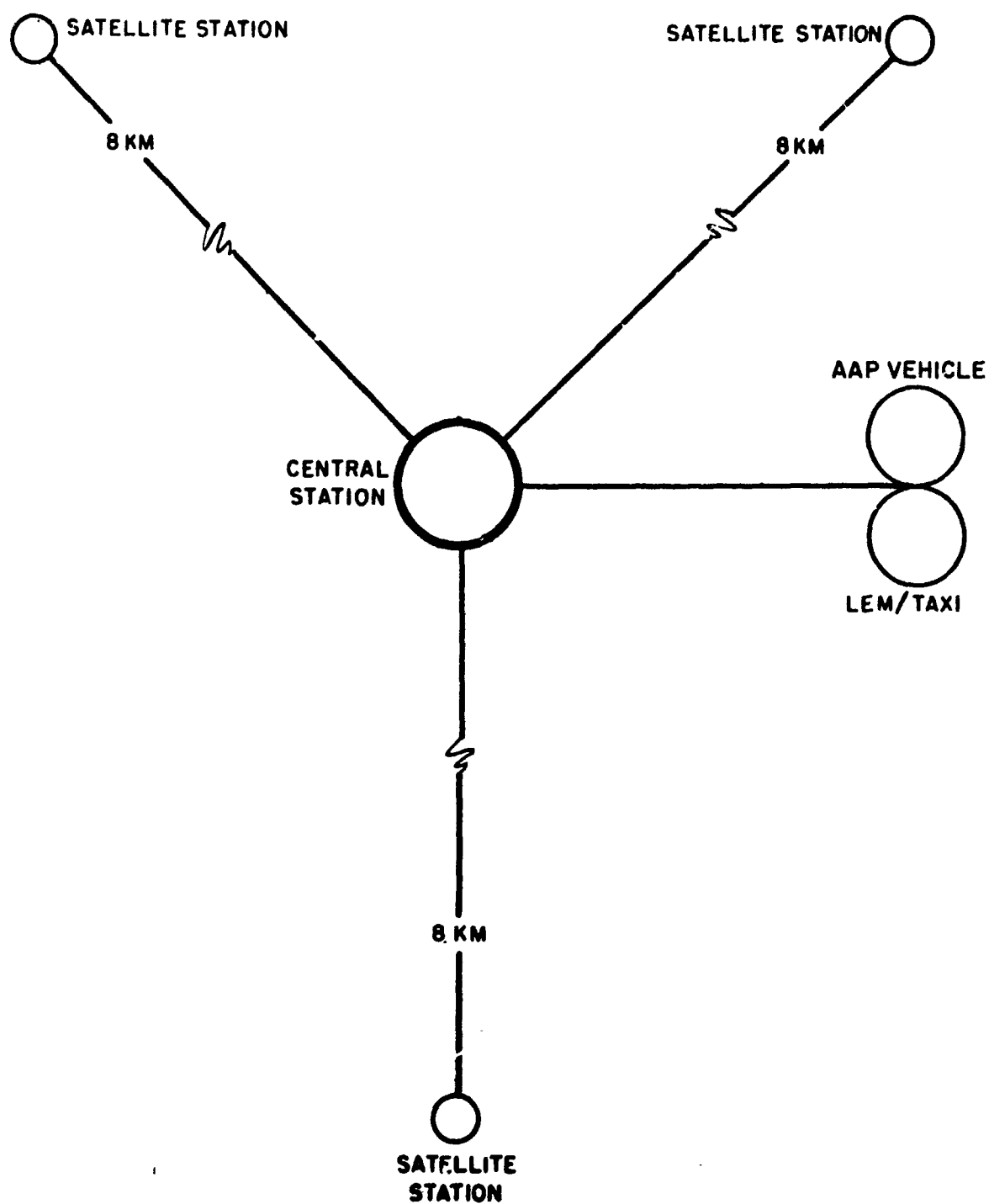


**Figure 3 Arrangement of ESS on Lunar Surface**

## TELESCOPE APPLICATIONS

The observations of the earth and the astronomical studies will probably require the pointing of multiple instruments for simultaneous imaging, and spectrometers will require simultaneous studies at different wavelengths. The most important ingredient of the orientable platform planned for the ESS would be a Cassegrainian-type 12" reflecting telescope.

In assessing the value of a telescope, there are a number of considerations. It is of little use to design a large expensive telescope if there is not a parallel quality in optical accuracy, pointing accuracy, platform stability, and tracking capabilities. The specific capabilities of the ESS should include a lunar seismic and gravity network, a solar astronomy observatory with a 12" diameter telescope with a receiving capability from 10 microns to 1/10 micron, and a radio observatory.

A lunar-based telescope could enjoy several advantages, such as a very long day for thermal equilibrium, no atmospheric absorption, a platform so stable that many good pictures could be taken even if the tracking devices failed, and a good means of tracking lunar landings and astronaut traverses. Image intensifiers for TV transmission and other advantages may make it possible to realize the theoretical capability of a small telescope on the lunar surface. One use of a lunar-based telescope would be to study the lunar motions, some of which are illustrated in Fig. 4, which shows the apparent motion of the earth in the lunar sky.

# FIELD OF EARTH'S MOTION IN LUNAR SKY

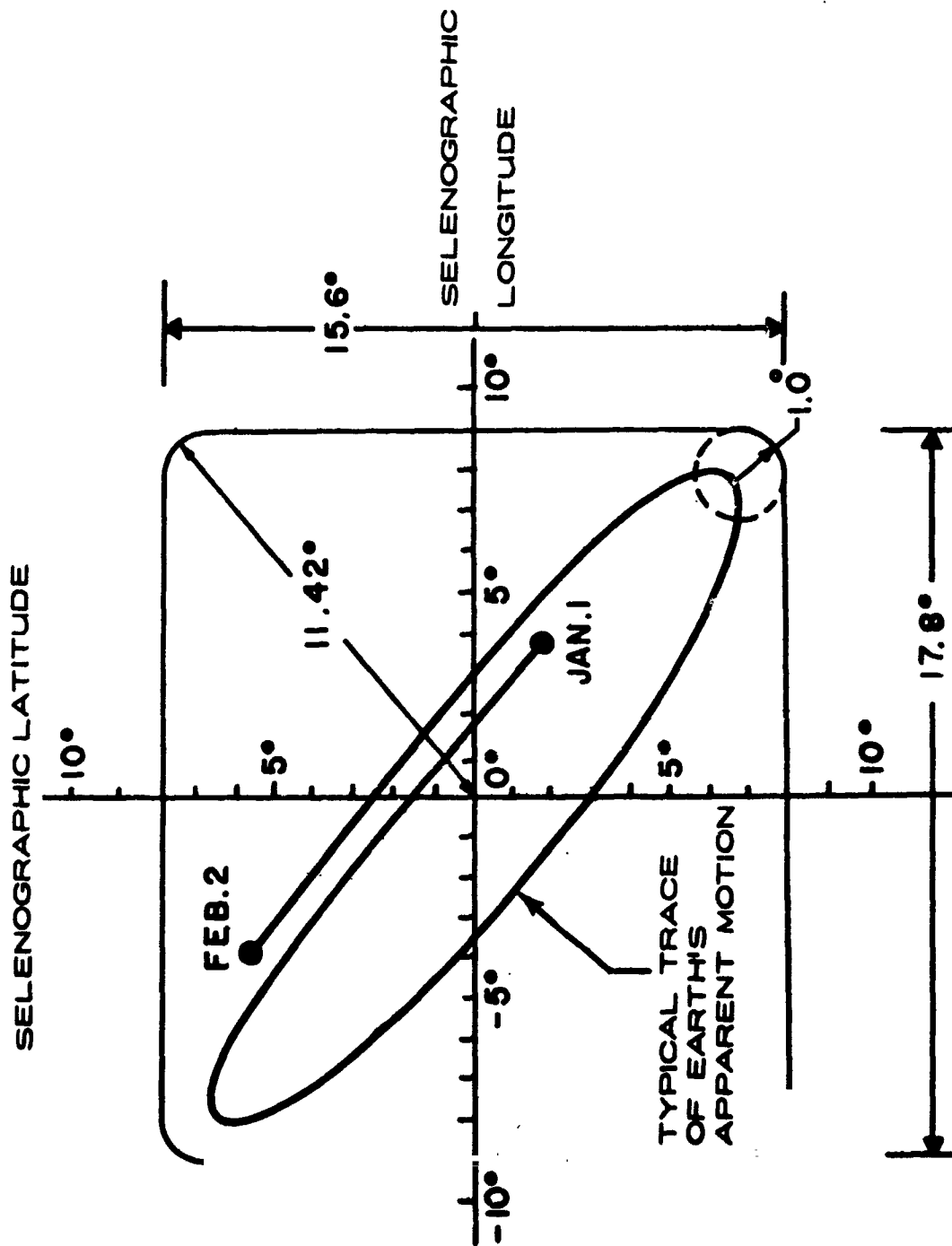


Fig. 4

In the central scientific station the instruments listed in Table I should be available. The listing reflects a crude order of priority which, of course, can be attacked from several viewpoints such as the area of most experimental importance, the interrelationships of various measurements, the reliability and availability of instruments, etc. For example, during the night or day the electric field meter measurement should be associated closely with the solar wind measurements and the magnetometer measurements.

### GENERAL CONSIDERATIONS

The radioisotope thermoelectric generator appears at this time to be the best choice for providing power to the ESS, although it is possible that a regenerative fuel cell plus a solar cell array will be a close contender. The advantages of the RTG power source are that it provides continuous power, is light in weight, occupies a small volume, is reliable, and is a source of heat. The disadvantages are that it presents a heat and radioactivity hazard during handling, requires special arrangements to dissipate (before deployment) the waste heat power, which is roughly 20 times the electrical power output, is of limited availability without long-range program planning, and is quite expensive.

A weight, volume and power summary of the ESS is shown in Tables I and II.

TABLE I      ESS WEIGHT AND VOLUME

	<u>Weight</u>	<u>Packaged Volume</u>
<b>CENTRAL STATION</b>		
<u>Package No. 1</u>		
1. Optical Telescope	20 kg ( 44 lbs)	
2. Pointed Instruments	20 kg ( 44 lbs)	
3. Orientable Platform	23 kg ( 51 lbs)	
<b>TOTAL PACKAGE NO. 1</b>	<u>63 kg (139 lbs)</u>	<b>330 liters*</b>
<u>Package No. 2</u>		
1. Fixed Instruments	51 kg (112 lbs)	
2. Telecom. Subsystem	25 kg ( 54 lbs)	
3. Intercon. Cabling & Connectors	15 kg ( 33 lbs)	
4. Structures	10 kg ( 22 lbs)	
<b>TOTAL PACKAGE NO. 2</b>	<u>101 kg (221 lbs)</u>	<b>220 liters*</b>
RTG Power Supply	25 kg ( 55 lbs)	
<b>TOTAL CENTRAL STATION</b>	<u>189 kg (415 lbs)</u>	<b>550 liters*</b>
<b>SATELLITE STATION</b>		
1. Instruments	14 kg ( 30 lbs)	
2. Telecom. Subsystem	6 kg ( 14 lbs)	
3. Intercon. Cabling & Connectors	5 kg ( 11 lbs)	
4. Structures	2 kg ( 5 lbs)	
5. RTG Power Supply	7 kg ( 15 lbs)	
<b>TOTAL SATELLITE STATION</b>	<u>34 kg ( 75 lbs)</u>	(not included in package No.3)
<b>TOTAL THREE SATELLITE STATIONS</b>	<u>102 kg (224 lbs)</u>	<b>110 liters*</b>
<b>TOTAL ESS</b>	<u>291 kg (639 lbs)</u>	<b>660 liters*</b>

\* Exclusive of power supplies.



TABLE II      MODE 1- DATA COLLECTION

Submode A - Orientable Platform Tracking	
Item	Average Power (watts)
(1) Fixed Instruments	33.5
(2) Pointed Instruments	5.5
(3) Optical Telescope	8.0
(4) Orientable Platform	14.5 or 18.0
(5) Telecommunications	27.7
Total	89.2 or 92.7

Submode B - Transmission of Optical Telescope Video Data

(1) Fixed Instruments	33.5
(2) Pointed Instruments	standby
(3) Optical Telescope	8.0
(4) Orientable Platform	14.5
(5) Telecommunications	46.0
Total	102.0

## REFERENCES

1. NASA 1965 Summer Conference on Lunar Exploration and Science, Falmouth, Mass., July 19 - 31, 1965. Proceedings published by National Aeronautics and Space Administration, Washington, D. C., NASA SP-88, 1965.
2. Space Research Directions for the Future. Report of a study by the Space Science Board, National Academy of Sciences, National Research Council, Washington, D. C., Parts I, II, and III, December 1965, January 1966, and February 1966, respectively.

# **SIMULATED WEIGHTLESSNESS UNDER NEUTRAL BUOYANCY**

By

Robert D. Dean  
and  
Robert P. Langan  
The Boeing Company

**N67-24278**

The use of neutral buoyancy is a relatively new zero-gravity simulation technique that permits measurement of operator performance in full-scale mock-ups with six degrees of freedom. This includes the use of a large water-filled tank in which subjects and work materials are ballasted to approach weightlessness. As a simulation of zero gravity, it is limited by the viscosity of water and resulting hydrodynamic damping effects, which precludes its use when rapid, gross body movements are required of the subject, or when very large objects must be moved. It is also limited by the density of water (800 times greater than air), which precludes gross changes in depth when compressible materials are used. A further limitation is that during deflection, the body entrains the water for a period of time after the initial force of movement disappears. This is equivalent to an apparent increase in mass and results in further deflection.

In a true zero gravity environment, there are no damping effects, no density of the surrounding medium, and no apparent increase in mass. The significance of these limitations will be fully understood only when data obtained in neutrally buoyant environments can be correlated with data obtained in free space. These comparisons will be possible when more complete performance data are available from future manned space flights. In the meantime, the simulation technique is good so long as the limitations are recognized.

In spite of the inherent limitations of neutral buoyancy, experience indicates that it can provide an inexpensive and reliable means of evaluating designs for

space-vehicle hatches, compartments, airlocks, restraints and transfer devices. Comparisons between performance under one-g and neutrally buoyant conditions can provide designers with an understanding of the qualitative effects of zero gravity; some tasks such as hand tool manipulation become more difficult in the neutrally buoyant environment, others such as hatch traverse become easier. Neutral buoyancy can also provide an invaluable training aid, in that it permits practice on performance in an environment that approximates true zero gravity.

Boeing work with neutral buoyancy was begun in September, 1963. Five major studies were conducted from September, 1963, to August, 1965. Early studies were conducted in an underwater facility located in a small lake outside Seattle. Studies are now conducted in a 25-foot diameter tank specifically designed for neutral buoyancy work.

The first study was completed in November, 1963. This study evaluated the effects of neutral buoyancy on the time required to traverse 20- and 28-inch circular hatches. Subjects wore wet suits and scuba equipment ballasted for neutral buoyancy. Average hatch traverse time was approximately half that in the one-g environment.

The second study, in July, 1964, was designed to evaluate the effects of neutral buoyancy on man's ability to manipulate hand tools (wrenches and screw drivers). One task, fastener removal, was used throughout. Again, subjects wore wet suits and scuba equipment modified to achieve neutral buoyancy (Fig. 1). There was a 50 percent increase in average time required to remove fasteners compared to one-g control data.

The third study, completed in February, 1965, was concerned with extravehicular assembly. The subject wore a full pressure suit (3.5 psig) and life support backpack. The suit and equipment were neutrally buoyant (Fig. 2).

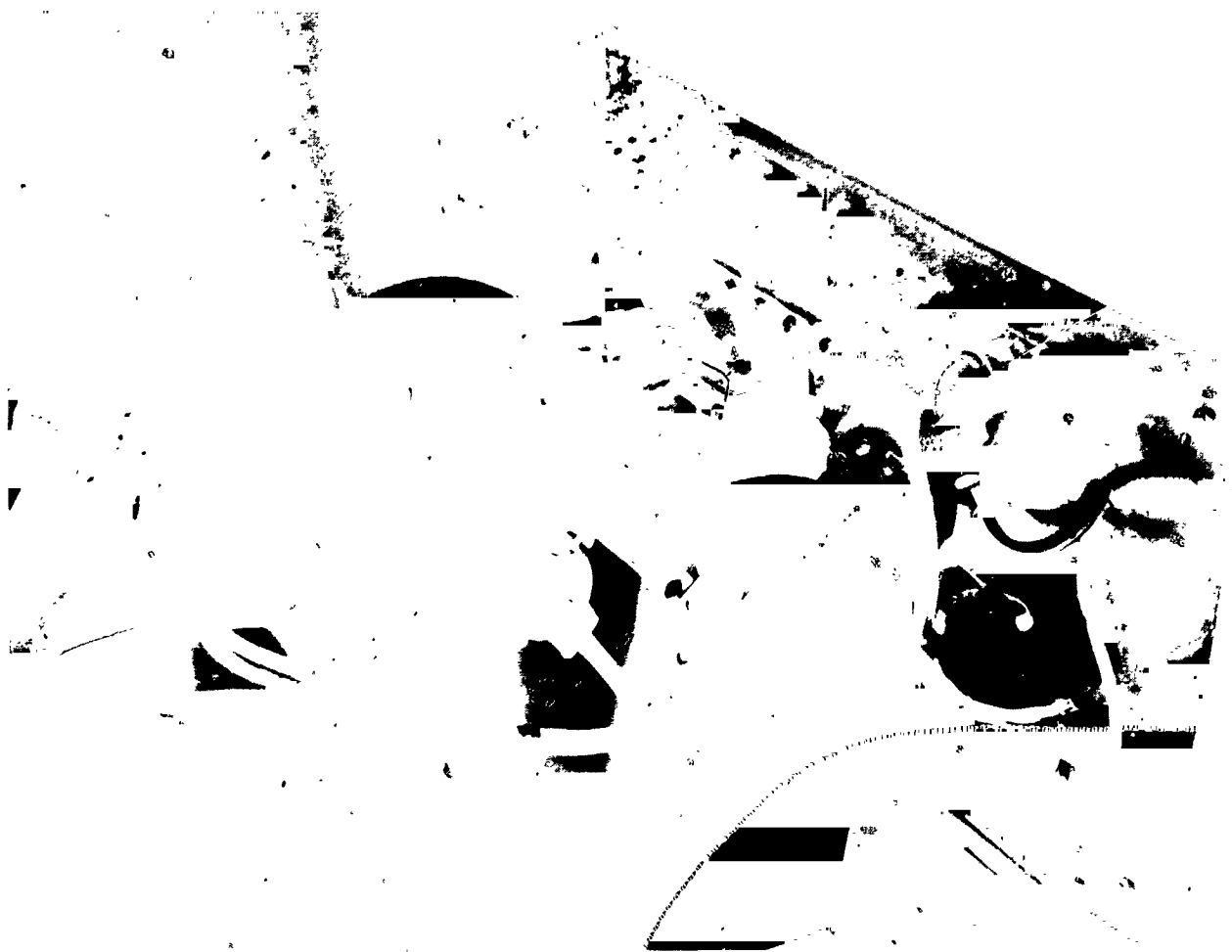


**FIGURE 1. SUBJECT PERFORMS FASTENER REMOVAL**

Lighting was arranged to provide a single source of high-intensity illumination to simulate sunlight. The task was to assemble a 12-foot length of triangular truss structure. The results suggested that assembly operations could be performed with greater ease while wearing a 3.5 psig pressure suit under water than under shirt-sleeve conditions in a one-g environment. A significant result of this study demonstrated the need for self-locking connecting devices to prevent them drifting away. A need was also indicated for diffuse reflecting surfaces on the gloves and for semi-rigid non-snagging tethers.

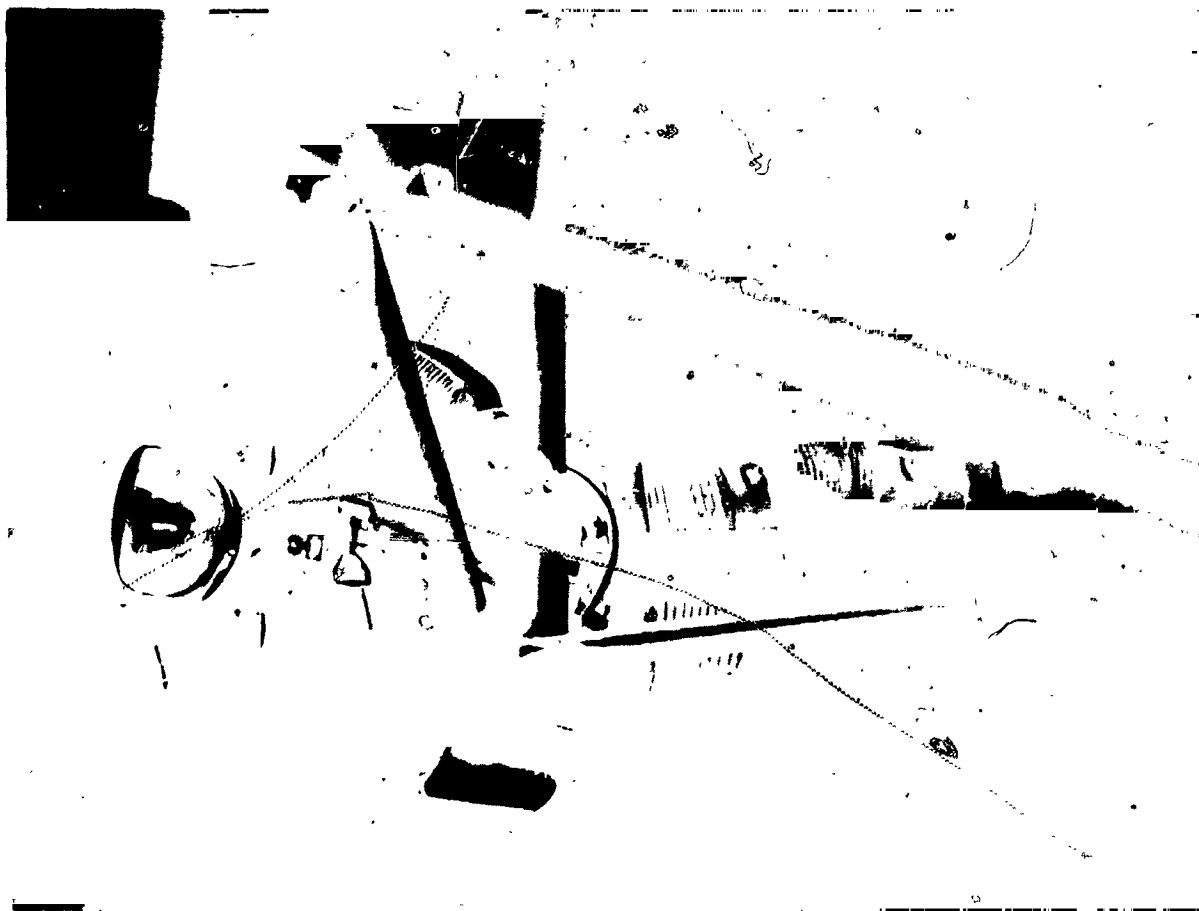


**FIGURE 2. EXTRAVEHICULAR ASSEMBLY**

The fourth study, completed in April, 1965, was to assess a variety of restraint concepts. These included hand rails in traversing a 30-inch circular hatch (Fig. 3), toe rails (Fig. 4), lap belts (Fig. 5) and Velcro tape as restraints for performing console operations, and Velcro tape as an aid in traversing the length of a compartment. The subjects wore coveralls designed for neutral buoyancy simulating shift-sleeve clothing that may be worn in future space vehicles and a standard scuba regulator connected to a specially designed scuba chest pack. The results indicated that although the hand rails had no effect on the time required to traverse the hatch, they did provide greater control over body movements in preventing inappropriate actions such as stepping on console



**FIGURE 3. USE OF HAND RAIL**

controls. Toe rails proved to be very helpful in positioning the body. Both lap belt and Velcro tape were unacceptable as restraints when performing console operations. The lap belt made it difficult for subjects to change position, and the Velcro tape gave insufficient support. Velcro tape increased average compartment traverse time by a factor of five.

The fifth study, completed in August, 1965, had two objectives. The first was to assess a prototype airlock design to determine whether it was large enough to permit the astronaut to turn around inside the airlock (Fig. 6), to



**FIGURE 4. USE OF TOE RAIL**



**FIGURE 5. USE OF LAP BELT**



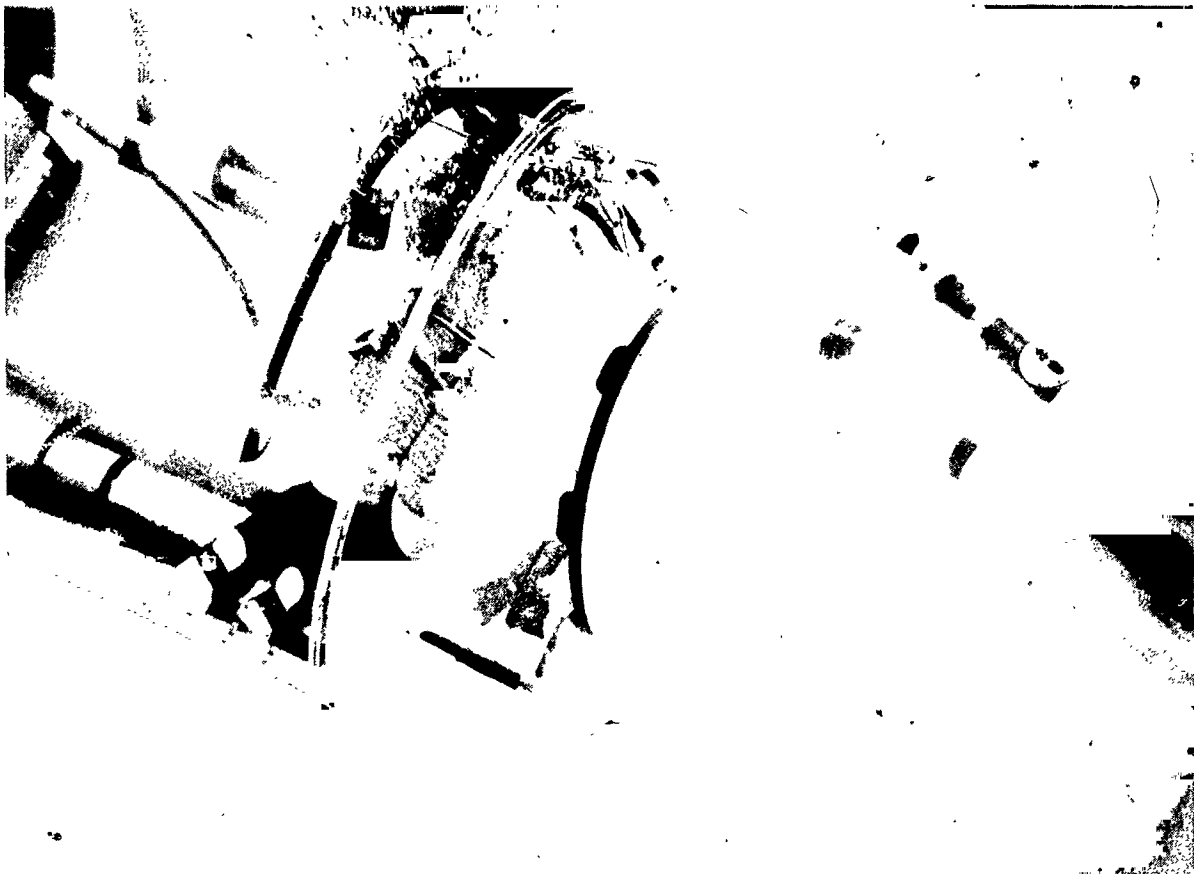


**FIGURE 6. ASSESSING PROTOTYPE AIRLOCK DESIGN**

permit exit and entry through an extravehicular hatch (Fig. 7), and to permit donning and doffing of a simulated Apollo suit. The second objective was to evaluate the effects of weightlessness on ergometric performance in terms of push, pull and torque (Fig. 8). The study results indicated that the airlock design permitted performance of all three tasks. The ergometric data indicated that weightlessness degraded the ability to push and to torque, but facilitated the ability to pull. Ability to pull was apparently improved as a result of greater freedom to position the legs. Comparisons between data obtained under different suit pressures indicated that increasing suit pressure from 0 to 3.5 psig resulted in poorer performance.



**FIGURE 7. EXIT THROUGH EXTRAVEHICULAR HATCH**



**FIGURE 8. SUBJECT PERFORMS TORQUE TEST**

The neutral buoyancy experimental approach used at Boeing has been one of repeated measures on a small number of subjects in a wide variety of experimental conditions. Despite the obvious difficulty of generalizing to a larger population, this approach has four distinct advantages. First, a large sample of subjects, trained to work under water in a full pressure suit, is not available. Second, equipment of sufficient reliability and quantity to permit rigid experimental research is still under development. For example, a minimum of seven pressure suits, modified for underwater operations, would be required to conduct a study involving five subjects ranging in anthropometry from 5th to 95th percentile; Boeing presently has three such suits (Fig. 9). A third advantage

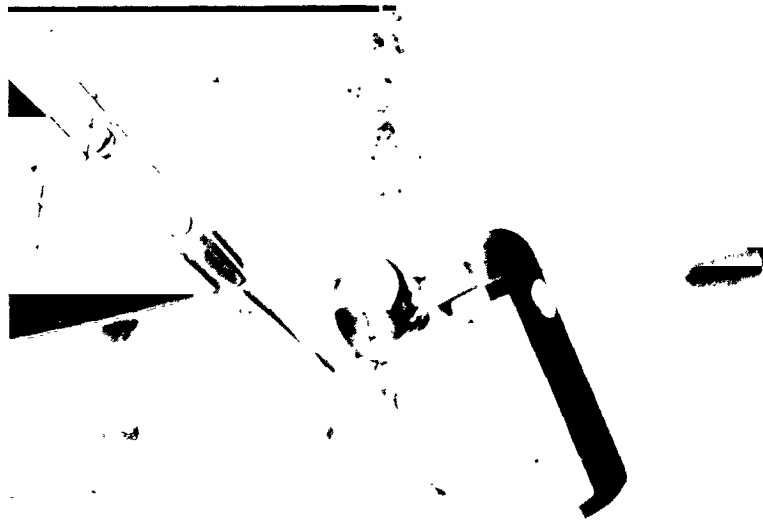


**FIGURE 9. VIEW OF PRESSURE SUIT**

is that critical problem areas can be identified without incurring the high cost of obtaining normative data on large subject samples. The fourth and most significant advantage of the present experimental approach is the use of neutral buoyancy as a design tool. When used as a design tool, rather than as a research device, neutral buoyancy becomes a part of an iterative process in which a design concept (for example, a restraint system) is initially formalized and then tested (Fig. 10). The initial concept is rejected, or modified as a result



**FIGURE 10. CHECKOUT OF DESIGN CONCEPT FOR A RESTRAINT SYSTEM**

of the test data, and tested again. This process of successive design modification and testing is continued until an acceptable design is developed. When the

neutral buoyancy simulator is used in this manner, there is rarely sufficient time between successive iterations to obtain data on more than a few subjects. Experience has shown that intelligent redesign can typically be undertaken after only a few preliminary observations in the neutrally buoyant environment. When this occurs, as it usually does, there is little justification for continuing an extensive evaluation of a design concept that is already in the process of modification.

Perhaps, in summation, the advantages of time and cost should be mentioned. Compared with Keplerian trajectory flights, in which weightlessness is achieved only for some seconds, the time advantage is tremendous. Testing in the neutral buoyancy facility can be conducted during a normal eight-hour day or on a multiple shift basis. Since aircraft and flight crews are obviously not necessary, there is a very respectable cost reduction in equipment and training, as well as a significant reduction of hazard. Further, materials and designs to be tested are limited in size only by the volume of the facility used.

The potential as well as the immediate value of this technique as an aid to engineering analysis and design has been proven. It is relatively simple and economical to use in comparison with other methods, but the returns can be great.

## REFERENCES

1. Chaffee, J. W. , "Project OGER (0-g Effects Research): Hatch Traverse Study," Boeing Intercompany Coordination Sheet 2-5483-EP-132, November 26, 1963.
2. Mabry, J. E. , "Maintenance Performance as a Function of 0-g Effect (Neutral Buoyancy)," Boeing Document D2-90762-1, June 18, 1965.
3. Chaffee, J. W. , "Assembling Large Structures in Space: Impressions of a Pressure-Suited Operator in 0-g Effects Environment," Boeing Document D2-82210-1, March 19, 1965.
4. Schlinder, R. A. , Mabry, J. E. , Chase, G. A. , and Elworth, C. L. , "Human Factors Studies for Manned Space Stations," Boeing Document D2-82232-1, April 23, 1965.
5. Mabry, J. E. , "Shirt-Sleeved Crew Compartment Tasks as Performed by Neutrally Buoyancy Operators," Boeing Intercompany Coordination Sheet 2-7720-82, April 15, 1965.
6. Dean, R. D. , Langan, R. P. , and Erickson, E. R. , "Airlock Assessment and Ergometric Evaluation Under Simulated Weightlessness (Neutral Buoyancy)," Boeing Document D2-90793-1, August, 1965.

DEVELOPMENT OF A DEVICE FOR PHYSICAL  
CONDITIONING DURING WEIGHTLESSNESS

By

( Gary Chase, Caswell Grave, John Goode, Gary Graham )  
| The Boeing Company

ABSTRACT

**N67-24279**

From analytical studies it was deduced that an exercise device, which would impart pulsatile head-to-foot acceleration to human subjects to maintain their gravity tolerance, would be useful in space vehicles. The criteria required that the subjects receive plus and minus 2G longitudinal acceleration, each acceleration to last three milliseconds. The completed device resembled a double trampoline, the subject vibrating on a cart between the impacting surfaces. A concept for a light-weight model for eventual application in a space station was also developed.

## INTRODUCTION

The maintenance of the functional integrity and physical well-being of astronauts during exposure to a weightless environment has generated considerable interest in the Aerospace community. It is generally agreed that some physical activity (exercise) will be desirable on short missions and necessary to prevent physical debilitations on longer, perhaps, 30-day missions.

Development of apparatus to achieve the goal of maintenance of well-being requires consideration of the undesirable physiological changes which would contribute to loss of physical capabilities of the astronaut. Experience has shown that prolonged lack of exercise leads to reduction of physical strength and the ability to do strenuous physical tasks. Among other things, research has revealed a decreased ability to transport oxygen in the blood stream to the muscles, as well as calcium loss from the bones. An equally significant finding is that humans in simulations of weightlessness tend to lose their ability to stand erect in the earth's gravitational field without fainting. This ability is termed orthostatic tolerance. Apparatus development should thus provide methods to flex the muscles, stress the skeleton and provide a force or treatment to substitute for gravity in the normal one-g environment.

No work has clearly shown that there is an efficient substitute for voluntary exercise in muscular and skeletal maintenance although many techniques such as massage, electrical stimulation and passive exercise have been employed. An acceptable device for maintaining well-being would thus



incorporate the ability to engage in voluntary exercise. Many approaches have been used, and such devices as bungee exercisers, isometric devices, dynamometers, rowing machines and bicycle ergometers, all of which can be used in space vehicles, have been developed. A shortcoming of this group is that they do not prevent the development of some degree of deconditioning.

The development described here was designed for testing in an experimental simulation - bed rest - of the zero-g environment. It provides conditioning for the muscular, skeletal and cardiovascular systems. This is done by imparting cyclic, pulsatile accelerations along the long axis of the body. A runner-mounted carrier supports the subject in a face-up, horizontal position and is free to move back and forth between two vertical, opposed trampolines (Fig. 1). The man oscillates by bouncing between the trampolines over a distance necessary to develop the desired acceleration-time profile. Such treatment provides a substitute for the conditioning normally afforded humans in their daily, one-g living in which gravitationally induced hydrostatic forces in the circulatory system are thought to play a significant role. It was originally hypothesized (Grave et al, 1964<sup>(1)</sup>) that oscillating linear acceleration would maintain normal cardiovascular reflexes if the duration of the acceleration was sufficient to cause fluid shifts in the circulatory system.\*

\*The hypothesis was based on observations by Whedon et al (1949)<sup>(2)</sup> that oscillation of bed rest subjects on a Sanders bed largely prevented the development of orthostatic intolerance during simple bed rest, as reported by Deitrick et al (1948)<sup>(3)</sup>. Other pertinent observations by Graveline (1962)<sup>(4)</sup> showed that intermittent venous occlusion by cuffs on the leg and arm prevented a similar development of orthostatic hypotension during water immersion. It was further suggested that fluid shifts which accompanied operation of the oscillating bed and occlusive cuffs could be produced by pulsatile accelerations (vibration) with much shorter time factors than were employed with the oscillating bed (105 seconds per cycle) or cuffs (120 seconds per cycle). Studies by Stapp (1961)<sup>(5)</sup>, Kornhauser (1961)<sup>(6)</sup>, Thompson (1962)<sup>(7)</sup>, and Gage (1950)<sup>(8)</sup> showed that the threshold for fluid shifts probably lies in the range from 70 to 350 milliseconds. Accordingly we designed our device to furnish the subject an impact  $\pm g_z$  for a duration of at least 300 milliseconds, with a peak force of  $\pm 2 g$ .

We have conducted laboratory studies in the Biotechnology organization of The Boeing Company over the past two years using long term bed rest as the method of simulating the effects of reduced gravity on human systems. During these tests, subjects were given daily exposures to passive and/or active peak rebound accelerations of 2 g's at each end of the bed travel. Only the active mode provides a significant amount of isotonic exercise. This exercise provided test subjects with the physical conditioning required to complete tests of orthostatic tolerance without major ill effect. A detailed report of the procedures and results of these tests will be presented elsewhere.

#### DETAILS OF MACHINE CONSTRUCTION

The carrier is mounted on precision ball bushings running on hardened steel shafts. The shafts are supported between canvas tarpaulins suspended by shock cord on frames at either end of the shafts, resulting in a double trampoline device (Figure 1). The platform is padded for comfort and fitted with adjustable restraints to allow for a variety of positions and sizes of test subjects. The bed can be propelled either by a standing operator (passive exercise) or by the legs of the test subject (active exercise). The quantity of exercise can be adjusted by changes to the mass of the cart and regulation of the duration of the ride. The accelerometer provides a continuous readout on a Brush recorder so that by monitoring the peak acceleration, the efforts of the operator or subject can be adjusted to produce the desired acceleration profile. From time to time it was also necessary to replace or adjust the tension of the shock cord supporting the tarpaulins since this affected the time profile of the rebound accelerations.

## HARDWARE ADAPTATIONS OF METHOD TO SPACE VEHICLES

During laboratory tests periodic engineering design studies were being conducted. Some ideas for the application of the "trampoline" device are shown in Figure 2.

It is believed that the configuration labelled Concept A is probably the best and can easily fit the dimensions of most space laboratories.

In order to provide a complete physical conditioning system in one location it was deemed desirable to locate other exercise, and test equipment on or around the trampoline.

## CONCLUSIONS

Only by means of orbital laboratory studies utilizing the trampoline or some similar system of physiological support will the true need for a conditioning program become clearly established. Quite possibly the magnitude of the deconditioning problem will be proven inconsequential and further consideration will be totally unnecessary. However, nobody can make a certain prediction with the information at hand, and we must anticipate the worst possibilities until the critical data become available. Manned space flight and the emphasis here rides on the man component - obviously imposes a different and more demanding set of objectives on the total mission, as contrasted to unmanned flight. We must plan for a safe round trip of our astronauts and recognize that not only are they an important part of the scientific package, but their viability also carries an acknowledged and very large political impact. [These considerations suggest analysis and test of the trampoline device along with other methods for prevention of deconditioning of the astronaut.]

# HORIZONTAL TRAMPOLINE



SUBJECT RIDING CART ACTIVELY

## TRAMPOLINE ACCELERATION CHARACTERISTICS

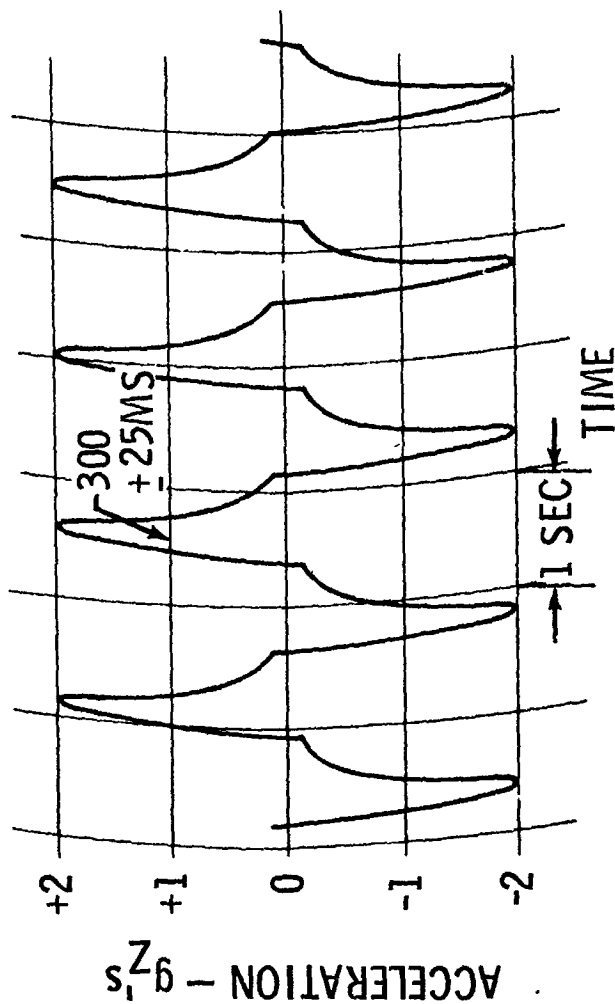
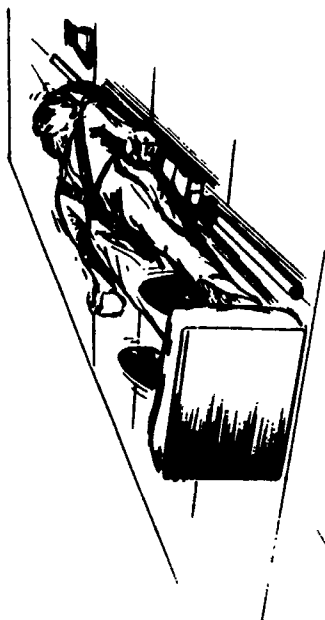
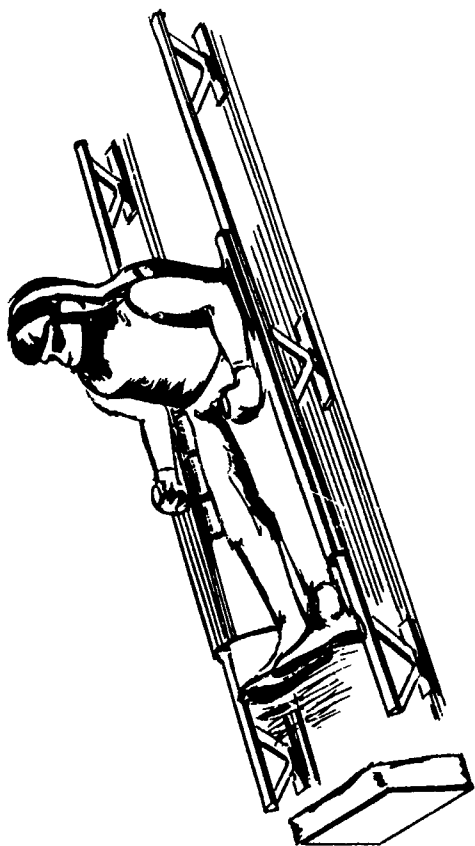


FIGURE 1. EXPERIMENTAL VERIFICATION



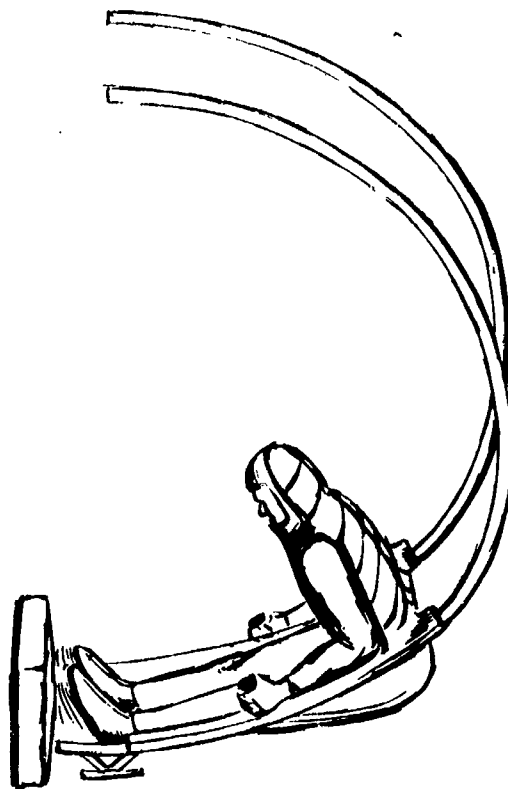
CONCEPT A



CONCEPT B



CONCEPT C



CONCEPT D

PROPOSED APPLICATIONS  
FIGURE 2

## REFERENCE

1. Grave, C., J. E. Mabry and D. H. Stuhling. "Maintaining Cardiovascular Reflexes during Simulation of a Zero Gravity Effect: An Experimental Study," Aerospace Med. 35: 268-269, (1964), (abstract).
2. Whedon, G. D., J. E. Deitrick and E. Shorr, "Modification of the Effects of Immobilization upon Metabolic and Physiologic Functions of Normal Men by the Use of an Oscillating Bed," Am. J. Med. 6:684-711, 1949.
3. Deitrick, J. E., G. D. Whedon and E. Shorr, "Effects of Immobilization upon various Metabolic and Physiologic Functions of Normal Men," Am. J. Med. 4:3-36, 1948.
4. Graveline, D. E, "Maintenance of Cardiovascular Adaptability during Prolonged Weightlessness," Aerospace Med. 33, 297-302, 1962.
5. Stapp, J. P. In Gravitational Stress in Aerospace Medicine. O. H. Gaver and G. D. Zuidema, eds. Little, Brown and Co. Boston, 1961.
6. Kornhauser, M, "Theoretical Prediction of the Effect of Rate-of-Onset on Man's G-Tolerance," Aerospace Med. 32: 412-21 1961.
7. Thompson, A. B. "A Proposed New Concept for Estimating the Limit of Human Tolerance to Impact Acceleration," Aerospace Med. 33: 1349-55, 1962.
8. Gagge, A. P. and R. S. Shaw, Aviation Medicine. In: Medical Physics, Vol. 2 The Year Book Publishers Chicago, 1950. O. Glasser, Ed. pp 41-65.

# HYPERSONIC NONEQUILIBRIUM FLOW AT RE-ENTRY OF SPACE VEHICLES AND ITS THERMODYNAMIC RELATIONS<sup>1,2</sup>

By

Rudolf Hermann<sup>3</sup>

/ University of Alabama Research Institute

## INTRODUCTION

**N67-24280**

With the availability of the Saturn/Apollo vehicle, it will be possible to perform many different types of space missions with a broad range of applications. In many cases, the space vehicle has to return safely to the Earth's surface after completion of its mission. Even though re-entry and soft landing of space capsules, such as Mercury and Gemini, have been technically mastered, analytical calculations of flow fields at hypersonic velocities, as they are encountered during re-entry from outer space, are still in the beginning phase and include many uncertainties. Therefore, all present investigations make use of simplifying assumptions.

In this paper, the following two restrictions have been employed:

First, with respect to the body shape, the calculations presented are carried out for a circular cylinder, the prototype of a blunt body. The next logical step is the calculation for a sphere, which is a first approximation for the front portion of the Apollo Command Module during re-entry. This task has been attacked by various laboratories including our Institute.

Second, with respect to the flow field, this paper deals with the inviscid flow region up to the equator of the body in such a range of temperatures and pressures where only oxygen dissociation and, of course, molecular vibration occur. Later calculations should include nitrogen dissociation and formation of nitric oxide. After the inviscid flow region is known, the calculation of the boundary layer and the wake can be started.

---

<sup>1</sup> The preparation of this paper was supported by the National Aeronautics and Space Administration under research grant NsG-381.

<sup>2</sup> The author acknowledges the efforts of Mr. Manfred J. Loh, Dipl.-Ing., for valuable assistance in the preparation of this manuscript.

<sup>3</sup> Professor of Physics and of Aerospace Engineering, and Director of Research Institute.

## NONEQUILIBRIUM HYPERSONIC FLOW FIELDS AND RE-ENTRY CORRIDORS

### Flow Fields and Flight Regions During Re-Entry

The configuration of the Apollo vehicle with the schematic flow field is shown in Figure 1 (Ref. 1). It is a typical blunt body which, in high speed flight, generates a detached bow shock. The front region between the shock wave and the outer edge of the boundary layer, called the inviscid shock layer, has a subsonic portion in the vicinity of the stagnation point; farther downstream the flow is supersonic. Besides the subsonic-supersonic inviscid shock layer, there is the boundary layer, and behind the body, a viscous separated region. The latter two regions interact in the viscous mixing region which poses almost unsurmountable difficulties for a theoretical analysis. Unfortunately, because of the location of antennas, this is also an important region as far as electromagnetic wave propagation is concerned.

For axisymmetric flow at zero angle of attack, flow fields are symmetric with respect to the body axis; and the inviscid portions can be calculated by presently available methods even though they require considerable computational effort. In the case of Apollo re-entry flight, the capsule itself is still an axisymmetric blunt body, but typically it descends at some angle of attack (to a maximum of  $33^\circ$ ) which is varied for control purposes. The flow field is now unsymmetric, thus, adding a major complication to the problem, and analytical methods are not readily available.

Before an analysis of the boundary layer or the wake can be made, the inviscid flow field must be known. The initial effort must, therefore, be directed toward the determination of the inviscid flow field. Since air is a rather complicated mixture of gases, especially when dissociation and ionization must be considered, a truly exact representation is not possible at the present time. In order to properly select a model, it is advantageous to study the conditions that are encountered along a typical re-entry trajectory, usually plotted in a velocity-altitude diagram.

In Figure 2, the cross-hatched region indicates the re-entry corridors of manned space capsules from circular orbit around Earth with about 7.9 km/sec and for lunar return with about 11.3 km/sec. Also included are equilibrium conditions behind a normal shock; thus the temperature, the pressure, and the density as they occur in the stagnation point



region of a blunt body re-entering the Earth's atmosphere can be read from the graph. Thermodynamic data for the graph were taken from References 2 and 3.

It is interesting to observe that a major portion of the space vehicle trajectory is approximately parallel to a line  $p_s = \text{const}$ . The temperature lines at low velocities are practically vertical, that is, the temperature depends only on the square of the velocity. For higher velocities, the temperature depends on both velocity and altitude. The lower density of high altitudes has the effect of increasing the degree of dissociation which in turn results in a reduced temperature since the dissociation process absorbs energy. Nevertheless, the stagnation temperature reaches very large values, up to 11,000 °K in the case of lunar return.

#### Nonequilibrium Flow Features

In most hypersonic applications, the flow field in the shock layer will generally be in some nonequilibrium state, because there is insufficient time to obtain thermodynamic equilibrium. Depending on free stream velocity, density, temperature, atmospheric composition, and the absolute size of the body, two limiting cases exist; either the flow may be almost frozen, or the flow may reach very nearly equilibrium.

A gas at rest is, by definition, in thermodynamic equilibrium, if a particular volume of the gas has sufficient, or better, infinite time to bring all its internal modes of energy in equilibrium with the translational energy of the molecular motion. For our consideration those modes are molecular vibration, dissociation, electronic excitation, and ionization. Considering flow processes of a gas, it is obvious that equilibrium flow is only one limiting case, namely, when the changes of the state of the gas flowing along a streamline are so slow that at any point equilibrium is obtained, or stated more exactly, equilibrium is very closely approached.

At hypersonic velocities, the time available is, in general, too short for the gas particles which are undergoing rapid density, temperature, and composition changes to reach thermodynamic equilibrium. Hence, in general, there will be nonequilibrium flow. The degree of molecular vibration, the degree of dissociation (chemical composition), and the degree of ionization will still change from point to point along the streamline but will not reach thermodynamic equilibrium at any point.

The second limiting case occurs when the gas moves so fast that the internal energy modes have no time to follow the changing density and temperature with the result that the vibrational energy, the energy in dissociation, and the energy in ionization stay very nearly constant. This flow is called frozen; the gas might be vibrationally frozen, and/or chemically frozen (frozen dissociation or no change in degree of dissociation), and/or the gas has frozen ionization.

The departure from equilibrium of a flowing gas depends upon the ratio of a characteristic translational time needed by the macroscopic motion of the particles to cover a typical distance, relative to the magnitude of the respective relaxation time which is different for each mode of excitation. Since the characteristic translational time is dependent on the body size, and since relaxation times are dependent on the temperature, density, and to some extent on local composition, it is obvious that nonequilibrium flow fields are generally not similar for geometrically similar bodies even at completely equal free stream conditions; this is a very important fact.

## THERMODYNAMIC RELATIONS INCLUDING REAL GAS EFFECTS

### Simplified Air Model, Degree of Dissociation

At the present time it is not possible to consider simultaneously all possible individual reactions which can occur between all components in air. Therefore, we must concentrate our efforts on the study of those components and reactions that are of greatest engineering concern today.

The simplified air model used in the calculations presented consists of oxygen and nitrogen only. The chosen composition in undissociated state is 21 per cent  $O_2$  and 79 per cent  $N_2$ , by volume. Furthermore, we will restrict the range of application expressed in the appropriate ranges of temperature and pressure such that only oxygen may dissociate.

The mole fraction of oxygen molecules in our air model, before dissociation, is expressed as

$$\frac{n_{O_2}}{n_{O_2} + n_{N_2}} = b = 0.21 \quad (1)$$

where  $n_i$  denote the number of particles of the  $i$ th species per unit volume of the gas.

In general, at a given pressure and temperature, only a certain fraction of the molecules are dissociated into atoms. The degree of oxygen dissociation,  $\alpha$ , can be defined as the ratio of the number of dissociated oxygen atoms per unit volume to the initial number of undissociated oxygen atoms per unit volume which are, of course, in molecular state.

#### Thermal Equation of State, Internal Energy, and Enthalpy Equation

Assuming that the individual species obey the perfect gas law, the total pressure of the mixture is the sum of its partial pressures, or

$$p = \sum_i p_i = \sum_i p_i R_i T. \quad (2)$$

Combining expressions for  $p_i$ ,  $R_i$ ,  $\alpha$ , and  $b$ , we finally obtain

$$p = (1 + b\alpha) p R T = Z p R T \quad (3)$$

where  $R_i$  is the specific gas constant of each species,  $R$  is the gas constant of the undissociated mixture, and  $Z = (1 + b\alpha)$  is called the compressibility factor.

The internal energy of the gas mixture,  $E$ , is the weighted sum of the internal energies of each species,  $e_i$ , due to the various modes of excitation (translation, rotation, vibration) and of the dissociation energy,  $D$ , of the dissociating component,

$$E = \sum_i f_i e_i + \frac{f_O}{2} D_{O_2} \quad (4)$$

where  $f_i$  denotes the mole fractions for the dissociated mixture.

The enthalpy of the gas mixture is defined in the same way as the enthalpy of a gas with only one component

$$h = E + \frac{p}{\rho}. \quad (5)$$

After determining the mole fractions, and obtaining the internal energy of the mixture from statistical thermodynamics, the enthalpy equation finally becomes

$$h = R \left[ b\alpha D'_{O_2} + \frac{3}{2} b\alpha T + \frac{7}{2} T + (1 - \alpha) b \frac{\theta_{O_2}}{\theta_{O_2} - 1} + (1 - b) \frac{\theta_{N_2}}{\theta_{N_2} - 1} \right]. \quad (6)$$

Here  $\theta_i$  is the characteristic temperature of vibration (2270 °K for  $O_2$ ; 3390 °K for  $N_2$ ), and  $D'_{O_2}$  is the characteristic temperature of oxygen dissociation (59366 °K).

### Rate Equation, Dissociation Rate Constant, and Equilibrium Constant

In general, a large number of collisions among the particles is required to bring molecular vibration, dissociation, and higher degrees of excitation in equilibrium with the local translational temperature. This means that a finite amount of time (relaxation time) is needed for the gas properties to approach thermodynamic equilibrium. The departure from equilibrium of a flowing gas is characterized by the magnitude of this relaxation time relative to some translational time (residence time) needed by the particles to move over a characteristic distance on a body within a nozzle. Since only oxygen dissociation is considered, only one chemical rate equation is needed. Molecular vibrations are assumed to be in equilibrium.

In the process of dissociation, an oxygen molecule must collide with another particle having enough energy to break up the oxygen molecule. The recombination process is the inverse of the dissociation. In order to occur, it is necessary that two atoms collide at the same time with a third body, which is able to carry away the energy that the two separate atoms must release to form a stable diatomic molecule (three-body collision).

In a flow field with a local velocity vector  $\vec{q}$  and a variable degree of dissociation, characterized by  $\alpha$ , the following relation can be derived, called the rate equation:

$$\vec{q} \cdot \text{grad } \alpha = F \quad (7)$$

where

$$F = \frac{C^2 p^2 Z k_d}{2 b} \left[ \frac{(1 - \alpha)}{2 C p} - \frac{\alpha^2}{K_c} \right] \quad (8)$$

The expression for  $F$  is called the source function for oxygen atoms. Among others, it contains the number of oxygen atoms per unit mass of the gas,  $C$ , furthermore the dissociation rate constant,  $k_d$ , which depends strongly on the type of the colliding body and some other gas properties, and finally the concentration equilibrium constant,  $K_c$ , which is a function of temperature only. In order to evaluate the rate equation (12), we still need expressions for  $k_d$  and  $K_c$ .

The dissociation rate constant,  $k_d$ , cannot be predicted by ordinary kinetic gas theory. Wray (Ref. 4) has given a comprehensive review of recent work carried out in that field, and his values will be used in the present investigation. In order to account

for the influence of the catalytic species, we are using a dissociation rate constant, which is averaged with the respect to population. This finally results in the expression

$$k_d = \frac{2.5 \cdot 10^8}{T N_A} \cdot \left(\frac{D}{R^*}\right)^{1.5} e^{-\frac{D}{R^*T}} \left(\frac{41ba + 7b + 2}{1 + ba}\right) \quad (9)$$

It can be seen that the dissociation rate "constant" is actually a function of temperature,  $T$ , and composition,  $a$ . Fig. 3 shows the range of this equation for  $a$  between 0 and 1, together with the values of other authors for various colliding bodies.  $k_d$  has the dimension  $[m^3 \text{ particle}^{-1} \text{ sec}^{-1}]$ .

Equation (8) was obtained through elimination of the recombination rate constant,  $k_r$ , by introducing the concentration equilibrium constant,  $K_c$ . This is a function of temperature only and results from statistical thermodynamics like  $k_d$ .  $K_c$  has the dimension  $[\text{particle } m^{-3}]$  and its final expression for the numerical calculation is:

$$K_c = 2.444056 \cdot 10^5 \frac{T^{1/2}}{k} \left[1 - e^{-\frac{2270}{T}}\right] \frac{\left[5 + 3e^{-\frac{228}{T}} + e^{-\frac{326}{T}}\right]^2}{3 + 2e^{-\frac{11390}{T}}} \left[e^{-\frac{59366}{T}}\right] \quad (10)$$

Only a few important relations needed for the following flow calculations have been given in this section. More details can be found in Reference 5.

## NONEQUILIBRIUM FLOW AROUND BLUNT BODIES WITHOUT AND WITH DISSOCIATION IN THE FREE STREAM

### Direct and Inverse Methods for Flow Calculation

The importance of blunted shapes in the hypersonic flight of a vehicle re-entering the atmosphere from outer space has led to many investigations of hypersonic flows with detached shock waves, using both inverse and direct methods. At the inverse method, a certain shock shape is assumed or prescribed, and then the governing equations are integrated through the flow field, and the associated body shape follows from the calculation. The author and his associates at the University of Alabama Research Institute in Huntsville have applied a direct method, where the body shape is given and the flow field, including the shock shape, is a result of the calculation. This method uses "integral relations", first described by Dorodnitsyn (Ref. 6) in 1959 for the solution of two-dimensional boundary value

problems, later applied by Belotserkovskii (Ref. 7) to the calculation of supersonic flow of a perfect gas past a circular cylinder.

Up to now a limited number of investigators obtained results for real gas flows in connection with the integral method. Recently Hermann and Thoenes (Ref. 8) have given new extended and improved results for nonequilibrium hypersonic flow of air past a circular cylinder, which are presented in this section. They have also treated, for the first time to the author's knowledge, the case of dissociation in the free stream. Such conditions are encountered either in the atmosphere at high altitude (above 90 km), or in the nozzle of high temperature hypersonic flow facilities designed to simulate re-entry flight conditions, where appreciable frozen dissociation may occur.

#### Basic Equations for Inviscid Flow Past a Circular Cylinder

We are restricting our analysis to inviscid flow and, in addition, we are neglecting heat conduction and radiation. Figure 4 shows the cylinder with the selected polar coordinate system. The basic equations of motion for steady adiabatic flow, after transformation from the vectorial form to polar coordinates, yield the following first three partial differential equations. The fourth equation, expressing the conservation of oxygen atoms, had to be added since the gas under consideration is reacting.  $F$  is the source function of oxygen atoms, Equation (8).

Conservation of mass:

$$\frac{\partial}{\partial \theta} (\rho u) + \frac{\partial}{\partial r} (\rho v r) = 0 \quad (11)$$

$\theta$ -momentum:

$$u \frac{\partial u}{\partial \theta} + v r \frac{\partial u}{\partial r} + u v + \frac{1}{\rho} \frac{\partial p}{\partial \theta} = 0 \quad (12)$$

$r$ -momentum:

$$\frac{\partial}{\partial \theta} (\rho u v) + \frac{\partial}{\partial r} \left[ (\rho + \rho v^2) r \right] - (\rho + \rho u^2) = 0 \quad (13)$$

Rate equation:

$$u \frac{\partial a}{\partial \theta} + v r \frac{\partial a}{\partial r} - F r = 0. \quad (14)$$

In order to solve these equations for the flow field variables, they must be supplemented by the equation for the conservation of energy, containing an expression for the enthalpy,

Eq. (6), and by the thermal equation of state, Eq. (3). Note that the first three equations (conservation of mass and of the two momenta) are independent of the particular gas model, while the last three equations (rate, energy, equation of state) do depend strongly on the selected gas model. The conservation of mass and the  $r$ -momentum equation are given in the so-called divergence form, which is required for the application of the integral method.

### Boundary Conditions

The condition for flow tangency on the body surface is  $v_b = 0$ . The conditions behind the shock are obtained from the conservation of mass, momentum and energy across the shock. For the present nonequilibrium flow calculation, it will be assumed that the chemical composition of the air does not change across the shock, i.e.,  $\alpha_1 = \alpha_s$ .

Various relations between the velocity components in front of and behind the shock which will be needed later are obtained from Figure 4. From the same figure, one can also derive the following relation between the local dimensionless shock wave distance from the body,  $\epsilon$ , and the shock wave angle,  $\sigma$ , both being functions of  $\theta$ :

$$\frac{d\epsilon}{d\theta} = -(1 + \epsilon) \cot(\sigma + \theta). \quad (15)$$

### Application of the One-Strip Integral Method for the Cylinder

Due to the boundary condition  $v_b = 0$ , it can be seen that the  $\theta$ -momentum equation and the rate equation may be used in their exact forms. Hence, only two equations of the set, namely the conservation of mass and the  $r$ -momentum equation, have to be approximated by assuming a linear variation of certain integrands across the shock layer. Thus, an integration of the equations in the direction of the radial coordinate can be performed, which in turn results in two ordinary differential equations with the tangential coordinate as independent variable.

The result is the following complete set of governing equations:

Continuity:

$$\rho_b \frac{du_b}{d\theta} + u_b \frac{d\rho_b}{d\theta} + \rho_s \frac{du_s}{d\theta} + u_s \frac{d\rho_s}{d\theta} = \frac{1 + \epsilon}{\epsilon} \left[ (\rho_b u_b - \rho_s u_s) \cot(\sigma + \theta) - 2 \rho_s v_s \right] \quad (16)$$

$\theta$ -momentum:

$$\rho_b u_b \frac{du_b}{d\theta} + \frac{d\rho_b}{d\theta} = 0 \quad (17)$$

r-momentum:

$$\frac{d}{d\theta} (\rho_s u_s v_s) = \frac{2+\epsilon}{\epsilon} (p_b - p_s) + \rho_b u_b^2 + \rho_s u_s^2 - \frac{1+\epsilon}{\epsilon} \left[ \rho_s u_s v_s \cot(\sigma + \theta) + 2 \rho_s v_s^2 \right] \quad (18)$$

Rate:

$$u_b \frac{da_b}{d\theta} = F_b r_b \quad (19)$$

Energy:

$$\frac{u_b^2}{2} + h_b = h_t = \frac{u_1^2}{2} + h_1 = \text{constant} \quad (20)$$

Equation of State:

$$p_b = \rho_b R Z_b T_b \quad (21)$$

The five ordinary differential equations (15, 16, 17, 18, 19) and the two algebraic equations (20, 21) constitute a system of seven equations for the seven unknowns, which are the five parameters along the wall of the cylinder  $u_b$ ,  $\rho_b$ ,  $p_b$ ,  $T_b$ ,  $a_b$ , and the two parameters for the shock shape,  $\epsilon$  and  $\sigma$ . Special subroutines during the process of the solution are necessary to calculate those variables in the above equations that are functions of some unknowns (mainly  $a_b$  and  $T_b$ ) and of free stream conditions.

Before the numerical integration of the system of equations for the flow around the circular cylinder can be started, the stagnation point parameters, serving as initial values, must be determined. For this purpose, the governing equations are specialized for the stagnation streamline, where  $\theta = 0$  and  $u_b = u_s = 0$ .

Henceforth, the further calculation of the flow parameters consists of two principal sections: first, the calculation of the flow along the stagnation streamline including the stagnation point itself; second, the calculation of the flow variables along the cylinder surface and behind the shock. Both parts still require considerable analytical effort in getting the final equations for the computer program. This procedure is described in more detail in Reference (8).



In the first section, the resulting system of six equations can be solved for any particular chosen value for the stagnation point shock detachment distance  $\epsilon_0$ . To find the solution, a stagnation point pressure  $p_b$  must be assumed as a first trial, then the system is integrated and iterated on  $p_b$ , until the assumed value  $p_b$  agrees with that resulting from the integration.

After the stagnation point conditions have been obtained, the integration around the body is started with an unknown, but assumed shock detachment distance  $\epsilon_0$ . The equations for the variables along the cylinder surface are strongly dependent on the selected value  $\epsilon_0$ , and smooth transitions of all variables from the subsonic to the supersonic flow regime are only obtained for a correctly chosen  $\epsilon_0$ . Depending on the case, between ten and fifteen iterations were needed to determine  $\epsilon_0$  to four significant figures.

A fixed-step Runge-Kutta technique of fourth-order accuracy was used for both the integration along the stagnation streamline and for the integration along the body surface. One thousand steps were chosen for the stagnation streamline from the shock to the stagnation point. In the second part, the step size was fixed at 0.002 radians, and approximately 800 steps were used for the integration from the stagnation point to the equator ( $\theta = \pi/2$ ). All calculations were performed on a UNIVAC 1107 high speed digital computer, which is located in the University of Alabama Research Institute.

#### Discussion of the Results for the Cylinder

For chemical nonequilibrium flow, the degree of dissociation and the temperature are particularly interesting parameters which are shown in Figs. 5 and 6 along the stagnation streamline between shock and body. The free stream velocity is 4300 m/sec at an altitude of 30 km, corresponding to  $M_1 = 14.2$ . It can be seen that, depending on the size of the body, quite different regimes of nonequilibrium flow are encountered. For relatively large bodies, a characteristic flow time is large compared to the local chemical relaxation time, which causes the flow to reach the state of thermodynamic equilibrium close behind the shock. During this process, the degree of oxygen dissociation increases up to approximately 90%, while the temperature decreases correspondingly within a small region behind the shock. On the other hand, for small bodies, a characteristic flow time is very short if

compared to the relaxation time. In this case, the flow remains essentially frozen and equilibrates only near the stagnation point, where the velocity approaches zero and the local residence time of a flow particle again is large compared to the relaxation time. It was found that the flow always reaches thermodynamic equilibrium at the stagnation point. Note that with  $T_1 = 225^\circ\text{K}$ , the temperature scale goes from  $4500^\circ\text{K}$  to  $7650^\circ\text{K}$ . For small bodies (nose radius  $< 0.1\text{ cm}$ ) the nonequilibrium temperature in the main part of the shock layer near the stagnation streamline is between  $2000^\circ\text{K}$  and  $3000^\circ\text{K}$  higher than the equilibrium temperature which exists for a sufficiently large body (nose radius  $= 10\text{ cm}$ ).

In both figures, the present results from the integral method are compared with data calculated by Conti (Ref. 10), who used an inverse method, also a basically different approach. The air model was the same as ours, but the reaction rate constants are somewhat different. The comparison is very gratifying.

Calculated shock shapes up to the equator of the cylinder (body radius  $10\text{ cm}$ ) are shown in Fig. 7 for Mach numbers 3.0 to 14.2, without and with dissociation in the free stream. With increasing free stream Mach number, the bow shock moves much closer to the body. This trend is already well known from perfect gas calculations and is retained in chemical nonequilibrium flow. The figure also indicates the location of the sonic point on the body surface, which moves toward the stagnation point with increasing Mach number. The shock shape deviates considerably from a concentric circle, even where the velocity in the shock layer is still subsonic.

The shock detachment distance at the stagnation streamline as function of the free stream Mach number is presented in Fig. 8, where our nonequilibrium flow results with and without free stream dissociation ( $\alpha_1 = 0.5$ ;  $\alpha_1 = 0$ ) are compared with perfect gas results ( $\gamma = 1.4$ ) from References (11) and (7). Figures 7 and 8 indicate clearly that dissociation of the free stream, keeping all other free stream parameters unchanged, causes the bow shock to move away from the body. One reason for this effect is that, for a dissociated free stream, the density behind the shock is lower than for corresponding conditions without free stream dissociation. The effect is seen to increase with decreasing free stream Mach number.

From Fig. 8 it is observed that the present calculations for an undissociated free stream yield a stagnation shock detachment distance which is much smaller than the values obtained from perfect gas calculations. Responsible for this effect, in the range of Mach numbers

approximately between 4 and 7, is the fact that our calculations include the energy of molecular vibration, which is assumed to be in equilibrium. For Mach number 6.6, the present calculation, which includes dissociation, does not show any degree of dissociation in the flow field (Fig. 10). Beyond Mach number 7, the influence of the dissociation on the shock detachment distance becomes more pronounced. At free stream Mach number 3, where the temperature caused by the bow shock does not yet cause appreciable molecular vibration in the shock layer, the present calculation furnishes a value which is very close to the known perfect gas results. Finally, in the higher Mach number range, at  $M = 14.2$  our results agree closely with those of Conti (Ref. 10), which were obtained by an entirely different approach.

The velocity distribution along the surface of the cylinder as evident from Fig. 9 is almost linear up to the sonic point. A distinct effect of free stream dissociation can be seen.

The degree of oxygen dissociation along the noncatalytic body surface is presented in Fig. 10. For zero free stream dissociation, it is seen that at  $M_1 = 6.6$  no dissociation occurs along the body. The degree of dissociation increases strongly with increasing Mach number and reaches about 0.95 at Mach number 14.2. Especially for higher Mach numbers, it is seen that the recombination process dominates in the subsonic regime as the flow expands around the body. The degree of dissociation decreases slowly until, in the supersonic regime, the local residence time of a particle becomes so small compared to the relaxation time that the flow freezes.

Finally, Fig. 11 shows the temperature distribution along the surface of the cylinder for selected free stream Mach numbers with and without dissociation of the free stream. As expected, free stream dissociation has a strong effect on the temperature. Note that for  $M_1 = 6.6$  the presence of free stream dissociation raises the stagnation temperature about  $1000^\circ\text{K}$ . It should be mentioned that the pressure distribution, not shown here, along the body surface is similar to the "Modified Newtonian" distribution, and that free stream dissociation has practically no effect on the pressure.

#### Comparison with Flow Around A Sphere

From an engineering point of view, the sphere or the spherically capped cone has a greater interest than the cylinder. However, only a few data for the sphere are available

for nonequilibrium flow. Fig. 12 shows a comparison of the shock detachment distance between cylinder and sphere with the results for the sphere taken from Ref. 12. Note that the Mach number is nearly identical; however, the altitude is markedly different. Both are valid for zero free stream dissociation. It is seen that the shock wave for the sphere is much closer to the body and has less than one half of the distance of the shock wave for the cylinder. Results with exactly equal free stream conditions for both cases are not available at the present time. The fact that the shock wave of the sphere is much closer to the body than for the cylinder should be true also for identical free stream conditions; this is known to be the case for supersonic flow of a perfect gas. It has been found that the location of the sonic point is very sensitive, thus one cannot compare sonic point locations of two bodies with different free stream conditions.

#### SUMMARY

Analytical investigations of hypersonic nonequilibrium flow around blunt bodies are reported as contribution to the Interdisciplinary Symposium on Apollo Application Programs. Flight regions and equilibrium values of flow parameters behind the normal shock of a space vehicle, such as Apollo capsule, re-entering the Earth's atmosphere are presented. Basic features of equilibrium, nonequilibrium, and frozen flow are discussed.

Real gas effects are treated using a simplified air model. With restriction to oxygen dissociation only, the thermal equation of state, the thermodynamic expressions of energy and enthalpy, and the rate equation for the net production of oxygen atoms are shown. Hypersonic inviscid flow about the forward portions of cylinders up to the equator has been numerically calculated in the range of oxygen dissociation, using the direct one-strip integral method of Dorodnitsyn. The investigations include the influence of the absolute body size and the effects of the free stream dissociation on the shock detachment distance and the flow field.

For a cylinder flying at 30 km altitude, real gas effects can be detected beginning above  $M = 3$  due to molecular vibration, and beyond  $M = 8$ , due to molecular vibration and dissociation. Dissociation of oxygen only occurs in the range between Mach numbers 8 and 14, approximately, while at higher Mach numbers, nitrogen dissociation must be considered. The shock detachment distance for a real gas is much smaller than for a perfect gas. Free stream dissociation causes the bow shock to move away from the body.

# LIST OF SYMBOLS

<b>b</b>	Constant [ - ], def. by Eq. (1)	<b>u, v</b>	Velocity components in x, y direction, respectively, [ m sec <sup>-1</sup> ]
<b>C</b>	Number of oxygen atoms per unit mass of the gas [ particles kg <sup>-1</sup> ]	<b>x, y</b>	Coordinates [ m ]
<b>D</b>	Dissociation energy [ J kmol <sup>-1</sup> ]	<b>Z</b>	Compressibility factor [ - ]
<b>D'</b>	Characteristic temperature of dissociation [ °K ]	<b>α</b>	Degree of oxygen dissociation [ - ]
<b>e, E</b>	Internal energy [ J kg <sup>-1</sup> ] or [ J kmol <sup>-1</sup> ]	<b>γ</b>	Ratio of specific heats [ - ]
<b>f<sub>i</sub></b>	Mole fractions [ - ]	<b>Δ</b>	Local shockwave detachment distance [ m ]
<b>F</b>	Source function for oxygen atoms [ sec <sup>-1</sup> ], Eq. (8)	<b>ε</b>	Dimensionless shockwave distance from body [ - ]
<b>h</b>	Enthalpy [ J kg <sup>-1</sup> ]	<b>θ</b>	Characteristic vibrational temperature [ °K ], and body angular coordinate [ radians or degree ]
<b>h<sub>t</sub></b>	Total enthalpy [ J kg <sup>-1</sup> ]	<b>ρ</b>	Density [ kg m <sup>-3</sup> ]
<b>k</b>	Boltzmann's constant [ J particle <sup>-1</sup> °K <sup>-1</sup> ]	<b>σ</b>	Oblique shock angle [ radians or degree ]
<b>k<sub>d</sub></b>	Dissociation rate constant [ m <sup>3</sup> particle <sup>-1</sup> sec <sup>-1</sup> ]		
<b>K<sub>c</sub></b>	Concentration equilibrium constant [ particles m <sup>-3</sup> ]		
<b>M</b>	Mach number [ - ]		
<b>n<sub>i</sub></b>	Number of particles of ith species per unit volume [ particles m <sup>-3</sup> ]		
<b>N<sub>A</sub></b>	Avogadro's number [ particles kmol <sup>-1</sup> ]		
<b>p</b>	Pressure [ N m <sup>-2</sup> ]		
<b><math>\vec{q}</math></b>	Velocity vector [ m sec <sup>-1</sup> ]		
<b>r, θ</b>	Radial and angular coordinates [ m; radians or degree ]		
<b>R</b>	Gas constant of undissociated gas [ J kg <sup>-1</sup> °K <sup>-1</sup> ]		
<b>R*</b>	Universal gas constant [ J kmol <sup>-1</sup> °K <sup>-1</sup> ]		
<b>T</b>	Temperature [ °K ]		

## Subscripts

<b>1</b>	Free stream
<b>b</b>	Body surface
<b>s</b>	Behind the shock
<b>n</b>	Normal component
<b>t</b>	Tangential component, also total conditions
<b>N<sub>2</sub></b>	Molecular nitrogen
<b>O<sub>2</sub></b>	Molecular oxygen
<b>O</b>	Atomic oxygen
<b>o</b>	Standard conditions, also stagnation streamline conditions

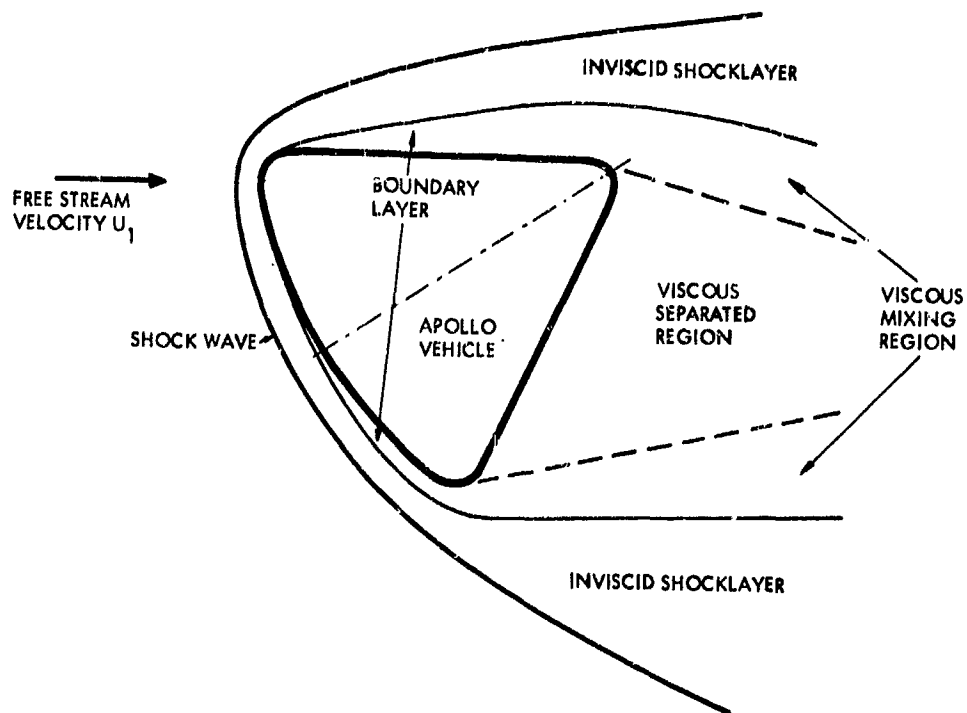


FIG. 1. HYPERSONIC FLOW REGIONS (SCHEMATIC) FOR APOLLO VEHICLE, REF. 1.

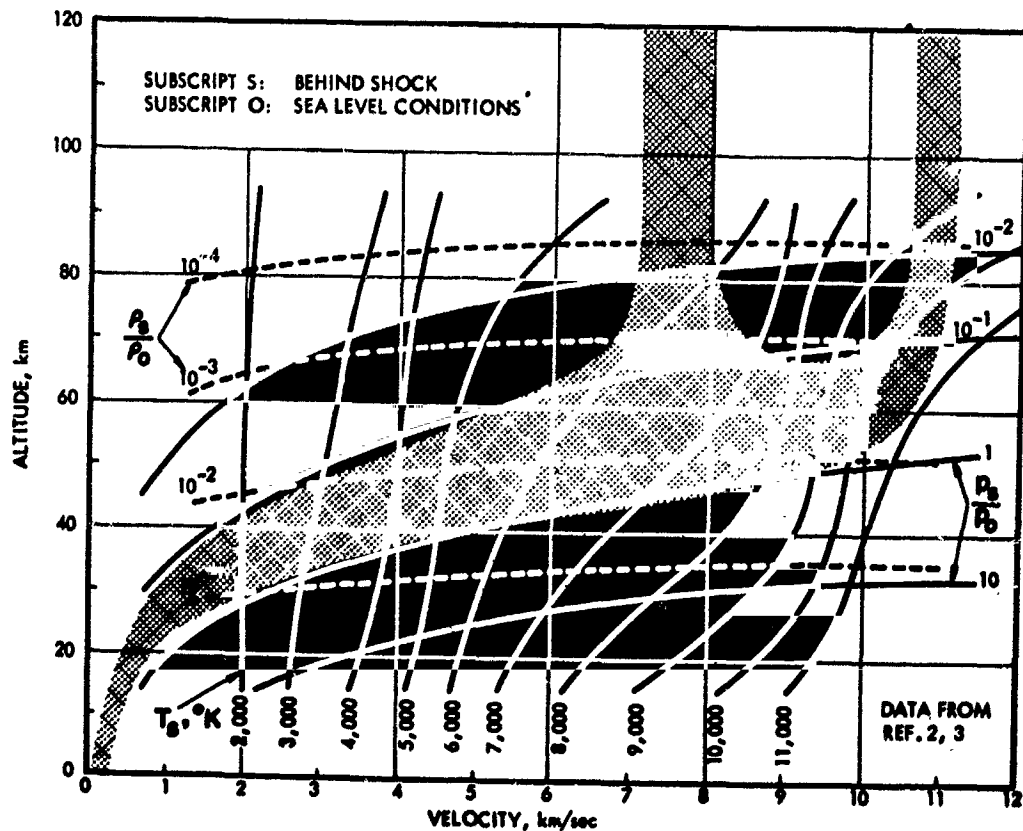
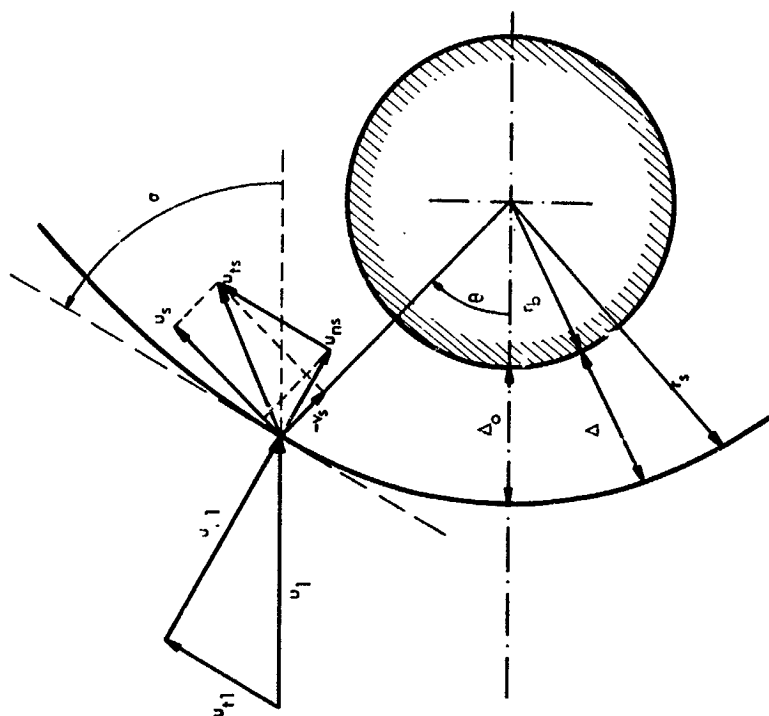
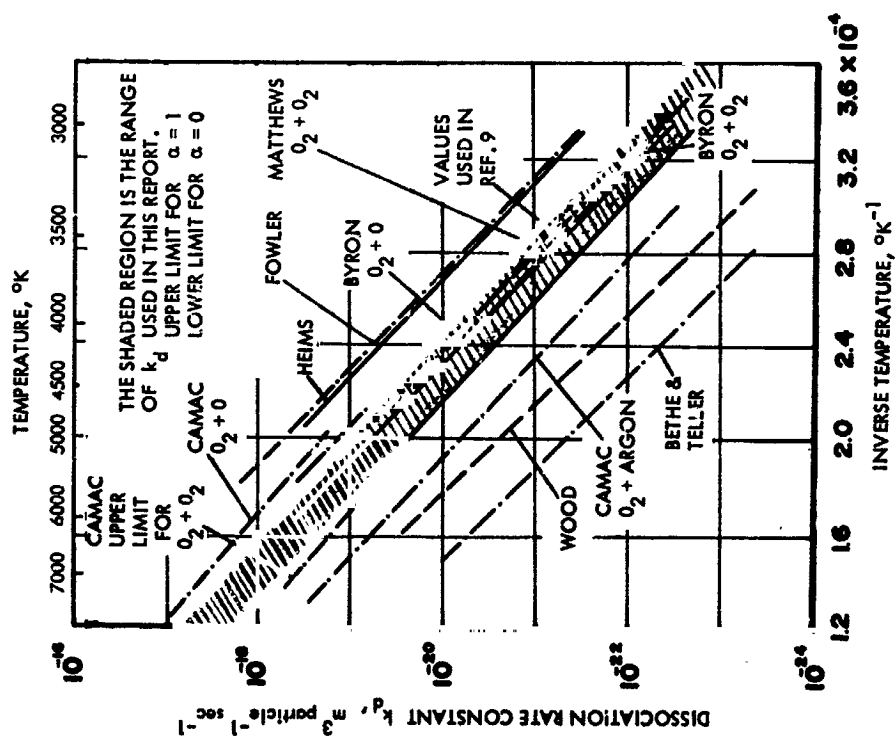


FIG. 2. FLIGHT REGION OF MANNED RE-ENTRY VEHICLES FROM CIRCULAR ORBIT AND LUNAR RETURN. ALSO EQUILIBRIUM CONDITIONS BEHIND A NORMAL SHOCK.



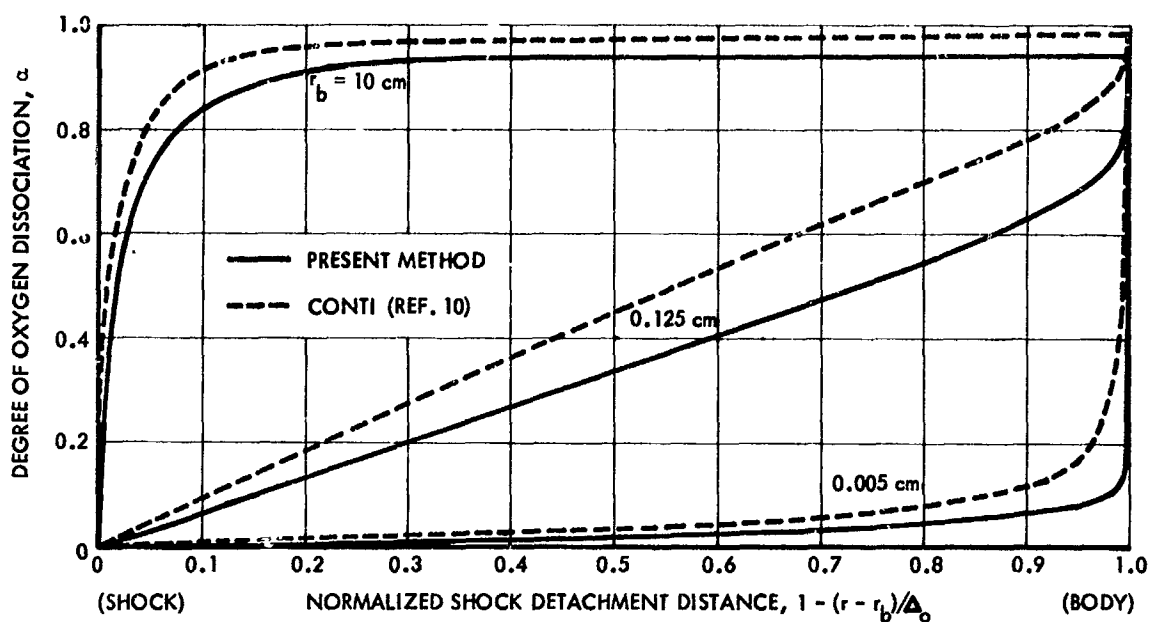


FIG. 5. DEGREE OF OXYGEN DISSOCIATION ALONG STAGNATION STREAMLINE FOR VARIOUS BODY RADII (FLIGHT SPEED 4300 m/sec, ALTITUDE 30 km,  $M_1 = 14.2$ ).

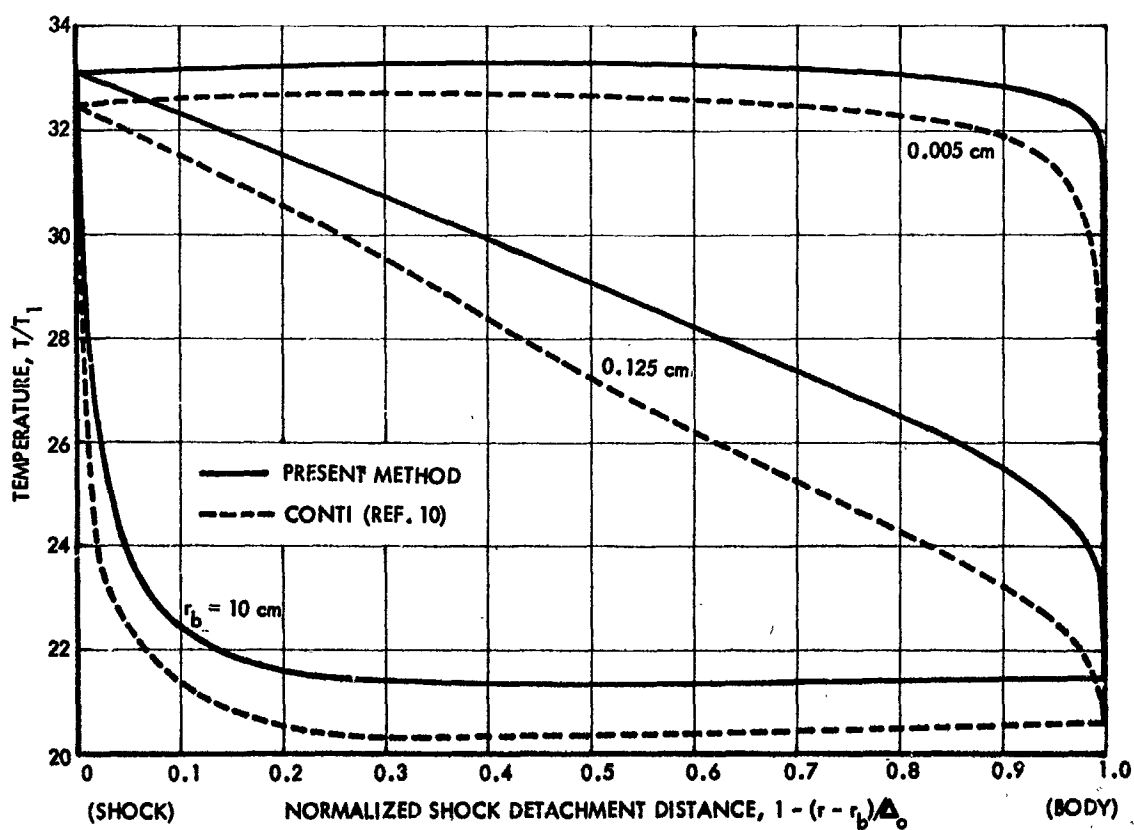


FIG. 6. TEMPERATURE ALONG STAGNATION STREAMLINE FOR VARIOUS BODY RADII (FLIGHT SPEED 4300 m/sec, ALTITUDE 30 km,  $M_1 = 14.2$ ).



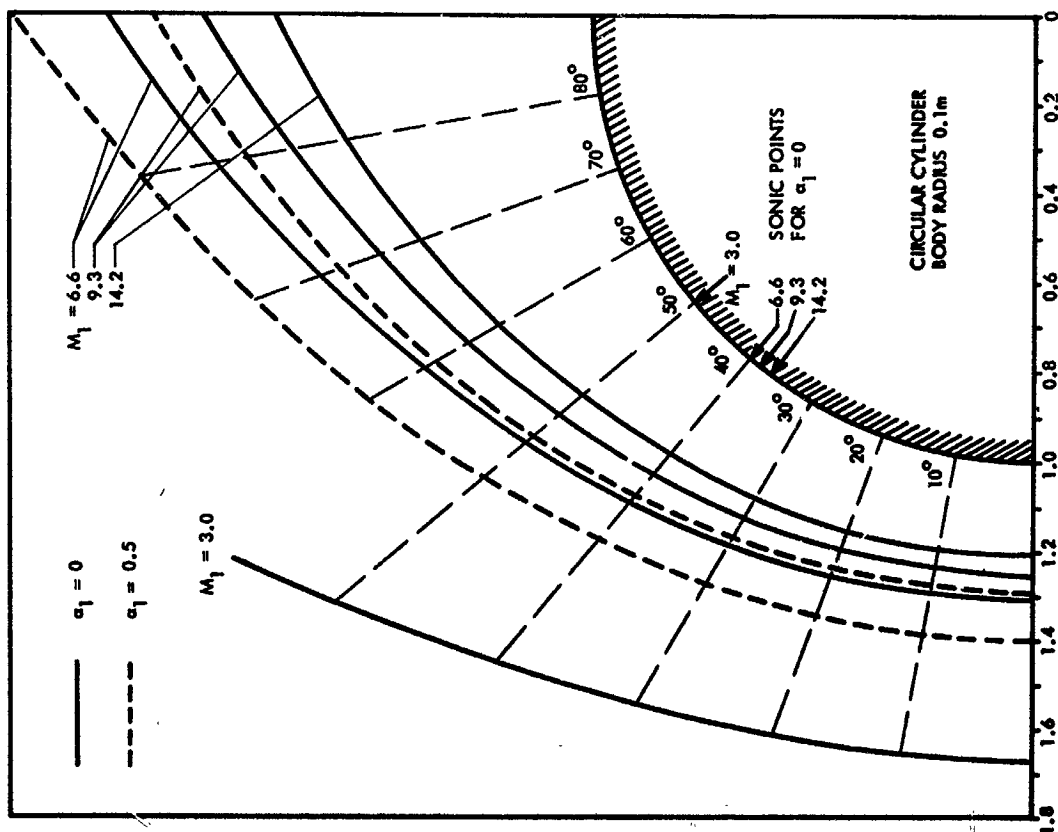


FIG. 7. CALCULATED SHOCK WAVES IN FRONT OF A CIRCULAR CYLINDER FOR 4 MACH NUMBERS (ALTITUDE 30 km).

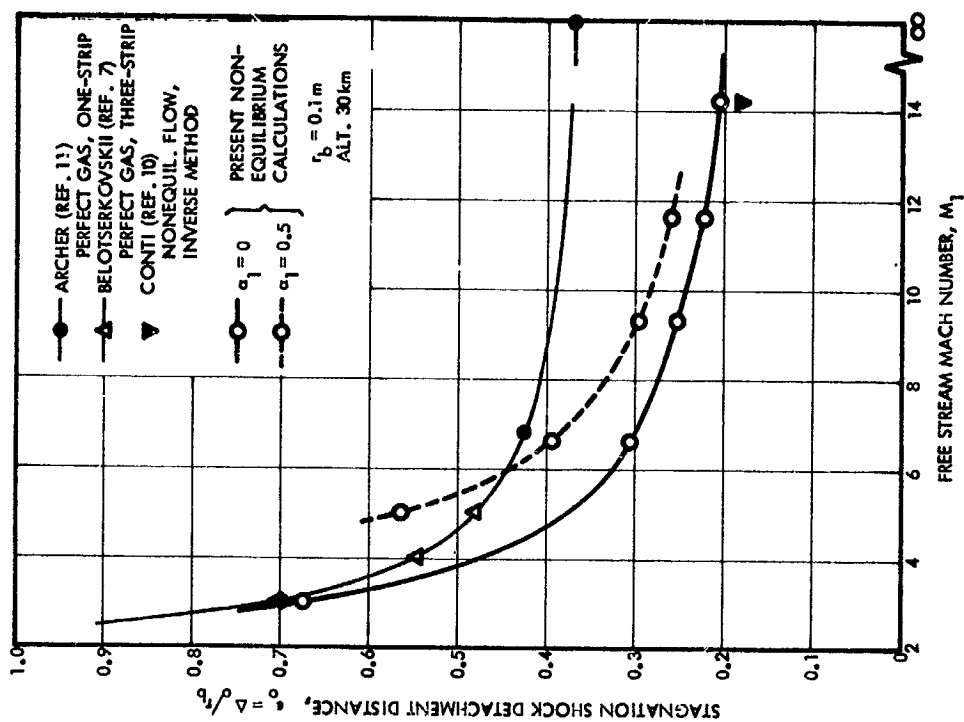


FIG. 8. SHOCK DETACHMENT DISTANCE AT STAGNATION STREAMLINE FOR CIRCULAR CYLINDER AS FUNCTION OF MACH NUMBER.

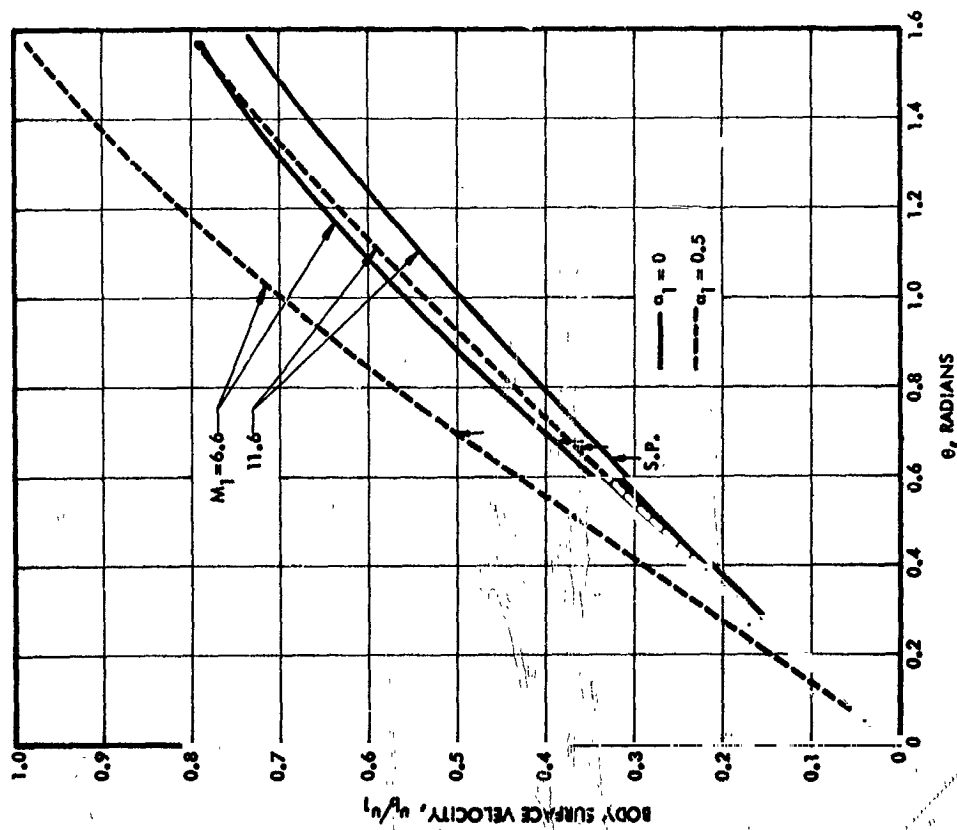


FIG. 9. VELOCITY DISTRIBUTION ALONG BODY SURFACE  
( $r_0 = 10$  cm, ALTITUDE 30 km).

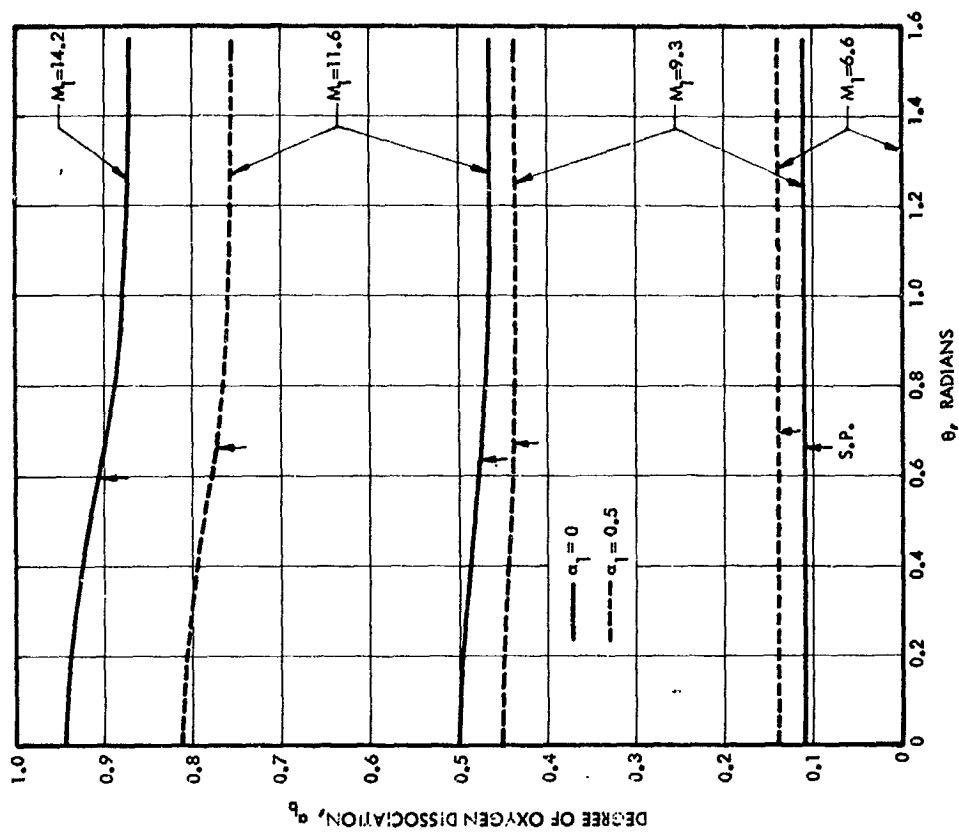


FIG. 10. DEGREE OF OXYGEN DISSOCIATION ALONG BODY SURFACE  
( $r_0 = 10$  cm, ALTITUDE 30 km).

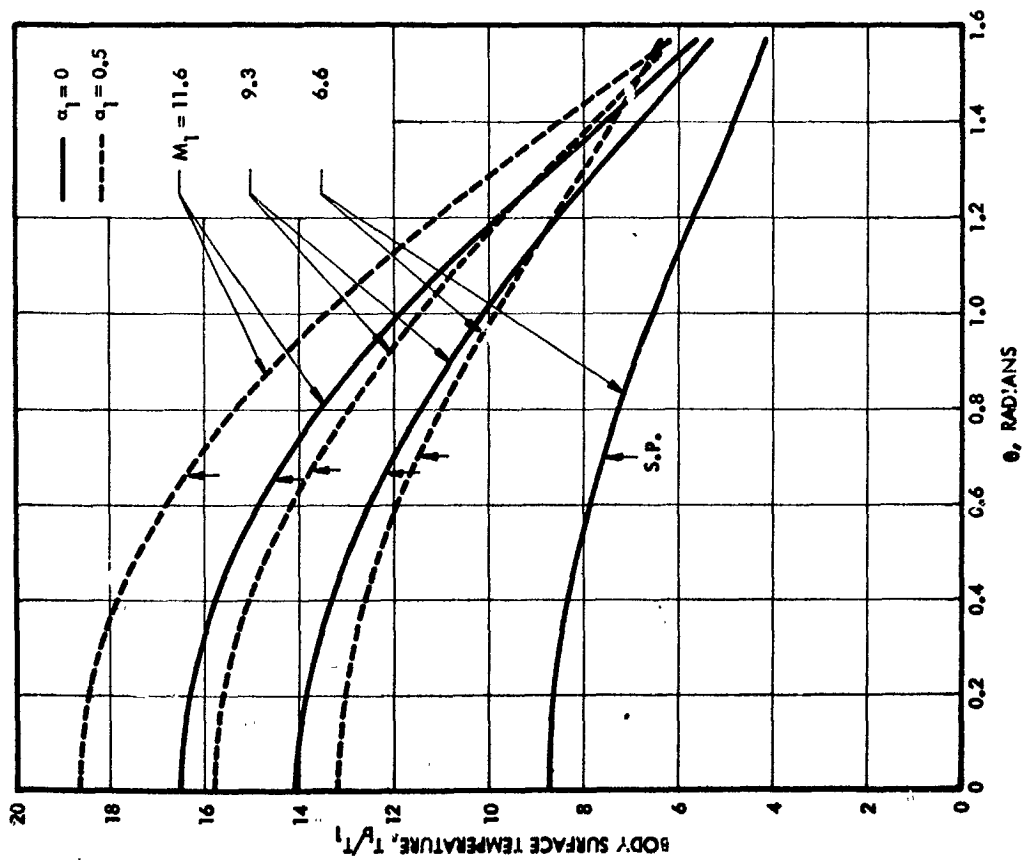


FIG. 11. TEMPERATURE DISTRIBUTION ALONG BODY SURFACE  
( $c_b = 10$  cm, ALTITUDE 30 km).

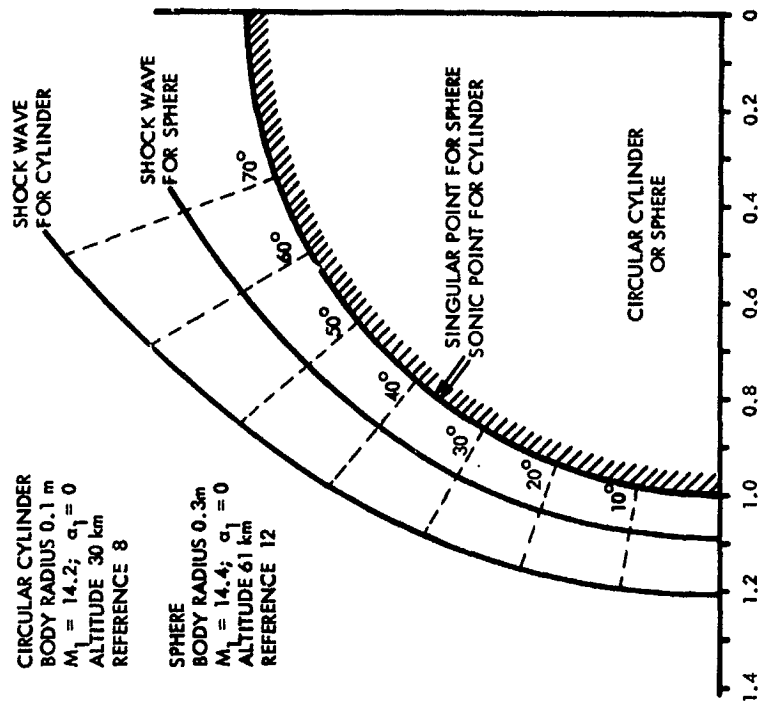


FIG. 12. SHOCK WAVES IN FRONT OF A CYLINDER  
AND A SPHERE FOR NONEQUILIBRIUM FLOW.

## REFERENCES

1. Lehnert, R., Rosenbaum, B., "Plasma Effects on Apollo Re-Entry Communications," Report X-513-64-8, Goddard Space Flight Center, Greenbelt, Maryland, Jan. 1964.
2. Wittliff, C. E., Curtis, J. T., "Normal Shock Wave Parameters in Equilibrium Air," Cornell Aero. Lab., CAL Report No. CAL-111, November 1961.
3. Marrone, P. V., "Normal Shock Waves in Air: Equilibrium Composition and Flow Parameters for Velocities from 26,000 to 50,000 ft/sec," Cornell Aero. Lab., CAL Report No. AG-1729-A-2, August 1962.
4. Wray, K. L., "Chemical Kinetics of High Temperature Air," in "Hypersonic Flow Research," Progress in Astronautics and Rocketry, Vol. 7, Academic Press, 1962.
5. Hermann, R., "Hypersonic Non-Equilibrium Flow and Its Thermodynamic Relations," Invited lecture presented at the 4. Space Symposium at the University of Goettingen, Germany, Oct. 18-22, 1965. Also University of Alabama Research Institute, Huntsville, UARI Res. Rep. No. 30, November 1965.
6. Dorodnitsyn, A. A., "A Contribution to the Solution of Mixed Problems of Transonic Aerodynamics," Advances in Aeronautical Sciences, Vol. 2, Pergamon Press, New York, 1959, pp. 832-844.
7. Belotserkovskii, O. M., "Flow Past a Circular Cylinder with a Detached Shock Wave," Dokl. Akad. Nauk SSSR 113, No. 3, 1957. Also AVCO RAD-9-TM-59-66, 1959.
8. Hermann, R., Thoenes, J., "Hypersonic Flow of Air Past a Circular Cylinder with Non-Equilibrium Oxygen Dissociation Including Dissociation of the Free Stream," Paper presented at the VI European Aeron. Congress at Munich, Germany, Sept. 1965. Yearbook 1965, Wissenschaftliche Gesellschaft fuer Luft-und Raumfahrt, Braunschweig, Germany. Also University of Alabama Research Institute, Huntsville, UARI Res. Rep. No. 28, Sept. 1965.
9. Hermann, R., Yalamanchili, J., "Hypersonic Flow With Non-Equilibrium Dissociation Around Blunt Bodies in Flow Facilities and in Free Flight," Yearbook 1963, Wissenschaftliche Gesellschaft fuer Luftfahrt, Braunschweig, Germany.
10. Conti, R. J., "Stagnation Equilibrium Layer in Nonequilibrium Blunt-Body Flows," AIAA Journal, Vol. 2, November 1964, pp. 2044-2046.
11. Archer, R. D., Hermann, R., "Supersonic and Hypersonic Flow of an Ideal Gas Around an Elliptic Nose," AIAA Journal, Vol. 3, No. 5, pp. 987-988, May 1965.
12. Shih, W. C. L., Baron, J. R., Krupp, R. S., and Towle, W. J., "Nonequilibrium Blunt Body Flow Using the Method of Integral Relations," Massachusetts Institute of Technology, Aerophysics Lab., Tech. Rep. 66. Also DDC AD No. 415 934, May 1963.